



The
University
Of
Sheffield.

Quantum Optical Circuits using III-V
Nanophotonic Structures

Rikki James Coles

Submitted for the degree of Doctor of Philosophy

Department of Physics and Astronomy

April 2015

Abstract

This thesis describes the optical spectroscopic measurements of optical circuit elements for development of integrated quantum optical circuits using III-V semiconductors and self-assembled quantum dots.

A proposal for an on-chip spin-photon interface is made using an embedded quantum dot in the center of an unpolarised optical cavity which is selectively coupled to separate waveguides. The selectivity of the device is demonstrated using finite-difference time-domain simulations and ensemble quantum dot photoluminescence experiments. Demonstration of single photon routing using electrical control of a single quantum dot is also presented.

The demonstration of a directional coupler using III-V materials, a key component of any quantum optical circuit, with embedded quantum emitters is made. The device is demonstrated to operate at the single photon level using correlation measurements from the two output ports of the coupler using an embedded SAQD at the input.

The principle of direct readout of single quantum dot spin states in a non-chiral waveguide system is presented. The origin of directional emission of the quantum dot is explained using theoretical arguments and electromagnetic simulations. The effect is confirmed using photoluminescence spectroscopy experiments for two types of nanophotonic waveguides.

The use of whispering gallery mode resonators for on-chip filtering applications is studied. The device is designed using finite-difference time-domain simulations. Photoluminescence spectroscopy measurements are presented which demonstrate the on-chip splitting and filtering of a single quantum dot emission line by a whispering gallery mode resonator coupled to a single mode waveguide.

Development towards broadband spontaneous emission enhancement of single quantum dots in photonic crystal waveguides is presented for the purpose of on-chip indistinguishable single photon generation. The Purcell enhancement of the slow-light mode of a photonic crystal waveguide is used to enhance the spontaneous emission of emitters within the waveguide.

Acknowledgements

I have been most fortunate to study with the Low Dimensional Structures and Devices group in the Department of Physics and Astronomy at the University of Sheffield. It has been a great privilege to work with so many adept individuals from whom I have learned so much.

I therefore extend my most sincere gratitude to all those who work as part of the LSD group and to all those who support it, past and present. In particular, I would like to thank my supervisor Maurice Skolnick for his endeavours for the group, for his continual guidance during my PhD, and for the opportunity to develop myself as a researcher in the company of experts.

Outside of the department I must also thank my family, friends, and to all those who lent a friendly ear, but especially my parents who were the first to teach me to question the world around me.

And finally my praise to Vickie, who has had to endure me the most during my studies and to whom I owe a great deal.

You are a child of the universe,
no less than the trees and the stars;
you have a right to be here.
And whether or not it is clear to you,
no doubt the universe is unfolding as it should.

—*Max Ehrmann, Desiridata (1927)*

Publications

N. A. Wasley, I.J. Luxmoore, **R.J. Coles**, E. Clarke, A.M. Fox and M.S. Skolnick. “Disorder-limited photon propagation and Anderson-localization in photonic crystal waveguides”. *Applied Physics Letters* **101**, 051116 (2012).

J.H. Quilter, **R.J. Coles**, A.J. Ramsay, A.M. Fox and M.S. Skolnick. “Enhanced photocurrent readout for a quantum dot qubit by bias modulation”. *Applied Physics Letters* **102**, 181108 (2013)

R.J. Coles, N. Prtljaga, B. Royall, I.J. Luxmoore, A.M. Fox and M.S. Skolnick. “Waveguide Coupled Photonic Crystal Cavity for Quantum Dot Spin Readout”. *Optics Express* **22**, 2376-2385 (2014)

N. Prtljaga, **R.J. Coles**, J. O’Hara, B. Royall, E. Clarke, A.M. Fox and M.S. Skolnick. “Monolithic integration of a quantum emitter with a compact on-chip beam-splitter”. *Applied Physics Letters* **104** 231107 (2014)

M.N. Makhonin, J.E. Dixon, **R.J. Coles**, B. Royall, I.J. Luxmoore, E. Clarke, M. Hugues, M.S. Skolnick and A.M. Fox. “Waveguide Coupled Resonance Fluorescence from On-Chip Quantum Emitter”. *Nano Letters* **14**, 6997-7002 (2014)

C. Bentham, I. E. Itskevich, **R. J. Coles**, B. Royall, E. Clarke, J. OHara, N. Prtljaga, A. M. Fox, M. S. Skolnick, and L. R. Wilson. “On-chip electrically controlled routing of photons from a single quantum dot”, *Applied Physics Letters* **106**, 221101 (2015)

Contents

1	Introduction	1
1.1	Quantum Information Processing	1
1.1.1	Background	1
1.1.2	Outline and Scope of this Thesis	3
1.1.3	Implementation of Quantum Information Processing in the Solid State	4
1.1.4	Quantum Optical Circuits	5
1.1.5	Linear Optical Quantum Computation	6
1.2	Confinement and Guiding of Light in a Planar Architecture	8
1.2.1	Confinement by Total Internal Reflection	8
1.2.2	Photonic Bandgap Confinement	12
1.2.3	Off-Chip Detection	16
1.3	Quantum Dots	17
1.3.1	Excitonic Structure	18
1.3.2	Quantum Dots as Qubits	20
1.4	Cavity Quantum Electrodynamics	21
1.4.1	Overview	21
1.4.2	Weak Coupling: The Purcell Effect	23
1.4.3	Strong Coupling: Rabi Splitting	23
2	Methods	25
2.1	Introduction	25
2.2	Computational Methods	26
2.2.1	Finite-Difference Time-Domain	26
2.2.2	Frequency-Domain Eigenmode Solver	34
2.3	Experimental Methods	36
2.3.1	Quantum Dot Growth	36
2.3.2	Device Fabrication	37
2.3.3	Photoluminescence Spectroscopy	41
2.3.4	Spatially Selective Micro-Photoluminescence	44

2.3.5	Time Resolved Measurements	46
2.3.6	Second-Order Correlation Measurements	48
2.3.7	Cryostats	50
3	Waveguide Coupled Photonic Crystal Cavity for Quantum Dot Spin Read-	
	out	53
3.1	Introduction	53
3.2	Principles of Selective Cavity Mode Coupling	55
3.2.1	Cavity Design	55
3.2.2	Waveguide Coupling Considerations	57
3.2.3	Proposed Selective Coupling Mechanism	58
3.3	Device Optimisation Procedure	59
3.3.1	Quantification of Selective Coupling	59
3.3.2	Adjustment of Coupling Efficiency using Waveguide Proximity	60
3.3.3	Fine-Tuning of Coupling Efficiency using Continuous Adjustment of Coupling Region	64
3.3.4	Fine-Tuning of Waveguide Dispersion	64
3.4	Experimental Arrangement	67
3.5	Non-Degenerate Cavity	69
3.5.1	Origin of Mode Degeneracy Lifting	69
3.5.2	Uncoupled Cavity	69
3.5.3	Coupled Cavity	71
3.5.4	Discussion	76
3.6	Near-Degenerate Cavity	76
3.6.1	Cavity Excitation	76
3.6.2	Waveguide Excitation	80
3.6.3	Discussion	83
3.7	Further Work: Single Photon Routing using Electro-Optical Tuning	83
3.8	Summary	87
4	Monolithic Integration of a Quantum Emitter with an On-Chip Beam-	
	Splitter	89
4.1	Introduction	89
4.2	Simulation and Optimisation of Directional Coupler	90
4.2.1	Principle of Operation	90
4.2.2	Designing a Single Mode Waveguide	94
4.2.3	Optimisation of Directional Coupler	97
4.3	Experimental Arrangement	103

4.3.1	Sample Fabrication	103
4.3.2	Experimental Apparatus	104
4.4	Device Characterisation	104
4.5	Autocorrelation Measurements of Single QD	108
4.6	Cross-correlation Measurements of Single QD	110
4.7	Further Work: Quantum Interference	112
4.7.1	Overview	112
4.7.2	Interference of two Quantum Dots	112
4.8	Summary	115
5	Directional Readout of Single Quantum Dot Spins in Non-Chiral Photonic Waveguides	117
5.1	Introduction	117
5.2	Infinite Nanobeam Waveguide	119
5.2.1	Modal Properties	119
5.2.2	Dipole Dependent Longitudinal Mode Symmetry	121
5.2.3	Chiral Coupling of a Single QD	124
5.3	Nanobeam Waveguide Terminated by Outcouplers	126
5.3.1	Modal Properties	126
5.3.2	Chiral Coupling of a Single QD	129
5.4	Photonic Crystal Waveguide	137
5.4.1	Chiral Coupling of Single QD	139
5.5	Comparison Between Nanobeam Waveguide and Photonic Crystal Waveguide	144
5.5.1	Theoretical Comparison	144
5.5.2	Experimental Comparison	145
5.6	Further Work	147
5.6.1	Increased Coupling Efficiency	147
5.6.2	Lifetime Limited Coherence	147
5.7	Summary	149
6	On-Chip Spectral Filtering using Whispering Gallery Mode Resonators	151
6.1	Introduction	151
6.2	Simulation and Design of Whispering Gallery Mode Resonators	152
6.2.1	Formation of Whispering Gallery Mode Resonances	152
6.2.2	Design of an On-Chip Filtering Beam Splitter using a GaAs Microdisk Resonator	155
6.3	Sample Details	158
6.4	Characterisation of Waveguide-Coupled Microdisk Cavities	158

6.5	On-Chip Splitting and Spectral Filtering of Single QD Emission	162
6.6	Future Work	166
6.6.1	Add-Drop Filters	166
6.6.2	Add-Drop Filters using Ring Resonators	169
6.7	Summary	170
7	Towards Broadband Spontaneous Emission Enhancement of Single Quantum Dots in Photonic Crystal Waveguides	173
7.1	Introduction	173
7.2	Overview	174
7.3	Theoretical Background	175
7.4	Dispersion Modification using Lateral Hole Displacement	177
7.5	Dispersion Modification using Longitudinal Hole Displacement	182
7.6	Discussion and Future Work	188
8	Conclusions and Future Directions	189
8.1	Summary	189
8.2	Outlook	191
8.2.1	Chapter 3: Waveguide Coupled Photonic Crystal Cavity for Quantum Dot Spin Readout	191
8.2.2	Chapter 5: Monolithic Integration of a Quantum Emitter with an On-Chip Beam-Splitter	192
8.2.3	Chapter 5: Directional Readout of Single Quantum Dot Spins in Non-Chiral Photonic Waveguides	193
8.2.4	Chapter 6: On-Chip Spectral Filtering using Whispering Gallery Mode Resonators	194

List of Figures

1.1	Proposed integrated quantum optical circuit with on-chip detection.	5
1.2	SEM image of air-clad ridge waveguide.	10
1.3	GaAs micro-ring resonator with supporting AlGaAs pedestal.	11
1.4	Triangular photonic crystal lattice and band structure.	13
1.5	SEM image and mode profiles of H1 photonic crystal cavity.	15
1.6	SEM image and band structure of W1 photonic crystal waveguide.	15
1.7	SEM image and far-field profile of $\lambda/2n$ outcoupler grating.	17
1.8	Energy level diagram for neutral exciton states within a self-assembled InAs quantum dot.	19
2.1	Yee lattice and discretisation used in FDTD simulations.	28
2.2	Example results from an FDTD simulation.	30
2.3	Examples of field symmetry.	32
2.4	Dispersion curve of GaAs ridge waveguide calculated using MPB.	35
2.5	Wafer growth structure.	38
2.6	Sample fabrication procedure	39
2.7	Supercritical point drying procedure	40
2.8	SEM images for devices with and without supercritical point drying.	41
2.9	Photoluminescence excitation schemes	42
2.10	Basic photoluminescence setup.	43
2.11	Photoluminescence imaging experimental setup.	45
2.12	Example time-resolved PL trace.	47
2.13	Autocorrelation setup and example results.	49
2.14	Cold finger cryostat.	51
2.15	Bath cryostat.	52
3.1	H1 photonic crystal cavity with adjusted holes.	55
3.2	Dipole modes of H1 cavity.	56
3.3	W1 waveguide and fields of guided mode.	57

3.4	Definition of N_x and N_y	58
3.5	H1 cavity coupling efficiency to W1 waveguide.	61
3.6	Parity of evanescent field components of H1 cavity modes.	62
3.7	H _z fields of waveguide coupled H1 cavity.	63
3.8	Wavelength shift of H1 cavity modes with waveguide proximity.	63
3.9	Fine tuning of coupling efficiency.	65
3.10	Dispersion adjustment of W1 waveguide.	66
3.11	H1 cavity SEMs and PL maps.	67
3.12	Uncoupled H1 cavity modes	70
3.13	Coupled H1 spectra and polarisation for nondegenerate cavity.	72
3.14	Fabry-Perot modes of waveguides coupled to H1 cavity.	73
3.15	H1 cavity spectra when excited from the waveguides.	75
3.16	Coupled H1 spectra and polarisation for near-degenerate cavity.	77
3.17	Splitting of near-degenerate H1 cavity modes.	78
3.18	Crosstalk of near-degenerate waveguide-coupled H1 cavity.	79
3.19	Cavity spectra for near-degenerate cavity when excited from the waveguides.	80
3.20	Cavity mode polarisation when excited from the waveguides.	81
3.21	FDTD simulations of cavity fields when excited from the waveguides.	82
3.22	PIN wafer layer structure and device schematic.	84
3.23	Tuning range of single QD with applied voltage.	85
3.24	QD PL routing.	86
4.1	Schematic of directional coupler.	91
4.2	Electric field intensity profile for single mode ridge waveguide.	91
4.3	Electric field profiles of directional coupler supermodes.	92
4.4	Band structure and coupling efficiency for a dipole emitter in a ridge waveguide.	96
4.5	50:50 coupling length for directional coupler.	98
4.6	Directional coupler mode conversion loss.	100
4.7	Splitting ratio of directional coupler for different fabrication parameters.	102
4.8	SEM image of directional coupler.	103
4.9	PL maps of directional couplers of differing splitting ratios.	105
4.10	QD ensemble PL map.	105
4.11	Single QD spectrum and filtered PL map.	107
4.12	Autocorrelation measurement of single QD in directional coupler.	109
4.13	Cross-correlation measurement of single QD in directional coupler.	111
4.14	Proposed integrated quantum optical circuit with on-chip detection.	114
5.1	Schematic of ridge waveguide and coordinate definition.	119

5.2	Amplitude and phase of modal fields in an infinite single mode ridge waveguide.	122
5.3	Contrast in emission intensity between oppositely polarised dipoles visible from opposite ends of an infinite ridge waveguide.	124
5.4	Electric fields of directional emission from circularly polarised sources in an infinite ridge waveguide in the $z=0$ plane.	125
5.5	Evolution of the modal fields of the infinite ridge waveguide at a C-point over time for left and right propagation.	127
5.6	Schematic of ridge waveguide with grating outcouplers	127
5.7	Amplitude and phase of modal fields in a single mode ridge waveguide terminated with outcoupler gratings.	128
5.8	Stokes parameters for the fundamental mode of a ridge waveguide terminated by outcoupler gratings.	130
5.9	Contrast in emission intensity between σ_+ and σ_- polarised dipoles visible from opposite ends of a ridge waveguide terminated by outcoupler gratings.	131
5.10	Experimental PL spectra of QD spin states visible from the outcouplers at the ends of a ridge waveguide.	132
5.11	Plot of contrast between oppositely polarised QD emission from the outcouplers of a ridge waveguide from experimental results.	133
5.12	Contrast in emission intensity between elliptically polarised dipoles visible from opposite ends of a ridge waveguide terminated by outcoupler gratings.	135
5.13	Plot of directional emission contrast for dipole sources in a ridge waveguide terminated with grating outcouplers for $0 \leq \delta \leq 0.5\pi$	136
5.14	3D schematic of a W1 photonic crystal waveguide.	137
5.15	Amplitude and phase of modal fields of a W1 photonic crystal waveguide.	138
5.16	Stokes parameters for the mode of a W1 photonic crystal waveguide.	139
5.17	Contrast in emission intensity between σ_+ and σ_- polarised dipoles visible from opposite ends of a W1 photonic crystal waveguide.	140
5.18	Contrast in emission intensity between elliptically polarised dipoles visible from opposite ends of a W1 photonic crystal waveguide.	141
5.19	Plot of directional emission contrast for dipole sources in a W1 photonic crystal waveguide for $0 \leq \delta \leq 0.5\pi$	142
5.20	Plot of contrast between oppositely polarised QD emission from the outcouplers of a photonic crystal waveguide from experimental results.	143
5.21	Comparison of theoretical spin readout statistics between ridge and photonic crystal waveguides.	144
5.22	Comparison of spin readout statistics between ridge and photonic crystal waveguides for theoretical and experimental data.	146
5.23	Electric field profiles and phase of a micro-ring resonator.	148

5.24	Contrast in emission intensity between oppositely polarised dipoles coupled to counter-propagating whispering gallery modes	149
6.1	Simulated electric field profile of whispering gallery mode in a microdisk resonator.	153
6.2	Simulated mode spectrum of uncoupled GaAs microdisk resonator.	154
6.3	FDTD simulation results for all-pass filter using a microdisk resonator.	157
6.4	SEM image of all-pass filter using microdisk cavity with $r = 1.5\mu\text{m}$	159
6.5	PL spectrum of all-pass filter using microdisk cavity with $r = 1.5\mu\text{m}$	160
6.6	Microdisk WGM Q-factor vs waveguide separation.	161
6.7	Temperature tuning of single QD coupled to WGM in microdisk cavity.	163
6.8	Low power PL spectra showing single QD splitting and filtering between waveguide outputs.	165
6.9	FDTD simulation results for add-drop filter using a microdisk resonator.	168
6.10	Confinement potential of microdisk resonator.	170
6.11	Schematic and simulated spectrum of add-drop filter using 'flywheel' resonator.	171
7.1	Dispersion curve for W1 photonic crystal waveguide.	176
7.2	Transverse hole shifts of the modified W1 waveguide.	177
7.3	Dispersion, group index and Purcell factor of W1 waveguides with lateral hole shifts.	178
7.4	SEM image of a photonic crystal waveguide with transverse displacement applied to the two rows of holes adjacent to the waveguide.	179
7.5	Comparison of simulated and experimental group index for unmodified W1 waveguide.	180
7.6	Comparison of simulated and experimental group index for a W1 waveguide with transverse hole shifts.	181
7.7	Dispersion of first and second gap-guided modes of the W1 waveguide.	182
7.8	Longitudinal hole shifts of the modified W1 waveguide.	183
7.9	Dispersion, group index and Purcell factor of W1 waveguides with longitudinal hole shifts.	183
7.10	Comparison of the Purcell factor for W1 waveguides with lateral and longitudinal hole shifts.	185
7.11	Comparison of simulated and experimental group index for a W1 waveguide with longitudinal hole shifts.	186
7.12	Time resolved QD PL from W1 waveguide with longitudinal hole shifts.	187

Chapter 1

Introduction

1.1 Quantum Information Processing

1.1.1 Background

Since the inception of the ‘Analytical Engine’ by Charles Babbage and Ada Lovelace during the 19th Century mankind has endeavoured to develop increasingly complex computational devices, the use of which, in turn, has accelerated the rate at which man can decipher both the nature of himself and of the universe in which he resides.

The seminal work of Alan Turing during the mid-20th century laid the foundations for an entirely new branch of research into the construction and operation of computers. From the introduction of the vacuum tube (valve) to the current state-of-the-art very-large-scale integration (VLSI) using complementary metal-oxide-semiconductor (CMOS) techniques, each successive introduction of a new electronic technology has enabled the bounds of computer performance to be pushed ever further. The trends in VLSI of CMOS technology have been predictable for so long that Gordon Moore famously conjectured that the number of transistors on a processor die will double every two years. However, in recent years the progress of CMOS technology has begun to deviate from this predicted trend as the number of atoms which comprise a transistor grows ever smaller and detrimental quantum mechanical effects become significant.

In 1982 Richard Feynman proposed the idea of a computer which uses quantum mechanics to its advantage: the quantum computer [1]. These ideas were reinforced over time as researchers theorised that quantum computers could potentially solve complex problems in exponentially less time than classical computers, for example prime factorisation [2] and many-body problems [3], and could do so with substantially fewer physical resources [4]. In the early 21st century, David DiVincenzo outlined a series of requirements and desiderata for the physical implementation of quantum computing [5] and increasing research effort has been devoted to the realisation of a universal quantum computer in recent years. Many architectures have been proposed for the realisation of a quantum computer. One of the early forerunners was III-V semiconductor technologies due to the excellent optical and electrical properties of III-V systems, a wealth of mature fabrication techniques and inclusion of embedded quantum emitters in the form of self-assembled quantum dots (SAQDs).

Demonstrations of the coherent control and manipulation of SAQDs have been made [6] which reinforce their potential for linear optics quantum information processing (QIP) [7], spintronics [8], and quantum communication [9], cluster state generation [10] and quantum metrology [11]. These schemes are possible using other optical sources, for example spontaneous parametric downconversion sources [12], however the use of SAQDs provides a more scalable, integrated architecture for on-demand single photon generation. The communication of quantum information between SAQDs is a highly active field of research and current proposals utilise the SAQD as a static quantum bit (qubit) and photons as the flying qubit which encode and transmit quantum information between static bits. The construction of photonic structures and circuits containing SAQDs, which will form building blocks of future QIP networks, is the current driving force behind this field of research, with the goal of realising the first fully functional integrated quantum optical circuit.

1.1.2 Outline and Scope of this Thesis

This thesis focusses on a number of devices and principles that are relevant to the development of integrated quantum optical circuits using III-V semiconductors and SAQDs.

It begins with a chapter that introduces the general principles of quantum information processing and the associated physics for implementation using SAQDs in III-V semiconductor photonic systems.

Following this introductory chapter, Chapter 2 contains the details of the computational, experimental and fabrication methods used to perform the measurements presented in subsequent chapters.

Chapter 3 presents a proposal for an on-chip spin-photon interface using which-path encoding by embedding a SAQD in the center of an unpolarised optical cavity that is selectively coupled to separate waveguides. The selectivity of the device is demonstrated using FDTD simulations and ensemble QD photoluminescence (PL) experiments. Demonstration of single photon routing using electrical control of the SAQD is also made.

Chapter 4 demonstrates a directional coupler using III-V materials, a key component of any quantum optical circuit, with embedded quantum emitters. The device is demonstrated to operate at the single photon level using correlation measurements between the two output ports of the coupler of an embedded SAQD at the input.

The principle of direct readout of single QD spin states in a non-chiral waveguide system is presented in Chapter 5. The origin of directional emission of the QD is explained using FDTD and eigenmode solver simulations, and confirmed using SAQD PL experiments for two types of nanophotonic waveguides.

In preparation for the incorporation of on-chip single photon detection, Chapter 6 explores the application of whispering gallery mode resonators (WGMs) to optical filtering applications.

Chapter 7 presents the development towards broadband spontaneous emission enhancement of SAQDs in photonic crystal waveguides for realisation of on-chip indistinguishable single photon generation.

Finally, Chapter 8 provides a summary of the conclusions drawn from the experimental chapters and discusses the potential directions in which work in these areas can be continued.

1.1.3 Implementation of Quantum Information Processing in the Solid State

Classical computers utilise the binary system to represent information. Each binary bit takes one of two values ‘0’ or ‘1’ which is physically represented in the hardware as the charge or current flow of an electronic element within the circuit. When a charge is present or current is flowing this represents the ‘1’ state whilst ‘0’ is represented by no charge or current flow. However for quantum computing the hardware must operate according to quantum mechanical rules. This means that a quantum bit consists of the orthogonal states $|0\rangle$ and $|1\rangle$ and can exist in any linear superposition of these two basis states described by a wavefunction $|\psi\rangle = \alpha|0\rangle + \beta|1\rangle$, where α and β are complex amplitudes with the normalisation condition $\alpha^2 + \beta^2 = 1$ [4]. The information about the qubit state is therefore encoded in α and β . The power of a quantum computer lies in the fact that since each bit can be placed in a superimposed state, a quantum computer acting on a qubit register containing N qubits acts upon all 2^N contained values simultaneously whereas a classical computer can only act upon one of the 2^N states of a classical bit register at a time.

In principle, any two-level system which obeys quantum mechanics can be used as a qubit such as the electronic transitions between electron levels in cold trapped atoms [13], the single Cooper pair box of a superconducting Josephson junction [14], the polarisation bases of single photons [15], spin states of atomic nuclei in a magnetic field [16] and the spin states of excitons within a self-assembled quantum dot [7].

The DiVincenzo criteria and desiderata [5] outline the requirements for realisation of a scalable quantum computer. The use of III-V materials and solid-state photonics satisfy many of these criteria, providing a scalable and stable architecture for QIP. In addition, the mature fabrication techniques for III-V materials allow for construction of solid-state nanophotonic devices for quantum optical circuit applications as discussed in the next section.

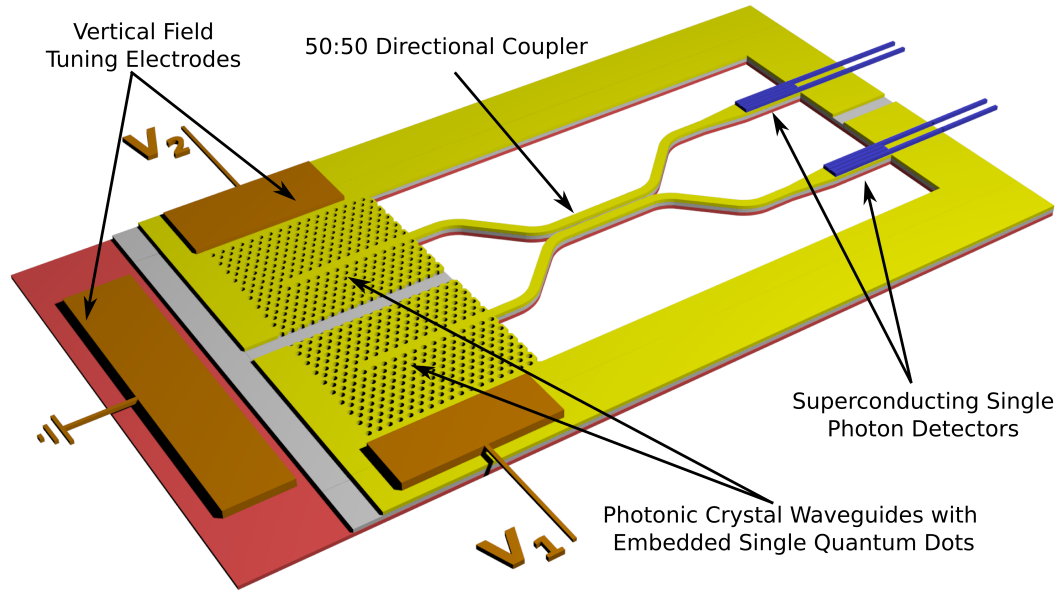


Figure 1.1: Proposed circuit model of a directional coupler on a wafer with PIN doping structure. Independent electrodes for each waveguide are made by splitting the top p-type layer (yellow) with common back n-type contact (red). The intrinsic layer is shown in grey and on-chip detectors are shown on the output waveguides in blue.

1.1.4 Quantum Optical Circuits

In essence, the purpose of a quantum optical circuit is to convey quantum information from one node to another in a reversible manner. The key challenges for any quantum optical circuits are the realisation of high-efficiency single photon sources, scalable and low-loss propagation channels, high-efficiency on-chip single-photon detection and interfacing each of these elements with minimal loss [15]. In proposed III-V systems, the on-demand single photon sources are provided by SAQDs embedded in optical cavities and waveguides [17]. The scalable optical propagation channels are provided by lithographically defined single-mode waveguides [18]. Proposals for III-V compatible single photon detectors come in the form of superconducting thin NbTiN films [19].

A proposal for such a circuit which is the current focus of research for the LDSD group at the University of Sheffield is shown in Figure 1.1. The design is for a monolithic Hong-Ou-

Mandel interferometer [20] which, if successful, will be the first demonstration of the on-chip detection of two-photon interference between separate integrated QDs on the same device. The design features two SAQDs in two input ports of a directional coupler with two single photon detectors on the output ports of the directional coupler. The device is fabricated on a wafer with P-I-N doping structure where the top P-contact is split such that the QD emission energies can be tuned via application of independent vertical electric fields to each of the QDs, using the quantum confined Stark effect.

1.1.5 Linear Optical Quantum Computation

Although, as stated in the previous section, quantum computation is possible to achieve using a variety of two-level systems the use of photons has several advantages. Firstly, the generation, manipulation and transfer of quantum states using single photons is comparatively more straightforward than in other systems [21, 22]. Indeed, one of the earliest proposals for a quantum logic gate utilised photons [23]. Secondly, photons are robust carriers of information and suffer little from interference, unlike electronic systems, which has led to their use in long-distance quantum cryptography applications [24] which is now available commercially [25–28].

It was originally assumed that for implementation of optical quantum computing that strong nonlinear interactions between optical modes were required, however in 2001 a breakthrough result showed that linear optics are sufficient for efficient quantum optical computing schemes [29]. In this scheme the only elements required are sources of single photons, optical beam splitters, optical phase shifters and single photon detectors with feedback.

Single photon sources may take the form of spontaneous parametric down conversion (SPDC) sources [30], single atoms [31] or quantum dots [32, 33] which all demonstrate antibunched single photon emission, the signature of quantum light. SPDC sources are used extensively by the silicon photonics community, whilst approaches using III-V materials utilise self-assembled quantum dots since these can be integrated within the optical structures. Detection of these single photons is typically accomplished using avalanche photodiodes, photo-

multiplier tubes or, more recently, superconducting thin NbTiN films [19] which have the added benefit of integrability into solid-state nanoscale optical circuits.

Encoding of quantum information in photons can be realised using which-path encoding to represent the photon qubit states. In this approach, two independent optical modes are used as the two-level system and it is characterised by the number of photons in each mode. For instance, the state $|20\rangle_{lm} \equiv |2\rangle_l|0\rangle_m$ is one where modes l and m contain two and zero photons respectively. In this basis, for example, $|0\rangle \rightarrow |01\rangle_{lm}$ and $|1\rangle \rightarrow |10\rangle_{lm}$. Any arbitrary input state $\alpha|0\rangle + \beta|1\rangle$ is therefore mapped onto the states $\alpha|01\rangle_{lm} + \beta|10\rangle_{lm}$ where $\alpha^2 + \beta^2 = 1$ and are complex. In an integrated optical circuit geometry, the optical modes are generally realised using two or more independent single mode waveguides.

The manipulation of the photon states in linear optical quantum computing (LOQC) is realised using straightforward optical elements: phase-shifters and beam splitters. Using these two basic components, a wide variety of quantum logic gates can be realised.

The operation of a phase shifter applies a determined phase shift to either or both of the qubit states. If the operator of the phase shifter is written \mathbf{P} then the unitary matrix associated with it is $u(\mathbf{P}) = e^{i\theta}$, where θ is the desired phase shift. An integrated phase shifter can be realised using photonic crystal waveguides [34] where the degree of phase shift applied is controlled by adjusting the location of the band edge of the guided mode. Since the W1 photonic crystal waveguide exhibits a monotonic decrease in the group velocity towards the band edge, adjustment of the dispersion of this mode controls the phase shift experienced by a photon travelling through it.

The beam splitter is used to divide light between different optical modes and to interfere them. If the operator of the beam splitter is written \mathbf{B} then its unitary matrix is

$$u(\mathbf{B}) = \begin{pmatrix} \cos(\theta) & -e^{i\phi} \sin(\theta) \\ e^{-i\phi} \sin(\theta) & \cos(\theta) \end{pmatrix} \quad (1.1)$$

where ϕ is the phase shift experienced by a photon initially in mode l which couples to m and θ is a global phase shift. For the directional coupler based beam splitters explored in

Chapter 4, the phase shift ϕ is due to evanescent tunnelling of the photon from one mode to the other and can be controlled by adjusting the relative width of the waveguides comprising the directional coupler. The global phase shift θ is a function of the coupling strength between modes l and m , and the length of the coupling region.

LQOC is based upon a series of non-deterministic operations with increasing probability of success. A series of these universal quantum gate operations can be combined together to realise all of the more complex logical operations (OR, AND, XOR, NAND etc). For quantum computation the controlled-NOT (CNOT), Hadamard and all phase-shift gates form a universal set of quantum gates [21] meaning any other logical operation can be realised through combinations of these gates. The CNOT gate conditionally reverses the state of a target qubit based upon the state of a control qubit. The Hadamard gate takes a single input qubit and performs the transformations $|0\rangle \rightarrow (|0\rangle + |1\rangle)/\sqrt{2}$ and $|1\rangle \rightarrow (|0\rangle - |1\rangle)/\sqrt{2}$.

By combining these universal gates it is theoretically possible to create a universal quantum computer. Recent work has taken important steps towards this goal by demonstrating a complex reconfigurable quantum optical circuit using these basic elements [35].

1.2 Confinement and Guiding of Light in a Planar Architecture

1.2.1 Confinement by Total Internal Reflection

The most straightforward way to confine light in a dielectric medium is using total internal reflection (TIR). At QD emission wavelengths, GaAs is a transparent dielectric with low dispersion and a refractive index of ~ 3.4 at 4K. To minimise the critical angle, the cladding material used is air which gives a critical angle of $\theta_c \sim 17^\circ$. This large refractive index contrast is beneficial for incorporation of SAQDs within the GaAs as it allows for a large fraction of the isotropic QD emission to be confined within the GaAs layer [36]. To confine the single photons emitted by a QD to a single vertical optical mode within a GaAs membrane, a slab height of 140nm is used which corresponds to $\lambda/2n$ at the centre of the QD emission

band. A thinner slab expels the guided mode from the GaAs: any thicker and higher order vertical modes can be confined to the slab. Within these upper and lower bounds 140nm was selected as this confines a mode with a transversely polarised electric field component whose maximum lies in the centre of the slab (see Section 4.2.2 for further details). The electric dipole of the QD lies in the slab plane, so the thickness is chosen to optimally confine a TE-like (even z-parity) mode which ensures the QD dipole and optical mode overlap well and are co-polarised. To restrict optical propagation to a single lateral mode, two main approaches are used. This section discusses the use of total internal reflection for in-plane confinement. Photonic bandgap confinement is discussed in the next section.

Suspended Nanobeam Waveguides

The suspended nanobeam waveguide (SNB) utilises TIR for confinement out-of-plane and one in-plane direction, producing a thin wire of rectangular cross section. The device is air-clad in two directions which is achieved by etching of the surrounding material and the waveguide is attached to the surrounding GaAs membrane at its ends. The vertical height of the waveguide is fixed during wafer growth (at 140nm) so the choice of lateral dimension is crucial in determining the mode structure of the resulting waveguide. This optimisation is discussed in more detail in Chapter 4.

The high refractive index contrast of GaAs in air couples up to 95% of the emission from a linearly polarised QD and provides strong confinement of a single optical mode for a cross-sectional aspect ratio of ~ 2 . Since the mode is strongly confined to the waveguide, the propagation loss is very low [37] and tight bend radii of $< 1\mu\text{m}$ can be achieved without significant radiative losses [38]. An SEM image of a typical SNB waveguide is shown in Figure 1.2 for $280\text{nm} \times 15\mu\text{m} \times 140\text{nm}$ dimensions.

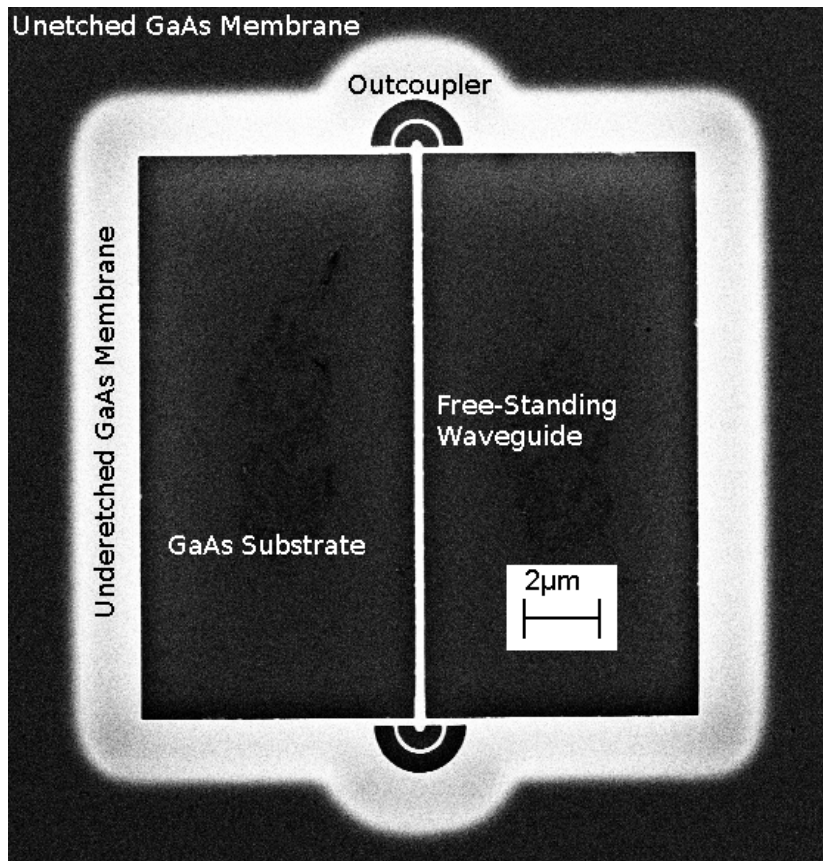


Figure 1.2: SEM image of air-clad ridge waveguide with outcoupler gratings.

The principal use of SNBs is for the propagation of light between different circuit elements. The waveguides are either directly connected to other circuit elements [39] or coupled using the evanescent fields of the waveguide mode [40, 41]. Since the group velocity of the waveguide mode is $\sim c/n$ the photon local density of states is not increased significantly over that of bulk GaAs. As such, the spontaneous emission rate of a coupled QD in the waveguide is comparable to that of a QD in bulk GaAs [42, 43]. To provide spontaneous emission enhancement, inclusion of an optical cavity is required.

Whispering Gallery Mode Resonators

A whispering gallery mode (WGM) resonator is composed of a dielectric material with cylindrical or circular symmetry. In GaAs, whispering gallery mode resonators are formed by etching the membrane into a disk or ring shape with an AlGaAs pedestal underneath to support the resonator. A ring-like resonator is shown in Figure 1.3. The outer edge of the resonator is air clad, and modes are guided along its circumference by total internal reflection. Since the modes must complete an integer number of periods around the disk, resonances are formed at discrete wavelengths. The mode structure of WGMs is discussed in more detail in Chapter 6.

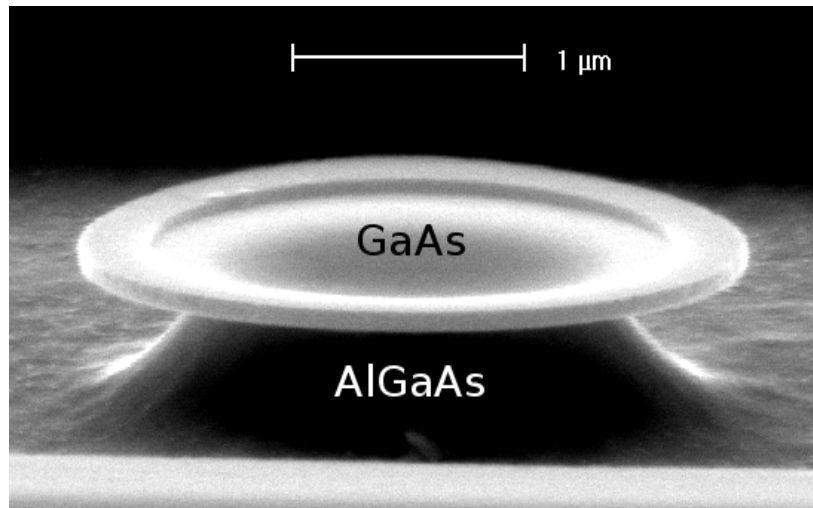


Figure 1.3: GaAs micro-ring resonator with supporting AlGaAs pedestal. The inner and ring radius is $1.2\mu\text{m}$ and $1.5\mu\text{m}$ respectively.

Whispering gallery mode resonators have many applications in the field of quantum optics. Using III-V semiconductors allows for the incorporation of SAQDs within the resonator [44]. Demonstrations of many cavity quantum electrodynamic effects have been made for the weak coupling regime [44, 45] and strong coupling regime [46, 47] including lasing [48] and production of a single photon source [45, 49]. Monolithic fabrication of the resonators also facilitates coupling to air-suspended SNBs for integrated optical circuit applications [41, 50].

1.2.2 Photonic Bandgap Confinement

Photonic crystals (PHC) slabs are two-dimensional structures with periodic dielectric structure. This periodicity causes optical modes propagating through the crystal to separate into two bands known as dielectric and air bands which, by comparison with electronic band structures, are analogous to the valence and conduction bands of semiconductor crystals, respectively. The bands are so named since modes in the dielectric band have their field maxima in the dielectric slab material and modes in the air band, the air holes. For sufficiently large refractive index contrast, a photonic band gap (PBG) occurs between the two bands where propagation of light is forbidden [51, 52]. Light whose wavelength lies within this PBG is evanescent within the PHC lattice and the PHC acts as a mirror. The PHCs used in this thesis consist of a triangular lattice of air holes etched into a GaAs membrane as shown in Figure 1.4(a). The optical band structure of such a PHC is shown in Figure 1.4(b). Since out-of-plane confinement is provided by TIR, only modes which violate Snell's law are confined to the slab. The boundary of this condition (known as the light line) is shown in grey in the band structure Figure 1.4(b): modes which lie below this are confined to the slab. Although better mode confinement is achieved using fully three dimensional PHCs, the planar slab type PHC integrates well with other monolithic optical circuit elements whilst still providing good out-of-plane optical confinement [53].

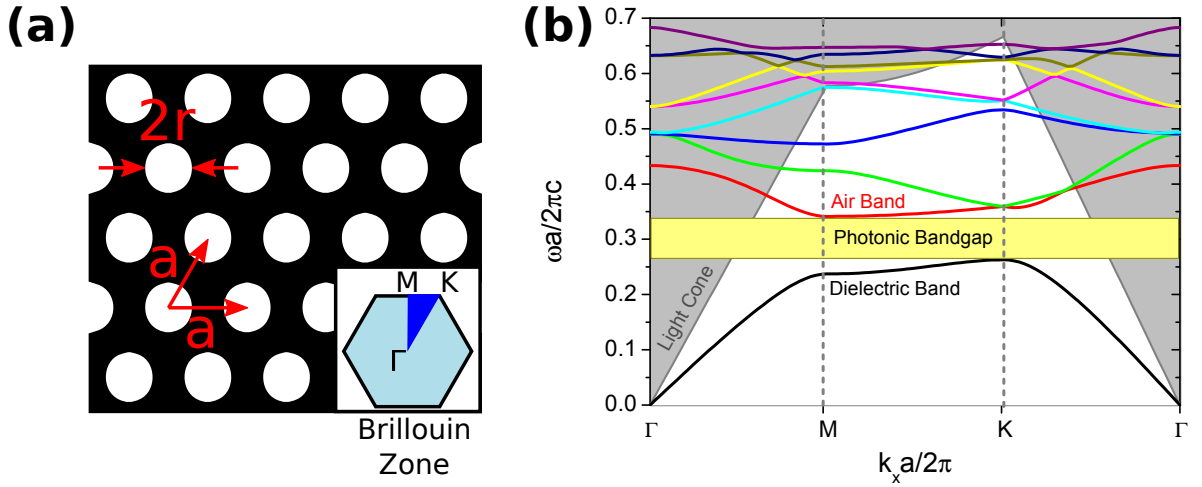


Figure 1.4: (a) Hexagonal photonic crystal lattice and (b) band structure. The photonic crystal is composed of a triangular lattice of holes (white), radius r with lattice constant a etched into a GaAs membrane (black). Band structure is calculated between symmetry points of the irreducible Brillouin zone using MPB [54].

Localised Defect States

Filling in holes within the photonic crystal creates defect states within the PBG. By comparison to semiconductor theory, these modes are donor-type [55] since the modes are pulled down from the air-band, analogous to n-type dopants in a semiconductor crystal. Acceptor-type states are possible, but are not compatible with SAQD integration since these modes are confined within air-filled regions. Because the defect mode is forbidden in the surrounding lattice it is well confined in two dimensions and a cavity is formed. PHC cavities are of particularly high interest due to the small mode volumes inherent to the design. Two cavities have proven to be useful for cavity QED applications, known as the L3 and H1 cavities.

The L3 cavity is formed when three holes are omitted in a line, producing a linear defect [56]. The modes of the L3 cavity are linearly polarised and have been the subject of much research. Demonstrations of strong coupling of an embedded SAQD [57], dipole induced transparency [58] and efficient single photon sources [59] illustrate a small selection of applications of the L3 cavity.

The H1 cavity is formed when a single hole is omitted, producing a point defect as shown in Figure 1.5(a). The electric field profiles of the fundamental dipole modes of the H1 cavity are shown in Figure 1.5(b). The holes adjacent to the cavity are displaced with reduced radius to increase the Q-factor of the cavity modes by reducing out-of-plane scattering losses [56, 60]. This cavity has been of substantial interest due to the exhibition of unpolarised modes [61–66] to which the spin states of a SAQD can be directly mapped [67]. From Figure 1.5(b) however it is not immediately apparent that these modes are indeed degenerate as the two exhibit different field profiles, but using group theory analysis it can be shown that this is indeed the case [61, 62, 68] due to C_{6v} symmetry of this point-defect cavity. Using FDTD simulations with a high resolution of 90 grid points per lattice constant, it can also be shown that these modes are spectrally degenerate [67] despite exhibition of non-degenerate field distributions. In FDTD simulation at low resolution the modes appear spectrally non-degenerate due to the use of a cubic Yee lattice. A triangular photonic crystal lattice has a vertical separation between holes of $\sqrt{3}a/2$ and therefore a high grid resolution is required to accurately resolve this irrational number to a suitable number of decimal places. In fabricated devices, systematic and random errors can also lead to breaking of symmetry which breaks the degeneracy of the modes. This can however be avoided by either stretching the photonic crystal lattice design to counter any systematic error [65] or by uniaxial strain applied to the wafer after fabrication [66].

The H1 cavity possesses among the smallest possible mode volumes which provides a large material interaction strength of the confined mode. This has made it possible to observe strong coupling [69] and indistinguishable single photon emission [70] of an SAQD coupled to the cavity mode.

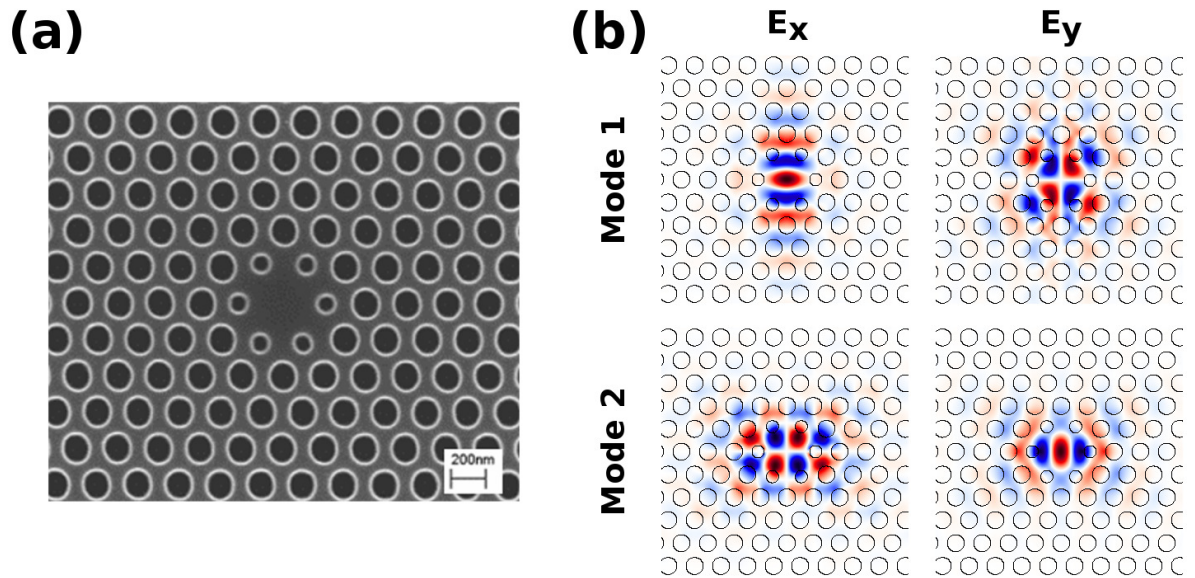


Figure 1.5: (a) SEM image of H1 photonic crystal cavity. (b) Electric field profiles of the two degenerate dipole modes of the H1 cavity.

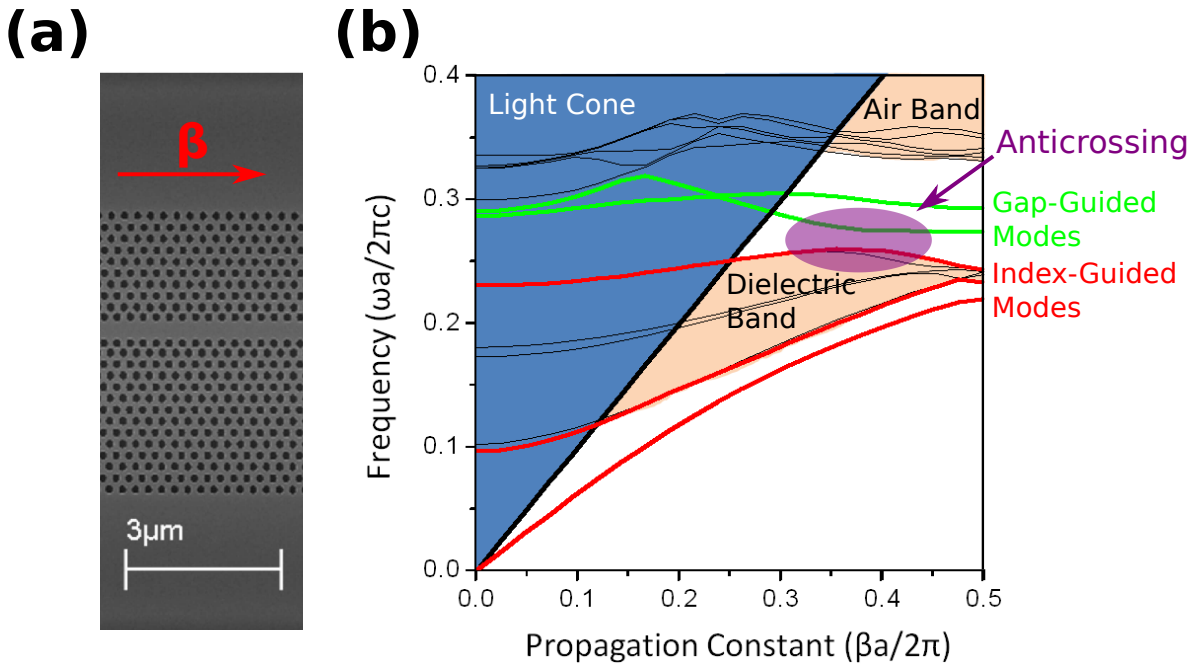


Figure 1.6: (a) SEM image and (b) band structure of W1 photonic crystal waveguide.

Propagating Defect States

Omitting air cylinders along a complete row of a PHC slab creates defect states within the PBG within which optical modes are free to propagate along the defect axis. This linear defect is known as a W1 waveguide. Figure 1.6(a) shows an SEM image of a section of a W1 waveguide with the associated band structure in Figure 1.6(b). Within the bandgap, two modes are confined by the PHC lattice.

The fundamental ‘gap-guided’ mode (green lines of Figure 1.6(b)) exhibits marked dispersive properties as it approaches the band edge. Since the waveguide is comprised of high refractive index material within a low index cladding, modes are also confined by TIR (red lines of Figure 1.6(b)). The fundamental ‘gap-guided’ mode is coupled to these ‘index-guided’ modes which produces an anticrossing between the lower ‘gap-guided’ mode and upper ‘index-guided’ mode of the dielectric band (shown in purple of Figure 1.6(b)). This anticrossing induces a monotonic decrease in the group velocity of the gap-guided mode, which tends towards zero as it approaches the edge of the Brillouin zone [71]. From frequency-domain simulations, near the light cone the group velocity of the fundamental gap-guided mode is $\sim c/4$, however at the band edge this drops to $\sim 10^{-3}c$ [72]. Termed the slow light mode [72, 73], the increased material interaction time afforded by the mode in this region has been the focus of quantum optics research groups for the realisation of highly efficient on-chip single photon sources [74–82] and on-chip delay lines [34].

1.2.3 Off-Chip Detection

One of the important goals for integrated quantum optical circuits is the ability to integrate single photon detectors onto the GaAs membrane [19, 83, 84]. For intermediate study of circuit designs however, it is advantageous to utilise off-chip detection methods. Since much effort has been made to ensure the optical modes are well confined to the GaAs membrane, efficient extraction of the light is non-trivial. One approach is to use Bragg gratings to scatter the light out of the device plane and into the detection apparatus [58, 82]. The grating period used is $\lambda/2n$ which minimises back reflection into the waveguide and a semicircular grating is

used to focus the scattered light vertically within a small angle. The design of outcoupler used in this thesis is shown in Figure 1.7(a) where the grating is attached to a SNB waveguide. The simulated far-field profile is shown in Figure 1.7(b), which is calculated for fields above the grating projected onto a hemisphere of radius 1 metre [85]. This includes the GaAs substrate $1\mu\text{m}$ beneath the grating.

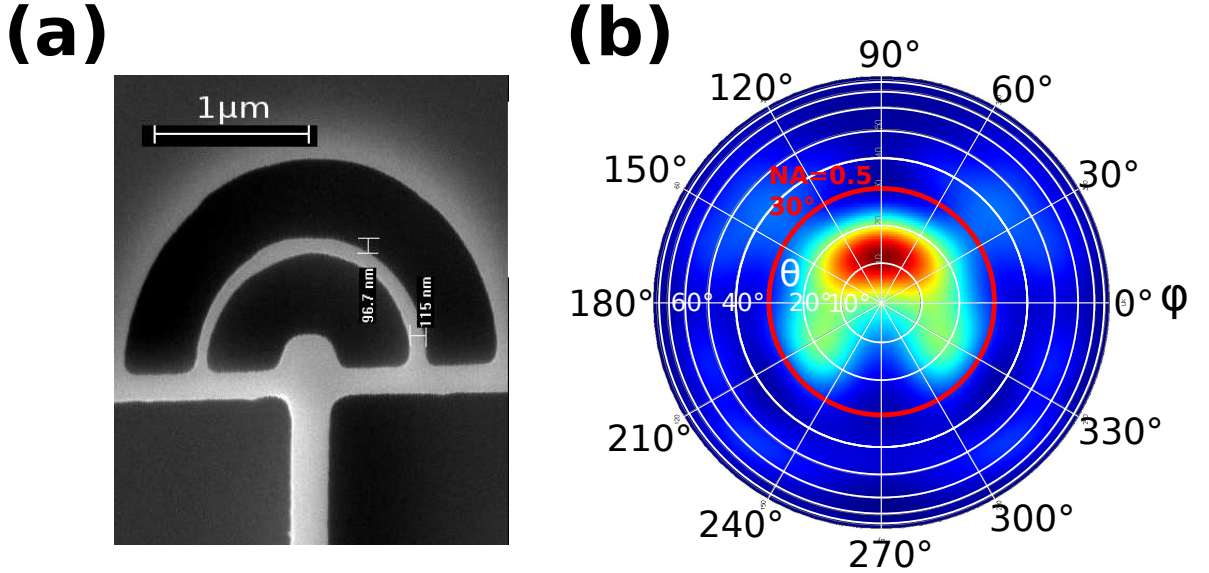


Figure 1.7: (a) SEM image and (b) far-field profile of $\lambda/2n$ outcoupler grating. The far-field profile is calculated for a hemisphere of radius 1m centered on the outcoupler. ϕ is the azimuthal angle and θ is the polar angle.

1.3 Quantum Dots

The quantum dots (QDs) used in this thesis consist of discrete, strained InAs islands $\sim 20\text{nm}$ wide and $\sim 2\text{nm}$ high incorporated in a [100] GaAs host matrix [86]. The growth of QDs is covered in Chapter 2. Since the bandgap of the surrounding material is greater than that of the QD material a potential well is formed which provides three-dimensional confinement of electrons. Due to complete size quantization of the electronic levels in the QD, the electron and hole densities of states are discrete. This gives the QD atomic-like emission properties and behaves as a two-level emitter [87].

The emission wavelength of the QD can be controlled by adjustment of the spatial extent of the QD. The QDs used in this thesis operate in the near infrared spectrum (900nm-1 μ m). This spectral region is used as it coincides with the high performance range of silicon photodetectors and the GaAs host matrix is transparent and weakly dispersive. Since the QD emission energy is close to the GaAs bandgap energy, carriers confined to the QD can be scattered out by phonon interactions at energies kT (where k is the Boltzman constant and T is temperature). To minimize the effect of phonon scattering for efficient QD fluorescence the QDs must be cooled to temperatures below 50K using the liquid helium cryostat systems presented in Chapter 2.

1.3.1 Excitonic Structure

Owing to the nanoscale dimensions of the quantum dot in all three dimensions, electrons are confined within a very small volume. Solutions of the Schrödinger equation yield discrete energy levels for the electrons and holes. At cryogenic temperatures of 50K and below, the thermal energy of the electrons, $k_B T$, is much lower than the energy separation between these levels. Therefore, a single electron (hole) added to the QD populates only the first level in the conduction (valence) band. This discrete behaviour of QDs is why they are often referred to as ‘artificial atoms’ and provides the two-level system required for QIP applications.

Trapped electrons and holes form bound excitonic states within the QD. Electrons in the conduction band have an s-type wavefunction with spin $s = \pm 1/2$ and zero angular momentum whilst holes in the valence band have a p-type wavefunction with spin $s = \pm 1/2$ and orbital angular momentum $l = 1$. Strain within the quantum dots cause by the GaAs-InAs lattice mismatch lifts the degeneracy of light ($m_j = \pm 1/2$) and heavy holes ($m_j = \pm 3/2$), producing a typical splitting of ~ 30 meV. The light hole states can therefore be neglected when considering the lowest energy levels of the quantum dots. The total angular momentum projections of the lowest energy exciton states are $m_j = \pm 1, \pm 2$. The states with $m_j = \pm 2$ do not optically couple as this requires an angular momentum transfer of twice that provided by photons and are therefore known as dark states. The short range electron-hole exchange interaction couples

the electron and hole spins which lifts the degeneracy of the bright and dark exciton states. For dots with asymmetry, the degeneracy of both bright and dark excitonic manifolds is lifted, known as fine structure splitting (FSS). The FSS is larger in magnitude for the bright excitons due to the long range part of the exchange interaction affecting only the bright excitons, whilst the short range part of the exchange interaction mainly affects the splitting between bright and dark manifolds [88]. A schematic of the excitonic energy levels of the QD is shown in Figure 1.8.

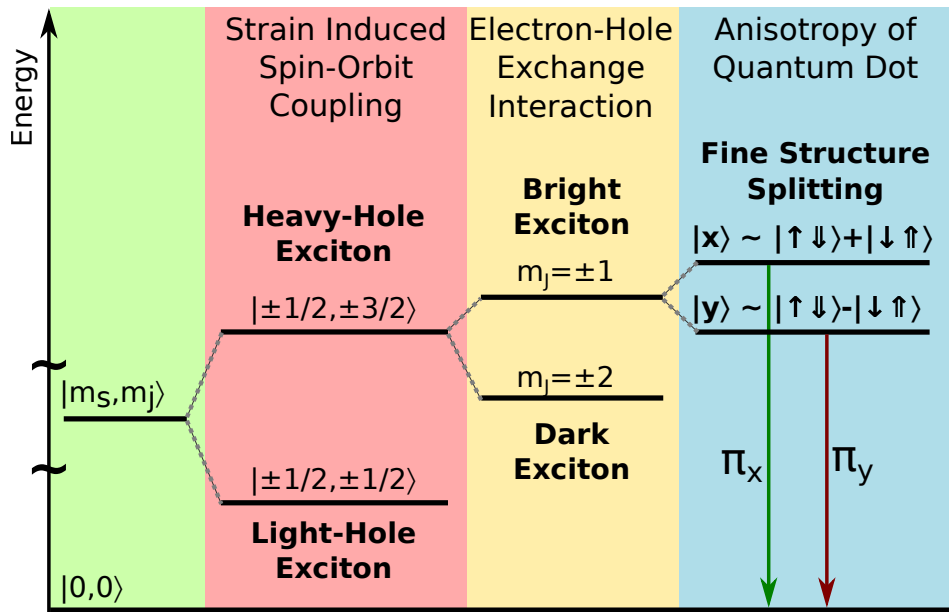


Figure 1.8: Energy level diagram for neutral exciton states within a self-assembled InAs quantum dot. Multi-excitonic and charged species are not shown.

The two FSS states of the bright exciton radiatively recombine and emit photons which are orthogonally polarised to one another (π_x and π_y), coincident with the $[110]$ and $[1\bar{1}0]$ crystal axes. For QDs with zero FSS, the X_0 emission is unpolarised. The application of an external magnetic field can be used to further lift the degeneracy of the QD spin states. At high fields, applied parallel to the QD growth direction, the Zeeman interaction exceeds the exchange interaction and the linearly polarised FSS states become circularly polarised [88].

The neutral exciton transition in a QD produces antibunched single photon emission. The origin of this phenomenon can be understood by considering the cascade from the biexciton

state to the ground state via the neutral exciton state. When one exciton from the biexciton state recombines, the resulting photon energy is that of the exciton energy plus the Coulomb interaction energy between the two confined excitons in the QD. The sign and magnitude of this interaction energy can vary between different QD systems, but is always present due to small distances between the excitons in a QD. The second exciton (neutral exciton state) subsequently decays, emitting a photon with energy equal to the neutral exciton energy [89]. Therefore, the two transitions are spectrally distinct such that emission from the exciton-ground state transition is antibunched with single photons separated by the radiative lifetime [49] and resonant excitation of this transition addresses only the neutral exciton [42, 90]. This radiative cascade is central to proposals for single photon generation, as in [89]. Since the carriers in the QD must obey the Pauli exclusion principle, the biexciton is a spin singlet state and exhibits neither exchange nor Zeeman splitting [88]. However, since the neutral exciton state is split by the Zeeman interaction, the biexciton-neutral exciton transitions are split by a similar energy.

1.3.2 Quantum Dots as Qubits

The two-level system of the exciton in a QD represents a good candidate for a qubit. Efficient optical coupling of QDs [91] facilitates the direct transfer of quantum information between static (QD) and flying qubits (single photons) [92]. Complete optical control of the exciton [93], electron [94] and hole [95] spins have been demonstrated, which illustrate the QDs candidacy for a solid state qubit.

The coherence time of the neutral exciton depends on many experimental conditions which, since quantum dots are solid-state systems, arise mainly from interactions with the environment in and surrounding the QD. These consist of crystal lattice vibrations (LA-phonons), heavy-light hole mixing, nuclear spin interactions and charge fluctuations, amongst others [6]. At low temperatures ($\sim 4\text{K}$), the coherence of a QD in bulk GaAs is limited by the radiative recombination [96], with coherence times of 400-1000ps [97, 98]. In photonic structures however, this figure reduces due to the introduction of other dephasing processes from proximity

of etched surfaces to the QD, which include surface induced nonradiative recombination mechanisms [99] which can ultimately completely quench the QD emission. In addition, charge fluctuation and spin interactions with the nuclei present additional decoherence mechanisms [33] leading to a typical coherence time of ~ 150 ps. However, the effects of decoherence can be reduced using resonant excitation of the QD in the weak coherent scattering regime where the QD inherits the coherence of the driving field [42, 90] which, for laser excitation, can produce coherence times of up to 22ns [100].

The use of individual carrier spins in QDs has gained much research interest, with demonstrated spin lifetimes up to 1ms for the electron [101]. The wavefunction of the heavy hole has a p-type wavefunction which means the hyperfine interaction with the atomic nuclei in the QD which is responsible for decoherence processes is substantially reduced compared to the electron [102]. A challenge with using carrier spins is that they do not directly interact with photons, so ultrafast optical pulses are required using charged excitonic complexes. For neutral excitons however, the effects of decoherence can be circumvented by embedding the QD in an optical cavity. The Purcell enhancement of this system can be such that the radiative emission time dominates over the dephasing time in determining the coherence time [70, 103].

1.4 Cavity Quantum Electrodynamics

1.4.1 Overview

If a quantum emitter is embedded in a cavity such that the emitter can absorb photons from the cavity modes and also emit photons into the cavity modes and the two are in resonance then a number of interesting physical phenomena can be observed. The behaviour describing this system is referred to as cavity Quantum Electrodynamics (cQED) and is characterised by three interactions parameters, which are discussed for a quantum dot emitter. These are the photon loss rate of the cavity, κ , the non-resonant emission rate of the emitter, γ , and the emitter-photon coupling rate, g_0 .

The cavity loss rate κ represents how long a photon can remain in the cavity, related to the Q-factor by $\kappa = \omega/Q$ where ω is the angular frequency of the cavity resonance. This quantity is controlled by the cavity geometry and mirror reflectivity.

The nonresonant emission rate γ is the off-resonance population decay rate, which includes emission into the continuum of non-resonant cavity modes and non-radiative recombination processes. The non-radiative recombination rate in QDs is typically negligible at 4K [33]. The emission into non-resonant cavity modes can be suppressed by reducing the spectral density of non-resonant cavity modes. This can be achieved by using photonic crystals and distributed Bragg reflectors which establish an optical band gap spectrally and spatially adjacent to the cavity mode(s).

The emitter-photon coupling rate determines how quickly energy is exchanged between the emitter and the cavity mode at resonance. This quantity, known as the Rabi frequency, is given by

$$g_0 = \left(\frac{\mu^2 \omega}{2\epsilon_0 \hbar V_0} \right)^{1/2} \quad (1.2)$$

where μ is the electric dipole matrix element of the emitter transition, ω is the angular frequency, V_0 is the modal volume of the cavity mode. The dipole matrix element of a quantum dot is largely determined by its size, which in addition affects the emission frequency. However for fixed QD parameters the emitter-photon coupling rate is determined by the size of the cavity, which is why nanophotonic cavities are of such interest since the modal volume is on the order of $(\lambda/n)^3$.

The relative magnitude of these three parameters allow the system to be characterised into two regimes of operation. The system is operating in the weak coupling regime when photons in the cavity are lost before the emitter can reabsorb them, when $g_0 \ll (\kappa, \gamma)$. When operating in the weak coupling regime, the emission of the quantum dot is irreversible but the emission rate of the quantum dot is affected by the cavity. By contrast, in the strong coupling regime the emission is a reversible process as the emitted photon can be reabsorbed by the emitter before leaving the cavity, i.e. when $g_0 \gg (\kappa, \gamma)$.

1.4.2 Weak Coupling: The Purcell Effect

As stated in the previous section, when the system is operating in the weak coupling regime the quantum dot emission is irreversible but the emission rate is affected by the cavity. Since the local density of final photon states is greater for the confined modes of a cavity than those of free space, according to Fermi's golden rule the emission rate of the quantum dot is increased on resonance with the cavity mode. This is quantified by the Purcell factor which is given by the ratio of the emission rate in the cavity, Γ_{cav} , to that of free space, Γ_{FS} , given by

$$F_p = \frac{\Gamma_{cav}}{\Gamma_{FS}} = \frac{3Q(\lambda/n)^3}{4\pi^2V_0}\xi^2L(\omega) \quad (1.3)$$

where Q is the cavity Q-factor, λ and ω are the wavelength and angular frequency of the emitter respectively. The normalised dipole orientation factor $\xi = |\mathbf{p} \cdot \mathbf{E}|/|\mathbf{p}||\mathbf{E}|$ represents the polarisation and spatial alignment between the emitter and cavity mode fields, where \mathbf{p} is the dipole moment of the emitter and \mathbf{E} is the electric field of the cavity. The spectral lineshape of the cavity $L(\omega) = \Delta\omega_c^2/[4(\omega - \omega_c)^2 + \Delta\omega_c^2]$ is Lorentzian with centre angular frequency ω_c and half linewidth $\Delta\omega_c$ so the spontaneous emission enhancement follows the same spectral dependence. A full derivation of the expression for the Purcell factor is available in [104].

The experimental signature of weak coupling is an increase in the emission intensity and shortening of the radiative lifetime of an emitter within the cavity when tuned onto resonance with the cavity mode [105].

1.4.3 Strong Coupling: Rabi Splitting

In the strong coupling regime the emission is a reversible process as the emitted photon can be reabsorbed by the emitter before leaving the cavity. If the ground and excited states of the emitter are written as $|g\rangle$ and $|e\rangle$ and the number of photons in the cavity, n , then when strongly coupled the degeneracy between the emitter and cavity states is lifted, producing the doublet states $\psi_n^\pm = \frac{1}{\sqrt{2}}(|g; n\rangle \mp |e; n-1\rangle)$ with an energy splitting $\Delta E_n = \sqrt{n}\hbar g_0$, known

as the vacuum Rabi energy. This system is described by the Jaynes-Cummings Hamiltonian [106]. Since the two states are superimposed emitter and cavity states they are polaritonic in nature, being neither purely photon-based or exciton-based.

The experimental signature of strong coupling is a splitting between the emitter and cavity peaks at resonance in the emission spectrum. When the two are tuned through resonance, the two peaks show an avoided crossing (anticrossing) [46, 57, 107, 108].

Chapter 2

Methods

2.1 Introduction

This chapter contains details of the computational and experimental methods used for modelling and study of the devices presented in subsequent chapters.

It begins with information on the computational techniques used to simulate the electromagnetic properties of the devices. The general principles of finite-difference time-domain simulations are presented along with a discussion of the accuracy and computational cost of accurate modelling. Schemes used to circumvent some of these issues are also discussed. Following this, a description of frequency-domain simulation principles are presented, using the eigenmode solver method.

Following this, principles of the growth of quantum dots (QD) and the procedures used to fabricate the devices used for measurements in subsequent chapters are shown. That section begins by presenting the method of self-assembled QD growth using molecular beam epitaxy (MBE), followed by a presentation of the lithographic procedure used for turning a bare wafer into an integrated quantum optical device.

Subsequently, a presentation of the spectroscopic, spatial and temporal optical measurement techniques is made alongside details of the experimental implementations of these techniques in the laboratory. Starting with an explanation of the principle of photoluminescence spectroscopy using resonant and non-resonant excitation schemes, this section goes on to dis-

cuss the methods used for analysis of QD emission using spectral, temporal and correlation measurements. The principles of the experiment and laboratory implementation are presented alongside example results.

This chapter concludes with an overview of the cryogenic systems used for QD measurements. The two architectures used consist of continuous flow and bath liquid helium cryostats respectively.

2.2 Computational Methods

Computational electromagnetic simulations are performed in order to investigate the behaviour of semiconductor nano-optical devices prior to fabrication. These tools allow for the study of device performance using the framework of Maxwells equations and facilitate the optimisation of device design parameters to ensure that fabricated devices perform as expected. Two distinct methods are employed in this thesis: time domain (Section 2.2.1) and frequency domain simulations (Section 2.2.2). Time domain simulations were employed when the temporal response of a photonic device was under investigation: for example the calculation of Q-factors of resonant modes and transmission spectra. Frequency domain simulations were employed when the properties of propagating modes were under investigation, such as the dispersion of waveguide modes, propagation constants and effective indices.

2.2.1 Finite-Difference Time-Domain

Software Used

Time-domain simulations were performed with the finite-difference time-domain (FDTD) method [109], using either the freely available software package MEEP [110], a commercial-grade simulator based on the FDTD method, Lumerical FDTD [85] or a commercial-grade simulator eigenmode solver and propagator, Lumerical Mode Solutions [111]. Time domain simulations were employed when the temporal response of a photonic device was under investigation. The FDTD method is common to all software used, but each has a different implementation or individual advantage, which are explored in the next section.

Principle of Operation

The finite-difference time-domain (FDTD) method is used for prediction of the steady-state electromagnetic field propagation through arbitrary dielectrics and conductors [109]. It operates by iteratively propagating the fields from a light source in the system according to Maxwell's equations in discrete time steps over a finite lattice of cells which include the structure under investigation.

There are numerous implementations of the FDTD method, but central to each method are the differential versions of Faraday's Law of Induction and Ampère's Circuital Law (with Maxwell's correction):

$$\frac{\partial \mathbf{B}}{\partial t} = -\nabla \times \mathbf{E} - \mathbf{J}_B, \quad (2.1)$$

$$\frac{\partial \mathbf{D}}{\partial t} = \nabla \times \mathbf{H} - \mathbf{J} \quad (2.2)$$

where (respectively) \mathbf{E} and \mathbf{H} are the macroscopic electric and magnetic fields, $\mathbf{D} = \epsilon \mathbf{E}$ and $\mathbf{B} = \mu \mathbf{H}$ are the electric displacement and magnetic induction fields, \mathbf{J} is the electric-charge current density and \mathbf{J}_B is a fictitious magnetic-charge current-density (added as a computational convenience when dealing with magnetic dipole sources) [110].

A dielectric map $\epsilon(\mathbf{r})$, which represents the device structure, and a current source $\mathbf{J}(\mathbf{r}, t)$ or $\mathbf{J}_B(\mathbf{r}, t)$ are defined within a simulation volume, where $\mathbf{J}(\mathbf{r}, t) = \mathbf{J}_B(\mathbf{r}, t) = 0$ for $t < 0$. The simulation domain is divided into a cubic lattice of cell size $\Delta \mathbf{r}$, which approximates the dielectric map $\epsilon(\mathbf{r})$ onto a voxel array $\epsilon(\Delta \mathbf{r})$, as shown in Figure 2.1(a). The electric fields are recorded along the vertices of each voxel and the magnetic fields through the faces. This cubic lattice structure is known as a Yee lattice [112] and is illustrated in Figure 2.1(b).

The spatial and time derivatives of Equations (2.1) and (2.2) are then approximated by finite differences in space (using the Yee lattice $\Delta \mathbf{r}$) and time (by iterating the simulation over discrete time steps Δt). The current sources are switched on at time $t = 0$ and the central algorithm of the simulation proceeds in a two step 'leap-frog' fashion using these discretised

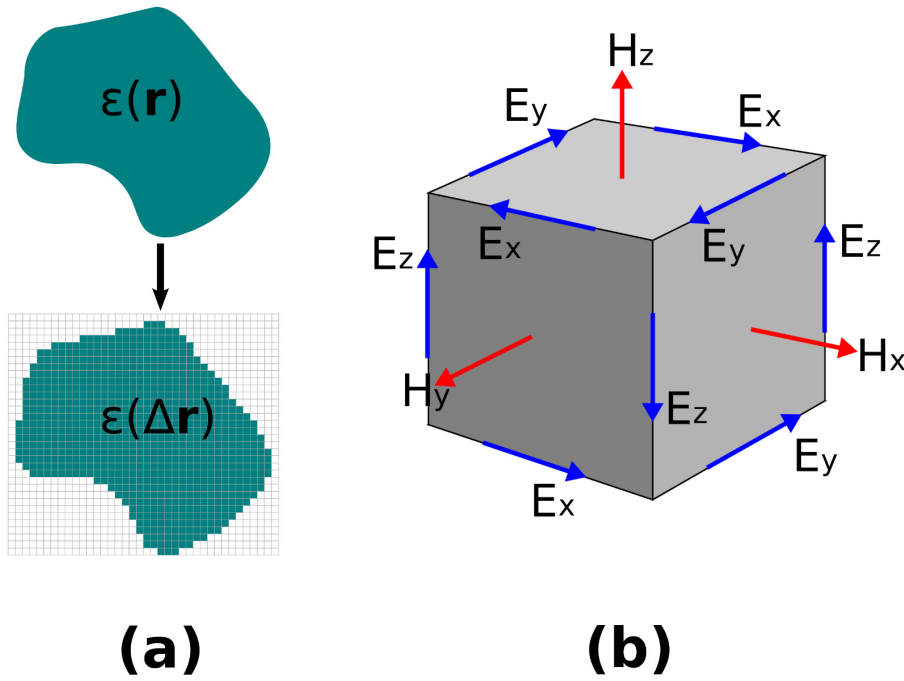


Figure 2.1: (a) Schematic illustrating the procedure by which an arbitrary dielectric map $\epsilon(\mathbf{r})$ is mapped onto a cubic voxel array to produce $\epsilon(\Delta\mathbf{r})$. In actual simulations, lattice cells that are intersected by a dielectric boundary are filled with a weighted intermediate dielectric constant or the lattice resolution is increased to ensure the interface lies along a vertex of the lattice. (b) Schematic of the electromagnetic fields on a single voxel of the Yee lattice used in FDTD simulations. The electric fields are calculated along the vertices whilst the magnetic fields are calculated for the faces.

equations as follows:

1. The electric fields are computed at time t using the electric fields at $t - \Delta t$, the magnetic fields at $t - \frac{\Delta t}{2}$ and any source currents $\mathbf{J}(\mathbf{r}, t)$, $\mathbf{J}_B(\mathbf{r}, t)$.
2. The magnetic fields at $t + \frac{\Delta t}{2}$ are computed from the magnetic fields at $t - \frac{\Delta t}{2}$ along with the electric fields at t and any source currents $\mathbf{J}(\mathbf{r}, t)$, $\mathbf{J}_B(\mathbf{r}, t)$.

These two processes form a single iteration of the FDTD algorithm. The procedure repeats again for the electric and magnetic fields every Δt , with the magnetic fields offset by $\pm\Delta t/2$.

The end point of the simulation may be defined either by a maximum time limit T , or a minimum threshold of remaining energy within the simulation domain. Further details are available in [113].

An example of the results from an FDTD simulation are shown in Figure 2.2. The simulation consists of a linearly polarised dipole source in the centre of a GaAs waveguide ($n = 3.4$) in a background medium of air. A short impulse is used which has a Gaussian profile with a centre normalised frequency $\omega_0 a / 2\pi c = 0.5$ and FWHM $\Delta\omega a / 2\pi c = 1$ and provides a broad spectral window for study. The simulation is run for long times to ensure good spectral resolution. The propagation of the fields is illustrated in Figure 2.2(a) at three different time steps during the simulation. Flux monitors are placed at the ends of the waveguide, and the power flow of the fields through these planes are recorded. The transmission of the dipole power through both ends of the waveguide is shown in Figure 2.2(b). A drop in transmission is observed for a normalised frequency $\omega a / 2\pi c \sim 0.27$ due the appearance of dipole emission into higher order transverse modes which are less well confined to the waveguide than for lower order modes. The transmission monitor records the fields confined to the waveguide, so the partially delocalised fields of the higher order modes are not fully captured by the monitor.

Continuity

A challenge with discretisation of the system is maintaining accurate behaviour of continuity within the simulation. The dielectric map $\epsilon(\mathbf{r})$ is approximated by the simulation lattice to $\epsilon(l, m, n)$ where l, m, n are the voxel indices.

As $\Delta\mathbf{r}$ is reduced, the simulated results tend more towards the real physical system, subject to the numerical stability condition [114] $C \equiv \Delta t / \Delta r \leq n_{min} / \sqrt{N_D}$ where C is the Courant factor, n_{min} is the lowest value of the refractive index in the simulation and $N_D = 1, 2, 3$ is the number of spatial dimensions used in the simulation. The principle behind this condition is that if an electromagnetic wave is propagating across a discrete spatial grid Δr with speed v , and the amplitude of the wave is to be calculated at discrete time steps of equal duration

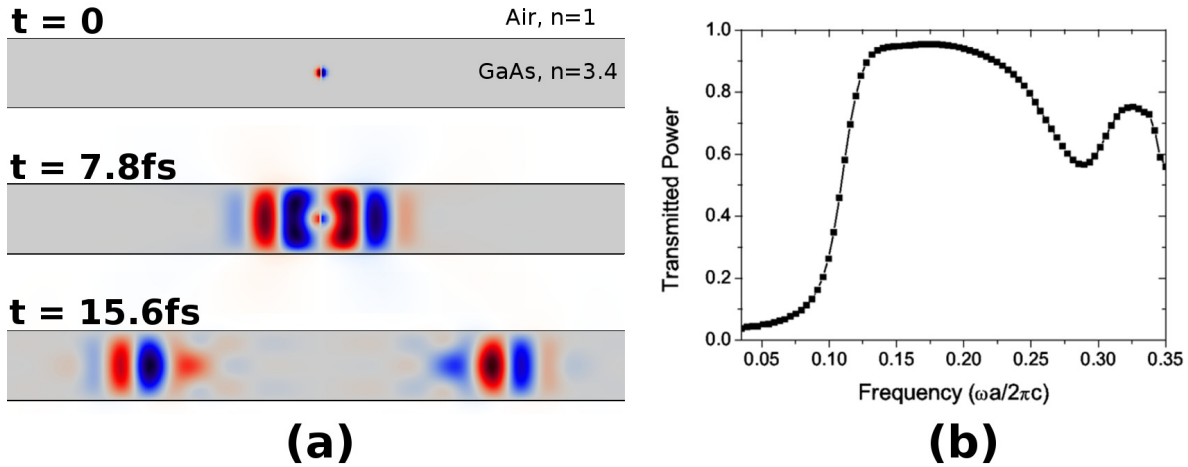


Figure 2.2: (a) Magnetic field profiles of a Gaussian dipole source placed in a GaAs ridge waveguide at different time intervals. At $t = 0$ the source is switched on and the fields propagate through the waveguide. (b) Transmitted power flux through a pair of source monitors at each end of the waveguide, normalised to the source power. A Gaussian impulse source is used which probes a broad spectral window of the waveguide transmission. The frequency is specified in dimensionless units, where ω is the angular frequency, a is the height of the waveguide and c is the speed of light in vacuum.

Δt , then Δt must be less than $\Delta r/v$ to fully resolve the wave.

For high refractive index contrast structures the discontinuities at the boundaries can cause errors to accumulate in the calculated fields. Decreasing $\Delta \mathbf{r}$ reduces these effects. However this also increases the number of voxels in the Yee lattice. A resolution scaling penalty is incurred when increasing the resolution along each spatial axis since this increases the required memory allocation by a factor $(S_{\Delta r})^N$ and the computational time by $(S_{\Delta r})^{N+1}$ where $S_{\Delta r} = \Delta \mathbf{r}_{new}/\Delta \mathbf{r}_{old}$ is the resolution scaling factor and N is the number of dimensions of the system.

This problem is circumvented in MEEP by smoothing the dielectric on a sub-voxel level to an intermediate value between the two materials [110]. For other quantities within the simulation, such as the electromagnetic fields, quasi-continuum is achieved by bilinear interpolation of quantities between the nearest grid points. For point-dipole current sources that

do not lie on the grid, the inverse operation is applied whereby the fields from the source are restricted to the lattice.

Alternatively in both software packages from Lumerical Solutions Inc., a non-uniform mesh is employed when discretising the dielectric map. This method increases the resolution of the Yee lattice near to dielectric interfaces, so that the fields over the interface can be accurately resolved. The benefit of this technique is that a more coarse lattice can be used in large regions of uniform dielectric constant, reducing the overall computation requirements for the simulation without compromising accuracy.

Boundary Conditions

When the fields reach the edge of the simulation domain, a range of different boundary conditions may be applied. The three main types of boundary conditions are absorbing, metallic and periodic. Metallic boundaries force the fields to zero at the edge of the simulation domain, behaving as a perfect metal with zero absorption and zero skin depth. Absorbing boundaries are implemented in various ways, but generally using perfectly matched layers (PML) which ensure that the fields are completely absorbed without any reflection [115–118]. Periodic boundary conditions are discussed in Section 2.2.2.

At the origin of the simulation coordinate system, additional boundary conditions can be applied along the principle axes in the form of symmetry constraints. Mirror and rotational symmetry constraints can be used to reduce the computational cost and force the parity of the electromagnetic fields to those of the symmetry axes. An example simulation domain is shown in Figure 2.3(a). The grey region represents the dielectric material and the red region depicts the electric field of an optical mode. The dielectric has mirror symmetry about the x and y axes and fourfold rotation symmetry about the origin. The polarisation of the fields represented by the arrows in Figure 2.3(a) possesses only mirror symmetry about the x and y axes. The fields in quadrant A are simply the mirror of the fields in quadrant B about the y -axis, $\mathbf{E}(x) = \mathbf{E}(-x)$, classed as even symmetry. However, the fields in quadrant C are not the direct mirror of the fields in quadrant B since the direction of the field vector is reversed when

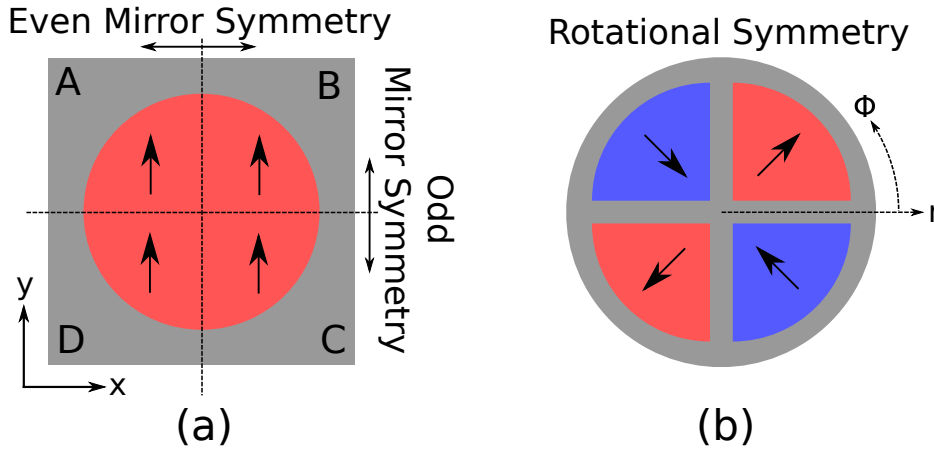


Figure 2.3: (a) Representation of a simulation domain containing y-polarised fields (red) in a symmetrical dielectric structure (grey). Only one quadrant is simulated, the remaining three are calculated from transformations of the fields in this quadrant. (b) Representation of a simulation domain containing r-polarised fields (blue and red) in a cylindrical dielectric structure (grey) with $m = 2$. Only the line along r is simulated, and the field dependence on ϕ is given by $e^{im\phi}$.

reflected about the x axis. Instead $\mathbf{E}(y) = -\mathbf{E}(-y)$, and the boundary has odd symmetry. Therefore, only one of the four quadrants of the simulation domain needs to be simulated; the remaining three can be calculated by transformation of the fields in one quadrant. The same principle can be applied for the z -axis, resulting in an eightfold reduction in the computer memory requirements for a 3D simulation and a 16-fold reduction in computational time.

Symmetry constraints may also increase the accuracy of the calculation of a simulation. For instance, when simulating a cylinder, a rotational symmetry may be applied along ϕ and only a cross section in the ρz plane must be modelled in cylindrical coordinates. In this case, the fields are assumed to be of the form $\mathbf{F}(r, \phi, z) = \mathbf{F}(r, z)e^{im\phi}$ where m is an integer. A 2D example of this is shown in Figure 2.3(b) for r-polarised fields with $m = 2$. Only a line along r is simulated and the fields along ϕ are calculated by transform from the fields at $\phi = 0$. The accuracy benefit of this approach is that the azimuthal properties of the cylinder are analytical and the cylinder surface is perfectly smooth. Without this, the cylinder must

be mapped to a cubic lattice, requiring a high resolution to faithfully reproduce the circular cross section in the $\rho\phi$ plane which carries the computational penalties listed previously.

“2.5D” FDTD

The FDTD method is a very general method that allows the study of arbitrary electromagnetic systems. With this generality comes the computational penalties listed in the previous section. However, the integrated optical circuits proposed for QIP are typically air-clad planar structures, which are uniform and of finite extent in the z dimension. This insight allows an approximation of the FDTD method to reduce the dimensionality of these systems without compromising accuracy. The procedure reduces a planar 3D problem into an effective 2D problem by converting the vertical slab structure to an effective 2D material that compensates for the dispersion due to the finite vertical thickness of the 3D structure.

The software used for simulation of these structures, Lumerical Mode Solutions [111], uses one of two approaches for effective index approximation. Based upon a variational procedure [119] or a procedure based upon the Reciprocity theorem [37, p. 610]. Central to each method is the assumption that there is only one vertical mode within the slab, which is satisfied for the devices studied in this thesis. The variational approach assumes that the fields are of the form $F(x, y, z) = \chi(x, y)\psi(z)$ where $\psi(z)$ and $\chi(x, y)$ describe the vertical and in-plane field profiles of a single mode, respectively. The effective permittivity can be found using

$$\epsilon_{eff} = \left(\frac{\beta}{k_0}\right)^2 + \frac{\int(\epsilon - \epsilon_r(z))\psi(z)^2, dz}{\int \psi(z)^2 dz} \quad (2.3)$$

where ϵ is the dielectric map of the 3D structure, $\epsilon_r(z)$ is the 1D vertical dielectric profile, β is the propagation constant of the slab mode along the x -axis and $k_0 = 2\pi/\lambda_0$ is the vacuum wavenumber. The propagation constant β and the field profiles $\chi(x, y), \psi(z)$ can be calculated by solving the Maxwell eigenproblem for a 2D cross-section of the waveguide, as discussed in the next section.

This method is particularly effective when considering the filter structures presented in Chapter 6 since the addition of straight waveguides breaks the cylindrical symmetry of the

system, leaving only mirror symmetry through the $z = 0$ plane. Reduction of a dimension in the system reduces the resolution scaling penalties by a factor of $S_{\Delta r}$, making the high resolution required for accurate modelling of circular structures computationally feasible when combined with variable meshing of the Yee lattice.

2.2.2 Frequency-Domain Eigenmode Solver

Frequency domain computational methods use an iterative approach to find the band structure $\omega(\mathbf{k})$ and the associated fields of the modes in a photonic system. This method was extensively used for designing the waveguide structures used throughout this thesis and is particularly useful when one wishes to consider the propagation of an optical mode in a structure with either continuous or discrete translational symmetry along the propagation axis: for example for calculation of the dispersion relation of a photonic crystal or ridge waveguide mode and the coupling coefficient between parallel waveguides. Because of the smaller simulation volume and performing calculations in the frequency domain these simulations are much less computationally intensive than FDTD methods, although FDTD may be used to obtain the same results as those found using frequency-domain methods. This section will discuss the operation of the MIT Photonic Bands package [54], however the eigenmode solver of Lumerical Mode Solutions [111] employs a similar strategy.

An example dispersion curve calculated using this method is shown for the ridge waveguide structure from 2.2.1 in Figure 2.4. The band structures for TE and TM modes are shown for a GaAs waveguide in air with an aspect ratio (width/height)= 2.

The dispersion relation is calculated by expressing the system as a finite matrix eigenproblem and using linear algebra techniques to find the eigenvectors and eigenvalues in a planewave basis [54]. The Maxwell eigenproblem derived from the curl equations for the magnetic field components is:

$$\nabla \times \left(\frac{1}{\epsilon(\mathbf{r})} \nabla \times \mathbf{H}(\mathbf{r}) \right) = \left(\frac{\omega}{c} \right)^2 \mathbf{H}(\mathbf{r}) \quad (2.4)$$

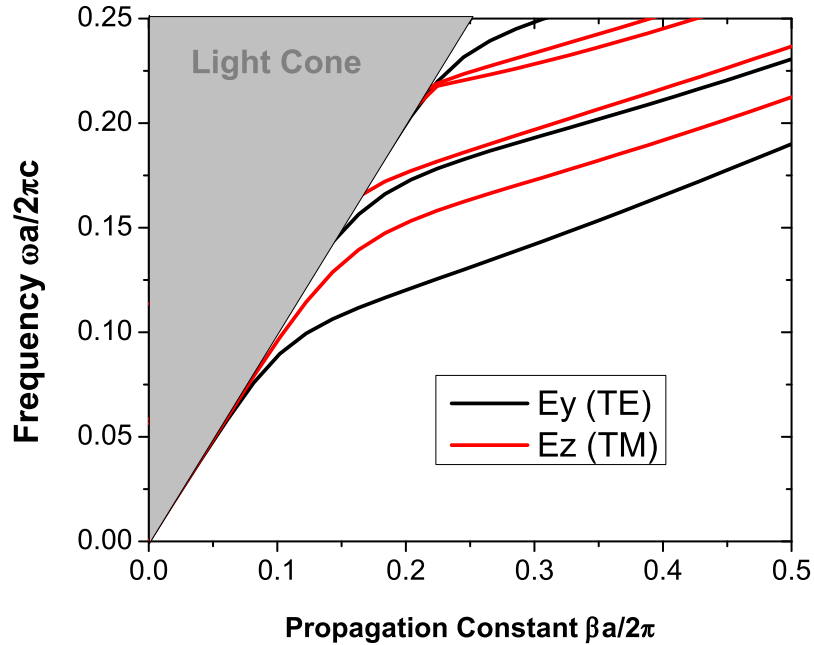


Figure 2.4: Calculated dispersion of the TE-like and TM-like modes of a GaAs ridge waveguide in air, with an aspect ratio (height/width)=2, using the frequency-domain eigenmode solver method.

where the electric fields can be found from

$$\mathbf{E}(\mathbf{r}) = \frac{i}{\omega\epsilon_0\epsilon(\mathbf{r})} \nabla \times \mathbf{H}(\mathbf{r}). \quad (2.5)$$

Periodic boundary conditions are used at the edge of a simulation domain consisting of a single unit cell of the structure. From Bloch's theorem, this forces fields of the form $\mathbf{F}(\mathbf{r}, t) = \mathbf{u}_k(\mathbf{r})e^{i\mathbf{k}\cdot\mathbf{r}}e^{i\omega t}$, where $\mathbf{u}_k(\mathbf{r}) = \mathbf{u}_k(\mathbf{r} + \mathbf{R})$ is the Bloch periodic field envelope and must satisfy

$$\left[(i\mathbf{k} + \nabla) \times \frac{1}{\epsilon(\mathbf{r})} (i\mathbf{k} + \nabla) \times \right] \mathbf{u}_k(\mathbf{r}) = \left(\frac{\omega(\mathbf{k})}{c} \right)^2 \mathbf{u}_k(\mathbf{r}) \quad (2.6)$$

For waveguides without periodicity, Bloch's theorem does not apply and Equation 2.4 is solved for a 2D unit cell. Equations 2.4 & 2.6 represent generalized eigenproblems of the form

$$Ah = \left(\frac{\omega}{c}\right)^2 Bh, \quad (2.7)$$

where A and B are $N \times N$ matrices and h is the eigenvector. The MIT Photonic Bands package [54] used in this thesis calculates the band structure by first finding the smallest eigenvalue ω_0^2 from

$$\omega_0^2 = \min_h \frac{h^\dagger Ah}{h^\dagger Bh}, \quad (2.8)$$

where h^\dagger denotes the adjoint of the column vector h , a process known as *Rayleigh-quotient minimization* with h_0 at the minimum being the lowest eigenvector. Each subsequent ω_n is then found by the same method, but subject to the orthogonality condition $h_n^\dagger Bh_{n-1} = 0$.

2.3 Experimental Methods

This section presents the experimental methods used to fabricate and characterise the photonic devices presented in this thesis. Firstly, the growth methods of quantum dot samples are presented followed by a discussion of the device fabrication techniques. Subsequently, the experimental measurement techniques and apparatus used to characterise these devices will be presented.

2.3.1 Quantum Dot Growth

Self-assembled quantum dots (QDs) are used throughout this thesis as they exhibit anti-bunched single photon emission with a high degree of spectral purity, which makes them excellent candidates for quantum optics experiments. They can also be readily grown in a host semiconductor matrix which facilitates the production of semiconductor photonic devices with embedded QDs that coupled efficiently to the optical modes.

QDs are produced via epitaxial growth techniques, commonly by molecular beam epitaxy (MBE) or metal organic vapour phase epitaxy (MOVPE) [120]. Current state of the art technologies are capable of deposition of high quality semiconductor material with monolayer

accuracy, allowing for abrupt changes in material composition and fine control over critical thicknesses.

Self-assembled quantum dots are produced using a bottom-up approach via the Stranskii-Krastanow method [121–123], in which under lattice-mismatch conditions a lower bandgap material forms discrete islands on a host substrate of higher bandgap energy. The example of InAs quantum dots on GaAs is used here.

During epitaxial growth, crystalline layers of InAs are deposited on a crystal substrate of GaAs, cleaved along the [100] plane. A lattice mismatch of approximately 7% exists between the two, and the initial layers of InAs form a strained quantum well structure. Beyond a critical thickness of around two monolayers the InAs relaxes to relieve the built up strain, forming 3D islands with diameter (height) of around 20nm (5nm) depending upon the environmental conditions in the growth chamber [87, 88]. The growth is stopped abruptly, leaving a random distribution of dots on a thin ‘wetting’ layer of InAs. If left exposed, the unterminated chemical bonds at the InAs-air interface provide efficient non-radiative recombination pathways, which quench optical emission of the quantum dots. Therefore, the quantum dots are covered with a capping layer of GaAs which moves the defects away from the dots resulting in superior optical properties. The quantum dot samples studied in this thesis were grown by Edmund Clarke at the EPSRC National Centre for III-V Technologies at the University of Sheffield.

2.3.2 Device Fabrication

The devices used in this thesis are prepared using both bottom-up (epitaxial growth) and top-down (lithographic) techniques. Here, the growth structure of a typical wafer is presented, followed by the lithographic procedures for preparing a photonic device. All device fabrication was performed by Dr. Ben Royall at the University of Sheffield.

Wafer Structure

The samples are grown by first depositing a sacrificial $1\mu\text{m}$ layer of $\text{Al}_{0.6}\text{Ga}_{0.4}\text{As}$ on a [100] GaAs substrate. Above this, 70nm of GaAs is deposited and a single layer of InAs QDs is grown before being capped with an additional 70nm of GaAs, forming a 140nm GaAs membrane with QDs embedded at its centre. A schematic representation of this structure is shown in Figure 2.5. Typically, the ensemble QD emission spectrum is centred around a wavelength of 950nm, so optimal vertical confinement of a single optical mode in the GaAs slab (once the sacrificial layer is removed) is provided by a slab of height $h = \lambda/2n = 140\text{nm}$, where $n = 3.4$ is the refractive index of GaAs at 4K. The thickness of the AlGaAs layer is chosen so that, once removed, the membrane is sufficiently far from the substrate so the optical modes of the membrane are not perturbed.

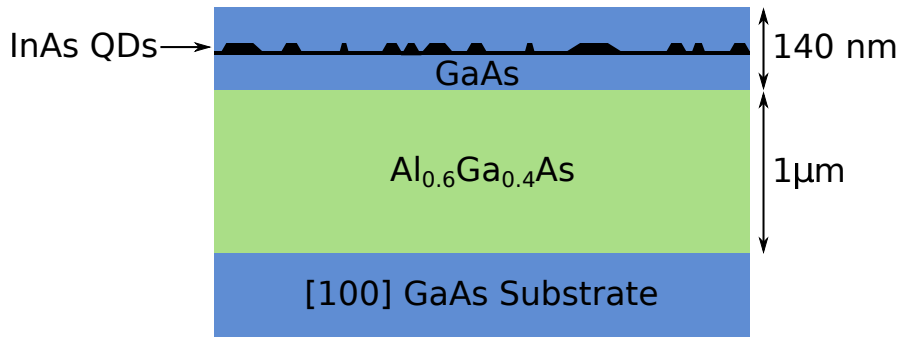


Figure 2.5: Schematic of the wafer structure used for planar photonic devices.

Lithography and Etching

The photonic structure is defined by electron beam lithography (EBL) and subsequent etching. An electron-sensitive resist, ZEP520A, is spin-coated onto the sample surface and baked at 180° for 5 minutes (Figure 2.6(b)). The desired pattern is defined by selective exposure of the resist to a scanning electron beam, which transfers a CAD-designed mask to the resist by serial writing (Figure 2.6(c)). The minimum feature size resolvable by this method using a high electron energy ($\sim 30\text{keV}$) is around 20nm. The resist is then developed in xylene, leaving a mask for etching of the desired pattern into the GaAs (Figure 2.6(d)). The etch is

performed using a highly anisotropic inductively coupled plasma (ICP) etch until the AlGaAs layer is reached (Figure 2.6(e)). The ZEP520A mask is then removed by heating the sample in n-methyl-pyrrolidone. Finally, the sacrificial AlGaAs layer is removed using a selective, isotropic hydrofluoric acid (HF) etch (Figure 2.6(f)). The structure is then rinsed and dried with nitrogen, leaving a free-standing membrane structure containing the desired pattern.

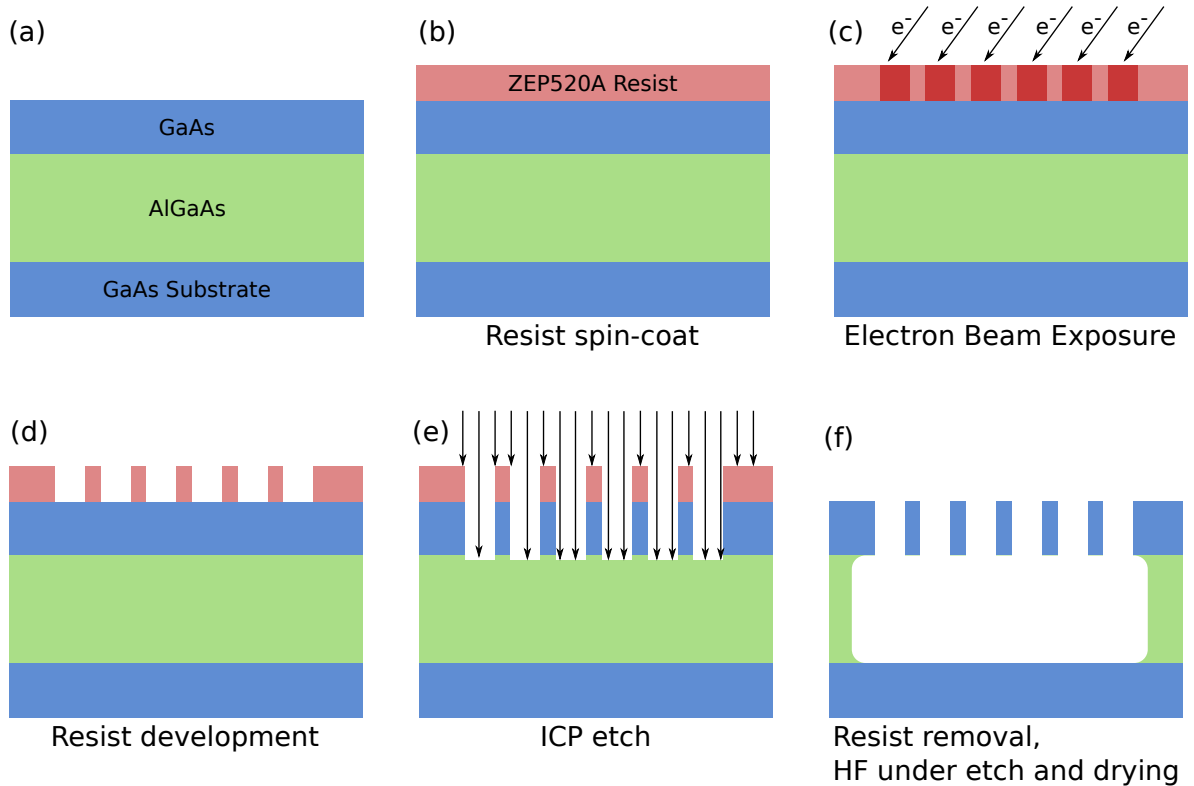


Figure 2.6: Schematic of the fabrication process used to create suspended photonic devices. (a) A sample containing an AlGaAs sacrificial layer. (b) ZEP520A resist is spin-coated onto the sample. (c) Electron beam lithography is performed upon the resist coated sample, exposing a pattern into the ZEP520A. (d) The resist is developed and exposed ZEP520A is removed. (e) The resist pattern is transferred to the GaAs membrane using an inductively coupled plasma etch. (f) The resist is removed and the sacrificial AlGaAs layer etched using a selective, isotropic HF acid etch.

Supercritical Point Drying

For suspended structures with a high aspect ratio, the effects of surface tension of the rinsing agent become significant. In this situation, droplets of the rinsing agent remain between the membrane and substrate. As the device is dried, the surface tension of the droplets increases and the membrane is pulled down towards the substrate, often breaking the suspended structure. To overcome this problem, supercritical point drying with CO_2 is used [124].

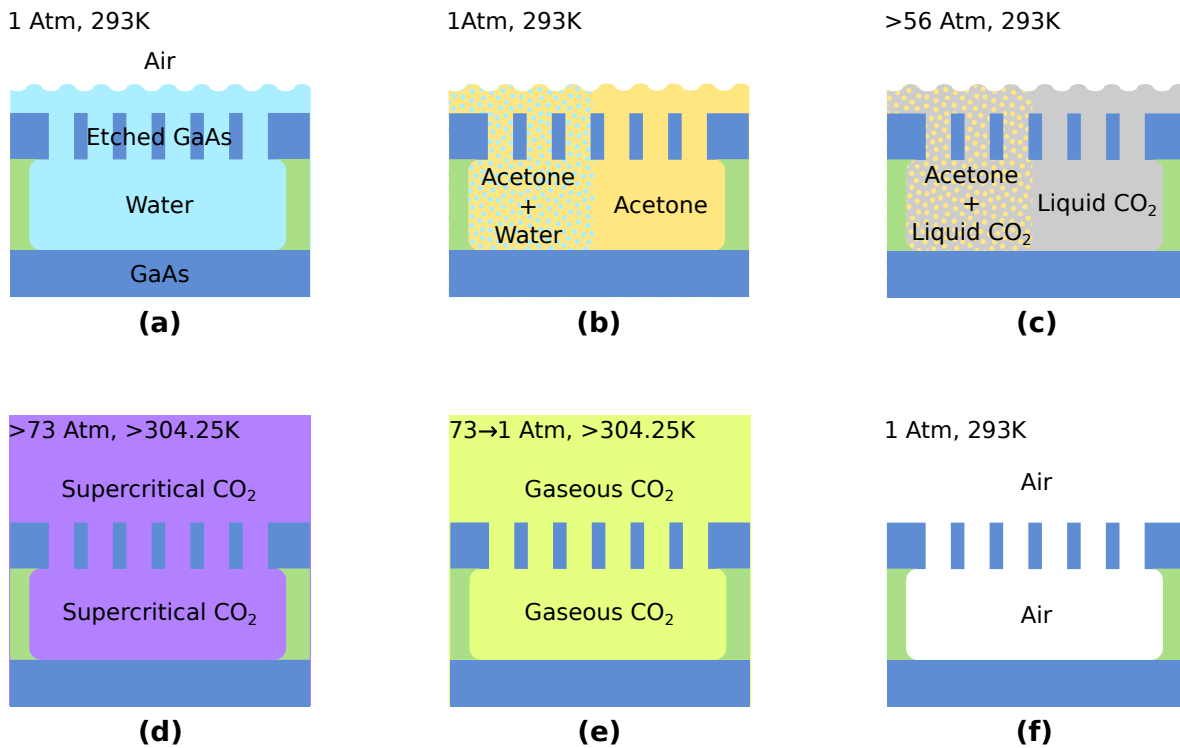


Figure 2.7: Schematic of the supercritical drying process using CO_2 . A sample immersed in water (a) is purged with acetone (b) which is miscible with both water and liquid CO_2 . (c) The drying chamber is pressurised to >56 Atm and the sample is purged with liquid CO_2 . (d) The chamber is then heated to >304.25K and the pressure increased to >73 Atm, under these conditions the CO_2 becomes a supercritical fluid. (e) The pressure in the chamber is reduced by venting and the CO_2 transitions to the gaseous phase and exits the chamber, leaving a dry sample (e).

A supercritical fluid possess no phase boundary and does not develop surface tension, allowing for very long suspended structures to be made. The benefits of using CO_2 is that it does not react with the sample and has a critical point well below the damage threshold temperature of the sample. The general procedure, illustrated in Figure 2.7, involves displacing the water from the sample using acetone (Figure 2.7(a)-(b)), then the acetone is purged using liquid CO_2 (Figure 2.7(c)). Acetone is used as it is miscible with both water and liquid CO_2 . The chamber is then heated until the CO_2 transitions to a supercritical fluid (Figure 2.7(d)), then the chamber is vented. The drop in pressure allows the supercritical CO_2 to transition to the gaseous phase (Figure 2.7(e)) and escape from the chamber, leaving a dry sample that has not been exposed to a liquid-gas phase phase boundary (Figure 2.7(e)). An example SEM image of a device with and without supercritical point drying is shown in Figure 2.8.

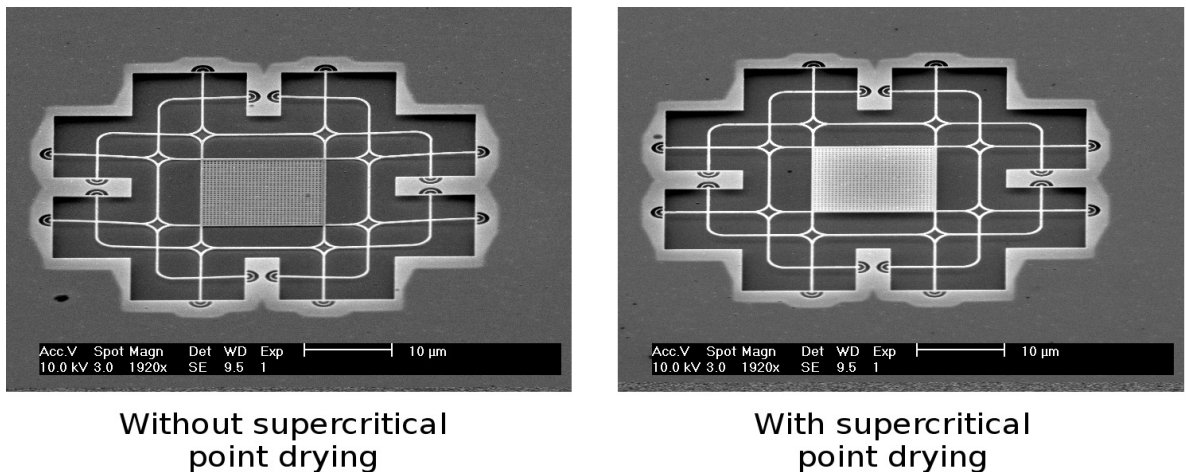


Figure 2.8: SEM images of free standing membrane structures after lithography with and without supercritical point drying. Devices and images were produced by Dr. Ben Royall.

2.3.3 Photoluminescence Spectroscopy

Quantum dots can be made to emit light via electrical or optical excitation: all experiments in this thesis were performed using optical excitation. Photoluminescence (PL) is the process by which an electron-hole pair formed by optical excitation recombines, emitting a single photon. Radiative recombination of an electron hole pair within the QD reveals information of the

energy level structure and properties of the QD.

In the single quantum dot system, there are three distinct methods by which this is achieved: resonant, quasi-resonant and non-resonant methods. The non-resonant methods involve excitation between the wetting layer and GaAs bandgap energies, or above the GaAs bandgap energy. Following creation, the carriers may either recombine to generate photons at the GaAs bandgap or wetting layer energy, or may be captured by the 3D potential well of the quantum dot. The carriers relax via carrier scattering or phonon interaction into the discrete QD exciton levels: these relaxation processes occur relatively quickly and remove any coherence with the excitation laser. These processes are schematically illustrated in Figure 2.9(a).

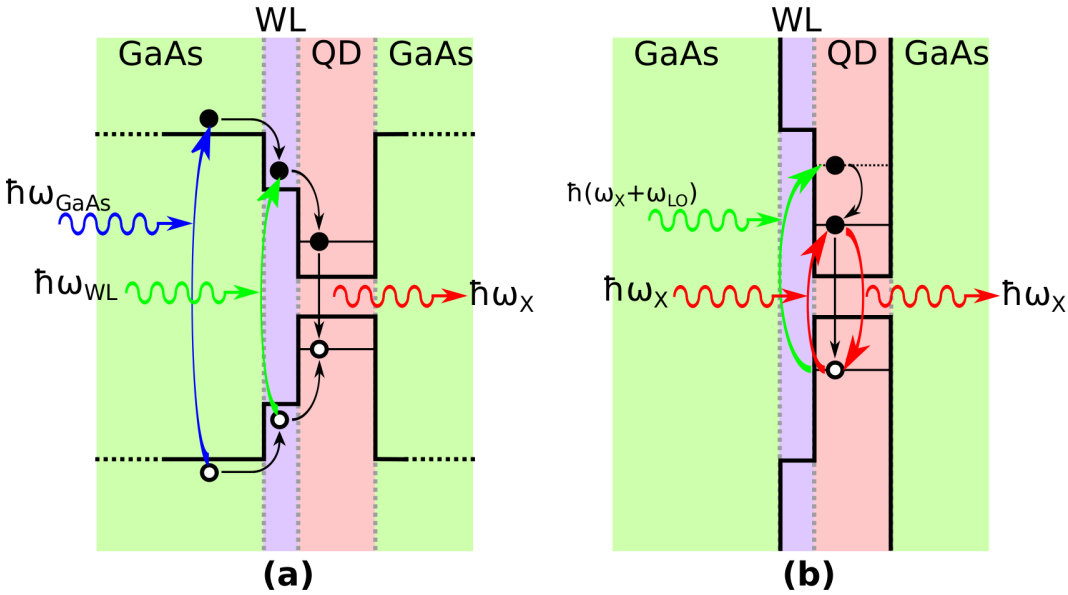


Figure 2.9: Photoluminescence schemes for a single QD. (a) Nonresonant excitation schemes showing above bandgap (blue) and wetting layer (green) excitation. (b) Resonant and quasi-resonant excitation showing resonant (red) and 1LO phonon (green) excitation. Black arrows represent nonradiative relaxation processes.

Quasi-resonant excitation of the exciton occurs via excitation of a longitudinal-optic (LO) phonon [125] or p-shell [103, 126] resonances within the QD. For LO phonon excitation, an incident photon is absorbed by a phonon-assisted optical transition which generates one LO

phonon and prepares the exciton in the ground state. For p-shell excitation, a polaron state is excited within the QD which decays into the exciton ground state within several picoseconds [127, 128]. Resonant excitation of the exciton directly drives the exciton transition at the Rabi frequency [129, 130]. Both resonant and quasi-resonant schemes maintain a degree of coherence with the driving laser due to a small number of non-radiative relaxation processes. These two schemes are depicted in Figure 2.9(b).

In this thesis, non-resonant μ PL techniques were used: wetting layer excitation was achieved using a tunable Ti:Sapphire infrared laser of wavelength 800-860nm; above GaAs bandgap excitation was implemented using a He:Ne red visible laser of wavelength 632.8nm or a diode laser of 808nm wavelength.

In a typical μ PL setup, the laser is incident upon a beam splitter (BS) where one exit path leads to an objective lens which focusses light onto the sample. The PL is collected by the same objective and passes through the other exit of the beam splitter into the detection apparatus. This basic configuration is shown in Figure 2.10.

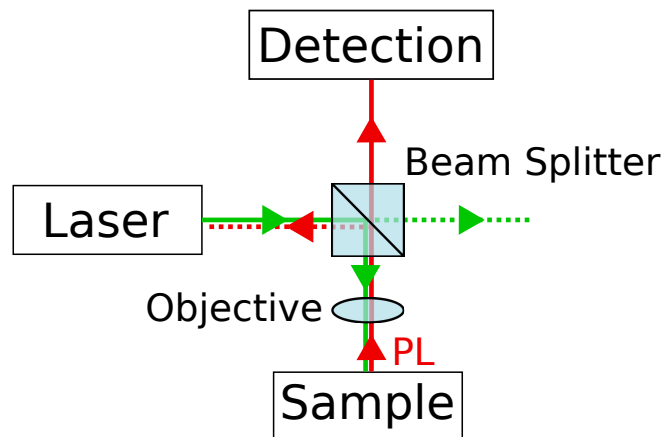


Figure 2.10: Simplified schematic of the experimental geometry for photoluminescence measurements.

Spectrally resolved measurements are enabled by a 0.55m single grating spectrometer which disperses the PL emission using a grating with 1200 lines/mm and is detected using a liquid nitrogen cooled charge coupled device (CCD). From the resulting spectra it is possible to identify the various excitonic complexes detailed in Section 1.3.1. It is also possible to study

QDs in both the strong and weak coupling regimes when the sample comprises photonic cavities with embedded QDs.

In addition to CCD detection, the spectrometer can redirect the dispersed light into an APD detector to enable time-resolved and correlation measurements of single spectral features.

2.3.4 Spatially Selective Micro-Photoluminescence

Key to the experimental demonstrations presented in this thesis is the ability to selectively excite and collect light from different regions of the sample whilst ensuring good isolation between the two. This was achieved using a confocal microscopy setup in addition to the basic experimental geometry above. Single mode optical fibres are used to couple light to/from the sample, where the $4.4\mu\text{m}$ guiding core provides the pinhole functionality required for confocal microscopy, producing a diffraction-limited spot of $\sim 1\mu\text{m}$ diameter on the sample. This ensures only light from/to a spatially defined spot on the sample is coupled with the fibre and by separating the two spots, transmission measurements through the sample may be performed. This experimental arrangement is illustrated in Figure 2.11. The section in red is mounted on a 'breadboard' which sits above the cryostat, whilst all other components reside on a floating optical bench.

The PL collected via an optical fibre on the collection side of the breadboard is passed to the spectrometer where it may be dispersed onto a CCD or out of a side port via a moveable mirror. Following the side port, a prism or beam splitter is used to split the PL between two fibre-coupled avalanche photodiodes (APDs). This arrangement provides the ability for spectral, time resolved and correlation measurements. A beam splitter at the output port allows the same PL signal to be sent to both APDs for autocorrelation measurements. Use of a 5mm prism facilitates cross-correlation measurements by sending spatially separated PL signal to each APD by 'cutting' the beam leaving the spectrometer side port. A lateral separation corresponds to spectral cross-correlation where the separation is generated by the dispersion of the spectrometer diffraction grating.

To control the position of excitation/collection on the sample, computer-controlled scan-

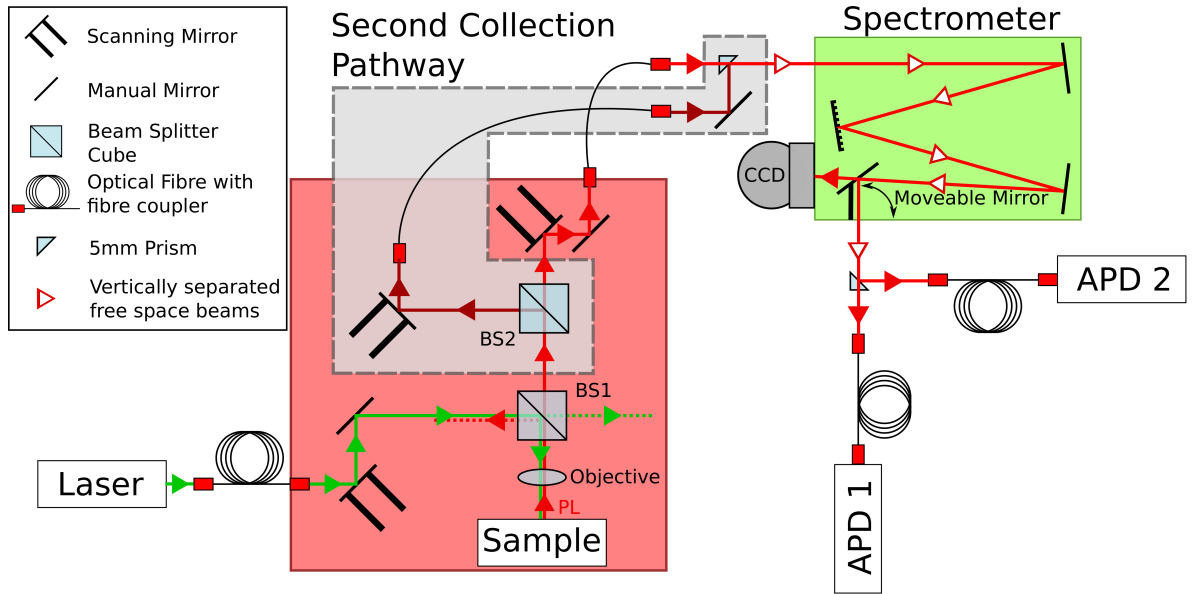


Figure 2.11: Schematic of the experimental setup used for spatially selective μ PL measurements. The grey box shows a second detection pathway that is added for some experiments. The section in red is mounted on top of the cryostat, whilst all other components are mounted on a floating optical bench. The second collection pathway in grey is an additional configuration, and may be isolated by removal of BS2.

ning mirrors are employed. Controls for the x and y axis of each mirror allows for a PL map of the sample to be generated. This method involves a raster scan of the collection or excitation spot over the sample and a spectral or intensity measurement is made at each position. The PL maps are used for identification of structures and their location within the device in addition to helping with alignment of the setup. This method was used to generate the PL maps presented in this thesis.

Twin-Channel Measurements with Common Spectrometer

The cross-correlation measurements presented in Chapter 4 require two isolated channels to collect PL from the sample at different positions. This is achieved by adding a second optical pathway to the experimental setup as shown in the grey section of Figure 2.11. Restrictions on available experimental apparatus require that a common spectrometer is used to filter each

channel, ensuring that correlation measurements are performed on only one QD.

This was realised by launching both channels from fibre launchers at different heights into the spectrometer with a vertical separation between the two. A vertical separation is used for correlation of different signals from isolated channels that are spectrally coincident. The spatial separation is maintained through the spectrometer and each of the two filtered beams are directed to different APDs using a 5mm prism to reflect one of the two beams whilst the other continues unperturbed.

When the two collection spots exactly overlap on the sample, the arrangement is equivalent to a standard autocorrelation experiment where the beam splitting occurs before the spectrometer (using BS2 as the beam splitter), rather than afterwards. By separating the two collection spots on the sample, the PL signal is divided within the sample itself and is coupled to different fibres.

2.3.5 Time Resolved Measurements

Although spectroscopic measurements as described in Section 2.3.3 are able to determine the transition energies between optically active excitonic species within the QD, it is unable to associate a timescale with the transitions. In order to achieve this, the QD is excited using non-resonant pulsed laser excitation with pulse length a few hundred femtoseconds to a few picosecond duration and repetition frequency $\sim 80\text{MHz}$.

Carrier capture by the QD occurs on the timescale of a few picoseconds, so after this time only the exciton within the QD remains. The exciton subsequently recombines via spontaneous emission at a random time with an exponentially decaying occupation probability. Therefore, by counting the number of photons emitted at different times after the incident laser pulse one may record a histogram of detection events that represents the probability of exciton occupation in the QD.

By fitting the decay of this histogram to an exponential the lifetime of the QD can be extracted. An ideal two-level system will produce a single exponential decay curve directly related to the radiative lifetime, and thus the natural linewidth of the transition when Fourier-

transformed. The decay transient of a typical QD however exhibits a biexponential decay curve whereby the two time constants represent the radiative lifetime and the spin-flip time between bright and dark exciton states due to the electron-hole exchange interaction in asymmetric QDs [131, 132]. Data from a single QD are shown in Figure 2.12.

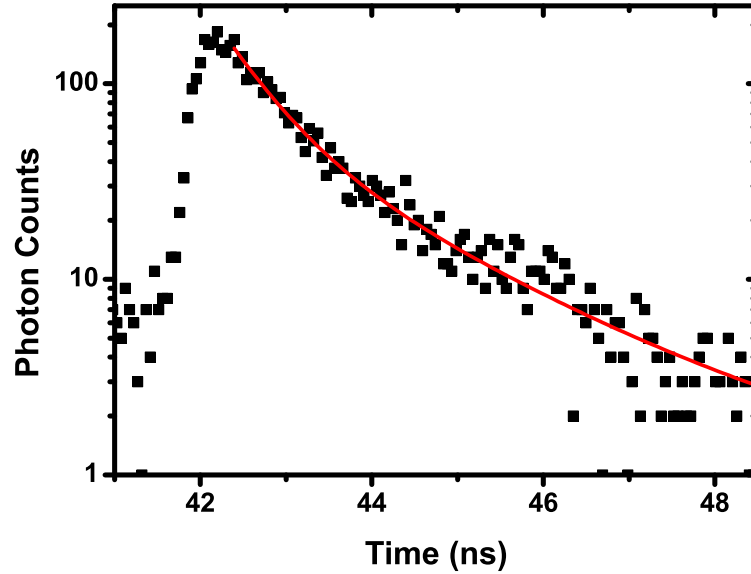


Figure 2.12: Decay transient recorded on an APD as a function of time for a single InAs QD excited by a pulsed laser (black). The decay curve is fitted with a biexponential decay (red), revealing a radiative lifetime of 542ps for the QD.

Time resolved measurements are implemented using a pulsed laser and photon counting hardware connected to a computer. A reference signal is taken from an internal photodiode within the laser and the detection events on a fast APD record the QD signal. A single photon counting module (SPCM) within the computer records the arrival time of photons at the APD relative to the laser signal by dividing a defined time window (typically 50ns) into 4096 time bins and counting the events within each time bin. Each event is triggered when the electrical signal from the APD exceeds a threshold parameter. A histogram is accumulated by repeating the measurement at the laser repetition rate and recording a cumulative total of every timing window. The photon counting card used for all time-resolved measurements

was a Becker and Hickl SPCM-630.

2.3.6 Second-Order Correlation Measurements

For many applications in quantum optics a single photon source is required that emits no more than one photon at any instant and each photon is separated by a well-defined time. This is the case for an ideal single QD. The two level system of a neutral exciton in an InAs QD combined with the Coulomb interaction between multiple carriers in different excitonic species mean that spectrally filtered emission from the neutral exciton is antibunched, emitting single photons separated by the exciton lifetime, as explained in Section 1.3.

A second order correlation measurement records the time correlation of an optical source, enabling identification of the source as random, coherent or antibunched. It achieves this by measuring the temporal coherence of a spatially-coherent source. The second order correlation function is defined as

$$g^{(2)} = \frac{\langle I(t)I(t + \tau) \rangle}{\langle I(t) \rangle \langle I(t + \tau) \rangle} \quad (2.9)$$

where $I(t)$ and $I(t + \tau)$ are the intensity of light at time t and $t + \tau$ respectively. The quantities in angled brackets $\langle \dots \rangle$ denote the time averaged value of the quantity within them. To perform a $g^{(2)}$ measurement, a Hanbury-Brown and Twiss (HBT) experiment is used, depicted schematically in Figure 2.13(a).

In an autocorrelation measurement, spectrally filtered PL from the QD is incident upon a 50:50 beam splitter and directed to two APDs. The recorded detection events from the APDs are sent electrically to the same single photon counting module (SPCM) as discussed in the previous section. In this configuration the two APDs act as start and stop buttons on a timer. A single photon detection at one APD starts a clock running and a photon detected at the other stops the clock. This is known as a coincidence count. The SPCM accumulates these events as before, summing for a defined integration time. The function $g^{(2)}(\tau) = 1 - (1 - g^{(2)}(0))e^{-|\tau|/\tau_d}$ can be fitted to the accumulated histogram of coincidences, where $g^{(2)}(0)$ is the multi-photon detection probability (the value of the second order correlation

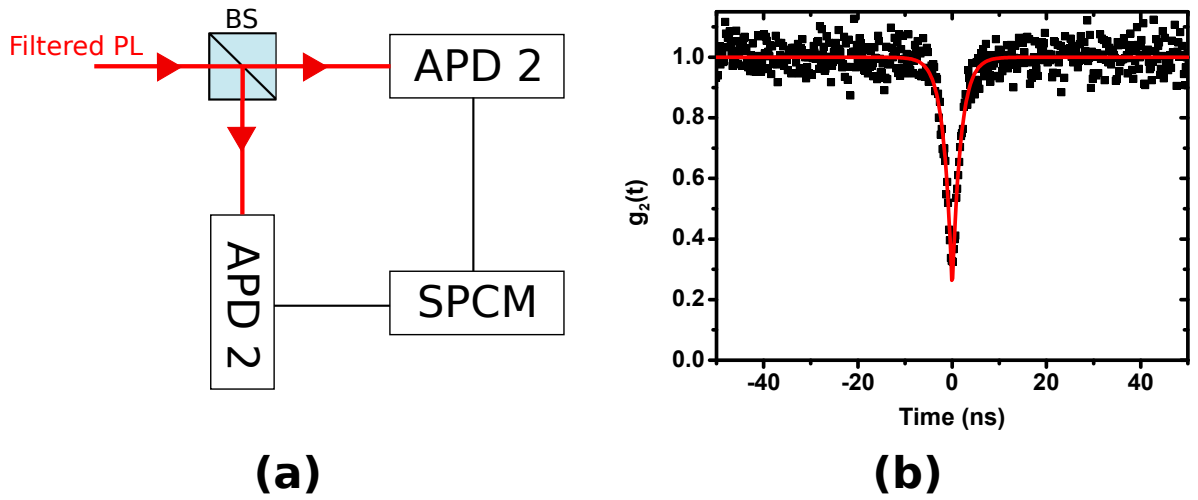


Figure 2.13: (a) Schematic diagram of a Hanbury-Brown and Twiss experiment. Spectrally filtered PL from the QD is incident upon a 50:50 beam splitter and directed to two APDs. The recorded detection events from the APDs are sent electrically to the single photon counting module (SPCM). The SPCM then records the number of detection events on each APD and the time that separates them. (b) Example of a coincidence count histogram from a HBT measurement. The red line shows a fit of $g^{(2)}(\tau) = 1 - (1 - g^{(2)}(0))e^{-|\tau|/\tau_d}$ to the data, which finds the multiphoton detection probability $g^{(2)}(0) = 0.23$ and the exciton lifetime $\tau_d = 1.79ns$.

function at $\tau = 0$), τ_d is the lifetime of the transition and τ is the time delay between coincidence counts, as shown in Figure 2.13(b).

A chaotic source, such as an atomic discharge lamp exhibits $g^{(2)}(0) > 1$ with $g^{(2)}(\tau \gg \tau_d) = 1$ since the light is bunched. For coherent light, such as a laser, the accumulated histogram exhibits no correlation and $g^{(2)}(\tau) = 1$ for all τ . For a quantum light source, such as an ideal two level system, $g^{(2)}(0) = 0$ and the light is anticorrelated, also known as photon antibunching. That is, the probability of simultaneous coincidence is zero for an ideal two level system. The data presented in Figure 2.13(b) (and indeed for many QDs) does not reach zero due to contribution from background sources and a limited APD response time. Corrections to these data by background subtraction and deconvolution of the APD response yield $g^{(2)}(0) \approx 0$.

In addition to auto-correlation measurements, the HBT experiment can be used to investigate cross correlation between different light sources or different spectral lines from the same light source. For spectrally coincident light, the same setup as for auto-correlation is used, except with the two beams separated vertically as detailed in Section 2.3.4. For correlation between different wavelengths, the slits on the spectrometer are opened sufficiently wide to allow both wavelengths into the APDs. The beam splitter is adjusted so that the two wavelengths enter different APDs: one wavelength triggers a start event and the other creates a stop event.

2.3.7 Cryostats

All of the experiments in this thesis were conducted at low base temperatures of 4.2K. To achieve this, the samples were housed within cryogenic systems cooled by liquid helium. Two main types of cryostat were used for this purpose, the design and operation of which are briefly described here.

Cold Finger Continuous Flow Cryostat

The cold finger continuous flow cryostat was used to conduct experiments that required a quick exchange of samples and did not require a very high degree of stability. The sample is contained within an evacuated chamber, mounted on a copper cold finger which provides thermal contact between the sample and a heat exchanger external to the sample chamber. Liquid helium is pumped through the heat exchanger from a dewar which can cool the sample to between 4-10K, depending on the particular system. Optical access to the sample is provided by a glass window in the top of the sample chamber. Movement around the sample and focus control is provided either on a fine scale by moving the optics above the cryostat or translating the cryostat on a coarse scale using micrometer driven manual translation stages. A schematic of the cryostat is provided in Figure 2.14.

Vibration of the system from the helium pump and continuous helium flow can compromise the stability of the system: typically the system will maintain alignment with the incident

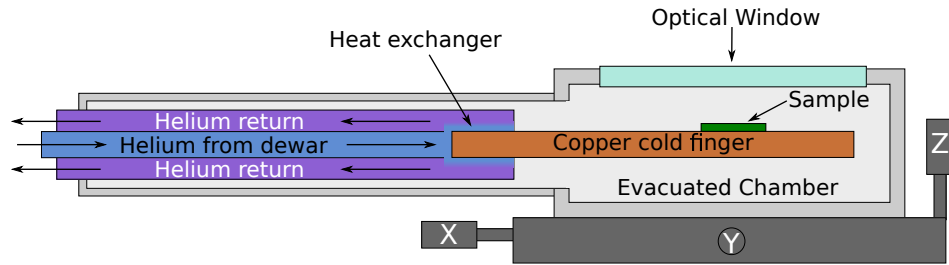


Figure 2.14: Side view schematic of a cold finger continuous flow cryostat.

laser for around an hour. For long exposure measurements this system is therefore unsuitable and a more stable solution is required. However for short exposure, fast characterisation of samples the flow cryostat is ideal.

Liquid Helium Bath Cryostat

A liquid helium bath cryostat achieves cryogenic temperatures by immersion of an evacuated chamber containing the sample in a dewar filled with liquid helium at 4.2K. Thermal equilibrium is achieved using a small amount of helium exchange gas within the sample chamber to thermally couple the sample to the chamber walls and hence to the liquid helium reservoir. The advantage of this system over a flow cryostat is that since there is no helium circulation, no vibrations are generated and the system can remain stable for up to several days.

Within the sample chamber is an optical cage system, at the bottom of which is a piezoelectric transducer stack upon which the sample is mounted. Movement around the sample and focus is achieved by electrical modulation of the piezoelectric stages in the 'stick-slip' regime. Above this is an aspheric lens ($NA=0.5$) for focussing the incident laser to a spot size of around $1\mu\text{m}$ diameter. Along the cage length are two achromatic doublets, which act to collimate and reduce aberration effects of the aspheric lens [133]. At the top of the tube is a window to allow optical access to the sample from optics affixed to a breadboard on top of the insert tube. The bath cryostat system is schematically illustrated in Figure 2.15. The large majority of measurements presented in this thesis, particularly those requiring stability over long time periods, were performed using the liquid helium bath cryostat system.

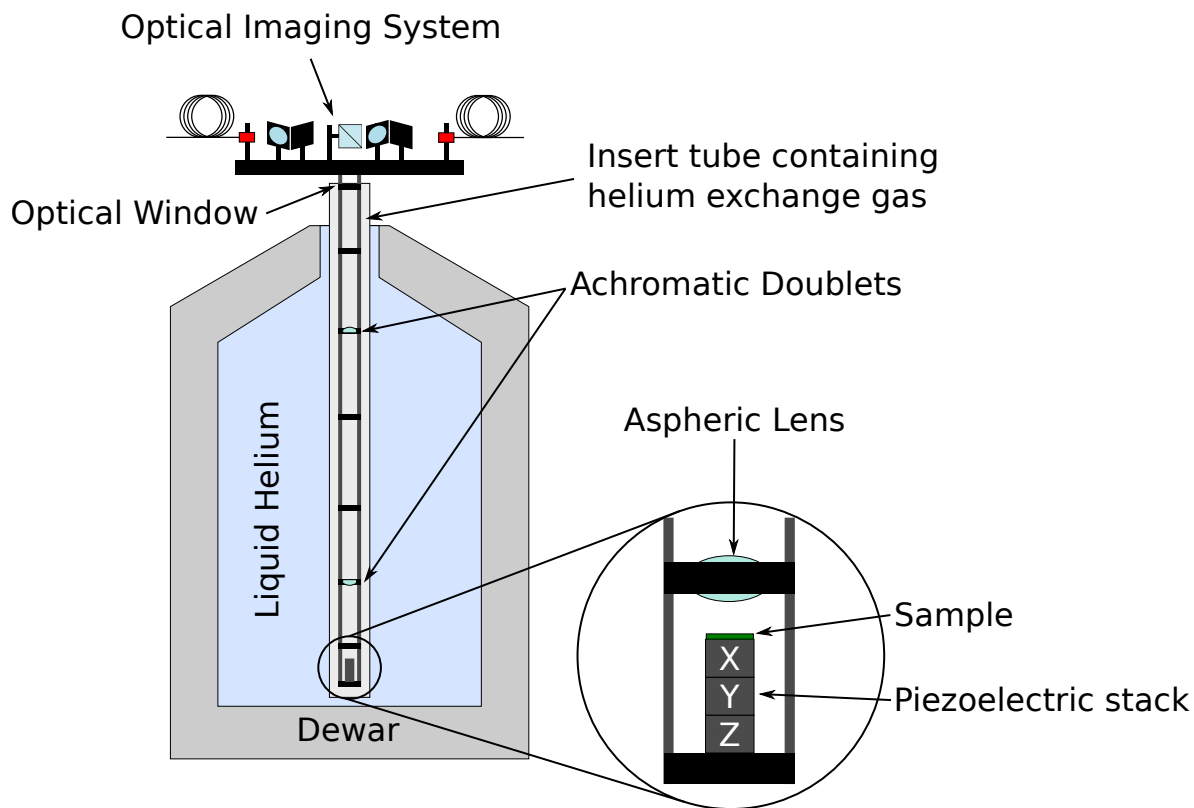


Figure 2.15: Schematic of a liquid helium bath cryostat with integrated optics and piezoelectric sample positioning. The optical imaging system from Figure 2.11 is shown mounted to the top of the cryostat.

Chapter 3

Waveguide Coupled Photonic Crystal Cavity for Quantum Dot Spin Readout

3.1 Introduction

Experiments at the University of Sheffield, with theoretical support from the University of Bristol in 2013 have shown that it is possible to read out the spin of a single quantum dot (QD) located at the centre of two intersecting ridge waveguides via emitted photons in a which-path encoding scheme [134, 135]. This chapter aims to improve upon these results by embedding the QD in a photonic nanocavity to enhance the emission rate of the QD via the Purcell effect. In order to maintain spin information, the cavity must be unpolarised and the H1 photonic crystal (PhC) cavity was selected for this purpose. A scheme to selectively couple the cavity modes of the H1 cavity to separate PhC waveguides to enable on-chip spin readout is the focus of this chapter.

Scalable all-optical quantum information processing (QIP) has been shown to be possible using only single-photon sources, linear optical elements and single-photon detectors [10, 21, 29]. The two-level spin system of a self-assembled quantum dot single-photon source is one of

the leading candidates for a static qubit implementation [7], with long dephasing times [96] and possibility of optical coherent control [126]. The pioneering work of M. Paillard et al. has shown perfect conservation of the exciton spin under strictly resonant pumping conditions [136] which demonstrates a key milestone in the preparation and preservation of a desired spin state within the QD for spin-photon entanglement. On chip integration using this solid state implementation requires a static to flying qubit interface to exchange quantum information between different static nodes [5]. Recent demonstrations of the entanglement between a QD and single photon [91, 137] and the mapping of QD spin states to path-encoded photons [134, 135] are important milestones in the development of QD-based solid-state QIP. Such developments demonstrate that the role of a static-flying qubit interface can be satisfied by a QD-photon interface in which spin information is exchanged between the two. For many purposes, path encoding with indistinguishable photons is desired [17] which could be achieved by inclusion of an unpolarised optical cavity [67].

Two orthogonal linearly polarised modes, $|X\rangle$, $|Y\rangle$, form a Poincaré-like sphere with states $\alpha |X\rangle \pm \beta |Y\rangle$ which have a one-to-one correspondence to the in-plane spin states of a single QD $\alpha |x\rangle \pm \beta |y\rangle$, with complex α and β [67]. The dipole modes of the H1 PhC cavity possess among the highest Q/V ratios of any PhC cavity with a mode volume of less than half a cubic wavelength [138]. The resulting high degree of spontaneous emission enhancement has been shown to provide indistinguishable single photon emission [70], strong coupling [69] and proposed for generation of entangled photon pairs [139]. On-chip coupling of the hexapole [140] and quadrupole [141] modes of the H1 cavity to waveguides has been investigated previously, but a demonstration of the selective coupling of the dipole modes to separate waveguides remains to be demonstrated as required for in-plane transmission of spin [134].

In this chapter, a scheme is proposed and demonstrated whereby the Poincaré-like states of the H1 cavity are mapped into two separate propagating photon channels, allowing the QD spin state to be transferred to the waveguides via the cavity. FDTD simulations are used to design a waveguide-coupled H1 device which exhibits selective coupling of each of the two dipole modes to its respective PhC waveguide. This design is then optimised using FDTD and

frequency domain eigenmode solver methods. The selective coupling behaviour of the device is experimentally demonstrated using ensemble QD photoluminescence (PL) measurements for near-degenerate and non-degenerate cavities. Finally, future directions and applications of the device are discussed, along with preliminary measurements of additional functionality.

3.2 Principles of Selective Cavity Mode Coupling

3.2.1 Cavity Design

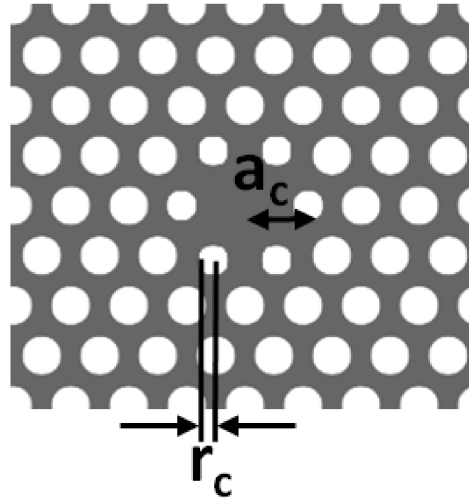


Figure 3.1: Schematic of H1 cavity in a triangular lattice hole-slab photonic crystal whereby a single hole is omitted to form the cavity. To reduce the out-of-plane losses, the first ring of holes adjacent to the cavity is displaced by $a_c = 1.09a$ and have reduced radius $r_c = 0.91r$. Grey regions represent GaAs and white, air.

The principle of selective coupling of the dipole modes of the H1 photonic crystal cavity to separate waveguides is presented here using FDTD simulations. The H1 cavity used in this experiment consists of an omitted air cylinder from a triangular-lattice photonic crystal (PhC) slab with lattice constant a , cylinder radius $r = 0.31a$, slab thickness $h = 0.71a$ and refractive index $n = 3.4$. The H1 cavity confines a pair of orthogonal and degenerate dipole modes, the Q-factors of which were maximised by tapering the cavity mode fields into the Bloch modes

of the surrounding photonic crystal [56]. This was achieved by, using the parameters in [60], reducing the radii of the six nearest-neighbour cylinders to $r_c = 0.91r$ and increasing their displacement $a_c = 1.09a$, as shown in Figure 3.1. This produced calculated Q factors for the dipole modes of $\sim 30,000$ with a mode volume $V = 0.39(\lambda/n)^3$.

The near-field profiles of the dipole modes are shown in Figure 3.2 where the modes are labelled according to the orientation of the H_z dipole at the cavity center. Herein referred to as the X and Y-dipole modes, the X-dipole has an H_z dipole along the x-axis and the Y-dipole along the y-axis. The H_z fields are used throughout this chapter as this field component is common to all of the optical modes in the device. Since the photonic crystal provides a TE bandgap, the H_z fields exhibit even parity along the z-axis by definition: TE-like modes exhibit even symmetry and TM-like modes exhibit odd symmetry along the z-axis [52].

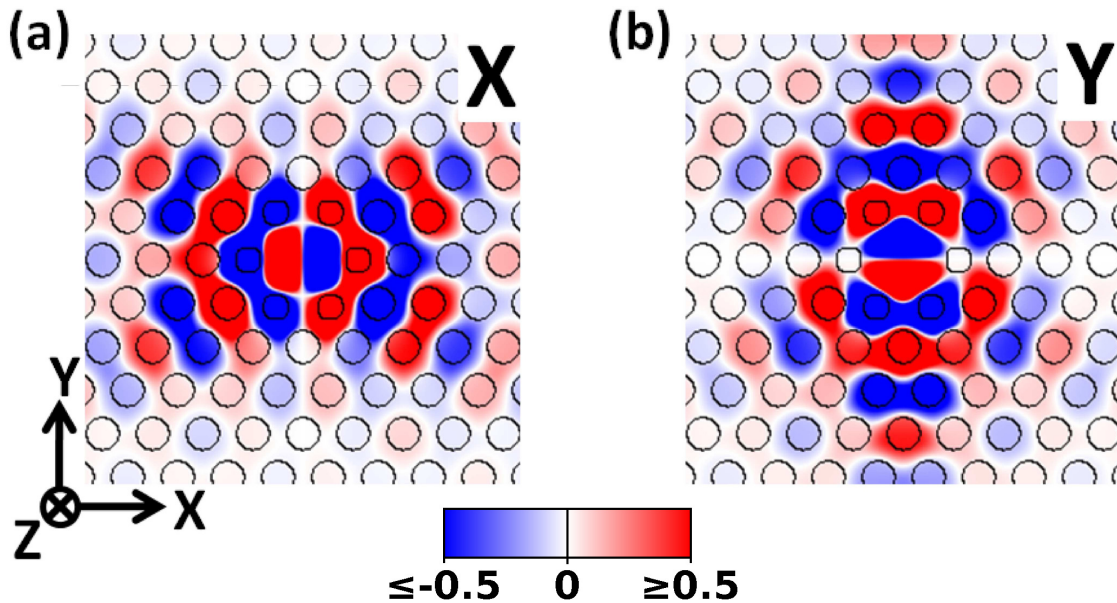


Figure 3.2: H_z field profiles of the (a) X- and (b) Y-dipole modes of the H1 photonic crystal cavity. The modes are labelled according to the orientation of the magnetic dipole. A linear red-white-blue colour scale is used to represent fields up to 50% of the maximum value, where red and blue denote fields of opposite polarity.

3.2.2 Waveguide Coupling Considerations

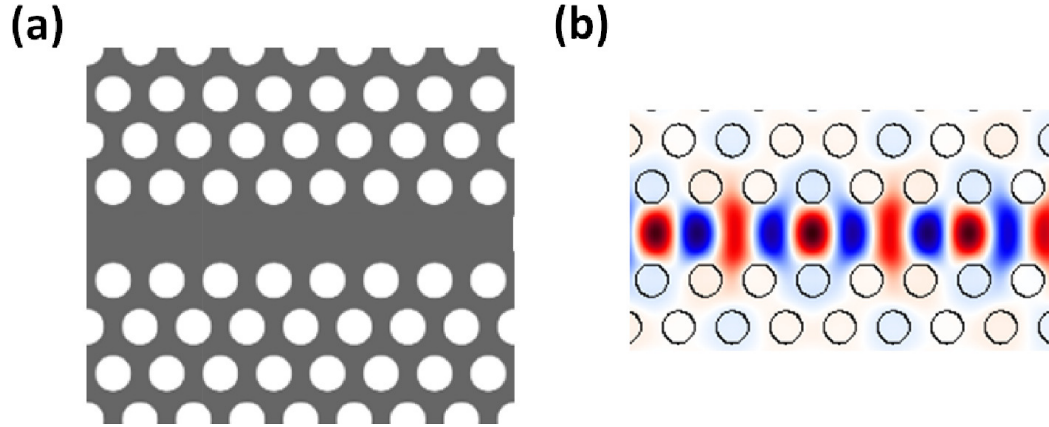


Figure 3.3: (a) Schematic of W1 photonic crystal waveguide in a triangular lattice photonic crystal. A single row of holes is omitted to produce the waveguide. (b) H_z field profile of the fundamental guided mode of the W1 photonic crystal waveguide.

The H_z fields of the cavity modes in Figure 3.2 decay evanescently into the surrounding photonic crystal, exhibiting significant penetration into the PhC along the dipole axis and vanishingly small fields orthogonal to it. Both cavity modes exhibit even parity along the H_z dipole axis and odd parity perpendicular to it. In the spectral region of the cavity modes, the linear defect (W1) waveguide shown in Figure 3.3(a) sustains a single, propagating TE mode [71], the H_z field profile of which is shown in Figure 3.3(b). The waveguide mode exhibits even parity along the propagation axis and odd parity perpendicular to the propagation axis. Therefore, if the waveguide is brought into close proximity to the cavity along the H_z dipole axis, the two will couple via the evanescent field of the cavity modes. The efficiency of this coupling is governed by the spatial and spectral coincidence of the fields [140, 142–145]. Spectral coincidence of the cavity and waveguide modes is reasonably straightforward due to the broadband nature of the waveguide mode. However care must be taken to avoid the waveguide cut-off regions and the slow-light region of the waveguide mode dispersion, as discussed in the next section.

3.2.3 Proposed Selective Coupling Mechanism

The proposed selective coupling mechanism is as follows. The propagating mode of a W1 waveguide, axis along x, that is brought into close proximity to the cavity along the x axis, shares field parity with the X-dipole mode and therefore will couple efficiently. The smaller the separation between the cavity and waveguide, the higher the overlap integral becomes and the coupling rate is increased. The waveguide mode field parity is opposite to that of the Y-dipole mode and is not expected to couple well. Moreover, the amplitude of the evanescent fields of the Y-dipole along this axis are significantly lower than those of the X-dipole. The same selection principle holds for coupling along the y-axis, except the symmetry of a triangular PhC lattice forbids a W1 waveguide along this axis due to the underlying sixfold rotational symmetry. However, a waveguide at 30° to the vertical can be employed if the waveguide terminates on a line parallel to the y-axis which passes through the cavity center as shown in Figure 3.4. Along this line, the waveguide field overlap remains high for the Y-dipole and low for the X-dipole mode.

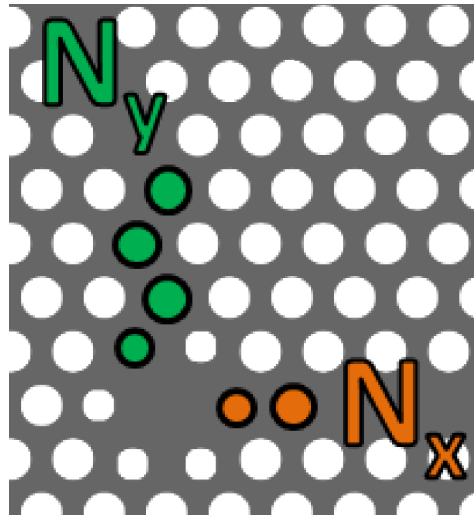


Figure 3.4: Schematic defining N_x and N_y , the number of holes separating the cavity from the x- and y-waveguide respectively. The 'zig-zag' arrangement of holes in y is due to the lack of fourfold rotational symmetry of the photonic crystal, the underlying lattice supporting only sixfold.

Whilst the cavity modes also exhibit significant penetration depths at 45° to the mode axis, these are common to both modes and are therefore unsuitable for selective coupling. Since both cavity modes will couple to a waveguide positioned here, it may be possible to implement a boolean OR gate using a three waveguide configuration. That is, if either or both of the two cavity modes are excited via selectively coupled waveguides, this will produce a measurable output from a non-selectively coupled waveguide.

3.3 Device Optimisation Procedure

3.3.1 Quantification of Selective Coupling

The optimisation of the H1 cavity selectively coupled to photonic crystal waveguides is presented here, using FDTD and Frequency-Domain Eigenmode methods. For optimal device operation, the modes must couple to the waveguides with equally high efficiencies whilst maintaining the highest Q-factor possible to provide maximum spontaneous emission enhancement to the QD. Equal coupling efficiencies are desirable as this allows direct mapping of the polarisation state of the cavity to the optical modes of the waveguides without systematic error. Whilst this can be corrected if the discrepancy is known, it is advantageous to not introduce these errors by design. The total Q factor (Q_c) of the waveguide-coupled cavity can be separated into an in-plane and out-of-plane Q factor, resulting from losses into the photonic crystal and into free space, respectively. The relation between these is given by

$$Q_c^{-1} = Q_u^{-1} + Q_{wg}^{-1} \quad (3.1)$$

where Q_c is the total Q factor of the coupled cavity, Q_u is the Q factor of the uncoupled cavity, and Q_{wg}^{-1} is the loss rate into the waveguide. Assuming a photonic crystal slab of infinite extent in-plane means the horizontal loss rate of the uncoupled cavity is zero, therefore Q_u represents the out-of-plane loss rate [140]. When the waveguide is introduced, an in-plane loss channel is created lowering the total Q of the cavity.

The coupling efficiency of the coupled cavity is defined as the fraction of the loss rate

into the waveguide to the total loss rate of the system [142]. The coupling efficiency was calculated for each mode as a function of the number of holes separating the cavity and waveguide, N_x and N_y for the x and y-waveguide respectively, as illustrated in Figure 3.4. The x(y)-waveguide is labelled as that which principally couples to the X(Y)-dipole. When substituting Equation 3.1, the expression for the coupling efficiency becomes

$$\eta(N_{x,y}) \equiv \frac{Q_{wg}(N_{x,y})^{-1}}{Q_c(N_{x,y})^{-1}} = 1 - \frac{Q_c(N_{x,y})}{Q_u} \quad (3.2)$$

For selective coupling of the cavity modes, the coupling efficiency to one waveguide must be high whilst coupling to the other waveguide (cross-coupling) must be minimal for both cavity modes. The coupling efficiencies were calculated by recording the Q factor of the cavity modes firstly for an uncoupled cavity, and then for a range of cavity-waveguide separations for each waveguide. This was achieved by with the MEEP software package [110] by placing a resonant mode monitor employing harmonic inversion [146] at the cavity centre to record the Q factor of the cavity modes.

3.3.2 Adjustment of Coupling Efficiency using Waveguide Proximity

The coupling efficiencies to each waveguide, calculated separately, are shown in Figure 3.5(a), with the corresponding coupled Q-factors shown in Figure 3.5(b). As expected, the coupling efficiency decreases with an approximately exponential dependence on the cavity-waveguide separation due to a reduction in the evanescent coupling rate between the cavity and waveguide. However, fluctuations are observed for the Y-dipole at $N_y=5-7$, due to the path taken when adjusting the cavity-waveguide separation: the waveguide moves in and out of the evanescent tail and produces fluctuations in the overlap integral of the two modes.

For the X-dipole, the coupling efficiency at $N_x=4$ again deviates from the expected exponential decay. This is due to a local change in the field parity of the cavity mode along the x-axis. As illustrated in Figure 3.6, when the waveguide is separated by 3 holes the parity of the evanescent fields in the next two unit cells (holes 4 and 5) along the x-axis have odd x-parity. These next two cells constitute the beginning of the waveguide and therefore largely

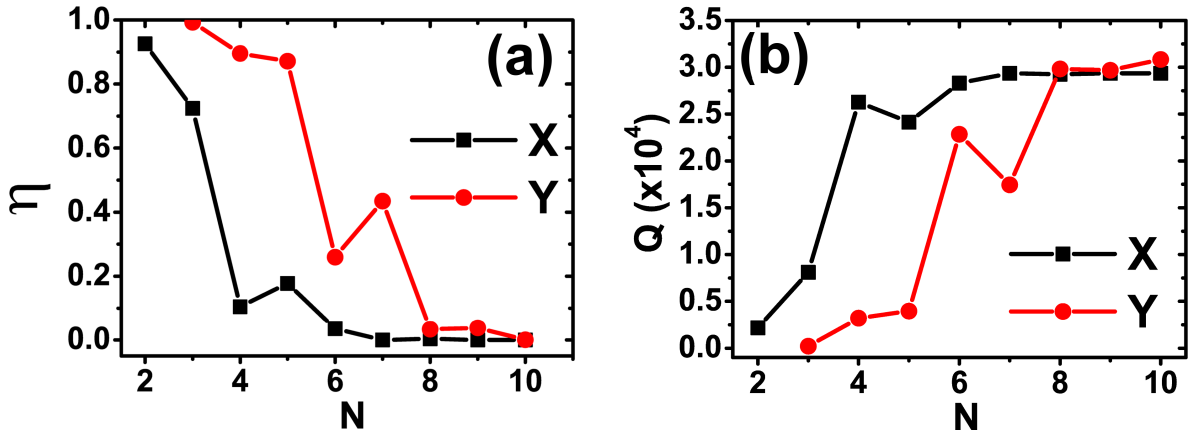


Figure 3.5: (a) Coupling efficiency of the cavity modes to their respective waveguides as a function of cavity-waveguide separation, N . (b) Corresponding Q-factors of the cavity modes when coupled to the waveguides as a function of cavity-waveguide separation. These data were calculated when only the corresponding waveguide was present.

determine the coupling characteristics. The fields of the waveguide mode in Figure 3.3 also possess odd parity in x , so the two couple efficiently due to high overlap. However, for 4 hole separation the evanescent fields of the next two unit cells (holes 5 and 6) have even parity in x which does not match the waveguide mode, resulting in a significantly reduced overlap integral and hence reduced coupling efficiency. For 5 hole separation the cavity fields return to odd parity and the cavity couples efficiently to the waveguide once again. The same is true for $N_x = 1$, however the cavity leak rate is so high that the Q factors for a resonant mode cannot be calculated.

There are two regions in Figure 3.5(a) where the coupling efficiencies for the X and Y-dipole modes are comparable. These are when $(N_x, N_y) = (2, 4)$, and $(5, 6)$. When both waveguides are introduced, the coupling efficiencies for the X(Y)-dipole are 89(93)% for $(2, 4)$ and 18(26)% for $(5, 6)$. The former parameters represent a regime in which the cavity is strongly coupled to the waveguide, whereby the latter represents a weakly coupled regime. For the purposes of this experiment, efficient coupling is required so the strongly coupled case was used. However, the weakly coupled case is desirable if one wishes to couple two such devices as in [147]. The H_z field profiles of the coupled modes for $(2, 4)$ are shown in Figures

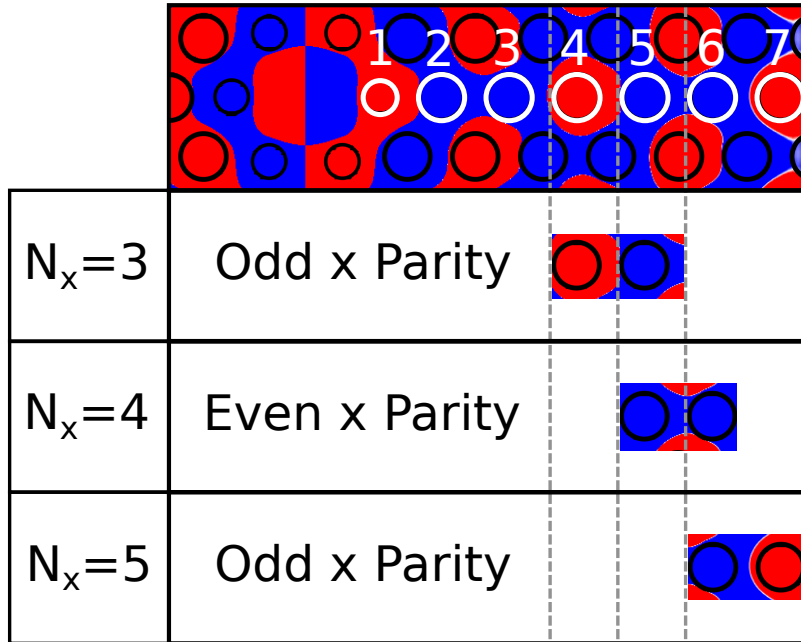


Figure 3.6: Parity of the X-dipole along the x-axis at different unit cells. A linear red-blue colour scale is applied where red and blue indicate positive and negative amplitude respectively. The parity for unit cells 4 and 6 are odd, matching the waveguide mode. For unit cell 5, the parity is even and coupling to the waveguide is poor.

3.7(a) and 3.7(b).

Due to the proximity of the waveguide, the cavity modes are perturbed and experience an increase in their resonant wavelength due to an increase in the effective mode volume. The wavelength shift of the cavity modes with the cavity waveguide-separation are shown in Figure 3.8. For the x-waveguide, both modes experience little perturbation until the waveguide is less than 4 holes away from the cavity. Beyond this, the X-dipole mode wavelength increases by around 0.1nm per hole. The Y-dipole only shows disturbance at a separation of 2 holes by a redshift of 0.1nm. Conversely, the X-dipole exhibits little disturbance by the presence of the y-waveguide at all separations used. The Y-dipole displays a monotonic increase in the resonant wavelength with decreasing separation of the y-waveguide. In summary, each cavity mode display a weak spectral dependence on the proximity of the opposite waveguide.

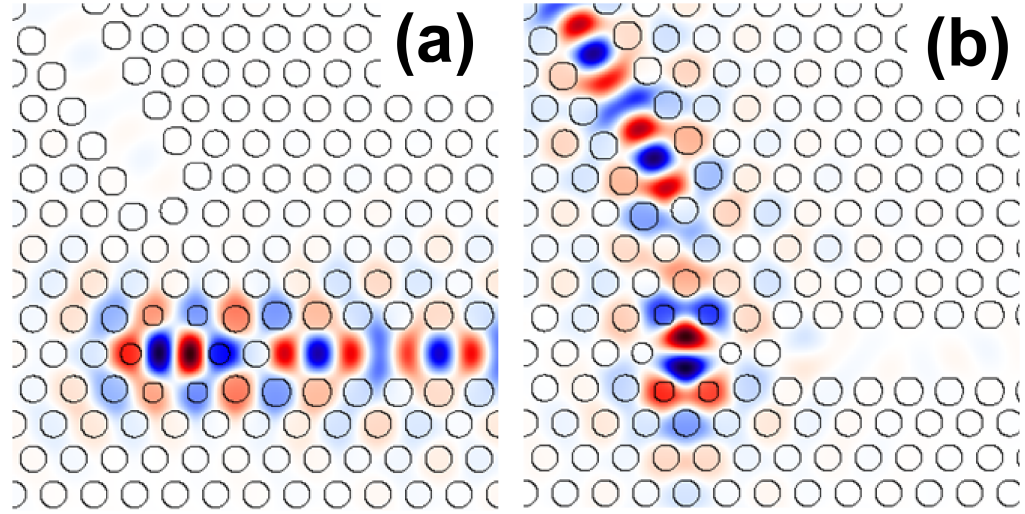


Figure 3.7: Normalised H_z field profiles of the waveguide-coupled cavity system for $N_x = 2$, $N_y = 4$. (a) The selective coupling of the X-dipole mode to the X-waveguide and (b) the Y-Dipole mode to the Y-waveguide.

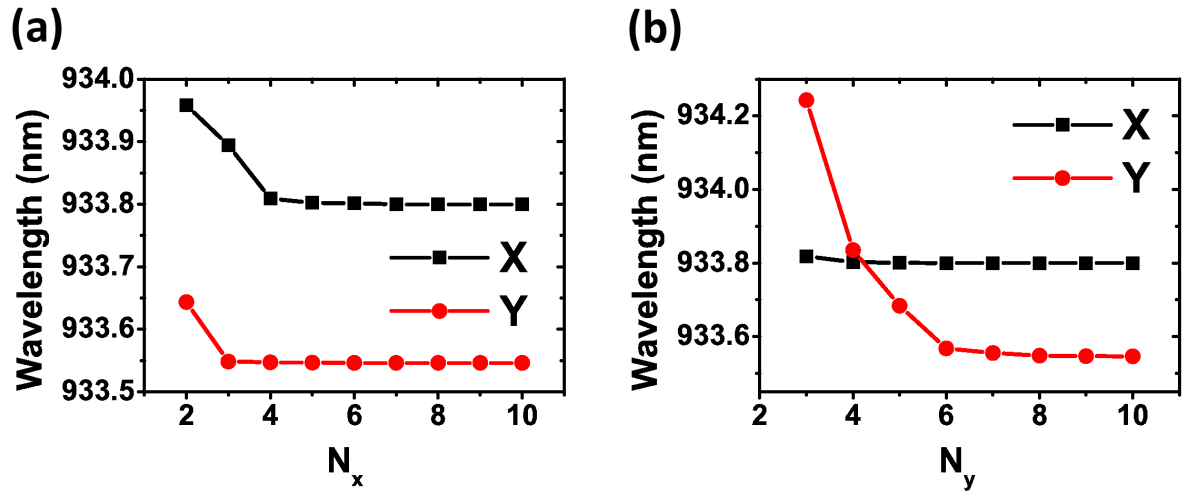


Figure 3.8: Resonant mode wavelengths as a function of waveguide for both cavity modes when adjusting the proximity of the (a) x- and (b) y-waveguide.

3.3.3 Fine-Tuning of Coupling Efficiency using Continuous Adjustment of Coupling Region

Whilst discrete adjustment of the number of holes between cavity and waveguide produces comparable coupling efficiencies, a continuous adjustment is needed to equalize these values. Modification of the photonic crystal in the coupling region between the cavity and waveguide is required to adjust the coupling rate of the cavity mode to the waveguide. Continuous adjustment can be achieved by altering the radius of the holes or displacing the holes in the coupling region, similar to the methods used to optimise the cavity. The method used was the displacement of the first hole in the Y-waveguide along the waveguide by δS_y , as defined in Figure 3.9(a) as this produced an overlap in the coupling efficiencies. The Y-dipole mode is most sensitive to δS_y , displaying a decrease in coupling efficiency of 3% for $\delta S_y = 0.2a$. The coupling efficiency of the X-dipole mode has a non-zero dependence on δS_y of <0.5% over the same range due to a small degree of cross-coupling to the Y-waveguide. The resulting reduction in coupling efficiency for the Y-dipole equalizes both efficiencies at 89.4% for $\delta S_y = 0.08a$ as shown in Figure 3.9(b).

3.3.4 Fine-Tuning of Waveguide Dispersion

The region of the W1 waveguide mode near to the zero-slope cut-off produces slow-light phenomena due to an anticrossing between the ‘index-guided’ and ‘PBG-guided’ modes of the W1 waveguide [52, 73] as discussed in Section 1.2.2. This can lead to increased scattering losses [148] due to the increased group index of the waveguide mode, and spectral truncation [149] due to close proximity to the cut-off frequency of the waveguide mode. Because of the shift in resonance frequency of the cavity modes from the adjustment of the first holes around the cavity, the resonant frequency of the cavity modes is close to the band edge of the waveguide dispersion as shown in Figure 3.10(b). To avoid the undesired effects of the slow light regime, the waveguide mode is red-shifted by displacing the first row of holes perpendicular to the waveguide by $\delta W = 0.08a$, Figure 3.10(a), ensuring the cavity mode lies within a higher group velocity region of the waveguide dispersion [140, 141] as shown in Figure 3.10(c). δW was

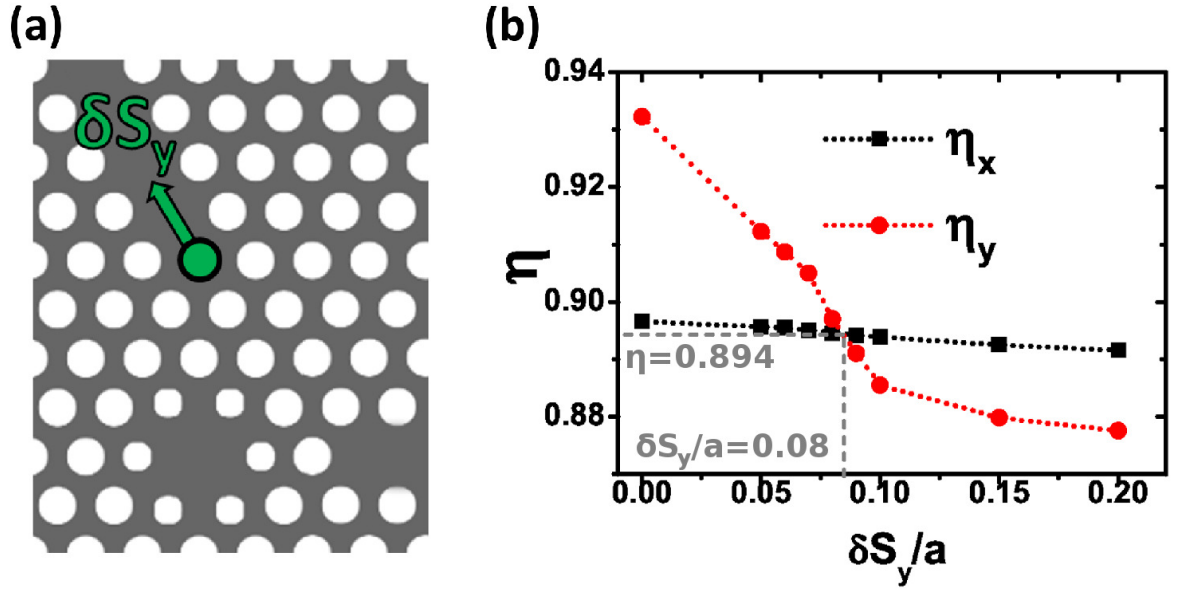


Figure 3.9: (a) Schematic defining the hole displacement in the y-waveguide, δS_y used to finely adjust the coupling efficiency of the Y-dipole mode. (b) Coupling efficiency of the cavity modes to their respective waveguides as a function of $\delta S_y/a$. The coupling efficiencies were equalised at $\eta = 0.894$ for $\delta S_y = 0.08a$.

applied to both waveguides, but is only illustrated for the X-waveguide in Figure 3.10(a) for clarity. These simulations were performed with MIT Photonic Bands (MPB) [54].

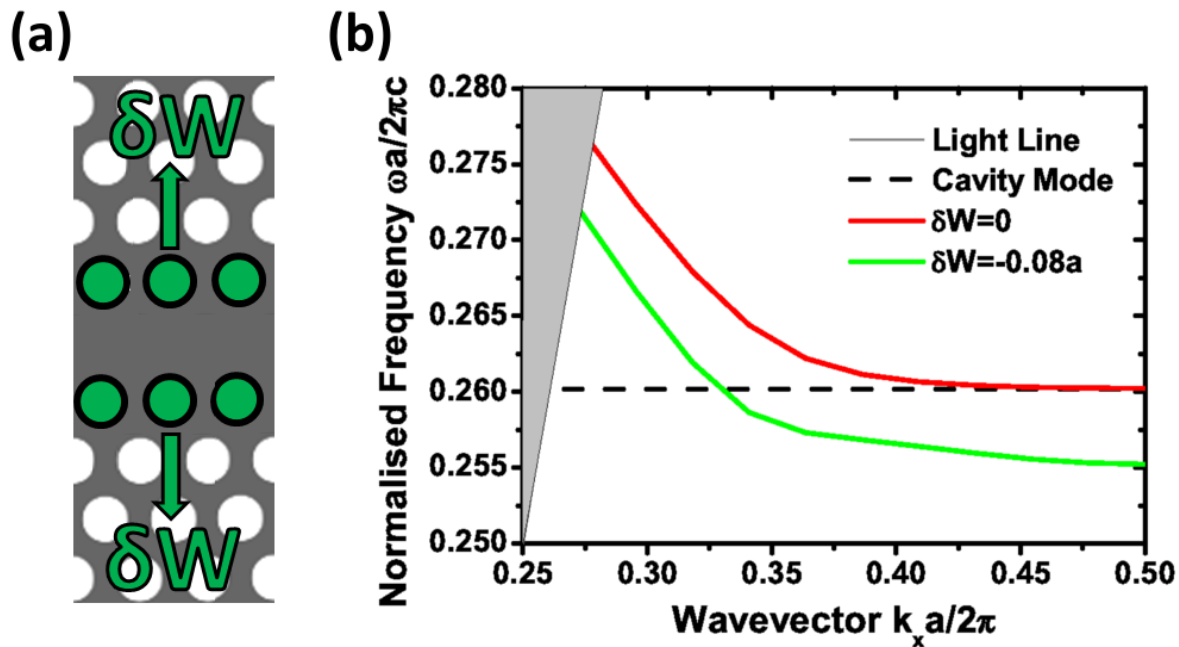


Figure 3.10: (a) Schematic defining the lateral hole shift δW used to adjust the W1 waveguide dispersion. (b) Band structure of the W1 waveguide showing the redshift when the first holes in the waveguide are displaced laterally outward. The waveguide mode is then red shifted, moving the cavity mode (dotted line) coincidence towards a region of the waveguide mode dispersion with higher group velocity, avoiding slow light and band edge effects.

3.4 Experimental Arrangement

In this section the device fabrication method and experimental setup are presented. The nomenclature used for demonstration of the selective cavity-waveguide coupling is defined.

The samples used in this study were fabricated using the procedure outlined in Section 2.3.2. A scanning electron microscope image of the fabricated device is shown in Figure 3.11(a). Semicircular $\lambda/2n$ air/GaAs grating outcouplers were added to the end of the waveguides to scatter light out of the device plane into the detection apparatus [58, 148].

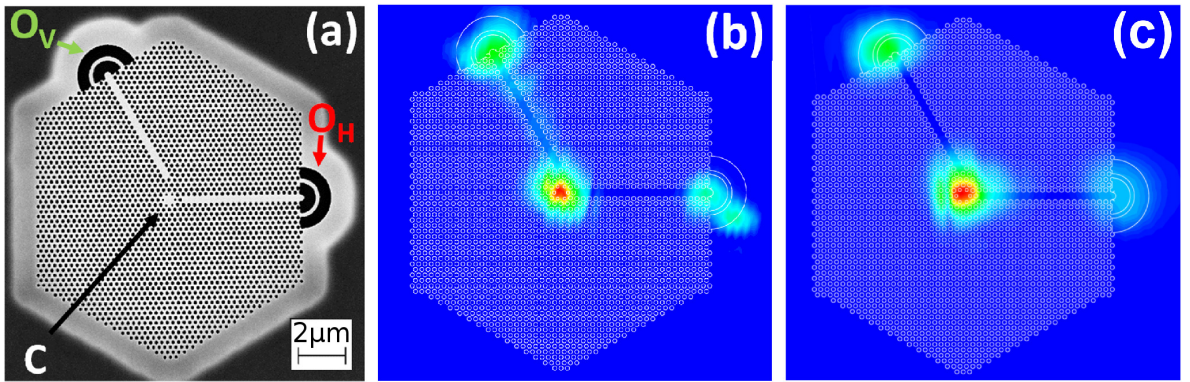


Figure 3.11: (a) SEM image of a fabricated device. The pale regions are underetched GaAs membrane, the dark grey is non-underetched GaAs and black regions are completely etched through the GaAs membrane. The nomenclature for the cavity (C), horizontal (O_H) and vertical (O_V) outcouplers are defined. PL map obtained when (b) the excitation spot is rastered across the device whilst the collection spot is kept fixed at the cavity and (c) the collection spot is rastered across the device whilst the excitation spot is kept fixed at the cavity. An outline of the device is overlaid to show that the three regions of high PL signal correspond to the cavity and outcouplers.

Photoluminescence measurements were performed with the confocal scanning microscopy setup presented in Section 2.3.4, with the sample mounted in a liquid helium bath-cryostat at 4.2K [133]. The QD ensemble was excited via wetting layer excitation using an 850nm CW Ti:Sapphire laser focussed to a spot of $\sim 1\mu\text{m}$ by a 0.55NA objective lens. The QD PL was collected using the same objective lens and is passed to a 0.55m spectrometer via a single mode fibre where it is dispersed onto either a charge-coupled device camera or a fast avalanche photodiode. A motorized scanning mirror was employed in both the excitation and detection paths which allows for spatially selective excitation and detection from the sample [134, 148]. Figure 3.11(b) shows a typical PL map obtained when the excitation spot is rastered across the device whilst the APD collects spectrally filtered PL at the cavity mode wavelength from a fixed collection spot over the cavity. This shows that PL from the waveguides is efficiently coupled to the cavity and transmitted vertically from the cavity. Figure 3.11(c) is a PL map obtained when the collection spot is rastered over the sample whilst the excitation spot is kept fixed over the cavity. This measurement shows that the cavity modes are efficiently coupled and transmitted by the waveguides and scattered vertically by the outcouplers. The different positions used for excitation and collection are defined in Figure 3.11(a): O_H and O_V are the horizontal and vertical outcouplers, respectively and C is the cavity. A notation is defined to identify these positions of excitation and collection spots as (excitation position)(collection position). For example, excitation of the cavity and collection from the horizontal outcoupler is denoted CO_H .

The polarisation-sensitive measurements shown in Figures 3.13, 3.16 and 3.20 in later sections of this chapter were conducted by insertion of a half-wave plate and Glan-Thompson polariser prior to the single mode fibre in the collection path. Firstly, the polariser was inserted and rotated until a maximum signal level was reached. This allows one to find the preferred polarisation of the fibre, induced by strain in the fibre. Once ascertained, the half-wave plate was inserted and used to rotate the polarisation of the incoming light into the plane of the polariser. Using this method eliminates artefacts in polarisation measurements due to the polarisation preference of the fibre. The PL emission was expected to be linearly polarised

from the outcouplers due to their design favouring transmission of light polarised transverse to the waveguide axis.

3.5 Non-Degenerate Cavity

3.5.1 Origin of Mode Degeneracy Lifting

The H1 cavity is highly sensitive to the symmetry of the surrounding photonic crystal. In fabrication, random disorder commonly leads to reduction of the cavity symmetry and lifting of the degeneracy of the dipole modes. A perfect cavity possesses sixfold discrete rotational symmetry and sixfold mirror symmetry, implying that the dipole modes occur in pairs separated by 30° , repeated every 60° . If the cavity is uniaxially deformed the only remaining symmetries are mirrors about this axis and perpendicular to it. Therefore, the only allowed modes are those with polarisation at 0° and $30^\circ + 60^\circ = 90^\circ$ to this axis. Since the cavity lengths are different along these axes, there is a splitting of the mode frequencies. Schemes have been demonstrated to remedy this by adjusting the ellipticity of the holes in the photonic crystal [65] and applying uniaxial strain to the wafer [66]. These techniques were not applied to the devices studied in this chapter however, as an average spectral splitting of $\sim 1.5\text{nm}$ facilitates mode identification, allowing spectral measurements to reveal the coupling behavior in addition to polarisation measurements.

3.5.2 Uncoupled Cavity

In order to calculate the coupling efficiency of the devices by ascertaining the intrinsic losses, the Q factors of uncoupled H1 cavities were measured. A typical uncoupled cavity spectrum is presented in Figure 3.12.

These data were taken by directly exciting the QD ensemble in the cavity and collecting PL from the same position (CC configuration). The cavity modes are fed via the quasi-continuum of excitonic transitions of the QD ensemble [150, 151] which, above saturation power of the QDs, produces a clean spectrum of the cavity modes as seen in Figure 3.12. The Q factors are

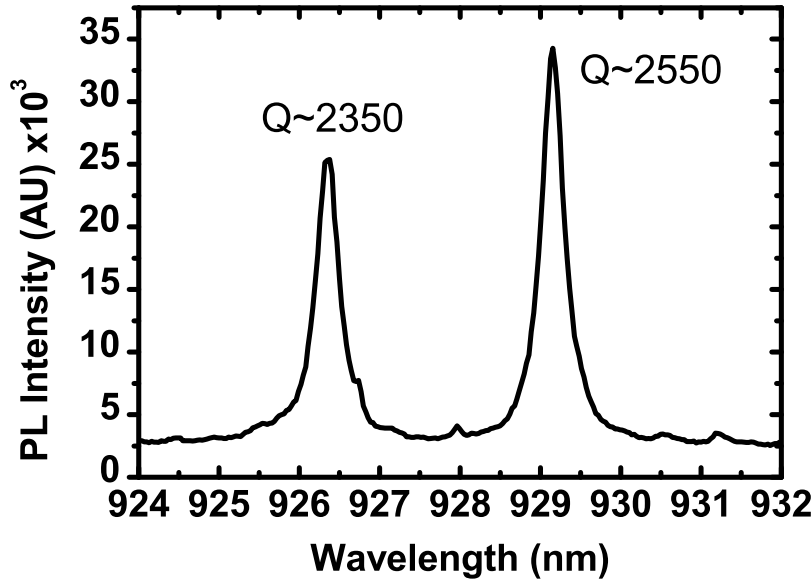


Figure 3.12: PL spectrum obtained for an uncoupled cavity. The modes have Q factors of 2350 and 2550, and are separated by 2.8nm. The degeneracy of the modes is lifted by geometrical imperfections of the cavity due to random fabrication errors.

<10% of the simulated Q-factors, on average $Q \sim 2333$, implying a high intrinsic loss rate. The photonic crystal lattice is the same size as that used in simulation, which is sufficiently large as to negate in-plane losses. Therefore scattering losses from fabrication imperfections are potentially the dominant sources of loss in these cavities. A secondary effect of QD scattering losses only become significant in high-Q cavities, but are not expected to significantly affect the loss rate in these devices. These mechanisms scatter light from the cavity into the light cone of the photonic crystal slab and therefore the cavity couples more efficiently to free space modes. The sample used for experiments comprised a uniformly high distribution of QDs, so it was not possible to isolate the two losses by moving to a region of lower QD density on the sample.

3.5.3 Coupled Cavity

To verify the selective coupling behaviour of the coupled devices, spectra were recorded for the CC configuration and the cavity Q factors and mode splitting assessed. A typical coupled device spectrum is shown as the black line in Figure 3.13(a). Two cavity modes are clearly visible at 944.0nm and 945.3nm, with coupled Q-factors (Q_c) of 1500 & 1600 respectively. The addition of the waveguides acts to reduce the splitting of the uncoupled cavity modes of an average of 2.9nm down to an average of 1.5nm for the waveguide coupled cavity. To verify the selectivity of the cavity mode coupling to the waveguides, the CO_H & CO_V configurations are used. In this arrangement the QD ensemble in the cavity is excited non-resonantly as before, but the cavity emission is collected from the gratings at the ends of the waveguides. Polarisation-sensitive measurements of the modes in the CC configuration cavity, shown in Figure 3.13(c), reveal that the modes are indeed orthogonal: the peak at 944.0nm is horizontally (x) polarised and 945.3nm is vertically (y) polarised. As can be seen from Figure 3.13(b), the peak at 944.0nm is principally observed from O_V and the 945.3nm peak from O_H . Therefore the behaviour of the device is in agreement with simulations, despite the non-degeneracy of the modes.

Using the Q factors obtained above for the coupled and uncoupled cavities, the coupling efficiencies of the X and Y-dipole modes were calculated to be 36% & 37% respectively. These are much lower than the expected value of 89% due to the large intrinsic loss rate of the uncoupled cavities. The out-of-plane losses dominate over the in-plane waveguide coupling rate in determining the overall loss rate, and so the cavity couples to the waveguide less efficiently. The intensities of the peaks as seen from the outcouplers are 20% and 18% of those observed from the cavity for the X and Y-dipole modes respectively. These values are lower than when comparing the Q-factors due to the additional losses of the outcouplers, which do not affect the Q-factors of the cavity modes. Further improvements to fabrication are expected to improve the device efficiency by reducing the out-of-plane losses, increasing the Q-factor of the uncoupled cavity and increasing the fraction of cavity emission that couples to the waveguide.

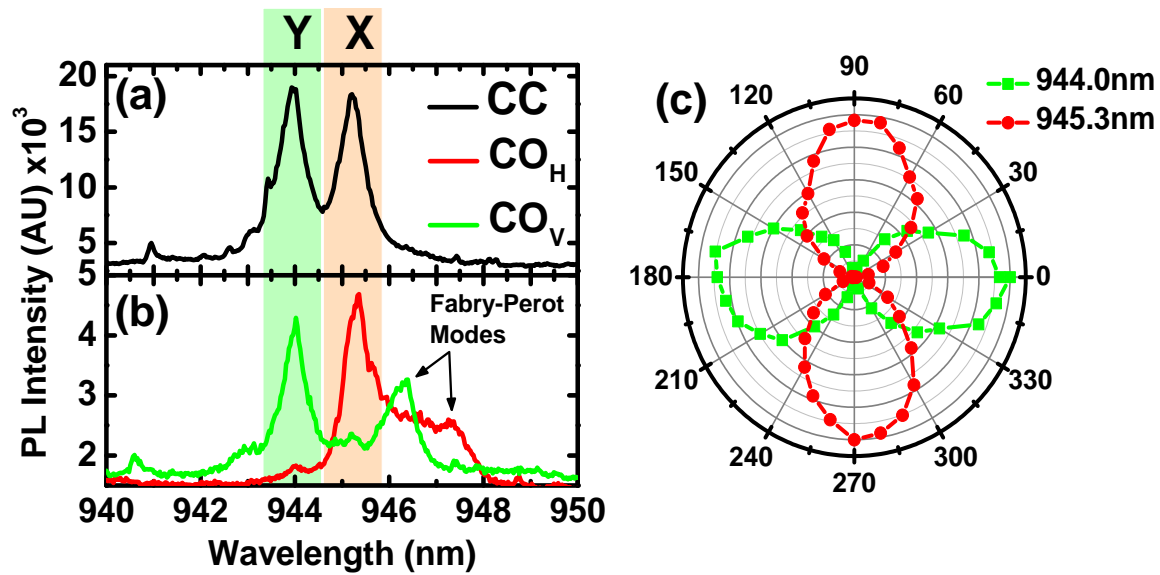


Figure 3.13: (a) PL Spectra for a waveguide-coupled non-degenerate cavity obtained when exciting the cavity and collecting from the cavity (b) PL Spectra obtained when exciting the cavity and collecting from the outcouplers. Fabry-Perot modes in the waveguides are indicated. (c) Polarisation-sensitive measurements of the cavity modes when exciting and collecting from the cavity.

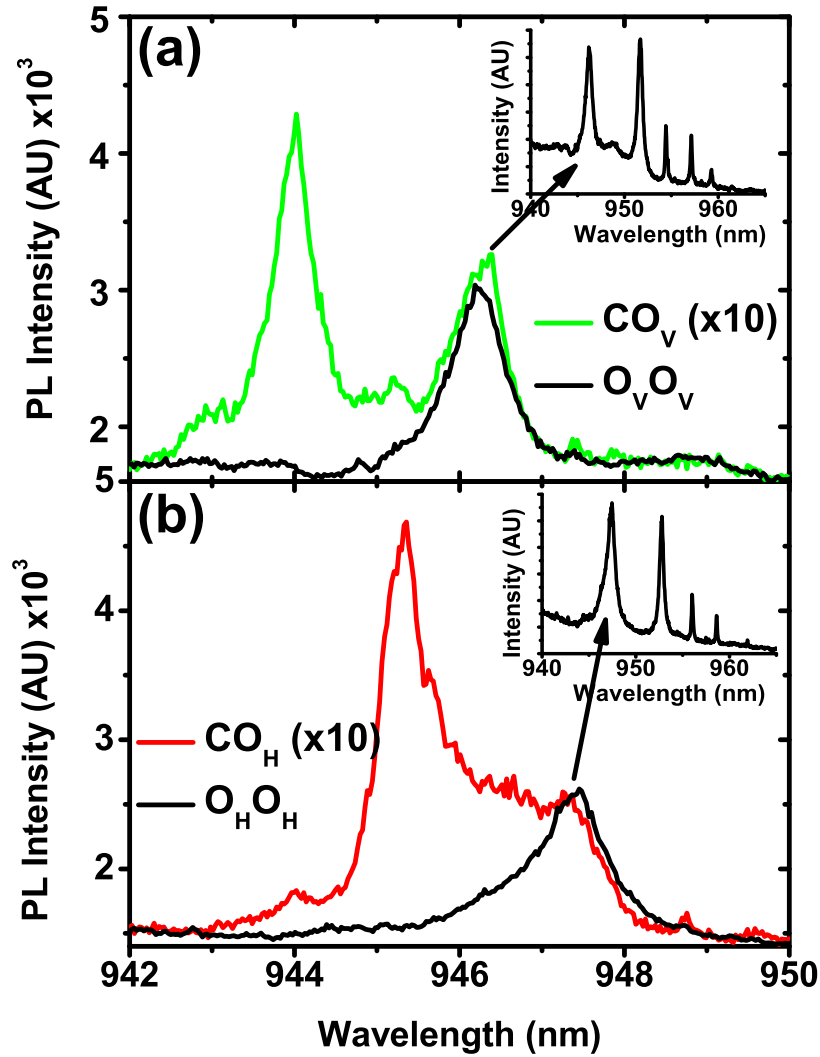


Figure 3.14: PL Spectra obtained when collecting from the (a) vertical (b) horizontal out-coupler. The (a) green (b) red trace is the same as Figure 3.13(b), obtained using the CC configuration. Overlaid in black is a spectrum taken when the excitation spot is on the same outcoupler to observe the Fabry Perot modes of the (a) Y (b) X waveguide, the $\text{O}_V \text{O}_V$ and $\text{O}_H \text{O}_H$ configurations respectively. (Inset) wider spectral window of the Fabry Perot spectrum obtained when using the (a) $\text{O}_V \text{O}_V$ and (b) $\text{O}_H \text{O}_H$ configurations respectively.

Additional peaks are observed in the spectra when exciting the cavity and collecting from the outcoupler, at 947.4nm for the X-waveguide and 946.2nm for the Y-waveguide. These features do not appear when collecting light from the cavity, so they must originate from the waveguides. Since the waveguides are of finite length, terminated at one end by the photonic crystal and the outcoupler at the other end, the waveguide forms a pseudo-cavity structure that supports Fabry-Perot resonances [148]. To investigate the hypothesis that the additional peaks are due to Fabry-Perot resonances, spectra were taken when exciting and collecting from the same outcoupler for each waveguide ($O_V O_V$ and $O_H O_H$ configurations) as these directly excite the Fabry Perot modes using QD PL, which isolates the cavity modes from the spectrum. These data, shown in Figure 3.14, reveal that there is indeed a family of Fabry-Perot modes supported by the waveguides. Moreover, the peak of one Fabry-Perot mode in each waveguide is spectrally coincident with the extra peak observed for $CO_{H/V}$ spectra. Spatial overlap of the excitation spot with the waveguide and spectral overlap of the cavity mode with this Fabry-Perot mode may drive it more strongly than other modes in the waveguides, producing an additional peak of comparable intensity to the cavity mode when observed from the outcoupler.

Further proof of the selective coupling is observed using the $O_H C$ and $O_V C$ configurations whereby the waveguide mode is excited from the outcoupler, which in turn drives the cavity modes at resonance. PL is then collected from the cavity, which maintains the same selectivity as when the cavity is excited directly; however a small degree of cross-coupling is observed from the X-waveguide (CO_H). These results are shown in Figure 3.15. The selective coupling in this reverse arrangement is still governed by the field overlap between cavity and waveguide modes, representing the probability of successful evanescent tunnelling of photons from the waveguide to the cavity. Therefore, the probability of cross-coupling is still low when light is injected into the cavity from the waveguide. The origin of the cross coupling is most likely due to defects in the photonic crystal lattice. Due to the proximity of the horizontal waveguide to the cavity, the unmatched parity between the Y-dipole and the waveguide mode is significant in determining the field overlap between them and hence maintaining the selectivity. If fabri-

cation imperfections are present, this symmetry is broken and the parity constraints are lifted which can result in an increase of the overlap integral between the Y-dipole and horizontal waveguide modes. For the vertical waveguide, the cavity-waveguide separation is much larger and the dominant effect in determining the selective coupling is the relative amplitudes of the two cavity modes in the coupling region, where the Y-dipole has a higher amplitude than the X-dipole. Since the parity is a secondary parameter here, the effects of disorder on parity breaking can be expected to be less significant which is reflected by the relative intensities of the two cavity peaks in Figure 3.15 being smaller for $O_V C$ than for $O_H C$. The cavity modes appear more intense than when collecting from the outcouplers due to the increased coupling rate of the cavity modes to free space as discussed previously. The Fabry-Perot modes from Figure 3.14 are heavily suppressed in these spectra due to resonant filtering by the cavity mode. In summary, measurements in this configurations provide a very clear demonstration of selective coupling with minimal interference from the Fabry-Perot modes of the wavguides.

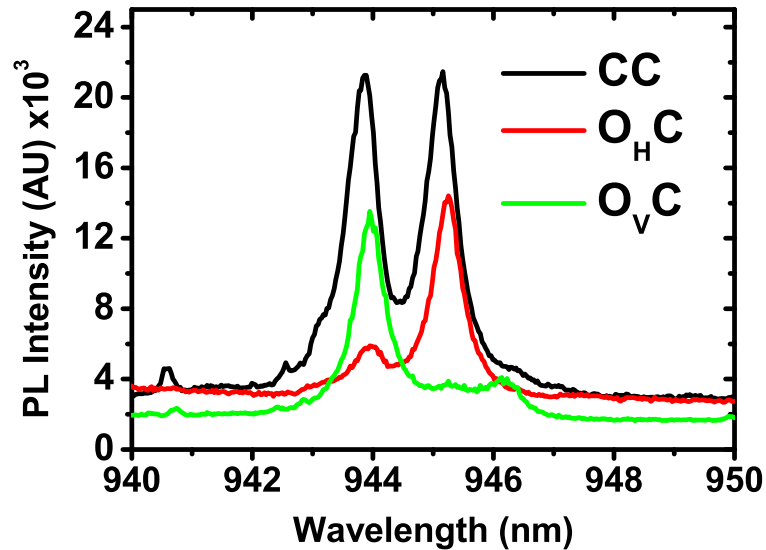


Figure 3.15: PL Spectra of fixed collection from the cavity with excitation at the cavity and outcouplers.

3.5.4 Discussion

The lifted degeneracy and low waveguide coupling efficiency of this device limits its use as a spin-photon interface, due to the difficulty in simultaneously coupling a single QD to both modes efficiently. However, since the coupling mechanisms rely upon spatial and not spectral discrimination the selective coupling behaviour of the cavity is maintained. Spectral and polarisation-sensitive measurements of the waveguide-coupled cavity modes have demonstrated that the device operates selectively, in accordance with FDTD simulations. Furthermore, the selective coupling is maintained when the cavity modes are excited from the waveguides which implies that the devices may be coupled to realise a network of selectively coupled cavities for on-chip spin-spin entanglement applications.

Single QD measurements were not made on these devices due to a low yield of fabricated devices which exhibited good selectivity of the cavity modes: of these devices, a single QD which couples to both cavity modes with comparable efficiency was not observed. This low yield can be attributed to the sensitivity of the device to fabrication imperfections and unavoidable random fabrication errors during patterning and etching of the photonic crystal. Such errors lead to lifted cavity mode degeneracy, dissimilar coupling efficiencies and reductions in selectivity. However, as presented in Section 3.7, single QD measurements are possible and the QD emission can be switched between the two waveguides by using an applied electric field to tune the QD exciton from one cavity mode to the other via the quantum confined Stark effect.

3.6 Near-Degenerate Cavity

3.6.1 Cavity Excitation

Amongst the range of cavity mode splitting produced during fabrication, there were cavities which exhibited a mode splitting that is of the order of, or less than, the cavity mode linewidth. In this regime, the cavity modes appear approximately unpolarised where they spectrally coincide and as such a single QD can couple to both modes simultaneously. This system

is not truly degenerate, since the mode splitting is still non-zero, but sub-linewidth. For this type of device, the argument for selective coupling is made using polarisation-sensitive measurements and measurement of the cross-talk of the device from one waveguide to another.

A typical PL spectrum from a waveguide-coupled near-degenerate cavity is shown in Figure 3.16(a) using the CC configuration. A single spectral feature is visible at 935.2nm. The cavity modes can be seen from the outcouplers, using the $CO_{H,V}$ configurations, as shown in Figure 3.16(b), where an offset is observed between the two peaks. Polarisation sensitive measurements of the cavity modes using the CC configuration, shown in Figure 3.16(c), confirm that the two peaks are orthogonally polarised.

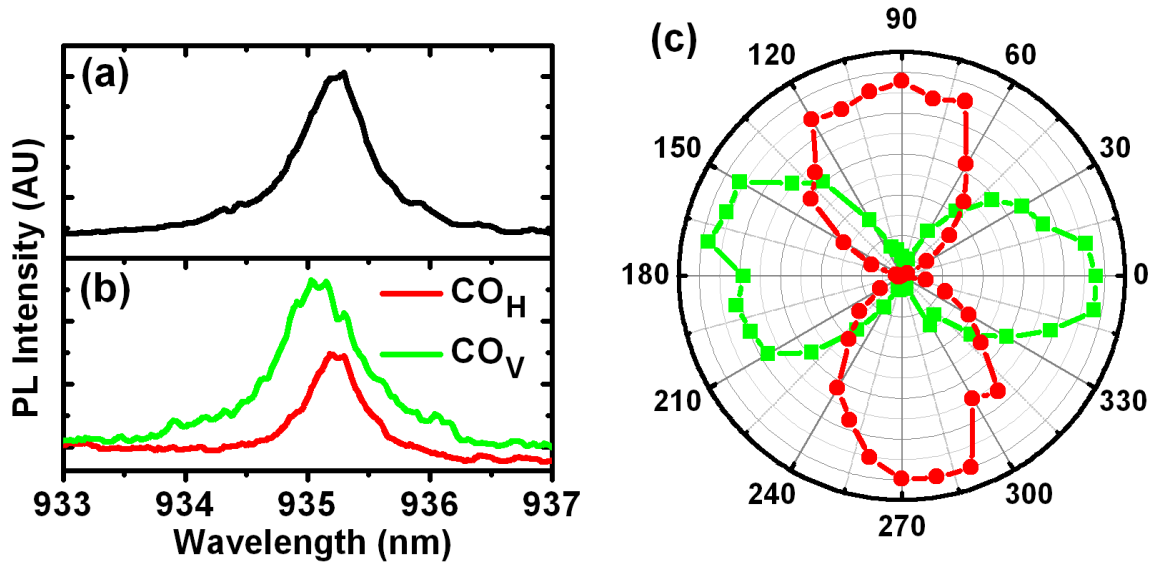


Figure 3.16: (a) PL Spectra obtained for a waveguide-coupled near-degenerate cavity when exciting the cavity and collecting from the cavity (b) PL Spectra obtained when exciting the cavity and collecting from the outcouplers. A splitting of 0.12nm is observed between the cavity modes when observed from the outcouplers. (b) Polarisation-sensitive measurements of the cavity modes from the spectra of Figure 3.17, using the CC configuration.

The Q-factors of the X and Y-dipole modes were measured to be 1600 and 1200 respectively. Using the Q factors for the uncoupled cavity from the previous section along with

Equation 3.1 the corresponding coupling efficiencies were calculated as 37% and 48% for the X and Y dipole modes respectively. Again, due to the low intrinsic Q factor of the uncoupled cavity, these coupling efficiencies are much lower than those intended by design.

From the polarisation-sensitive measurements of the cavity modes, the true splitting of the cavity modes can be deduced when the detection polarisations are aligned along the x and y axis of the cavity. These data are shown in Figure 3.17, where a true splitting of 0.18nm is measured using the CC configuration, compared to an observed splitting of 0.12nm from Figure 3.16(b).

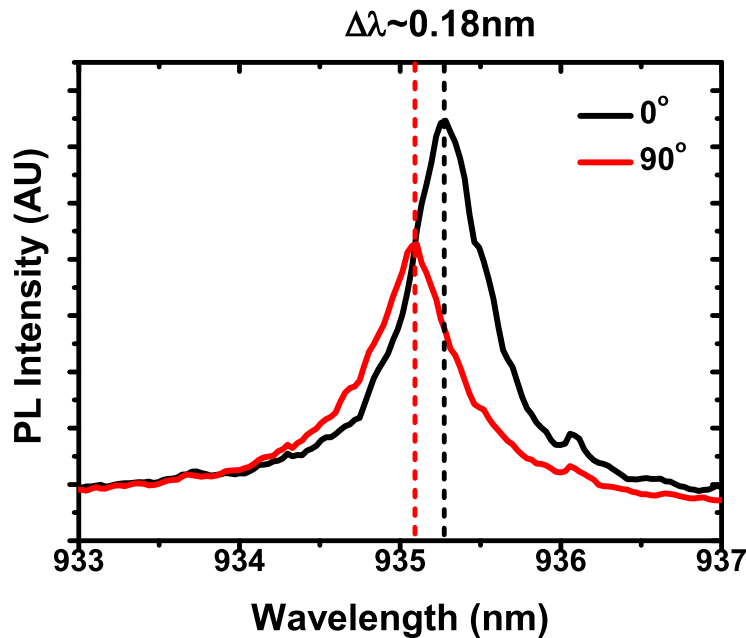


Figure 3.17: Polarisation-sensitive PL Spectra taken using the CC configuration for orthogonal polarisations. The cavity modes have a sub-linewidth splitting of 0.18nm.

Due to this sub-linewidth mode splitting spectral measurements are not sufficient to fully validate the selective coupling, although a splitting of 0.12nm is measured when the cavity modes are observed from the waveguides. For this device, the level of crosstalk is used to infer the presence of selective coupling of the cavity modes to their respective waveguides. The crosstalk is measured by placing the excitation spot on one outcoupler and collecting

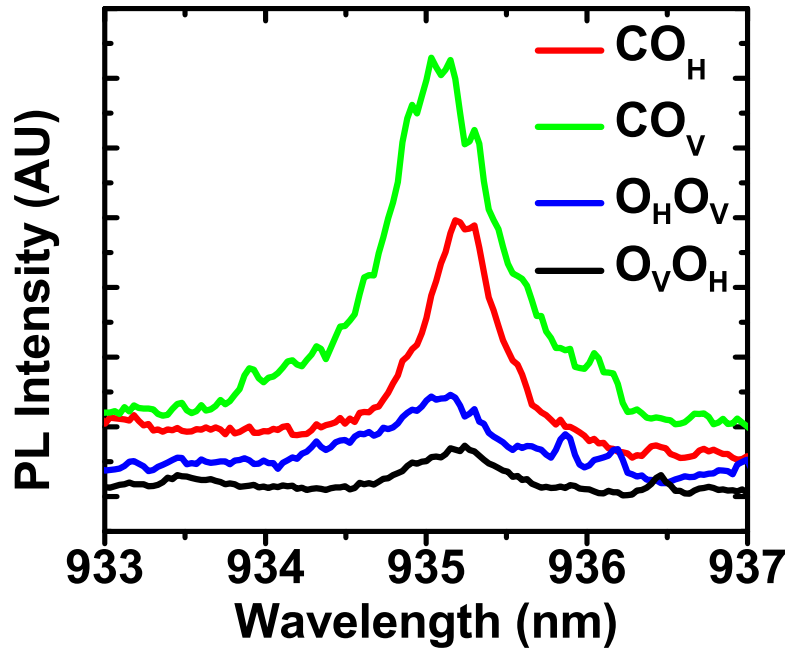


Figure 3.18: PL spectra showing the crosstalk of the device relative to the selective coupling of the cavity modes to the waveguides.

emission from the other (O_HO_V and O_VO_H configurations). For example, using the O_HO_V configuration, if the device is truly selectively coupled then only the X-dipole mode should be excited from the horizontal waveguide. In turn, the X-dipole mode should not couple to the vertical waveguide and no emission should be observed from O_V . However, if the device is not selectively coupled then both cavity modes can couple to each waveguide and the measured intensity from the opposite outcoupler is non-zero.

The measured cross talk spectra are presented in Figure 3.18. From these data, the cross talk is comparable to the background level of the $CO_{H,V}$ spectra, at around 20% of the peak intensity above background. Moreover, the peak intensity observed in each crosstalk measurement spectrally coincides with the same peak when exciting the cavity and collecting from the same outcoupler: that is, a peak is observed for O_VO_H within 0.036 ± 0.009 nm of the peak observed for CO_H and vice versa for the Y-waveguide. This insight suggests that the

Y-dipole is excited via scattered light from the x-waveguide and vice versa for the X-dipole and y-waveguide, since the peak for the X-dipole is not observed from the y-waveguide and the Y-dipole is not observed from the x-waveguide, which acts to increase the apparent level of cross coupling.

3.6.2 Waveguide Excitation

To further investigate the apparent cross-coupling behaviour, the selective coupling in the $O_{H,V}C$ configurations were measured. The PL spectra when collecting emission from the cavity are shown in Figure 3.19, where a splitting of 0.087nm is observed between the two cavity mode peaks. Similarly to the non-degenerate case, the intensity of the cavity modes are comparable to when the cavity is excited directly. This may again be attributed to the increased coupling rate of the cavity modes to free space leading to increased intensity when collecting from the cavity.

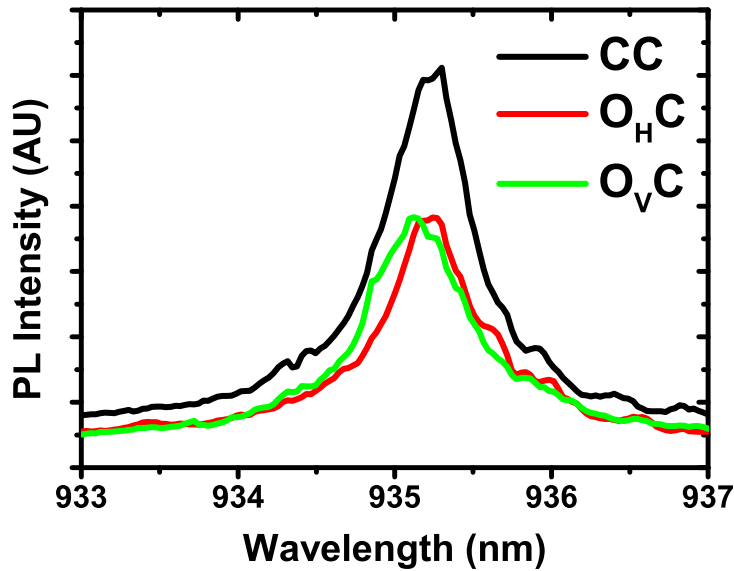


Figure 3.19: PL Spectra of fixed collection from the cavity with excitation at the cavity and outcouplers.

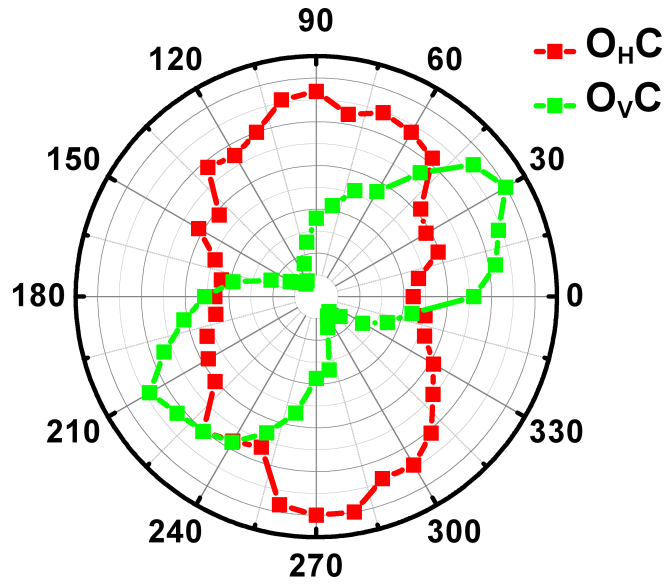


Figure 3.20: Polarisation sensitive PL measurements of the cavity modes when excited from the waveguides.

Polarisation-sensitive measurements of the cavity modes when excited from the outcouplers do not exhibit an orthogonal relationship. As demonstrated in Figure 3.20 the maximum intensity for the X-dipole occurs at polarisation angles of $90^\circ/180^\circ$ whilst for the Y-dipole, these occur at $30^\circ/210^\circ$. This is perhaps to be expected, since the cavity modes are being excited by the waveguide mode which is polarised orthogonal to the waveguide axis and the y-waveguide is rotated by 30° from the vertical. However, this polarisation must be supported by the cavity and must be coupled to the waveguide. The observation that the cavity mode intensity drops to only 40% of the maximum at orthogonal polarisation suggests that there is a higher degree of cross talk than observed from previous measurements of the selective coupling.

In order to explain this effect of non-orthogonal measured polarisation for $O_{H,V}C$ measurements, additional FDTD simulations were performed using a broadband dipole source in the waveguides to excite the fundamental waveguide mode: a scenario that is equivalent to the excitation of the waveguide modes via QD ensemble PL. The field profiles of the simulations, illustrating the principle field components (E_x , E_y and H_z), are shown in Figure

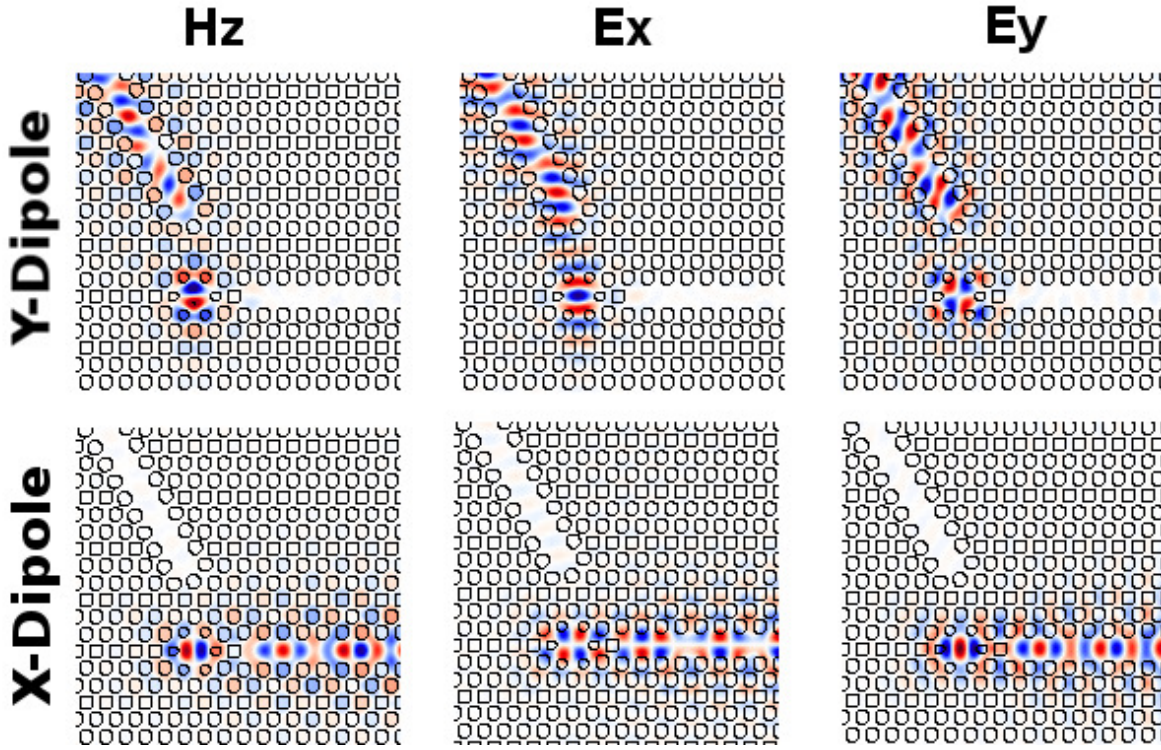


Figure 3.21: FDTD Simulation of cavity excitation via a broadband dipole source in the waveguides for the three principle field components. The field amplitude for each component is shown.

3.21. For y-waveguide excitation, the H_z fields show the Y-dipole mode being excited by the waveguide mode. The waveguide mode appears distorted due to back-reflections from the coupling region. The E_x fields also confirm that the Y-dipole is present. The E_y field profiles display a cavity field profile that matches the y-polarised fields of the Y-dipole mode as presented in Section 1.2.2. This confirms that the polarisation dependence observed in Figure 3.20 maintains selectivity.

At the cavity centre, the modal fields exhibit an antinode of the principal E-field component, which is orthogonal to the H_z dipole orientation. A single QD positioned here will principally couple to these field components and should be correspondingly polarised [99]. Therefore for a single QD, only E_x polarised emission should be visible from the y-waveguide and E_y polarised emission from the x-waveguide. Similarly, excitation of the cavity via the y-

waveguide should produce E_x polarised QD emission and E_y polarised emission when excited from the x-waveguide.

3.6.3 Discussion

Through spectroscopic and polarisation sensitive measurements the selective coupling behaviour of near-degenerate cavity modes to separate waveguides has been demonstrated. This work shows potential for efficient spin-photon interfaces using photonic crystals with optimised fabrication to increase the coupling efficiency. The device exhibits low cross talk, but care must be taken when using samples with high QD density due to potential scattering effects between the cavity modes. The selective coupling behaviour is maintained when exciting the cavity modes from the waveguides, although polarisation measurements reveal that a pure polarisation state is not created in the cavity. FDTD simulations reveal that for a single QD at the cavity however, pure polarisation transfer can be achieved.

Single QD measurements were not made on this sample due to a low yield of fabricated devices which exhibited good selectivity of the cavity modes: of these devices, a single QD which couples to both cavity modes with comparable efficiency was not observed. As discussed in [67], this criterion is very strict and requires a single QD to be positioned within 20nm of the cavity centre. The recent development of post-growth QD registration techniques may realise this, but such techniques were not available for these experimental measurements.

3.7 Further Work: Single Photon Routing using Electro-Optical Tuning

Further to the demonstration of selective coupling for a non-degenerate cavity, with application of an electric field across the device, tuning of the QD emission energy via the quantum confined Stark effect is possible. This additional control allows for the QD to be tuned from resonance with one cavity mode to the other mode. For a selectively coupled cavity, this facilitates the switching of QD emission from one waveguide to the other. Such a device may be

used to form an electrically controlled single photon router, whereby single photons emitted by the QD can be switched between two output channels.

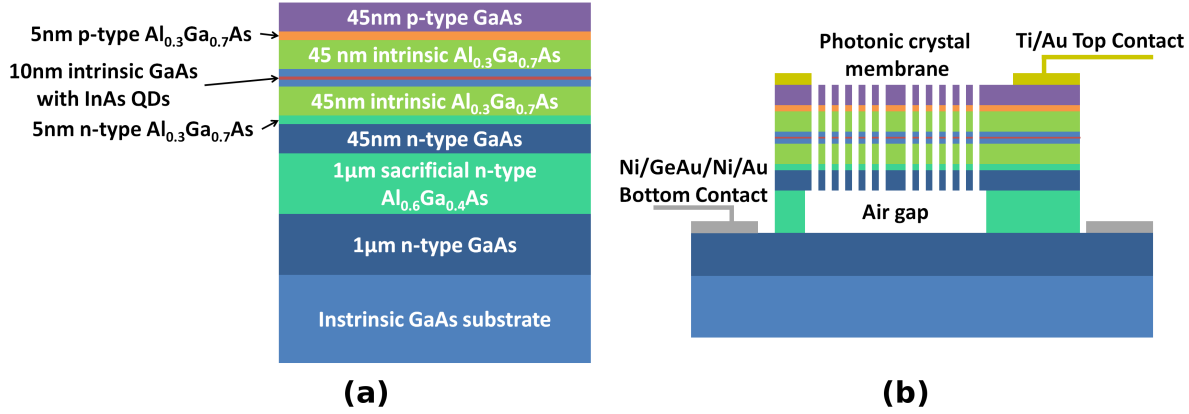


Figure 3.22: (a) Layer structure of wafer used for single photon routing experiments. (b) Schematic of device used for single photon routing experiments, showing etched regions and electrical contacts.

Subsequent to my experiments, C. Bentham, I.E. Itskevich and L.R. Wilson have performed experiments to demonstrate such a device using a PIN doped wafer to apply vertical field tuning. The QDs reside in the central intrinsic GaAs region, clad by a pair of AlGaAs barrier layers to prevent tunnelling of charge carriers from the QD at high electric fields. A schematic of the layer structure of the wafer is shown in Figure 3.22 (a). The photonic crystal device is etched into this sample in a similar way as for the other devices in this chapter and electrical contacts applied to the p-type and n-type layers as shown in Figure 3.22 (b). Using an external voltage source across these contacts manipulates the electric field across the QD layer, tuning the QD by up to 4.7nm using 0.5-1V in forward bias.

The average cavity mode splitting in these devices is 2nm and since the tuning range exceeds the mode splitting it is possible to tune the emission wavelength of a single QD over both cavity modes. A typical cavity spectrum is shown in Figure 3.23 alongside the tuning range of a single QD in the same cavity. As can be seen from the data, the tuning range of the QD fully covers the spectral range of the cavity modes.

The principle of single photon routing is as follows. When the QD is off-resonance, the

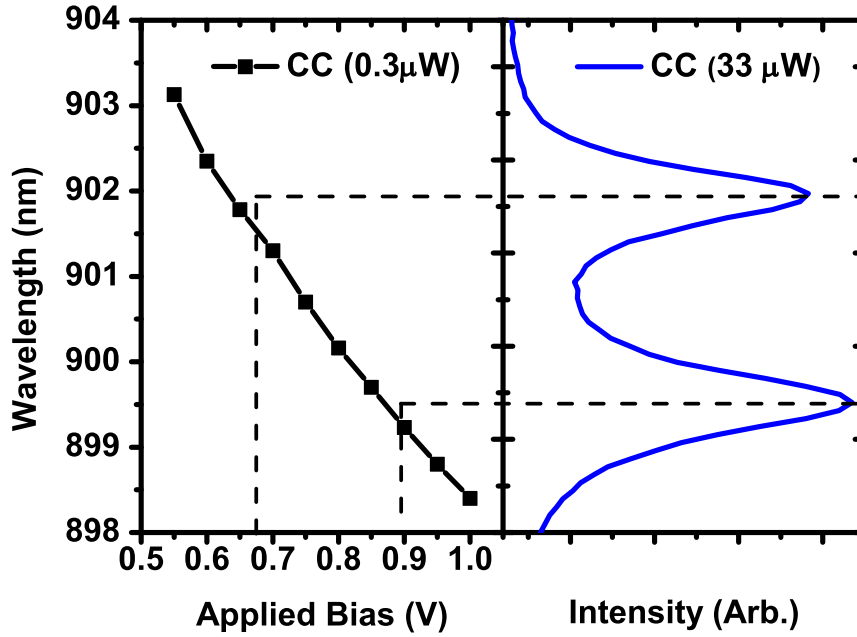


Figure 3.23: (Left) Tuning range of a single QD using an external voltage source within the cavity. (Right) The cavity spectrum at high power showing the position of intensity maxima of the cavity modes.

in-plane emission is suppressed as the QD emission lies within the photonic bandgap of the photonic crystal. When tuned into resonance with the first cavity mode, the QD emission rate is enhanced by the increased photon LDOS at resonance and the QD emits into this cavity mode. The QD is non-resonant with the second cavity mode and does not couple to it. Since the cavity is selectively coupled, the QD emission is channelled into the corresponding waveguide and is detected from one of the two waveguides. When the QD is tuned into resonance with the second cavity mode, the situation is reversed and the QD emission is transmitted into the other waveguide.

The PL intensity for a single QD tuned across the cavity resonances is shown in Figure 3.24. When collecting emission from the cavity (CC, black trace) peaks in the QD PL intensity are observed when resonant with the cavity modes. The emission rate is not equal for the two cavity modes due to two potential factors. At the lower voltage resonance a significant

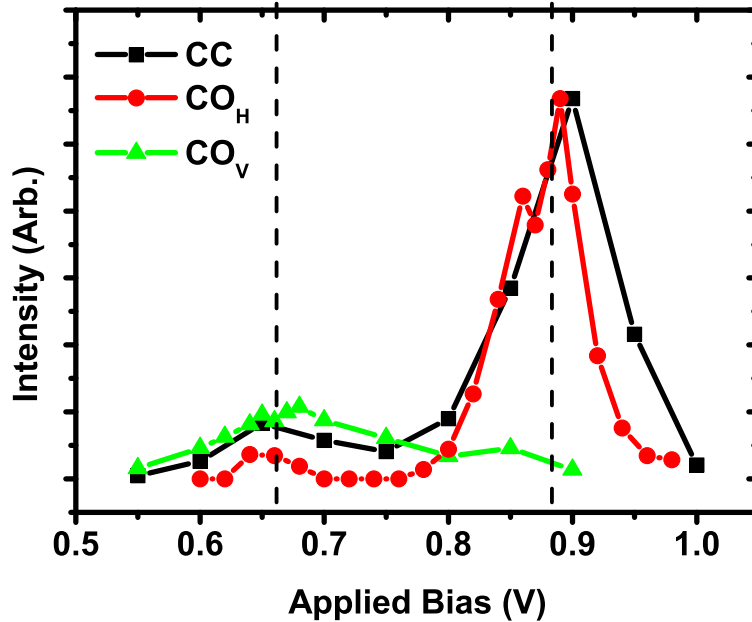


Figure 3.24: PL intensity of QD emission peak when tuned over the cavity spectrum using an applied external voltage. The corresponding voltages at which the QD is resonant with the cavity modes are indicated by dotted lines. Increased PL intensity is observed from the QD when resonant with the cavity modes. When observed from the outcouplers, maximum QD PL is observed when resonant with the corresponding cavity mode.

fraction of photoexcited carriers tunnel out of the QD whilst at higher voltages tunnelling is suppressed. Alternatively, the QD is located off-centre in the cavity and is more strongly coupled to the X-dipole. When PL is collected from the horizontal outcoupler (CO_H, red trace), the QD emission is most intense around 0.9V, which corresponds to when the QD is in resonance with the X-dipole mode. Similarly, for the vertical outcoupler (CO_V, green trace) the QD emission is most intense at ~ 0.65 V: the QD is resonant with the Y-dipole mode.

These measurements, published in [152] and to be presented in full in the thesis of C. Bentham, demonstrate the principle of single photon routing using a photonic crystal cavity selectively coupled to two waveguides, whereby routing is controlled by electrical tuning of a QD between the cavity resonances.

3.8 Summary

In summary, the design of an unpolarized photonic crystal cavity which exhibits selective coupling of the two orthogonally polarized dipole modes of an H1 cavity to two separate waveguides has been presented. Using FDTD simulations, the cavity-waveguide separation was optimized for equal coupling efficiencies of 89%, coupled Q-factors exceeding 2000 and the waveguide dispersion adjusted to reduce propagation losses of the coupled cavity emission. The selective coupling of the orthogonal dipole modes was experimentally demonstrated for a device with non-zero splitting of the cavity modes and for a device with a small splitting to linewidth ratio. The former may offer functionality as an electrically-controlled single-photon router; the latter is expected to act as a spin-photon interface for a resonant QD positioned at the cavity center. This provides a one-to-one correspondence between the Bloch sphere of the excitonic spin states of the QD and the Poincaré-like sphere of the cavity modes, encoding this information in a which-path regime. The device maintains selectivity when excited via either the cavity or the waveguides, such that several devices coupled together may realize a scalable quantum spin network, although single QD measurements remain to fully confirm these predictions. Preliminary results of single photon routing using a single QD in a selectively coupled device have also been presented. Routing of the single photon emission between the output waveguides is provided by vertical electric field tuning of the QD.

Chapter 4

Monolithic Integration of a Quantum Emitter with an On-Chip Beam-Splitter

4.1 Introduction

The proposal of linear optics quantum computing (LOQC) represents a significant step towards scalable optical quantum information processing [29]. Integrated optics offers a route forward to achieving the high component density that LOQC requires [21], while also improving the intrinsic stability of the circuitry and giving a significant reduction in the size and complexity of the experimental apparatus [153]. The use of III-V semiconductor circuits is supported by a wealth of mature semiconductor device fabrication techniques and facilitates incorporation of on-demand quantum emitters such as self-assembled quantum dots (QDs) within the circuit. This approach also allows for hybrid approaches beyond LOQC, for example, by forming spin-photon networks [21, 91, 154] for cluster state quantum computation. The incorporation of a quantum emitter within the device also offers a significantly more compact and efficient approach than the use of off-chip quantum emitters such as spontaneous parametric down conversion sources. In addition, QD emitters are deterministic sources so

there is no need for heralding.

In this chapter, the monolithic integration of a self-assembled InGaAs quantum dot with an on-chip directional coupler acting as a beam-splitter is demonstrated at the single photon level. The directional coupler, although conceptually simple, is a crucial component for on-chip quantum optical interference. The chapter begins with a discussion of the design and operating principles of a directional coupler, using FDTD and eigenmode solver simulations to produce an optimised design. Following this is a presentation of the optical characterisation of the directional couplers using micro-photoluminescence (μ PL) spectroscopy and the behaviour of the device at the single photon level is investigated using photon correlation measurements. The chapter concludes with a review of the future work arising from these experiments with applications in quantum interference experiments.

4.2 Simulation and Optimisation of Directional Coupler

4.2.1 Principle of Operation

The directional coupler consists of two single mode waveguides brought into close proximity along their length, as shown in Figure 4.1. In this experiment, the waveguide consists of a suspended nanobeam of GaAs in air which sustains a single TE mode as shown in Figure 4.2. The mode has a single y-polarised electric field antinode at the centre of the waveguide and decays evanescently into the surrounding air.

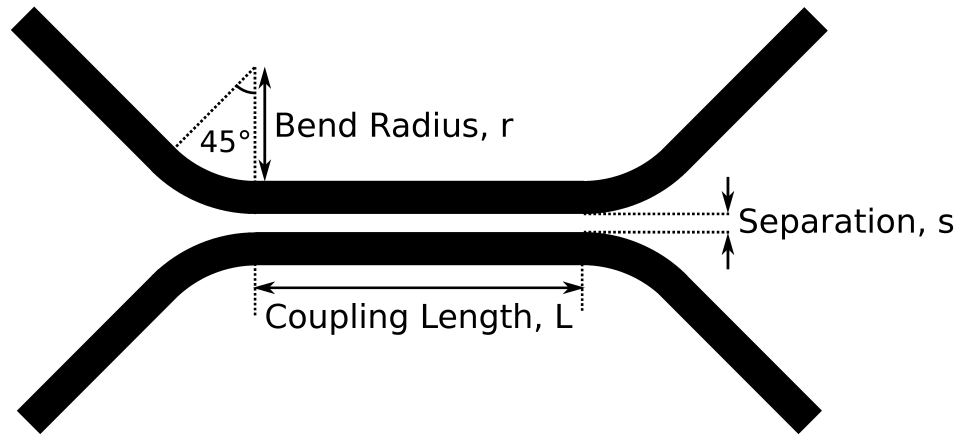


Figure 4.1: Bird's eye view schematic of a directional coupler device showing two waveguides in black separated by s for a distance L before making 45° bends of radius r away from the device.

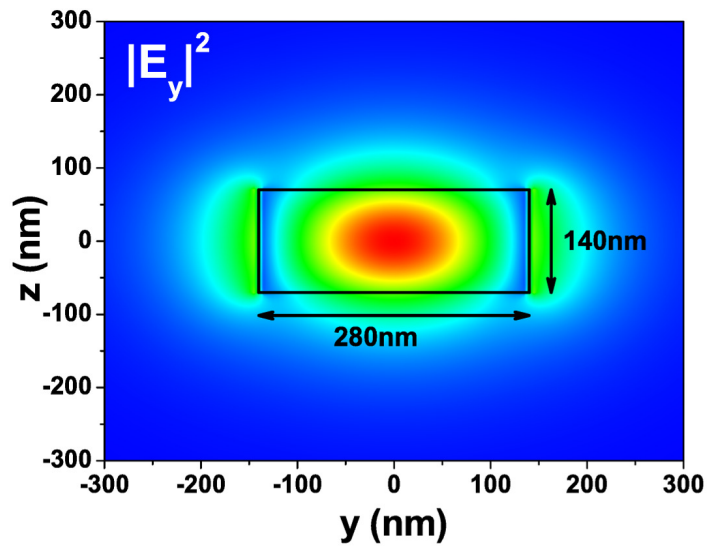


Figure 4.2: Y-polarised electric field intensity of the fundamental mode of a GaAs suspended nanobeam waveguide in air. The waveguide dimensions of 280x140nm are chosen so that only a single TE mode is supported by the waveguide, to which an embedded QD may couple.

If a second waveguide is brought into close proximity, the evanescent components of the two waveguide modes overlap and the modes couple to one another via evanescent tunnelling. Provided that the modes are weakly coupled, that is if the evanescent field from one waveguide does not overlap significantly with the core of the other, then the coupled modes can be approximated as symmetric and antisymmetric superpositions of the individual waveguide eigenmodes [37, 155, 156]. The field profiles of these ‘supermodes’ are shown in Figure 4.3.

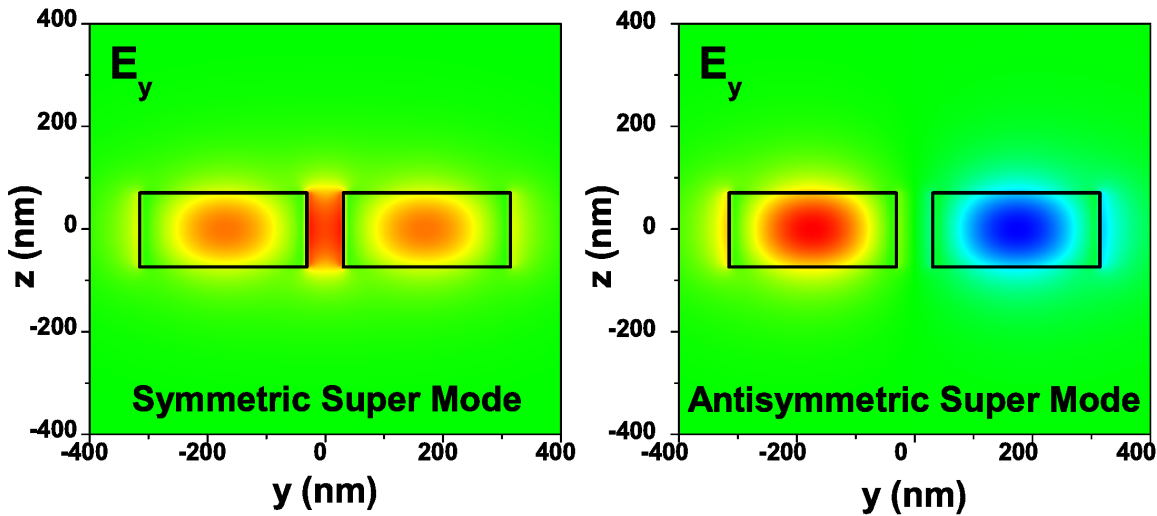


Figure 4.3: Y-polarised electric field profiles of the symmetric and antisymmetric supermodes formed when two single mode waveguides are weakly coupled.

If all the optical power is initially in one waveguide, this can be represented as a superposition of the two supermodes in which the fields interfere constructively in one waveguide and destructively in the other. The two supermodes possess different propagation constants and thus the phase relationship between them changes as a function of propagation distance, x .

The power in each waveguide is given by [156]:

$$\begin{pmatrix} P_1(x) \\ P_2(x) \end{pmatrix} = \mathbf{T}^2 \begin{pmatrix} P_1(0) \\ P_2(0) \end{pmatrix} \quad (4.1)$$

where $P_1(0)$ and $P_2(0)$ are the initial power in the first and second waveguides. \mathbf{T} is the transmission matrix of the directional coupler, given by:

$$\mathbf{T} = \begin{pmatrix} \cos(|\kappa|L) & -i \sin(|\kappa|L) \\ -i \sin(|\kappa|L) & \cos(|\kappa|L) \end{pmatrix} \quad (4.2)$$

where κ is the coupling coefficient between the two waveguides. Transmission to the second waveguide is accompanied by a $\pi/2$ phase shift as represented by the phase factor i . The power oscillates between the two waveguides with a beat length $L = \pi/2|\kappa|$. Therefore, the minimum coupling length required for the input power from one waveguide to be equally divided between the two waveguides is given by:

$$L_{50:50} = \frac{\pi}{4|\kappa|} = \frac{\pi}{2\Delta\beta} = \frac{\lambda_0}{4\Delta n_{eff}} \quad (4.3)$$

where λ_0 is the vacuum wavelength, $\Delta n_{eff} = \lambda_0\Delta\beta/2\pi$ is the difference in effective index between the supermodes, $\Delta\beta$ is the difference in propagation constants between the supermodes and $2|\kappa| = \Delta\beta$ using the supermode approximation [155]. Using frequency-domain eigenmode solver techniques, it is possible to calculate $\Delta\beta$ and thus Δn_{eff} for the supermodes of two coupled waveguides in order to design a directional coupler which equally divides the input optical power between both waveguides. This optimisation is the focus of the next section.

In contrast with silicon photonics approaches, where a silicon waveguide on a silicon dioxide substrate is used, the modes of an air-clad GaAs waveguide are much more strongly confined to the waveguide due to high refractive contrast on all lateral waveguide surfaces. The advantages of this approach are that the electric dipole interaction between embedded emitters and the optical modes is much larger than for weakly confined systems. Strong confinement also allows for more compact devices since tight bend radii can be achieved without significant

radiative losses [38]. One disadvantage of this approach however is that the interaction length between two strongly confined waveguides for a given separation is much longer than for weakly confined modes. However, this can be remedied using a longer coupling region, smaller waveguide separation or thinner waveguides.

4.2.2 Designing a Single Mode Waveguide

For optimal operation of the directional coupler in the single photon regime, the waveguides which comprise the device must confine only a single mode. The single mode waveguides used in this thesis are rectangular waveguides formed from a GaAs membrane suspended in air where the height of the waveguide is determined during MBE growth and the width is defined by lithography. The choice of slab height and waveguide width determine the number of allowed optical modes within the waveguide.

The slab height must be chosen such that only a single vertical mode is confined. A QD has an in-plane electric dipole moment which couples efficiently to TE-like modes of the waveguide so the design must aim for confinement of a single TE-like mode. To ensure single vertical mode confinement of a TE-like mode in the slab, the round trip phase of the fields between the upper and lower interfaces must be a multiple of 2π . This condition for light of wavelength λ_0 in a slab of height h and refractive index n is given by:

$$\frac{4\pi n \sin \theta}{\lambda_0} h - 2\phi_s = 2\pi m \quad (4.4)$$

where $m = 0, 1, 2 \dots$ is the mode index and ϕ_s is the phase acquired by fields upon reflection at the upper and lower GaAs-air boundaries, calculated from the Fresnel reflectivity for s-polarised light, r_s :

$$\phi_s = \arg\{r_s\} = 2 \arctan \left(\frac{\sqrt{n^2 \sin^2 \theta - 1}}{n \cos \theta} \right) \quad (4.5)$$

Therefore, the maximum height at which only the fundamental vertical mode is confined to the slab is found using $m = 0$, giving

$$h = \frac{\lambda_0 \phi_s}{2\pi n \sin \theta} = \frac{\lambda_0}{\pi n \sin \theta} \left[\arctan \left(\frac{\sqrt{n^2 \sin^2 \theta - 1}}{n \cos \theta} \right) \right], \quad (4.6)$$

which for tangential incidence ($\theta = \frac{\pi}{2}$) gives a maximum slab height of $h = \lambda_0/2n$. The spectral distribution of a QD ensemble is typically centred around a wavelength of 950nm, which corresponds to a slab height of 140nm.

Similarly, to ensure single lateral mode confinement a suitable choice of width must be made. Analytical solutions are not possible for the fields of a rectangular waveguide, so to find the correct waveguide width, an iterative approach must be employed using FDTD or eigenmode solver methods. One may use an intuitive initial guess for the waveguide width using Equation 4.4 with the phase coefficient for p-polarisation:

$$\phi_p = \arg\{r_p\} = 2 \arctan \left(n \frac{\sqrt{n^2 \sin^2 \theta - 1}}{\cos \theta} \right) \quad (4.7)$$

which for tangential incidence of the fundamental mode yields a waveguide width $w = \lambda_0/2n$, suggesting a waveguide of square cross section.

The band structure of this waveguide, calculated using MPB [54], is shown in Figure 4.4(a). Since the waveguide is symmetrical in cross section, the TE-like and TM-like modes are degenerate as indicated by the dashed black and red line. At the target wavelength the modes lie close to the light cone (where $\omega\beta = c$) and are poorly confined to the waveguide.

This is supported by FDTD simulations of a TE dipole source at the waveguide centre using MEEP [110]. The coupling efficiency of a linearly-polarised dipole source to a waveguide of square cross section was computed by placing flux monitors at the ends of a $20\mu\text{m}$ waveguide and calculating the power through these monitors as a fraction of the total power of the system. These results are shown in Figure 4.4(b) which indicate that at the target wavelength the coupling efficiency of the dipole is 9%. The field overlap with the dipole source is poor at this wavelength, as most of the field power lies outside of the waveguide as illustrated in Figure 4.4(c). This results in an inhibition of the QD emission which is dominated by coupling to free space modes [36, 99, 157].

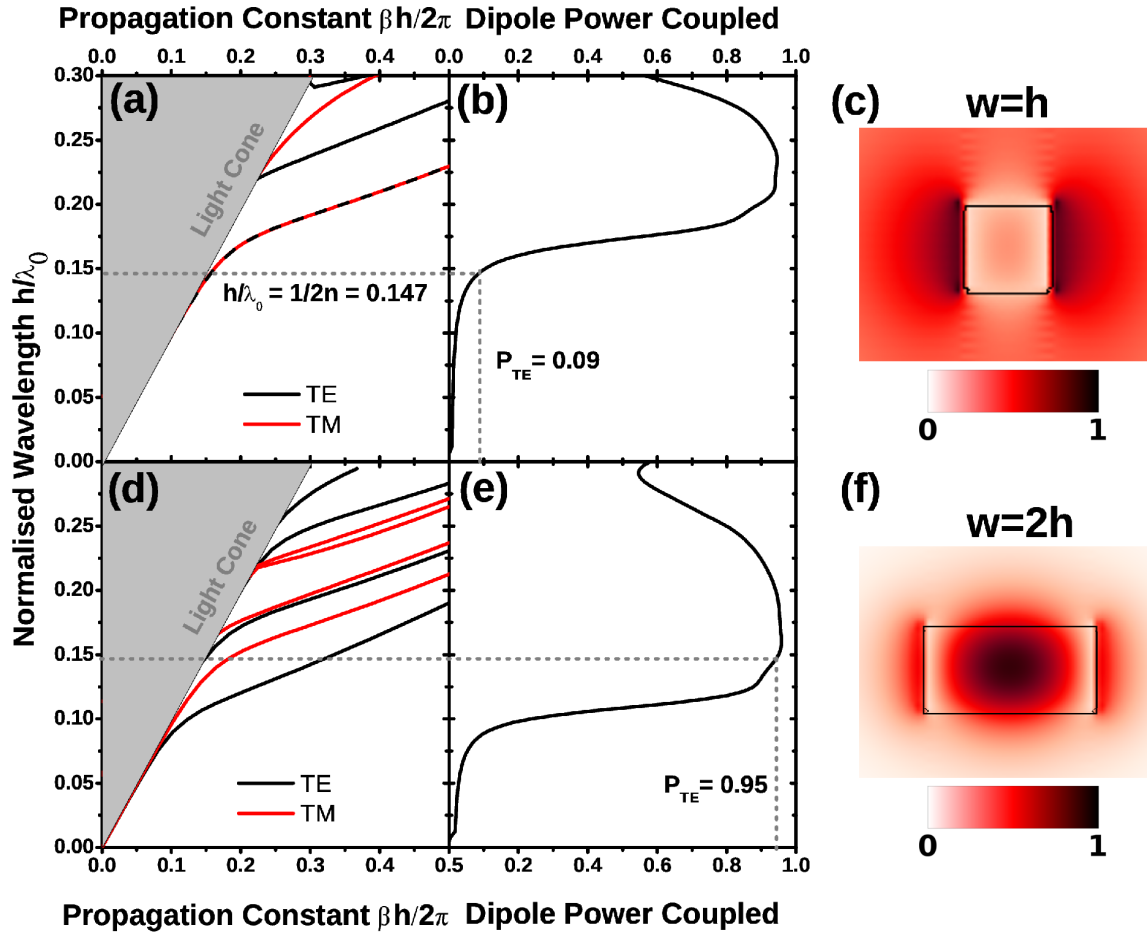


Figure 4.4: (a) Band structure, (b) coupled dipole power and (c) normalised TE-polarised electric field amplitude of a GaAs ridge waveguide of square cross section. (d) Band structure, (e) coupled dipole power and (f) normalised TE-polarised electric field amplitude of a GaAs ridge waveguide of rectangular cross section where $w = 2h$. Horizontal grey dashed lines represent the normalised wavelength when the slab height $h = \lambda_0/2n$. Vertical dashed lines show the coupling efficiency of a TE dipole to the waveguide at this normalised frequency.

A range of simulations were performed to find the waveguide width for which the fundamental mode is well-confined. For a waveguide width of $2h = \lambda_0/n$ the waveguide was calculated to be at the limit of single mode operation as shown in Figure 4.4(d), corresponding to a cross-sectional area of $\frac{1}{2} \left(\frac{\lambda_0}{n} \right)^2$. The fundamental TE-like mode lies far away from the

light cone with a calculated coupling efficiency for a TE dipole source of 95% as shown in Figure 4.4(e). The modal fields are well confined to the waveguide as illustrated in Figure 4.4(f). Degeneracy between the TE and TM-like modes is broken by the rectangular cross section, the latter remaining close to the light cone with poor confinement to the waveguide. These waveguide designs are used for optimisation of the directional coupler in the next section.

4.2.3 Optimisation of Directional Coupler

Appropriate design of a directional coupler requires calculation of the coupling constant between the waveguides which, for fixed waveguide dimensions and refractive index, is principally governed by their separation. The coupling constant can be derived from the difference in effective index of the two supermodes using the frequency-domain eigenmode solver method. This can then be used to determine the required length of the coupling region using Equation 4.3. The simulations in this section were performed by Dr. N. Prtljaga using Lumerical MODE Solutions [111].

Using the single-mode ridge waveguide designs from the previous section, the lateral separation was varied from 20nm to 140nm and the 50:50 coupling length calculated from the effective indices of the two supermodes shown in Figure 4.3. These results are shown in Figure 4.5. For a fixed waveguide separation, the coupling length decreases with increasing wavelength. Longer wavelengths are less well confined to the waveguide, resulting in a larger field overlap between the waveguides and a higher rate of power transfer, so a shorter coupling region is needed.

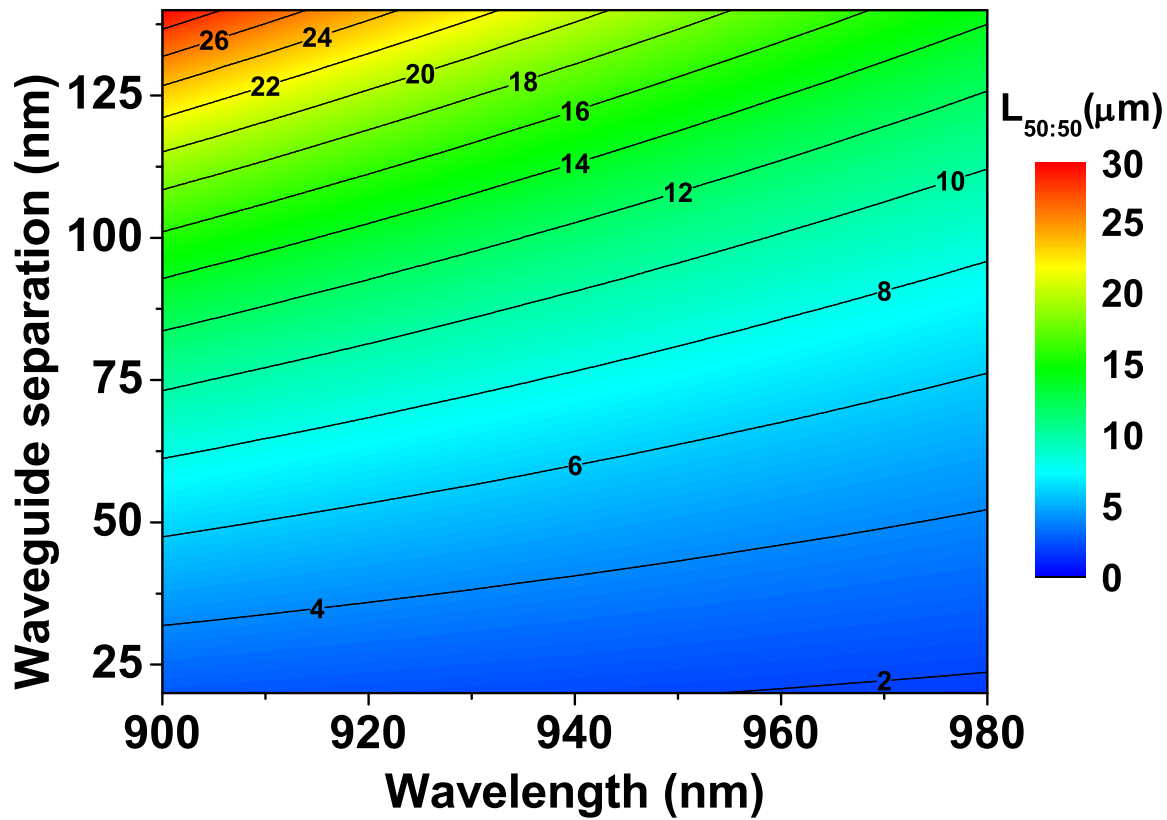


Figure 4.5: Calculations of the coupler length required for equal division of the incident waveguide power between the output waveguides.

For the directional coupler to be of practical use, the waveguides must be connected to other circuit elements. The waveguides must therefore extend from the coupling region of the directional coupler to the adjacent circuit element. In order to prevent the waveguides coupling away from the coupling region, the waveguides are bent in opposite directions after the coupling region (shown in Figures 4.1 and 4.8) to separate the waveguides. The choice of bend radius is crucial to minimize the radiative losses of the waveguide modes. The minimum bend radius, r_{min} is defined as the minimum waveguide curvature required for a 10% power loss in one wavelength of propagation. This can be calculated using Fraunhofer's diffraction theory [158], which for GaAs in air $r_{min} < 1\mu m$ [38]. A bend radius of $2\mu m$ was chosen to reduce these losses further without compromising the overall device size. From FDTD simulations of the complete devices, the effects of the waveguide bends on the splitting ratio was found to be negligible.

As the waveguide mode travels from a single waveguide to the coupling region the mode is perturbed by the presence of the second waveguide. If there is significant difference between the modes of the input waveguide and the waveguide in the coupling region, a mode conversion loss is created due to field mismatch between the single waveguide mode and supermodes of the coupler. This can be visualised as the difference between the field profiles of Figure 4.2 and the left half of one of the supermodes of Figure 4.3. The loss can be estimated from the overlap of the modal fields of the single waveguide with the two supermodes using:

$$L_{conversion} = 1 - \frac{(P_S + P_{AS})}{P_{in}} \quad (4.8)$$

where P_S , P_{AS} are the power in the symmetric and antisymmetric supermodes respectively and P_{in} is the power in the input waveguide. The fraction of input to output power for each supermode is calculated using:

$$\frac{P_{out}}{P_{in}} = Re \left\{ \frac{\int d\mathbf{S} \cdot \mathbf{E}_{out} \times \mathbf{H}_{in}^* \int d\mathbf{S} \cdot \mathbf{E}_{in} \times \mathbf{H}_{out}^*}{\int d\mathbf{S} \cdot \mathbf{E}_{out} \times \mathbf{H}_{out}^* \int d\mathbf{S} \cdot \mathbf{E}_{in} \times \mathbf{H}_{in}^*} \right\} \quad (4.9)$$

where \mathbf{E}_{out} and \mathbf{E}_{in} are the electric fields of the output and input waveguides respectively; \mathbf{H}_{out}^*

and \mathbf{H}_{in}^* are the complex conjugate of the magnetic fields of the output and input waveguides respectively [37, 159]. The results from these calculations for different waveguide separations are shown in Figure 4.6. The conversion loss is smaller for large waveguide separation due to the reduced coupling constant and the device tends towards the behaviour of two isolated waveguides. For small separations the loss increases as the waveguides become more strongly coupled and eventually behave as a single large waveguide which establishes a large mode mismatch between input and coupler. Intermediate separations maintain a small ($< 1\%$) loss whilst ensuring a shorter coupling region.

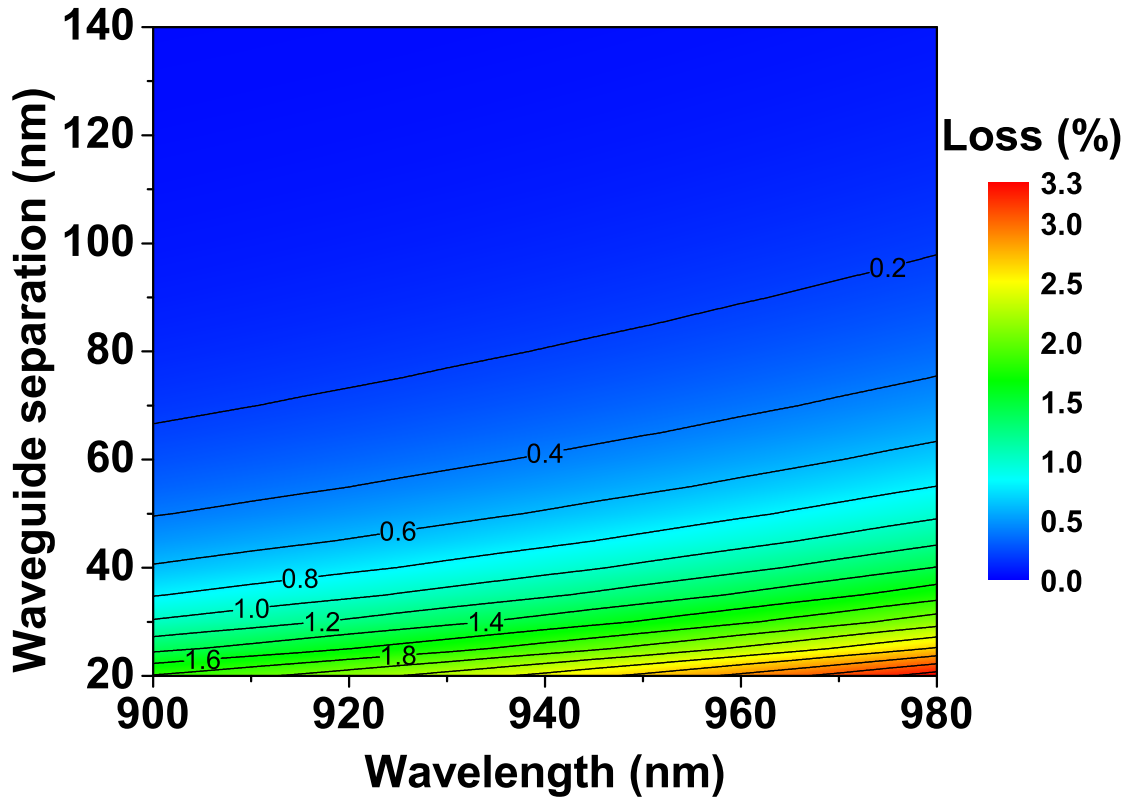


Figure 4.6: Calculated mode conversion loss when the fundamental waveguide mode couples to the supermodes of the directional coupler as a function of waveguide separation.

The final design step considers the tolerance of the device to fabrication imperfections: namely variation in the separation and width of the waveguides. Such variations will alter the measured power splitting ratio of the fabricated devices in experiment and reduces the

reproducibility of the directional couplers. To investigate the magnitude of these effects on the splitting ratio, the waveguide width and separation were varied and the power splitting ratio calculated for a fixed wavelength of 950nm and coupler length of $7\mu\text{m}$. These data are shown in Figure 4.7.

The resilience of the device to fabrication imperfections is assessed by considering the change in output power splitting when the waveguide width and separation deviate from example target values of 280nm and 80nm respectively. When the waveguide is developed and etched during fabrication the waveguides may increase or decrease in width depending on various fabrication parameters. Ideally, the shrinkage occurs symmetrically on both side of the waveguides. The change in separation, ΔS , is related to the change in width, ΔW by $\Delta S = -\Delta W$ which is represented by the solid white line in Figure 4.7. In this case for waveguide widths in the range 253-320nm the splitting ratio changes by $<10\%$. The distance between the waveguide centres, C , does not change in this case since $\Delta C = \Delta S + \Delta W = -\Delta W + \Delta W = 0$.

However, the actual etching dependence will fall between two extreme scenarios. The first scenario is if the waveguides shrink only from their inner edges and the waveguide centres effectively move apart. In this case, the change in separation is given by $\Delta S = -2\Delta W$ which is represented by the diagonal dashed white line (marked “Inner Etch” in Figure 4.7) and the waveguide centres move by $\Delta C = -\Delta W$. The 10% tolerance in the splitting ratio is only satisfied for waveguide widths in the range 271-290nm. This situation may arise due to increased EBL exposure during fabrication from the proximity of the EBL exposure of the second waveguide. The second scenario is where the waveguides shrink only from the outer edge and the waveguide centres effectively move together. This a situation may arise during fabrication due to the small separation between the waveguides preventing efficient circulation of reactant during etching to the inner waveguide edges. The inner edges do not change so $\Delta S = 0$ which is represented by the horizontal dashed white line in Figure 4.7 (marked “Outer Etch”) and the waveguide centres move by $\Delta C = \Delta W$. The 10% tolerance is most sensitive to this kind of fabrication imperfection, only being satisfied for widths of 271-286nm.

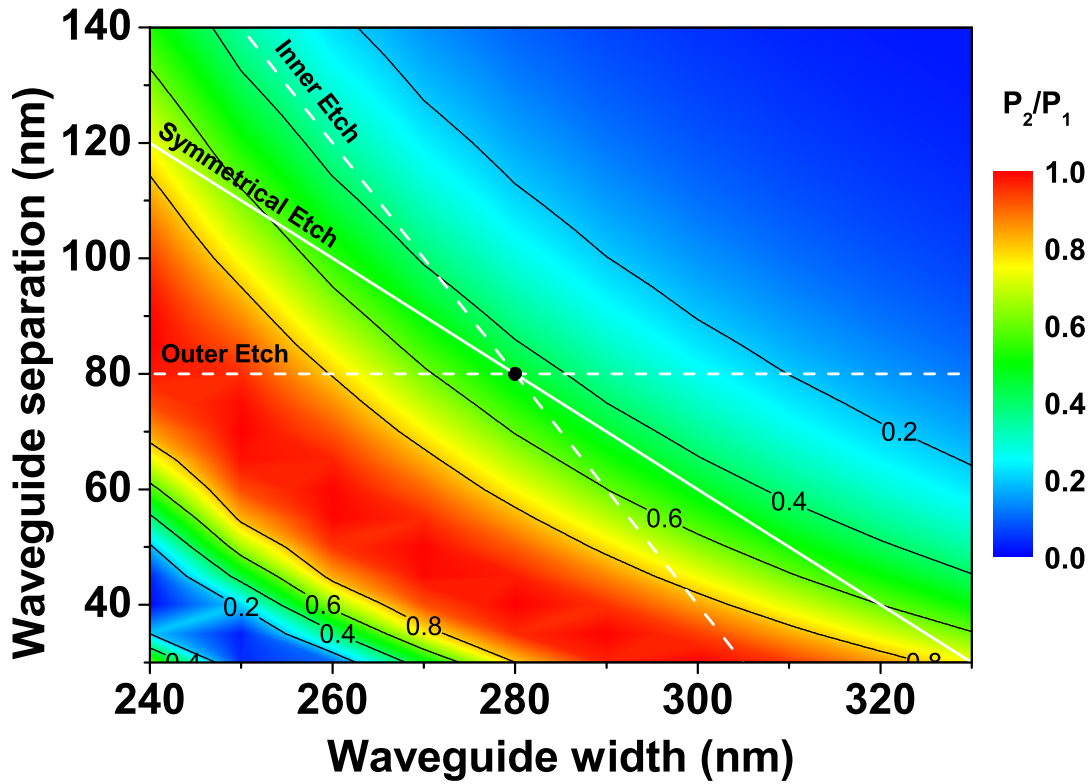


Figure 4.7: Variation of output power in one waveguide to input power for directional coupler of length $7\mu\text{m}$ at a wavelength of 950nm . White lines show device variation during etching for symmetrical, inner and outer surface etching of transverse waveguide edges.

The actual variations experienced during etching will be somewhere in between the two scenarios discussed here and is beyond the scope of this thesis. However, these upper and lower limits allow one to obtain a rough estimate of the resilience of the device to fabrication errors.

The target device design used for experiment was comprised of two single mode waveguides, of height 140nm and width 280nm , separated by 80nm for a coupling length of $7\mu\text{m}$. A separation of 80nm is chosen as this produces an equal splitting ratio for the single mode waveguide designs with low mode conversion losses and a ‘robust’ target separation. At the ends of the coupling region, the waveguides make a 45° bend away from one another, with a bend radius of $2\mu\text{m}$. These device parameters ensure the device operates in a low-loss regime whilst maintaining compactness with good tolerance to fabrication imperfections.

4.3 Experimental Arrangement

4.3.1 Sample Fabrication

The samples used in this study were fabricated as per Section 2.3.2 using the design parameters above. Semicircular $\lambda/2n$ air/GaAs grating outcouplers were added to the end of the waveguides to scatter light out of the device plane into the detection apparatus [58, 134, 148]. A scanning electron microscope image of the fabricated device is shown in Fig. 4.8.

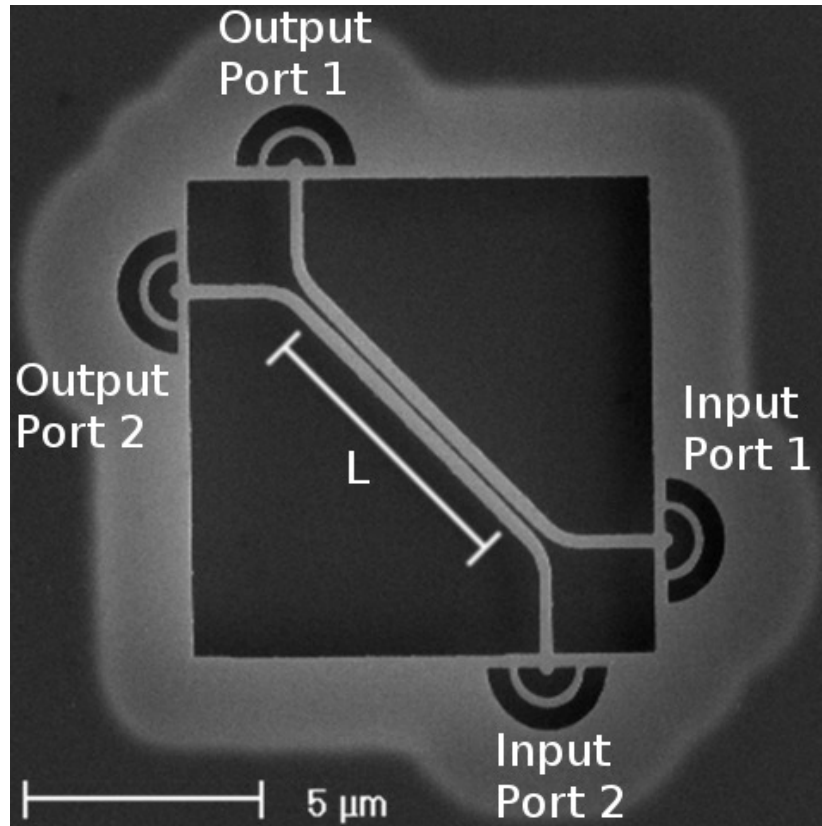


Figure 4.8: Scanning electron micrograph of a directional coupler. The pale regions are underetched GaAs membrane, the dark grey is non-underetched GaAs and black regions are completely etched through the GaAs membrane. The nomenclature used for identification of the input and output ports is defined. L is the coupling length of the directional coupler.

4.3.2 Experimental Apparatus

The experimental apparatus was arranged as in Section 2.3.4 using the liquid helium bath cryostat of Section 2.3.7. Optical measurements were performed at 4.2K in a stable confocal microscopy system with three independent optical paths (one excitation and two collection paths). The QDs were excited using an 850nm continuous wave (CW) Ti:Sapphire laser focussed by a 0.55NA aspheric lens to a diffraction-limited spot size of $\sim 1\mu\text{m}$ on the sample. The QD photoluminescence (PL) was collected from the outcoupler gratings by the same objective lens before being spectrally filtered by a 900nm long-pass filter and independently launched into separate single mode fibres. Following the fibres, the PL emission is detected using the experimental arrangement presented in Section 2.3.4.

4.4 Device Characterisation

To ensure that directional couplers with the correct dimensions were fabricated, a range of devices was etched with differing dimensions. The first measurements therefore were to find the directional coupler with the correct splitting ratio. Initial characterisation of the devices were performed using QD ensemble photoluminescence (PL) as an internal light source. This method facilitates the identification of directional couplers which exhibit equal power splitting within a 10% tolerance. This was achieved by positioning the excitation spot over the input port such that QD PL is excited near the outcoupler, which couples to and propagates through the device. The collection spot was then rastered across the sample to produce a PL map of the device, as shown in Figure 4.9 and the intensity of measured PL from the outcouplers was compared to assess the splitting ratio of each directional coupler. In each figure, intense PL signal is observed from the outcouplers. Figure 4.9(a) shows the PL map obtained for a device where the splitting ratio is 80:20, in which the majority of PL emission is observed from the same waveguide as excitation. Figure 4.9(b) shows the PL map for a device with $L = 7\mu\text{m}$ where the PL emission is divided equally between the two outcouplers. Figure 4.9(c) shows the PL map for a device where the splitting ratio is 40:60 and the most intense emission is observed from the opposite waveguide to excitation.

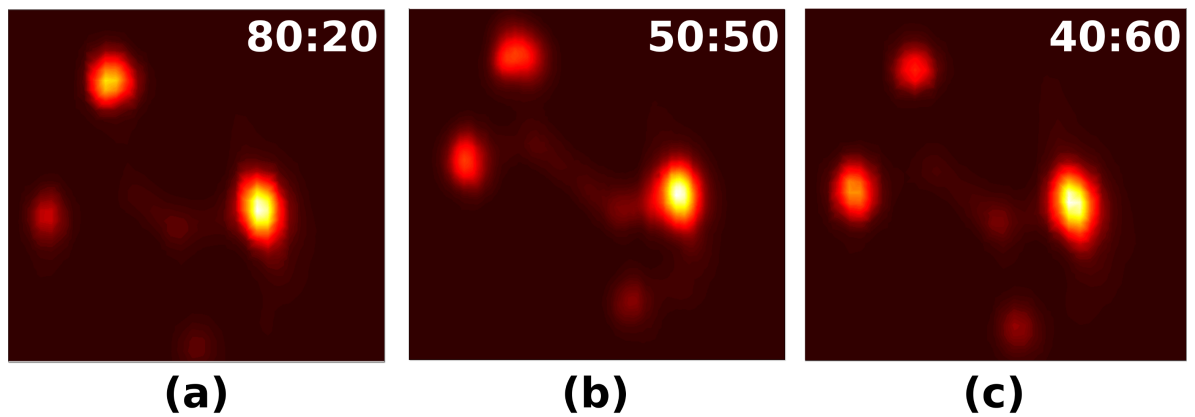


Figure 4.9: PL maps obtained for directional couplers with (a) 80:20, (b) 50:50 and (c) 40:60 splitting ratios. Excitation of the device was from the right outcoupler in all cases.

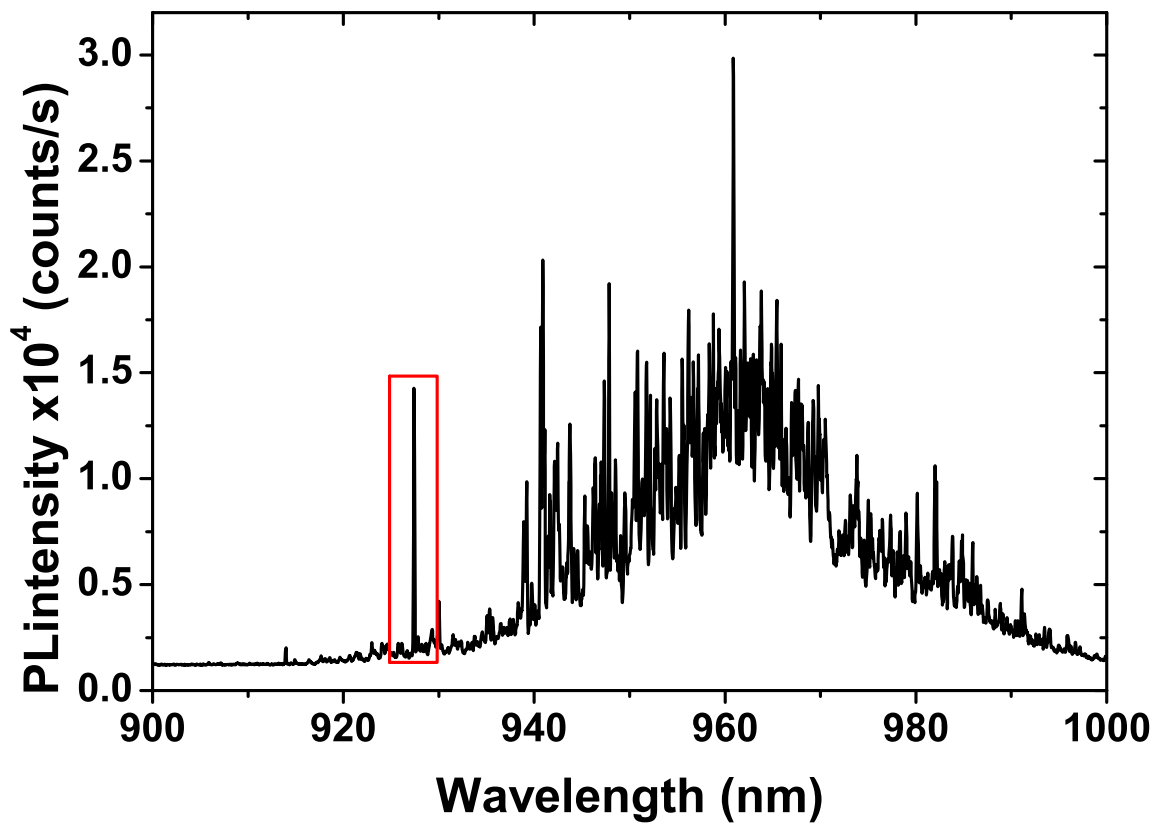


Figure 4.10: QD ensemble PL spectrum obtained when exciting and collecting from the input port. A single isolated QD is identified at 927.39nm.

The device in Figure 4.9(b) was selected for further study, beginning with the identification of suitable single QDs which exhibit a 50:50 splitting ratio. The PL spectrum taken from the input port of the directional coupler is shown in Figure 4.10. The QD ensemble follows an approximately Gaussian distribution centered around 961nm, however a single intense QD line was observed at 927.39nm which is suitably isolated for use as a single photon source for the directional coupler.

To ascertain how the emission from this single QD is split by the device, filtered PL maps were taken of the device at the QD emission wavelength. This was achieved by using the spectrometer to filter the QD emission which is detected by a single APD through slits on the output port of the spectrometer. The QD spectrum as seen by the APD is shown in Figure 4.11(a), obtained by scanning the spectrometer grating. The centre wavelength is offset by 0.54nm when observed from the APDs due to a small difference in alignment between CCD detection and APD detection via the side port of the spectrometer. The linewidth of the QD emission peak, when fitted to a Lorentzian curve, yields a spectrometer limited linewidth of 0.09nm ($\sim 130\mu\text{eV}$)

The PL map of the device when the collection was spectrally filtered at 926.85nm is shown in Figure 4.11(b). As can be seen from the figure, the QD PL is principally observed from the input and output ports of the device: the ratio of relative intensities at the outputs is 37:63. An additional maximum in the PL map is seen slightly to the left of the input port. This may be due to QD emission vertically from the waveguide, which identifies the QD location in the input waveguide.

As stated in Section 4.2.3, the coupling rate between the waveguides is expected to be reduced with decreasing wavelength. The fact that the coupling rate at the QD wavelength ($\sim 927\text{nm}$) appears to increase relative to the QD ensemble centre wavelength ($\sim 960\text{nm}$) suggests that this particular device was operating beyond the first 50:50 coupling point due to either a reduced separation between the waveguides or reduced waveguide width. The coupling constant κ is increased such that within the coupling length of the device the optical power is completely transferred from one waveguide to the other and over half is transferred back

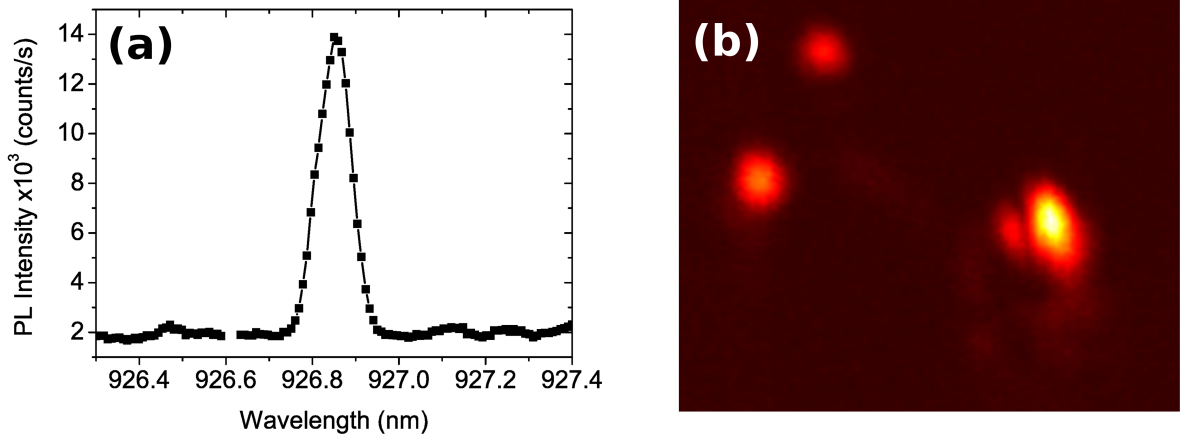


Figure 4.11: (a) PL spectrum of the QD as seen from an APD on the output port of the spectrometer. (b) PL map of the directional coupler when filtering at the QD emission wavelength with excitation on the right outcoupler.

again at the QD wavelength. This means that for the given waveguide width and separation, the coupling length of this device is $\sim 3L_{50:50}$ at 960nm wavelength and $2L_{50:50} < L < 3L_{50:50}$ at 927nm wavelength.

This imbalance in output is potentially due to several factors. Firstly, fabrication imperfections may have produced a directional coupler with waveguide widths and separations different from the ideal dimensions. This leads to an overall change in the splitting ratio of the device as discussed in Section 4.2.3. This can be alleviated by employing electro-mechanical control of the waveguide separation in order to ‘fine-tune’ the splitting ratio [160]. In addition, the device used for experimental characterisation comprised grating outcouplers which are known to possess non-zero reflectivity for modes incident from the waveguide [82, 148]. The formation of standing waves (Fabry-Perot modes) within the waveguides leads to modification of the QD emission rate and the splitting ratio between the output ports. The free spectral range of these resonances is much less than the width of the ensemble QD emission range so the splitting ratio varies over a small spectral bandwidth [161]. Tuning of the QD emission wavelength using electrical control [162] can be employed to adjust the splitting ratio within this small spectral bandwidth.

For the purpose of demonstration of single-photon operation, this imbalance in output manifests only as a reduction in the total number of coincidence counts in a Hanbury-Brown-Twiss (HBT) experiment: the observed correlation statistics of the light source is unaffected but a longer integration time is required to achieve the same number of events compared to a completely balanced experiment.

4.5 Autocorrelation Measurements of Single QD

To verify that the QD is operating as a single photon source, a HBT experiment was performed on the QD emission collected from the same port as excitation. In this geometry, the QD emission is not split by the device and hence represents an autocorrelation measurement using an external beam splitter, as in Section 2.3.6. The results of this measurement are shown in Figure 4.12. A fit to the data using $g^{(2)}(t) = 1 - (1 - g^{(2)}(0))e^{-|t|/\tau_d}$ yields $g^{(2)}(0) = 0.23 \pm 0.02$ with a decay constant $\tau_d = 1.79 \pm 0.08 ns$. $g^{(2)}(0) \neq 0$ due to background contributions from other QDs and the limited time resolution of the system ($\sim 520 ps$). Using the background subtraction method from [163] to remove these contributions, $g^{(2)}(0) = 0.03 \pm 0.03$. Because $g^{(2)}(0) < 0.5$ even without background correction, it is confirmed that the QD is emitting antibunched single photons. Since the QD is emitting single photons and the directional coupler is dividing and guiding this emission to the outcouplers, it therefore follows that single photon detection is possible from the output ports. The next section explores this by analysing the photon statistics of the QD emission from the output ports.

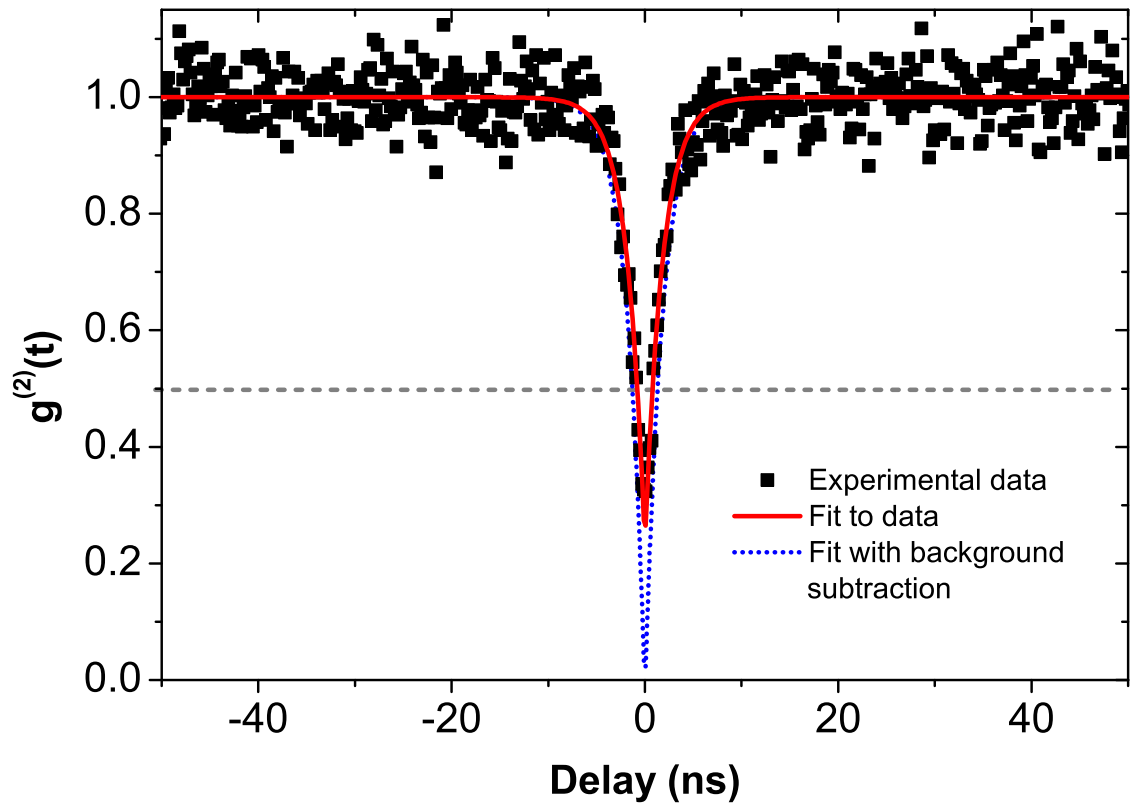


Figure 4.12: Autocorrelation measurement of the QD when collecting emission from the input port. Dashed grey line indicates quantum limit for a single emitter of $g^{(2)}(t) = 0.5$ and solid red line shows a fit to the data. A value of $g^{(2)}(0) = 0.23 \pm 0.02$ is found without background subtraction.

4.6 Cross-correlation Measurements of Single QD

Demonstration of the single-photon beam splitting behaviour of the directional coupler was accomplished by performing a cross-correlation measurement of the QD emission from the output ports. By comparison with autocorrelation measurements from the previous section the performance of the directional coupler as an on-chip beam splitter for single photons is evaluated.

The two collection pathways are aligned to collect PL from different output ports and the two corresponding outputs from the spectrometer were aligned with separate APDs. The configuration of the experimental geometry in this way ensures that the QD emission is split by the on-chip directional coupler and both channels are simultaneously filtered by the spectrometer.

The data from this measurement are presented in Figure 4.13. Fitting the data gives $g^{(2)}(0) = 0.31 \pm 0.03$ and a decay constant $\tau_d = 1.47 \pm 0.09 ns$. Again, this value is below the quantum limit of 0.5 for a single emitter. The value of $g^{(2)}(0)$ is higher than the autocorrelation value due to a reduced signal to noise ratio of the QD signal from the output ports. By applying corrections to the data for this increased background and temporal response of the system [163], a value of $g^{(2)}(0) = 0.08 \pm 0.04$ is found. This result demonstrates that the directional coupler is capable of splitting the emission of the QD at the single photon level.

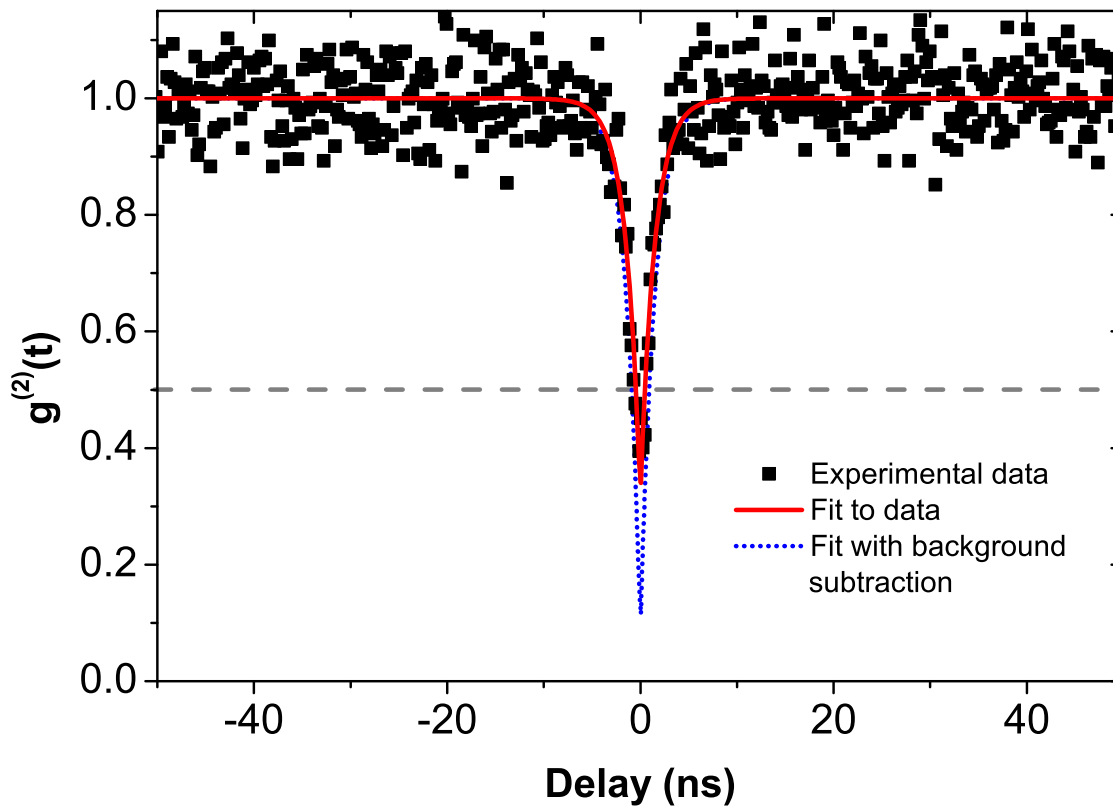


Figure 4.13: Cross-correlation measurement of the QD when collecting emission from the output ports. Dashed grey line indicates quantum limit of $g^{(2)}(t) = 0.5$ for a single emitter and solid red line shows a fit to the data. A value of $g^{(2)}(0) = 0.31 \pm 0.03$ is found without background subtraction.

4.7 Further Work: Quantum Interference

4.7.1 Overview

When a light source located in one waveguide of the directional coupler emits into the guided mode, the optical amplitude is divided between the output ports according to the transmission matrix in Equation 4.2. Equal distribution of power between the two outputs from a classical emitter of power P_{in} in one of the input waveguides is achieved for $\kappa L = \pi/4$, when $\mathbf{T}^2 = 1/2$ and the power at the outputs of the device is given by $P_1 = P_2 = P_{in}/2$.

However for a quantum emitter such as a quantum dot, the situation is different. If the states of the waveguide are written as the number of photons in each waveguide N_1 and N_2 , then the initial state of the system when the QD emits is $|\psi_i\rangle = |N_1 N_2\rangle$. If a single QD in one waveguide emits a single photon, $\psi_i = |10\rangle$ and the output state of the directional coupler is $|\psi_o\rangle = \cos(|\kappa|L)|10\rangle + i \sin(|\kappa|L)|01\rangle$. For a 50:50 directional coupler, the output state is $|\psi_o\rangle = \frac{1}{\sqrt{2}}(|10\rangle + i|01\rangle)$. Therefore, the operation of the directional coupler takes a single input state and outputs a which-path encoded superposition state for single photons.

If there is an emitter in each input waveguide which both simultaneously emit a photon that is indistinguishable from the other, then $\psi_i = |11\rangle$ and the output of the directional coupler is given by $|\psi_o\rangle = \frac{i}{\sqrt{2}} \sin(2|\kappa|L)(|20\rangle + |02\rangle) - \cos(2|\kappa|L)|11\rangle$.

For a 50:50 coupler, $\kappa L = \pi/4$ and the coincidence term disappears: the output state is then given by $|\psi_o\rangle = \frac{i}{\sqrt{2}}(|20\rangle + |02\rangle)$. This two-photon interference is known as the Hong-Ou-Mandel effect [20] and is a purely quantum mechanical effect. The experimental signature of this phenomenon is a drop in the coincidence count of simultaneous photons collected from the output ports which disappears when the photons are made distinguishable. What follows is a discussion of proposed schemes to demonstrate this effect using a monolithic GaAs directional coupler with two embedded QDs.

4.7.2 Interference of two Quantum Dots

By incorporating two QDs into the directional coupler, such that one resides in each input waveguide it is possible to perform two-photon interference experiments on-chip. The principle

challenges involved in realisation of such a device are ensuring that each QD is optimally positioned in each waveguide, achieving indistinguishability of the photons emitted by the QD and fine control of the splitting ratio of the directional coupler. Each of these challenges is currently being addressed by other researchers in the LDS group at the University of Sheffield.

The ability to guarantee that the QDs are optimally located in the input waveguides is under investigation by J.E. Dixon and Dr. M.N. Makhonin via post-growth QD registration techniques. This technique involves deposition of metal markers on the sample surface and performing rasterized μ PL measurements over the sample at defined wavelengths, producing a PL map. The metal markers are highly reflective and give a reference position on the PL maps. By scanning over several QDs, the location of the QDs can be determined to within 10nm accuracy relative to the markers. This therefore allows for the patterning of photonic devices such that the QDs are well placed within the structure.

The challenge of ensuring that the photons emitted by the QDs are indistinguishable centres on spectral coincidence of the QD emission and the coherence of the QDs. The effects of decoherence can be reduced by increasing the QD emission rate. Since the coherence time T_2 is related to the radiative lifetime T_1 and dephasing time T_2^* by $1/T_2 = 1/2T_1 + 1/T_2^*$, shortening the radiative lifetime allows it to dominate in determining the coherence time [70]. This can be achieved via a Purcell enhancement of the QD by placing the QD in photonic crystal waveguide, which is discussed in Section 7.2.

By embedding the QD in the intrinsic region of a wafer with a vertical PIN doping profile, the emission wavelength of the QD can be tuned via the quantum confined Stark effect using an applied vertical electric field [162, 164, 165]. However, in order to independently tune the two QDs each waveguide must be individually addressable. This may be achieved by splitting the top p-type layer such that each waveguide is electrically isolated as shown in Figure 4.14. In this way an applied voltage V_1 applies an electric field to the QD in the lower waveguide, whilst V_2 does the same for a QD in the top waveguide.

Realisation of this device, currently being undertaken by J. O'Hara, C. Bentham and

N. Prtljaga, is expected to demonstrate the functionality required for an on-chip Hong-Ou-Mandel experiment. It is expected that when the QDs are detuned from one another, no interference is observed and when tuned to resonance the Hong-Ou-Mandel dip is observed.

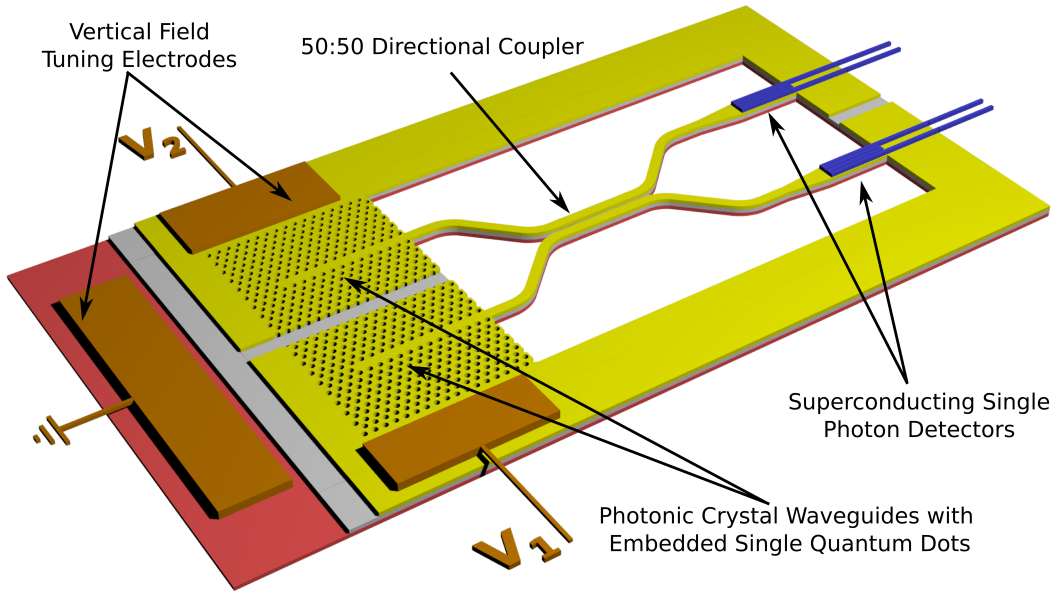


Figure 4.14: Proposed circuit model of a directional coupler on a wafer with PIN doping structure. Independent electrodes for each waveguide are made by splitting the top p-type layer (yellow) with common back n-type contact (red). The intrinsic layer is shown in grey and on-chip detectors are shown on the output waveguides in blue.

4.8 Summary

In conclusion, the monolithic integration of an on-demand quantum emitter in the form of a self-assembled InAs QD with an air-clad directional coupler has been demonstrated. Using FDTD and eigenmode solver simulations, single mode waveguides were designed which couple the emission of a single linearly polarised QD with $\sim 95\%$ efficiency and the optimal arrangement of these waveguides for equal division of optical power between output ports was found. Demonstration of the device was achieved using micro-photoluminescence (μPL) techniques to identify a directional coupler which exhibited approximately equal division of QD PL between the output ports. Using time-resolved μPL measurements the single-photon emission statistics of the QD were confirmed, with a measured $g^{(2)}(0) \simeq 0.23$ and an on-chip HBT measurement was made using the directional coupler as the beam splitting element, where $g^{(2)}(0) \simeq 0.31$ was measured.

This work paves the way towards demonstration of on-chip quantum optical circuits with monolithically integrated on-demand quantum emitters. The next step for our work is the demonstration of on-chip two-photon interference experiments, before they are incorporated into fully integrated quantum optical circuits with on-chip detection.

Chapter 5

Directional Readout of Single Quantum Dot Spins in Non-Chiral Photonic Waveguides

5.1 Introduction

The ability to manipulate and transmit spin information is at the heart of many quantum information processing schemes. Circuit proposals involve the preparation of an integrated emitter in a quantum spin state with the spin information propagated between different circuit elements by encoding the spin information in a photon as the ‘flying’ qubit. To achieve this, an emitter which possesses spin eigenstates is incorporated in an integrated circuit which supports the propagation of circularly polarised light. Several schemes have been proposed and demonstrated for this purpose so far including atoms and nanoparticles evanescently coupled to nanoscale optical elements [166–169] and passive SOI devices utilising off-chip light sources [170]. Solid-state, monolithic circuits present a compact and scalable route to integrated quantum optical applications by embedding the emitter within the light confining dielectric material. Schemes to read-out the spin of a self-assembled InAs quantum dot (QD) have been demonstrated where the QD is embedded at the centre of a pair of intersecting orthogonal

dielectric waveguides [134] where the spin information is recovered through interference of the light between different waveguide outputs. It was discovered however, that if the device is made chiral by a small diagonal offset of the QD, then the spin information can be read-out directly in-plane [135]. In this case, photons of opposing helicity are guided in opposite directions within the structure. The disadvantage of this approach is that the optical power emitted by the QD is divided between four output ports. This chapter demonstrates that this functionality is possible in a single waveguide with only two output ports.

A single optical mode in a nanophotonic waveguide comprises orthogonal electric field components which exhibit a $\pi/2$ phase offset. An emitter placed at a location where the fields are locally circular enables the QD spin to be mapped directly onto the modal fields of the waveguide. This introduced chirality produces spin-dependent directional emission, divided between only two output ports. Proposals have been made to achieve this using single QDs embedded within photonic crystal waveguides [78] and have been demonstrated using glide plane photonic crystal waveguides [171]. The disadvantage with these schemes is related to the use of photonic crystal waveguides: namely at high group index the waveguides are lossy and the waveguides must be small to reduce these losses, reducing the chances of coupling a self-assembled QD in the absence of deterministic QD growth. Secondly, the periodic nature of the photonic crystal waveguide reduces the number of positions at which the modal fields are locally circular. Thirdly at the high group index required for high QD coupling efficiency and spontaneous emission enhancement (Chapter 7) the propagation losses are much higher than for the ridge waveguide [148, 172, 173] due to unintentional fabrication disorder.

In this chapter the spin-dependent directional emission of a single QD in a ridge waveguide is explored. The continuous translational symmetry of the ridge waveguide along the propagation axis places no restriction of the directional emission on the position of the QD along this axis. The case of a waveguide terminated by grating outcouplers is presented, where reflections from the gratings introduce longitudinal phase variation of the modal fields along the propagation axis. For comparison, the case of a W1 photonic crystal waveguide is considered and directional emission is also observed. Finally, a discussion of future work

including the use of whispering gallery mode resonators for spontaneous emission enhanced spin readout is presented.

5.2 Infinite Nanobeam Waveguide

5.2.1 Modal Properties

As explained in sections 1.2.1 and 4.2.2 the ridge waveguide employed in this thesis is comprised of an air-clad nanobeam of GaAs. The waveguide dimensions are chosen such that the waveguide confines a single optical “TE-like” mode and self-assembled quantum dots (QDs) are incorporated in a layer at the centre of the waveguide ($z = 0$ plane) as shown in Figure 5.1.

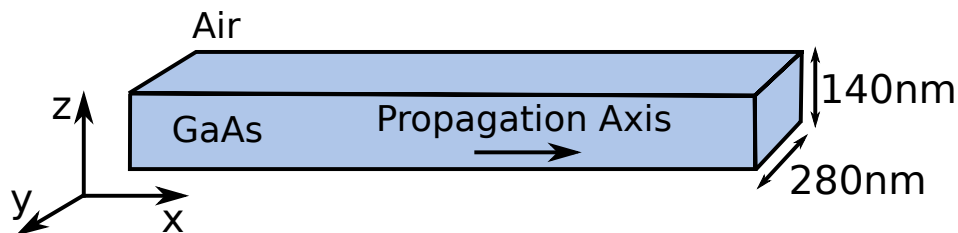


Figure 5.1: Schematic of ridge waveguide and coordinate definition.

Since the waveguide possesses mirror symmetry about all three Cartesian axes, the confined modes of the waveguide can be classified according to their field parity about these axes. Even and odd symmetry with respect to mirror symmetry about the z -axis defines whether the modes are ‘TE-like’ or ‘TM-like’ respectively. TE-like modes have only in-plane electric fields (E_x and E_y) whereas TM-like modes have only out-of-plane electric fields (E_z) [52]. Since the electric dipole of the QD is in the x - y plane, only the case of z -even (or TE-like) modes is considered, which for the ridge waveguide parameters given above are principally confined to the waveguide. Along the propagation axis (x -axis), the waveguide possesses continuous translational symmetry so the electric fields can be decomposed into $\mathbf{E}(x, y, z, t) = \mathbf{E}(y, z)e^{-ik_x x}e^{i\omega t}$, assuming harmonic time dependence, where $k_x = 2\pi n_{eff}/\lambda$ is the propagation constant of the guided mode with effective index n_{eff} .

To see why the modal fields contain electric field components parallel to the propagation direction one must first consider the Maxwell curl equations

$$\nabla \times \mathbf{E} = -\frac{\partial \mathbf{B}}{\partial t} \quad (5.1a)$$

$$\nabla \times \mathbf{B} = \mu \left(\mathbf{J} + \epsilon \frac{\partial \mathbf{E}}{\partial t} \right). \quad (5.1b)$$

Inserting the modal fields Equations 5.1 become

$$\frac{\partial E_y}{\partial z} = i\mu\omega H_x \quad (5.2a)$$

$$\frac{\partial E_x}{\partial z} = -i\mu\omega H_y \quad (5.2b)$$

$$ik_x E_y + \frac{\partial E_x}{\partial y} = i\mu\omega H_z \quad (5.2c)$$

$$\frac{\partial H_z}{\partial y} - \frac{\partial H_y}{\partial z} = i\epsilon\omega E_x \quad (5.2d)$$

$$\frac{\partial H_x}{\partial z} - ik_x H_z = i\epsilon\omega E_y \quad (5.2e)$$

$$ik_x H_y = \frac{\partial H_x}{\partial y} \quad (5.2f)$$

where it becomes clear that the modes are not strictly TE modes since they comprise additional field components besides E_y and H_z since $\frac{\partial}{\partial y} \neq 0$ and $\frac{\partial}{\partial z} \neq 0$ due to the finite width and height of the waveguide [155]. However, in the plane intersecting the vertical centre of the waveguide at $z = 0$, $\frac{\partial}{\partial z} = 0$ and these equations simplify to

$$k_x E_y - i \frac{\partial E_x}{\partial y} = \mu\omega H_z \quad (5.3a)$$

$$\frac{\partial H_z}{\partial y} = i\epsilon\omega E_x \quad (5.3b)$$

$$k_x H_z = -\epsilon\omega E_y \quad (5.3c)$$

so the only fields in the QD plane at $z = 0$ are E_x , E_y and H_z . The E_x fields are always imaginary with respect to the E_y and H_z fields, implying that the E_x fields have a fixed phase offset of $\pm\pi/2$. If the local fields of the waveguide follow $\mathbf{E} = E_x|x\rangle \pm iE_y|y\rangle$ at the location of an embedded QD with basis states $\mathbf{d} = \alpha|x\rangle \pm i\beta|y\rangle$ (where $\sqrt{\alpha^2 + \beta^2} = 1$) then the QD spin can be directly mapped onto the modal fields of the waveguide.

Since the fundamental TE-like mode of the waveguide has odd symmetry along y, Equations 5.3 can be solved to yield

$$E_x \propto -i \sin \tilde{k}y \quad (5.4a)$$

$$E_y \propto \cos \tilde{k}y \quad (5.4b)$$

$$H_z \propto -\cos \tilde{k}y \quad (5.4c)$$

where $\tilde{k} = k\sqrt{n^2 - 1}$. The important conclusions to be drawn from these equations are that:

1. In the QD plane, there are E_x , E_y and H_z fields present.
2. There is a $|\phi| = \pi/2$ phase shift between E_y and E_x .
3. The sign of ϕ is reversed when the direction of propagation (i.e. k) is reversed.

5.2.2 Dipole Dependent Longitudinal Mode Symmetry

Equations 5.2 cannot be solved analytically [174], so an eigenmode solver was employed to solve the fields of the waveguide. Figure 5.2(a) shows the absolute values of the electric field profiles in the $z = 0$ plane (at the vertical center of the waveguide) calculated for the 3D ridge waveguide using MPB [54] at $\lambda_0 = 930nm$. The fields exhibit odd symmetry with respect to mirror reflection in the y direction so this mode can be classified as z-even, y-odd.

Since the waveguide has continuous translational symmetry, E_y is purely real and E_x is purely imaginary and the two have a fixed relative phase of $\phi_{wg} = \pm\pi/2$ for $|y| \neq 0$ as

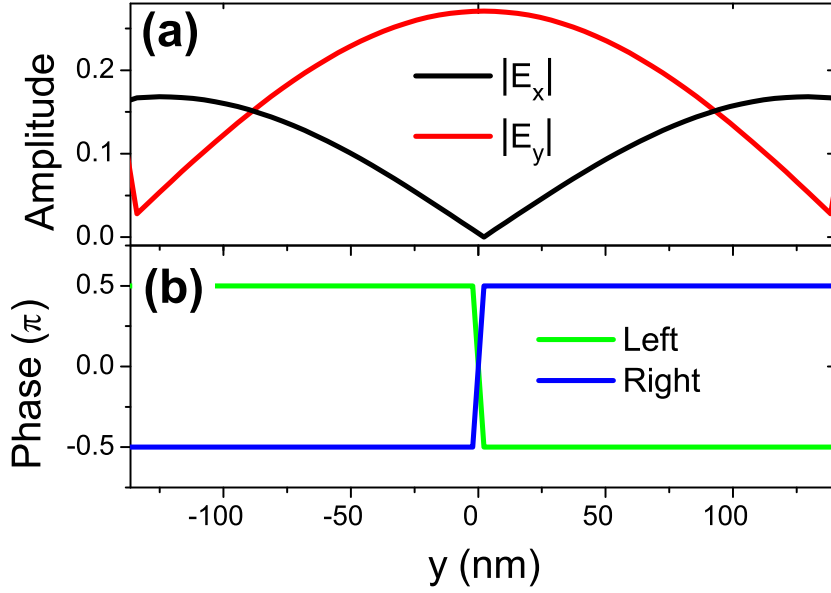


Figure 5.2: (a) Absolute Electric field amplitudes for x and y-polarised components of the waveguide mode. (b) Phase between the orthogonal electric field components for propagation in opposite directions.

shown in Figure 5.2(b). The phase between left and right propagating modes and hence the waveguide symmetry along x is determined by the symmetry of the source exciting the mode. To see this, one must consider the normalized dipole orientation factor from the electric dipole interaction:

$$\xi = \frac{\hbar g_0}{|\mathbf{E}||\mathbf{d}|} = \frac{|\mathbf{E} \cdot \mathbf{d}|}{|\mathbf{E}||\mathbf{d}|} = \frac{||E_x|\alpha + |E_y|\beta e^{i(\phi_{wg} + \phi_s)}|}{\sqrt{|E_x|^2 + |E_y|^2}} \quad (5.5)$$

where g_0 is the emitter-photon coupling rate and ϕ_s is the phase of the dipole source [104]. Since ξ is maximised for parallel dipole and electric field polarisation, it represents the efficiency with which a dipole source will couple to the electric fields of the waveguide mode. At $y = 0$, $\phi_{wg} = 0$ as $E_x = 0$ so $\xi = |\beta e^{i\phi_s}|$ and the waveguide has even mirror symmetry along x for any source polarization. Since the fields are locally linear, this point is referred to as an ‘L-point’. However for $y \neq 0$, $\phi_{wg} = \pm\pi/2$ and the dipole orientation factor must be

considered separately for modes propagating left and right which, for $y > 0$ are

$$\xi_{left} = \frac{||E_x|\alpha - i|E_y|\beta e^{i\phi_s}|}{\sqrt{|E_x|^2 + |E_y|^2}} \quad (5.6)$$

$$\xi_{right} = \frac{||E_x|\alpha + i|E_y|\beta e^{i\phi_s}|}{\sqrt{|E_x|^2 + |E_y|^2}}. \quad (5.7)$$

For a linearly polarised source, $e^{i\phi_s}$ is real so $\xi_{left} = \xi_{right}$ and the system again has even symmetry in x. However for a circularly polarized source, $e^{i\phi_s}$ is imaginary and $\alpha = \beta$ so the dipole orientation factors for left and right propagation become

$$\xi_{left}(\phi_s = \pm\pi/2) = \frac{||E_x| \pm |E_y||}{\sqrt{2(|E_x|^2 + |E_y|^2)}} \quad (5.8)$$

$$\xi_{right}(\phi_s = \pm\pi/2) = \frac{||E_x| \mp |E_y||}{\sqrt{2(|E_x|^2 + |E_y|^2)}} \quad (5.9)$$

for σ_+ and σ_- source polarisation respectively. At a location in the waveguide where $|E_x| = |E_y|$ then $\xi_{left} = (1 \pm 1)/2$ and $\xi_{right} = (1 \mp 1)/2$ and the mirror symmetry along the x-axis is broken. Since the dipole source is located at $|y| \neq 0$, the mirror symmetry along the y-axis is also broken. The locations within the waveguide where the fields are locally circularly polarised are herein referred to as ‘C-points’.

The implication of this introduced chirality is that a σ_+ polarised dipole source located at $y > 0$ will couple only to the right propagating mode and a σ_- dipole will couple only to the left. A second implication is that a QD situated at this position can be prepared in a corresponding spin state when excited by a propagating waveguide mode. That is, a mode propagating coherently from left to right presents a local field phase of $\phi_{wg} = \pi/2$ at the QD position, creating a σ_+ polarised state within the QD and vice versa for propagation from right to left.

5.2.3 Chiral Coupling of a Single QD

Spin Readout

To quantify the degree of selective coupling, the contrast of the dipole emission intensity is defined as

$$C = \frac{I_{\sigma+} - I_{\sigma-}}{I_{\sigma+} + I_{\sigma-}} = \frac{\xi_{\sigma+}^2 - \xi_{\sigma-}^2}{\xi_{\sigma+}^2 + \xi_{\sigma-}^2} \quad (5.10)$$

where $I_{\sigma+}$ and $I_{\sigma-}$ are the intensities of the dipole emission observed from one end of the waveguide, and $\xi_{\sigma+}$ and $\xi_{\sigma-}$ are the normalized dipole orientation factors for waveguide modes propagating towards one end of the waveguide for $\sigma+$ and $\sigma-$ polarised sources respectively. The contrast of selective coupling is plotted in Figure 5.3 for the left and right ends of the waveguide for $\sigma+$ and $\sigma-$ dipole moments. For a dipole placed at $|y| \approx 93\text{nm}$ the contrast is ± 1 and the dipole emission is directed either entirely left or entirely right along the waveguide.

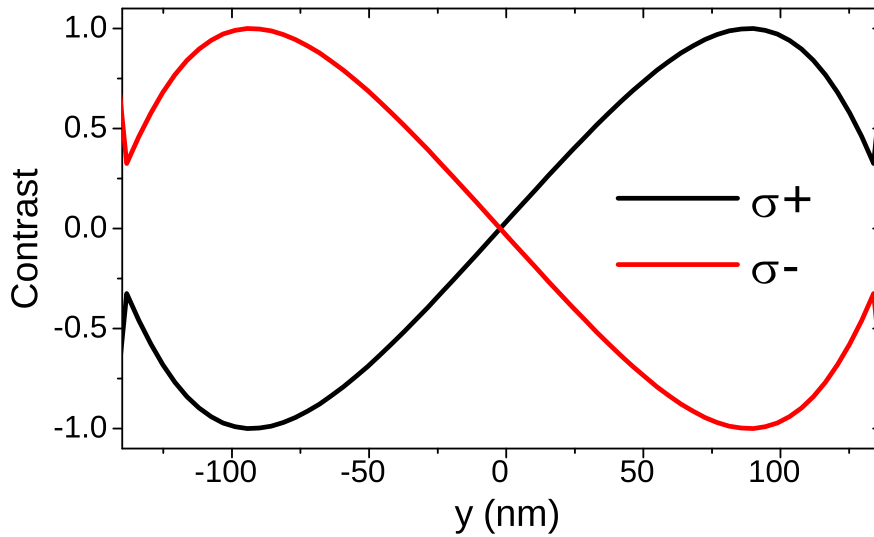


Figure 5.3: Contrast in emission intensity between oppositely polarised emission visible from opposite ends of an infinite ridge waveguide.

Figure 5.4 shows the absolute electric field amplitudes of FDTD simulations performed for circularly polarised dipole sources. These simulations were performed using Lumerical FDTD Solutions [85] and the field profiles in Figure 5.4 were recorded through the $z=0$ plane. Transmission monitors at the ends of the waveguide show that 68.5% of the emitted power from the circularly polarised dipole source is coupled in one direction and 0.04% in the opposite direction. The remaining 31.1% of the dipole emission is coupled to non-guided modes. When the circular dipole is at the centre of the waveguide (L-point), the total coupling efficiency is 69.7% and propagates equally in opposite directions in the waveguide. At the centre of the waveguide the coupling efficiency of a x- and y-polarised linear dipole source is 19.0% and 95.4% respectively. Therefore, at the L-point the y-polarised component of a circular dipole is well-coupled to the waveguide but the x-polarised component emits into leaky modes. At the C-point the coupling efficiency of the x-polarised dipole increases to 55.6% whilst for a y-polarised dipole the efficiency decreases to 88.7%. This implies that at the C-point, both components are coupled to the guided modes as well as to non-guided modes. Since the coupling efficiency for a circular dipole when moved from the centre to the C-point changes by $\sim 1\%$, the decreased coupling rate of the y-polarised component to the guided mode is mostly balanced by a increase in the coupling of the x-polarised component to the guided mode.

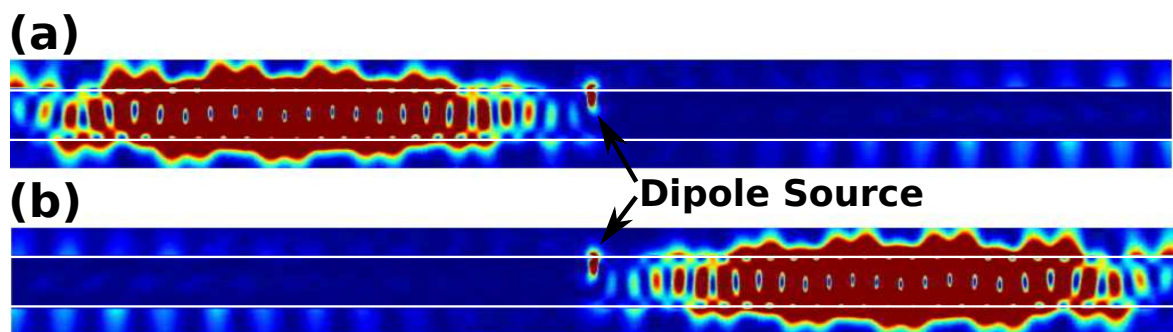


Figure 5.4: Electric fields of directional emission in an infinite ridge waveguide from (a) σ_- and (b) σ_+ polarised dipole sources displaced vertically by 93nm. Fields are shown in the $z=0$ plane for broadband excitation using pulsed sources with a centre wavelength 950nm and bandwidth 100nm. Boundaries of the waveguide are highlighted with white lines.

Spin Preparation

As stated in the previous section, a dipole source placed at a C-point within the waveguide will not only selectively emit photons from opposing spin states in opposite directions within the waveguide but can be prepared in a desired spin state by optical excitation from the corresponding direction within the waveguide. That is, if the QD is situated at a location where the fields are locally σ_+ polarised for mode propagation to the right then excitation from the left side in a waveguide mode will present σ_+ fields to the QD since the fields propagate to the right. This principle is illustrated in Figure 5.5 which plots the evolution of the modal fields at a C-point over time, calculated using Lumerical MODE Solutions [111]. In Figure 5.5(a) the waveguide mode is excited from the left and the field monitor at the C-point reports that $|E_x| \approx |E_y|$ and that E_y leads E_x in time by a quarter period. Therefore, the QD at this position will be excited in a σ_+ spin state. For Figure 5.5(b) the waveguide mode is excited from the right and the monitor at the same location as Figure 5.5(a) reports again that $|E_x| \approx |E_y|$ but in this case E_y follows E_x by a quarter of a period: the QD is excited in a σ_- spin state.

5.3 Nanobeam Waveguide Terminated by Outcouplers

5.3.1 Modal Properties

So far only the case of infinitely long ridge waveguides has been considered. However in experiment the ridge waveguides are terminated by grating outcouplers. The $\lambda/2n$ outcoupler gratings are employed to scatter light out of the device plane and into the detection apparatus [58]; they exhibit a reflectivity of light incident from the waveguide to which they are coupled of $\sim 30\%$. Since the waveguide is terminated at both ends by outcouplers, Fabry Perot modes are formed in the waveguide leading to a longitudinal phase dependence between the field components of the waveguide. A schematic of the waveguide terminated by outcouplers is shown in Figure 5.6.

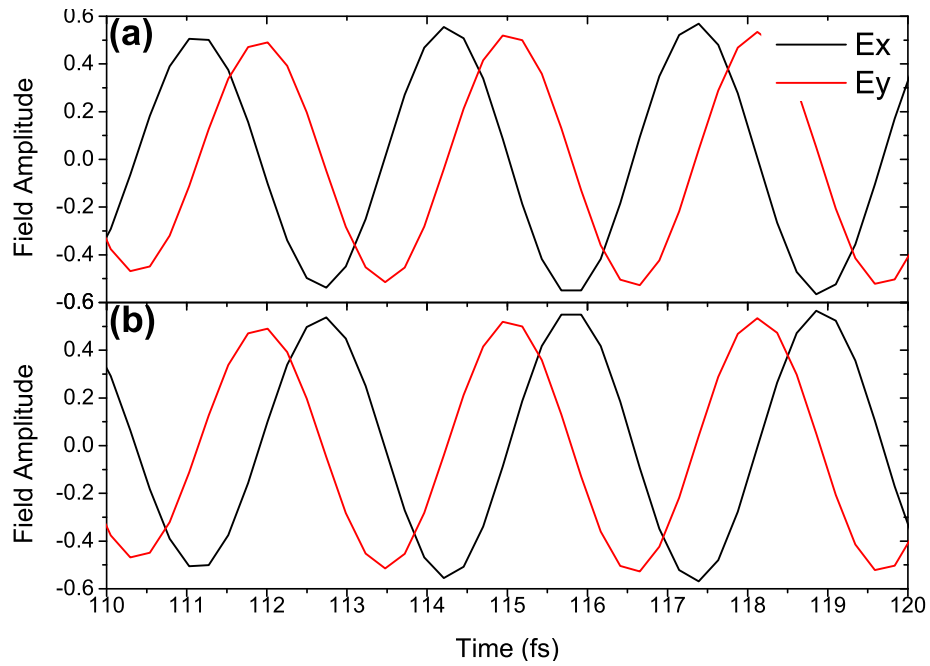


Figure 5.5: Evolution of the modal fields of the infinite ridge waveguide at a C-point over time for (a) left and (b) right propagation.

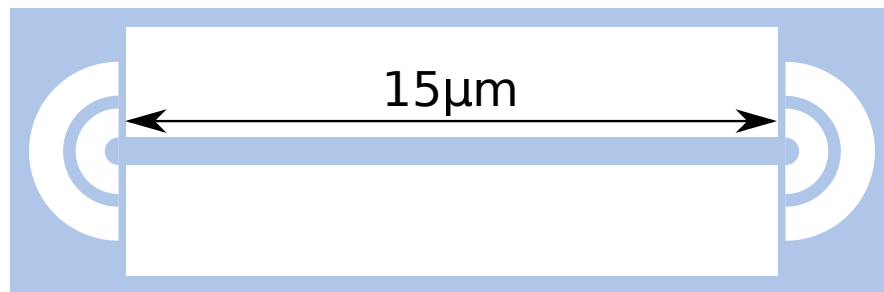


Figure 5.6: Bird's eye schematic of a ridge waveguide terminated by grating outcouplers. Regions in white are air, whilst coloured regions represent GaAs. The whole structure is underetched so that there is air cladding above and below the device plane.

The field profiles of a $15\mu\text{m}$ length ridge waveguide terminated by grating outcouplers were calculated using Lumerical FDTD Solutions [85] and are plotted in Figure 5.7(a) and (b) for $\lambda_0 = 934\text{nm}$ which corresponds to the maximum of a Fabry-Perot resonance. Off-resonance, the profiles are similar: however the intensity of the fields is reduced. Laterally, the waveguide mode profiles are similar to those of the infinite ridge waveguide case but longitudinally a quasi-periodic spatial dependence is observed in the field amplitude.

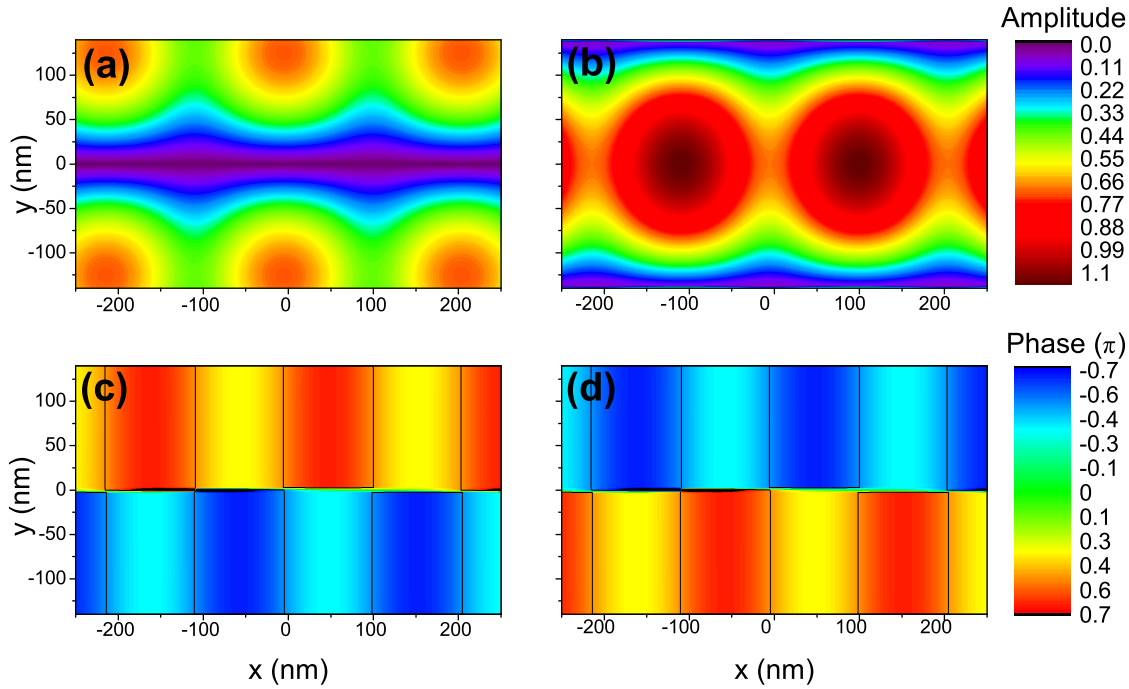


Figure 5.7: Absolute (a) E_x and (b) E_y fields of single mode ridge waveguide terminated by outcoupler gratings. (c) and (d) Phase between electric field components ϕ_{wg} for (c) left and (d) right propagation. Black lines show where $|\phi_{wg}| = \pi/2$.

The phase ϕ_{wg} between the E_x and E_y fields for mode propagation to the left and right are presented in Figure 5.7(c) and (d) respectively. Similar to the infinite ridge waveguide case, the polarity of the phase for $y > 0$ is opposite to that for $y < 0$. However, unlike the infinite waveguide case, they are not always equal and opposite along x . The black contour lines in Figures 5.7(c) and (d) show that $|\phi_{wg}| = \pi/2$ occurs only at discrete locations along

the x-direction. In between these regions, $0.344\pi \leq \phi_{wg}(x) \leq 0.654\pi$ and does not exhibit a transverse dependence in y .

To further analyse the polarisation of the modal fields, the Stokes parameters are calculated for the field profiles of Figure 5.7(a) and (b), defined as:

$$I = |E_x|^2 + |E_y|^2 \quad (5.11a)$$

$$Q = |E_x|^2 - |E_y|^2 \quad (5.11b)$$

$$U = 2\Re(E_x E_y^*) \quad (5.11c)$$

$$V = -2\Im(E_x E_y^*) \quad (5.11d)$$

where I is the intensity, Q , U and V are the degrees of linear, diagonal and circular polarisation, respectively and $*$ denotes the complex conjugate. The Stokes parameters for the ridge waveguide terminated by outcouplers are plotted in Figures 5.8(a)-(d) where the polarisation degrees Q, U and V are plotted as quantities normalised to the intensity, Q/I , U/I and V/I . From Figure 5.8(b) the fields at $y \approx 0$ seem to be linearly polarised with a polarisation degree of $> 95\%$, as with the infinite waveguide case. However, for $|y| > 0$ the modal fields exhibit regions of diagonal polarisation (Figure 5.8(c)) in addition to regions of circular polarisation of high ($> 95\%$) circular polarisation degree (Figure 5.8(d)). Since $|U| \leq 0.5$ and $|V| \sim 90\%$ in the regions of maximum U the fields are locally elliptically polarised rather than completely diagonally polarised.

5.3.2 Chiral Coupling of a Single QD

Simulation Results

Again, to quantify the degree of selective coupling, Equation 5.10 is evaluated using the field and phase profiles of Figure 5.7. The contrast in emission intensity for circularly polarised dipole sources ($\phi_s = \pm\pi/2$) from opposite ends of the waveguide is shown in Figure 5.9. As expected, the contrast follows the spatial profile of circular polarisation within the waveguide

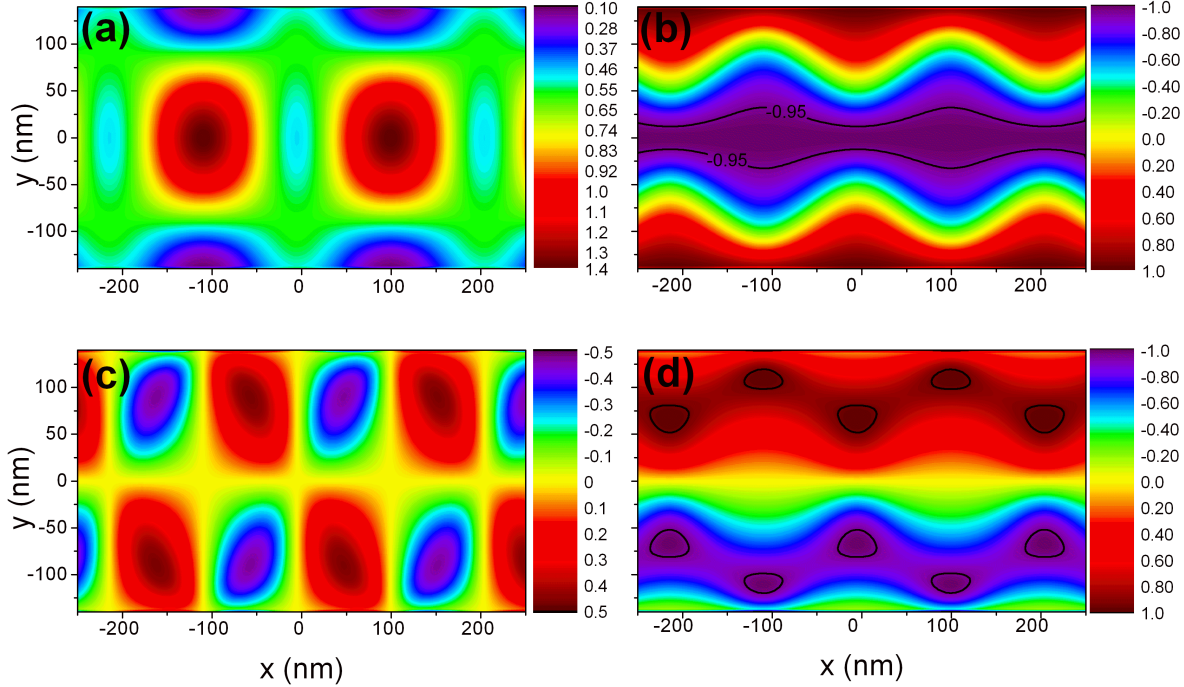


Figure 5.8: Stokes parameters for the fundamental mode of a ridge waveguide terminated by outcoupler gratings. (a) Intensity, I . (b) Normalised degree of linear polarisation, Q/I . (c) Normalised degree of diagonal polarisation, U/I . (d) Normalised degree of circular polarisation, V/I for propagation to the right. Black contours illustrate regions of $> 95\%$ polarisation degree.

from Figure 5.8(d) and is equal and opposite between the two ends of the waveguide. For $> 95\%$ contrast the emitter must be located within $\sim 40\text{nm}$ of a C-point, which are enclosed in black contours in Figure 5.9. The fractional area within which $> 95\%$ contrast is achieved is 0.061 for the outcoupler terminated waveguide, compared to 0.216 for the infinite waveguide case. This reduction is due to the discretisation of the C-points along the waveguide axis by the Fabry-Perot modes. In the regions connecting the C-points however, the contrast remains above 85%. Towards the centre of the waveguide, where the fields are linearly polarised, there is no contrast between σ_+ and σ_- dipole emission as for the infinite waveguide case.

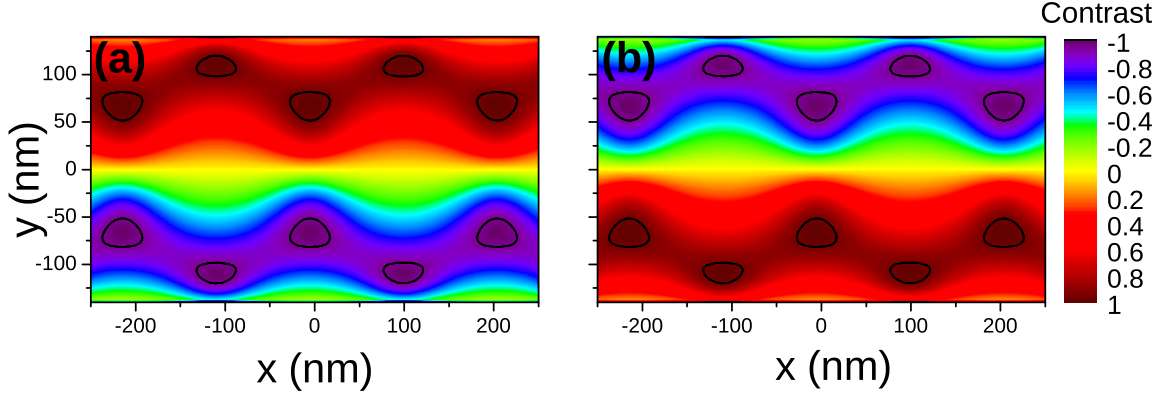


Figure 5.9: Contrast in emission intensity between σ_+ and σ_- polarised dipole sources visible from (a) left and (b) right ends of a ridge waveguide terminated by outcouplers. Black contours enclose regions of $> 95\%$ contrast.

Experimental Results

To demonstrate deterministic spin readout of single QDs, PL spectroscopy measurements were performed by Dr. Maxim Makhonin, James Dixon and David Price using an applied external magnetic field in Faraday geometry. Under this applied B-field, the degeneracy of nominally unpolarised excitonic emission lines of the QD is lifted by Zeeman splitting into spectrally distinct σ_+ and σ_- polarised states as shown in Figure 5.10. The spectral separation of these spin states facilitates identification of deterministic spin readout using the intensity form of Equation 5.10. Figure 5.10(a) shows the PL spectrum of a single QD which exhibits a contrast of spin readout ~ 1 . Spectra taken vertically from the waveguide at the QD location show both spin states are present whilst from the outcouplers only one of the two states is visible. Figure 5.10(b) presents the same measurement for a different QD where the observed contrast exhibits poor fidelity, but also asymmetry between opposite ends of the waveguide ($C_L \sim 0.7, C_R \sim 0$).

Further PL spectra were taken by Dr. Maxim Makhonin, James Dixon and David Price for a large distribution of QDs to enable statistical analysis. These results, plotted in Figure 5.11 reveal that many QDs exhibit asymmetrical spin readout which manifests as spread in the data away from the expected distribution along $C_R = -C_L$. This behaviour is unexpected

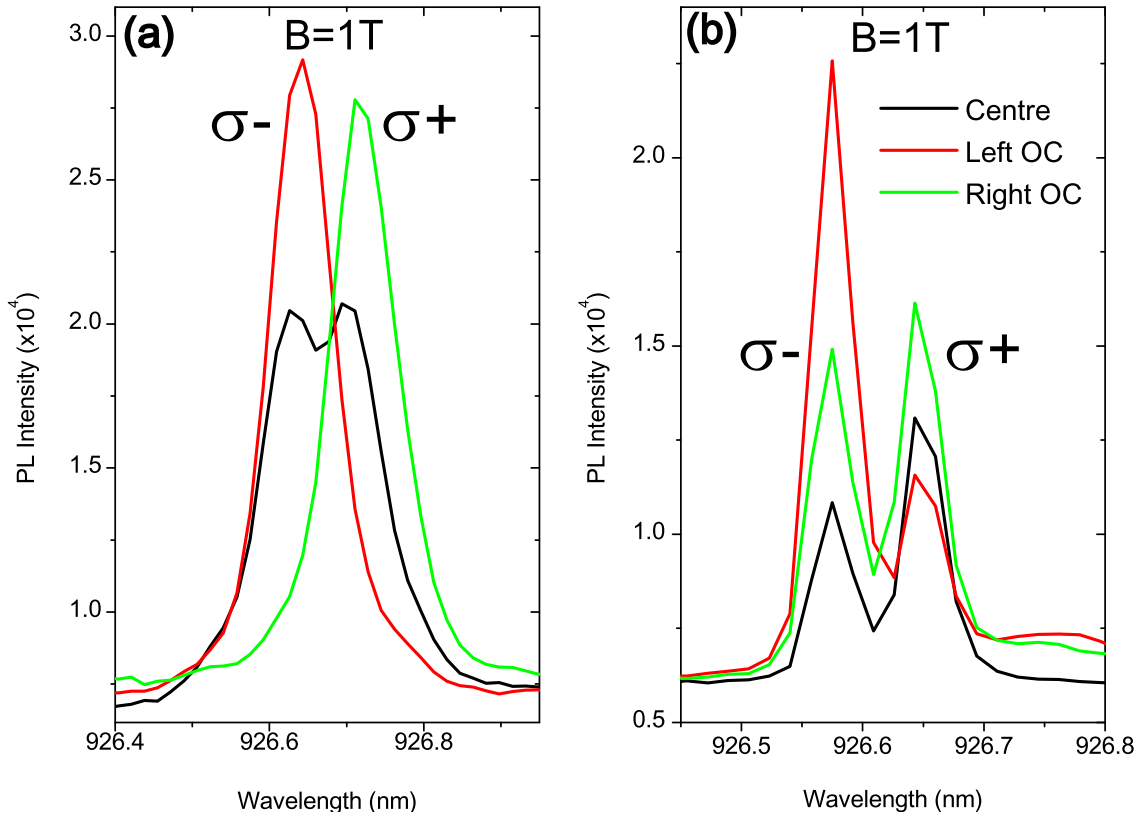


Figure 5.10: Experimental PL spectra of QD spin states visible from the outcouplers at the ends of a ridge waveguide. Two cases are shown: (a) Very high contrast confirming deterministic readout of QD spin (a) Asymmetrical contrast between spin states. Data taken by Dr. Maxim Makhonin, James Dixon and David Price.

since Equation 5.10 predicts that the contrast in spin readout should be equal and opposite for circularly polarised QDs at any location in the waveguide. To understand the cause of this statistical variation, it is necessary to revisit the simulated fields of the waveguide to find the origin of asymmetry.

Origin of Asymmetry in Spin Readout

The simulations presented previously imply that the contrast of spin readout for a circularly polarised emitter should be equal and opposite from opposing ends of the waveguide, except at the centre of the waveguide where the contrast is zero. The observation of asymmetry of

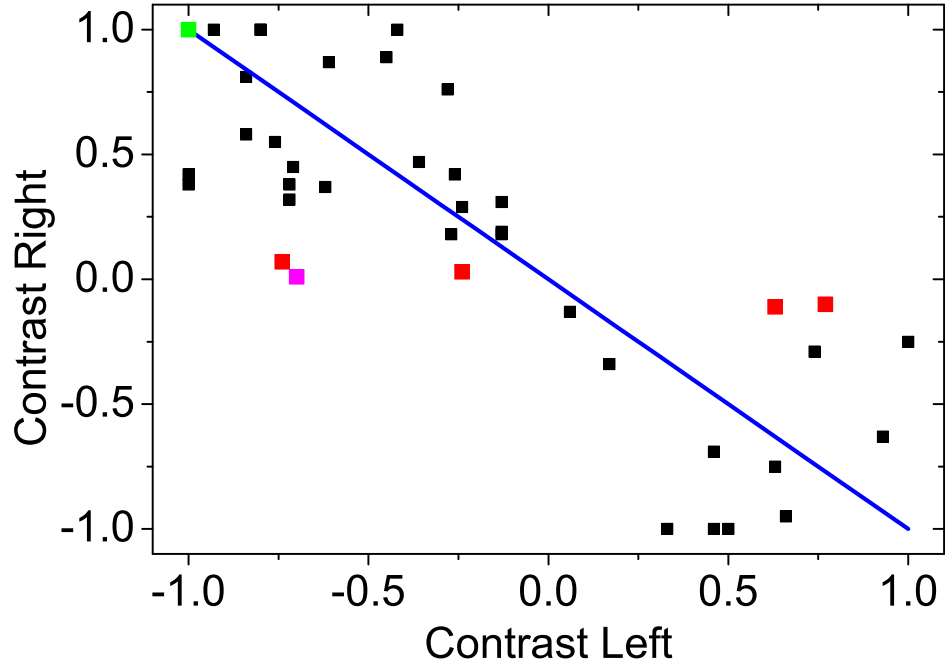


Figure 5.11: Plot of contrast between oppositely polarised QD emission from the outcouplers of a ridge waveguide from experimental results. Red points indicate QDs with highly asymmetrical contrast and the green point highlights a QD with near-perfect contrast correlation. Blue line shows expected trend for perfectly circularly polarised QDs. Data was obtained experimentally by Dr. Maxim Makhonin, James Dixon and David Price through statistical analysis of many QDs in waveguides.

spin readout in experiment suggests that some property of either the QDs or the waveguide breaks this principle when fabricated. It is however expected that with increasing magnetic field strength, the QD emission tends towards a higher circular polarisation degree and hence one may expect a restoration of symmetrical spin readout to the experimental data.

If one considers the effect of asymmetry of the waveguide, it is not clear that this manifests in asymmetry of spin readout. For example, if the waveguide has different scattering losses on either side of the QD (e.g. due to surface roughness) this will provide a reduction in the total intensity of the QD emission i.e. the relative intensities of the two spin states will not be affected.

The addition of outcouplers does create regions of elliptical polarisation in the electric fields

due to the formation of Fabry Perot modes, but for circularly polarised QDs the spin readout is not affected as shown previously. However, the back reflections from the outcouplers may act to reduce the contrast ratio. From FDTD simulations, the reflectivity of the outcouplers back along the waveguide is $\sim 17\%$ and the out-of-plane scattering efficiency of the outcouplers is $\sim 39\%$. Therefore, for QD emission to the right, $\sim 39\%$ of the emission is measured from the right outcoupler (neglecting losses in the detection apparatus) and $\sim 6.5\%$ measured from the left outcoupler due to back reflection from the right outcoupler. This effect should be symmetrical for each emission direction but if the fabrication parameters vary between the outcouplers their reflectivity is asymmetrical and so will be the measured contrast. However, the outcoupler dimensions nominally vary by no more than a few nanometers for a single device so this effect is likely to be small.

It is possible then that the QD emission is not in fact perfectly circularly polarised and may be elliptical. This elliptical polarisation may arise from the fine structure splitting of the neutral exciton within the QD [88, 175] or a combination of fine structure splitting and piezoelectric effects [176] due to strain in the waveguide. Similar effects are observed in [177–179]. From Figures 5.7 and 5.8 the modal fields of the outcoupler-terminated waveguide exhibit regions of elliptical polarisation, which for left and right propagation shows opposing polarity of the phase but with constant magnitude. This phase dependence between left and right propagation does not match the phase dependence for opposing helicities of elliptical polarisation states of the QD, where the polarity of the phase is again opposite, but with different magnitude.

To consider the effects of possible elliptical QD polarisation the contrast is evaluated using Equation 5.10 using $\phi_s = \delta \pm \pi/2$ where $0 \leq \delta \leq \pi/2$ represents a perturbation of the dipole phase from perfectly circular. Specifically, these scenarios correspond to elliptical polarisation of two QD spin states of opposing helicity where the major/minor axes of the polarisation ellipses do not coincide with the cartesian axes or with one another. The contrast in emission intensity for dipole sources with $\delta = 0.1\pi$ is plotted in Figure 5.12(a) and (b). What is immediately apparent from these plots is that at several locations within the waveguide

the contrast is no longer equal and opposite from the two ends of the waveguide. This is highlighted by Figure 5.12(c) which plots $C_L + C_R$ (which is zero at all positions for perfectly circularly polarised dipole sources), the profile of which follows the same spatial dependence as the diagonally polarised fields in Figure 5.8(c). Indeed, no asymmetry is observed for the infinite ridge waveguide which possesses no elliptical polarisation of the modal fields.

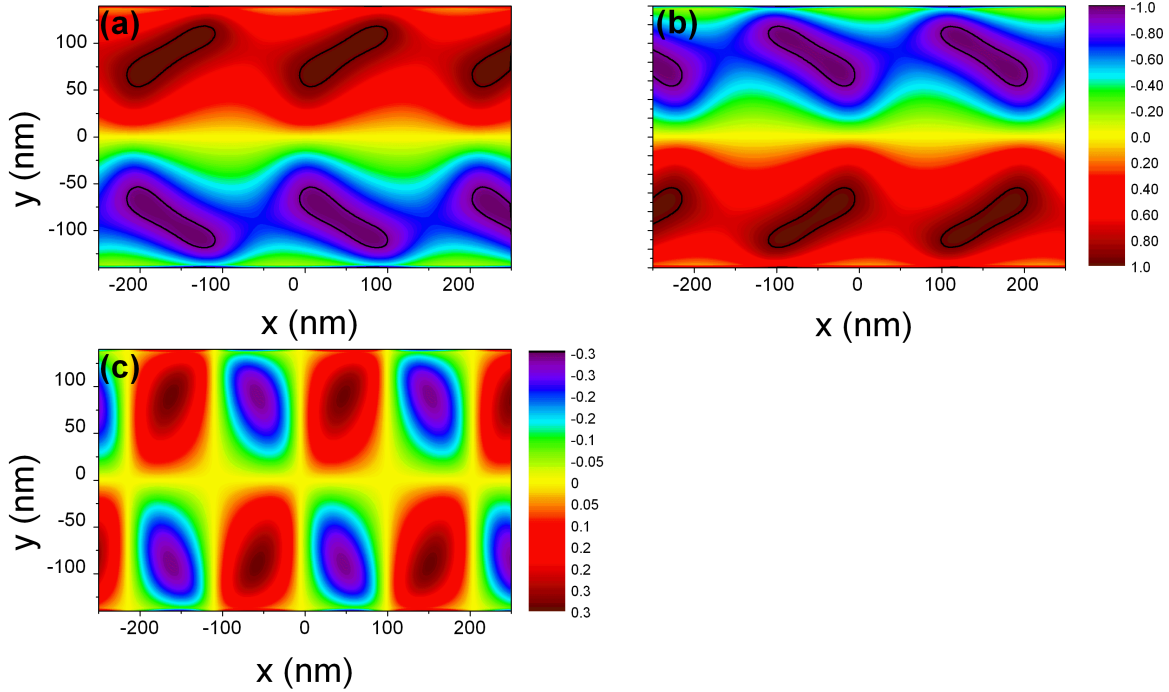


Figure 5.12: Contrast in emission intensity between elliptically polarised dipole sources ($\delta = 0.1\pi$) visible from (a) left and (b) right ends of a ridge waveguide terminated by outcouplers. (c) Sum of contrast in emission intensity from opposite ends of the waveguide.

If one plots the contrast between oppositely polarised dipole sources from the left end of the waveguide $C_L(x, y, \delta)$ against the contrast from the opposite end of the waveguide $C_R(x, y, \delta)$ for each pixel of the simulated electric field data, one obtains a plot which illustrates the possible distribution of measured contrasts for QD sources over a wide range of positions within the waveguide. These plots are shown in Figure 5.13 for $\delta = 0$ to $\delta = 0.5\pi$. Since the

contrast is equal and opposite for circularly polarised sources ($\delta = 0$) the data fall along a straight line with a negative gradient. As δ is increased, the distributions of points displays a spreading away from the diagonal in a ‘fan’ or ‘bow-tie’ -like pattern always crossing through (0,0) until $\delta = 0.5\pi$ (completely diagonally polarised dipole sources) where the plot follows a linear dependence with positive gradient.

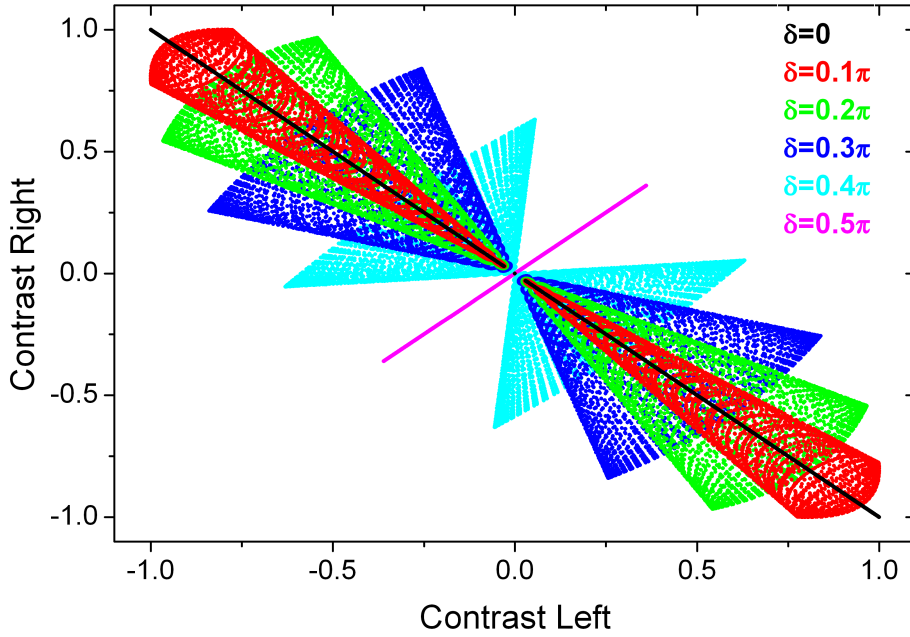


Figure 5.13: Plot of directional emission contrast for dipole sources in a ridge waveguide terminated with grating outcouplers for $0 \leq \delta \leq 0.5\pi$.

Comparison with the experimental data in Figure 5.11 highlights the similarity in statistical distribution using the assumption that the QDs are not perfectly circularly polarised. The experimental plot displays the statistical distribution of QDs with random phase and position whereas the simulated data assumes a source of fixed phase for different locations within the waveguide. The points in Figure 5.11 highlighted in red and magenta are QDs which exhibit the greatest degrees of asymmetry in spin readout which from comparison with Figure 5.13 suggest that the greatest degree of phase perturbation of the QDs in experiment is $0.3\pi < \delta < 0.4\pi$. On average however, the phase perturbation $\delta \leq 0.3\pi$.

5.4 Photonic Crystal Waveguide

As presented in Section 1.2.2, the W1 photonic crystal waveguide sustains a single propagating mode at QD emission wavelengths. As this mode approaches the Brillouin zone boundary, the mode experiences a monotonic increase in group index leading to spontaneous emission enhancement of embedded emitters [79]. The benefit of using photonic crystal waveguides for spin readout purposes is that this spontaneous emission enhancement can be used to move the QDs into a lifetime-limited coherence regime instead of a dephasing-limited regime such that the QD emits indistinguishable single photons. The proposal of using photonic crystals for spontaneous emission enhancement of QDs is explored in Section 7.2.

The photonic crystal waveguide comprises a triangular lattice of air holes etched into an air-clad GaAs membrane as illustrated in Figure 5.14. As with the ridge waveguide, the device possesses mirror symmetry along all three cartesian axes so the modes can also be classified according to their parity about these axes.

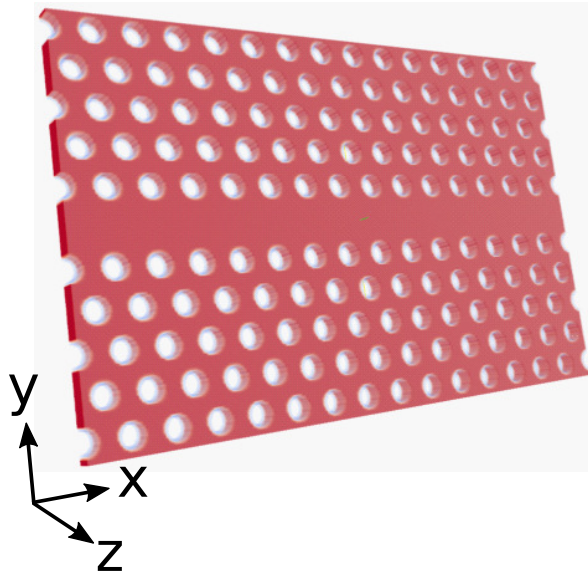


Figure 5.14: 3D schematic of a W1 photonic crystal waveguide.

Using MPB [54] the absolute electric field profiles of the fundamental ‘gap-guided’ mode was calculated for $k_x = 0.47(2\pi/a)$, which are plotted in Figure 5.15. Again, as with the ridge waveguide this mode is y-odd, z-even but with an x-dependence of $\mathbf{u}_{\mathbf{k}}e^{ik_x x}$ where $\mathbf{u}_{\mathbf{k}}$ is the

periodic Bloch function of the photonic crystal lattice. Since the waveguide mode is ‘TE-like’ it also consists of E_x (Figure 5.15(a)) and E_y (Figure 5.15(b)) fields which, due to the periodicity of the photonic crystal, exhibit a phase dependence between them which varies as a function of position in both x and y as shown in Figure 5.15(c) for a mode propagating to the right. For the mode propagating to the left, the phase is inverted i.e. $\phi_{left}(x, y) = -\phi_{right}(x, y)$.

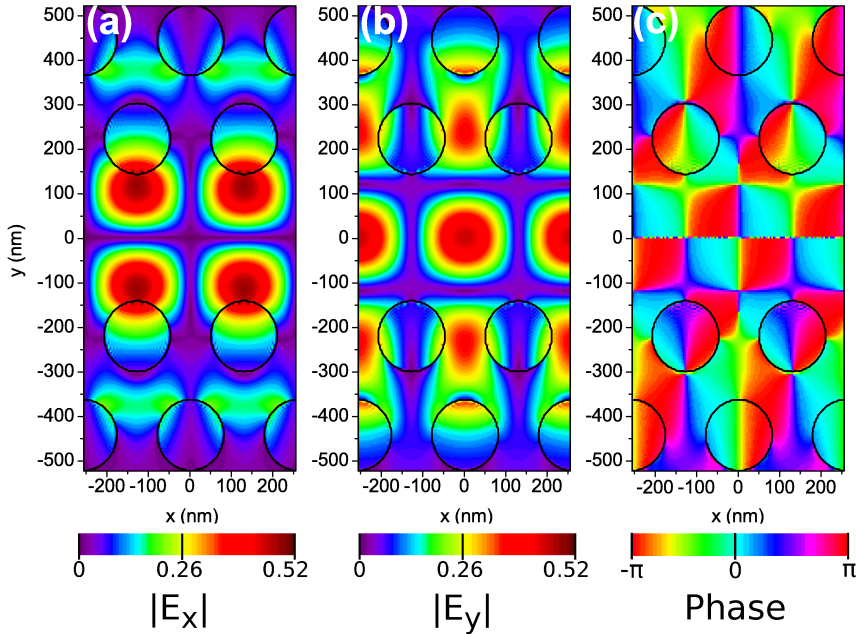


Figure 5.15: Absolute (a) E_x and (b) E_y field amplitudes of a W1 photonic crystal waveguide. (c) Phase between E_x and E_y fields for propagation to the right. The polarity of the phase is reversed for propagation to the left.

To gain a more intuitive insight into the local polarisation of the modal fields, it is convenient to consider the Stokes parameters from Equation 5.11 which are plotted in Figure 5.16(a)-(d), where again the polarisation degrees (Q, U and V) are plotted as quantities normalised to the intensity. Figure 5.16(a) shows the intensity of the electric fields. Figure 5.16(b) plots the degree of linear polarisation where it can be seen that the fields are y -polarised near $y = 0$ and x -polarised for $|y| > 0$, both periodic along x . The degree of diagonal polarisation is presented in Figure 5.16(c) where at certain locations the fields are completely diagonally polarised since $U/I = 1$ where $Q/I \sim 0$ and $V/I \sim 0$. Concerning the degree of circular po-

larisation, plotted in Figure 5.16(d), there are eight locations within the waveguide unit cell where the fields are completely circularly polarised. For propagation to the left, the profile of the circular polarisation degree is inverted. Due to the nature of the electric field profiles of the W1 waveguide, the C-points occur near to minima of the electric field intensity [78].

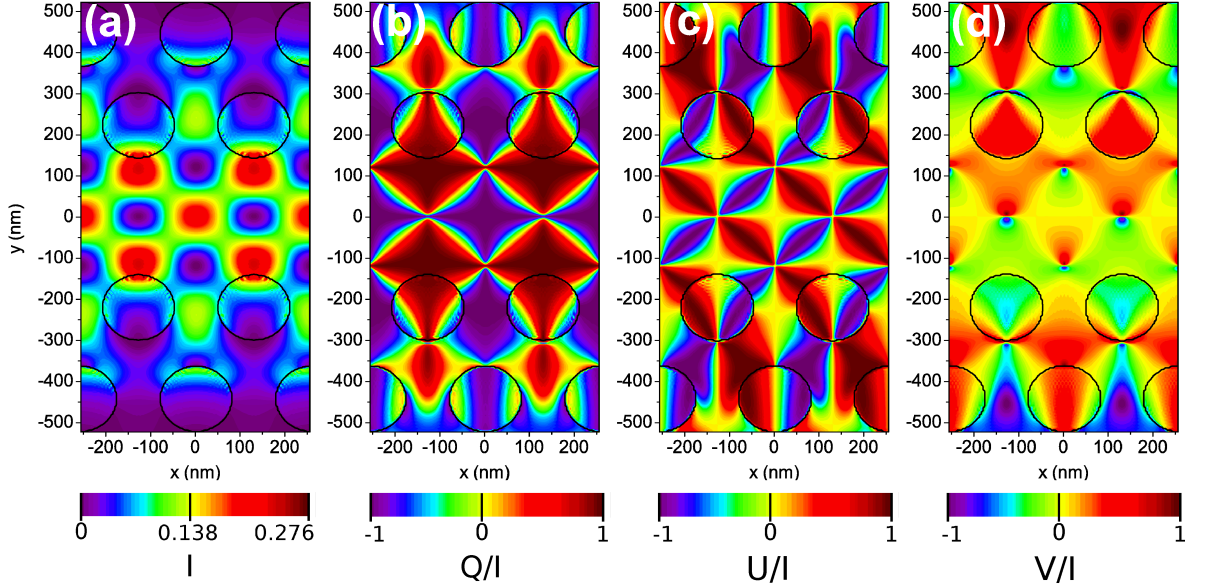


Figure 5.16: Stokes parameters for the guided mode of a photonic crystal waveguide. (a) Intensity, I . (b) Degree of linear polarisation, Q/I . (c) Degree of diagonal polarisation, U/I . (d) Degree of circular polarisation, V/I for propagation to the right.

5.4.1 Chiral Coupling of Single QD

Using Equation 5.10, the selective coupling contrast was evaluated for the modal fields of the W1 waveguide for a circularly polarised QD ($\delta = 0$). These results are plotted in Figure 5.17, which again follow the spatial profile of the Stokes V -parameter for degree of circular polarisation and are equal and opposite for both propagation directions. Comparing these profiles to those of the ridge waveguide it is apparent that the spatial constraint for selective coupling is stricter for the W1 waveguide: for $> 95\%$ contrast the emitter must be located within $\sim 10\text{nm}$ of the C-points and the fractional area over which this is exceeded is 6.42×10^{-4} , two orders of magnitude lower than for the ridge waveguide with outcouplers.

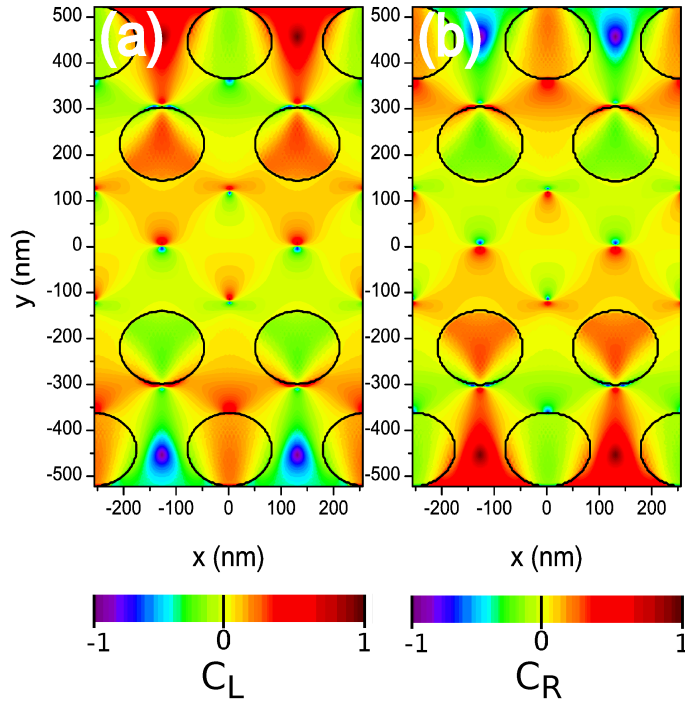


Figure 5.17: Contrast in emission intensity between σ_+ and σ_- polarised dipole sources visible from (a) left and (b) right ends of a W1 photonic crystal waveguide.

Since the modal fields possess a longitudinal phase dependence like the outcoupler-terminated ridge waveguide, it is expected that asymmetry is observed in the contrasts from opposite ends of the waveguide for elliptically polarised dipole sources. The calculations presented here are for a photonic crystal waveguide in the absence of outcouplers: the outcouplers have a negligible contribution to the longitudinal phase variation between the modal fields compared to the Bloch periodicity of the waveguide itself. The contrasts were calculated as for the ridge waveguide, using the modal fields and elliptically polarised dipole sources to investigate any asymmetry in the QD spin readout due to elliptically polarised QDs. The spatial profiles of these contrasts are presented in Figure 5.18 for $\delta = 0.1\pi$. Figure 5.18(a) shows the contrast from the left end of the waveguide and Figure 5.18(b) shows the contrast from the right. Asymmetry is observed in the spatial profiles suggesting that the regions of maximum contrast between left and right ends of the waveguide occur at different locations within the waveguide. That is, an elliptically polarised dipole source within the waveguide will show

asymmetrical contrast when observed from opposite ends of the waveguide. To highlight this difference, $C_L + C_R$ is plotted in Figure 5.18(c) which reveals that the deviation from symmetrical contrast follows the spatial profile of diagonal polarisation within the waveguide.

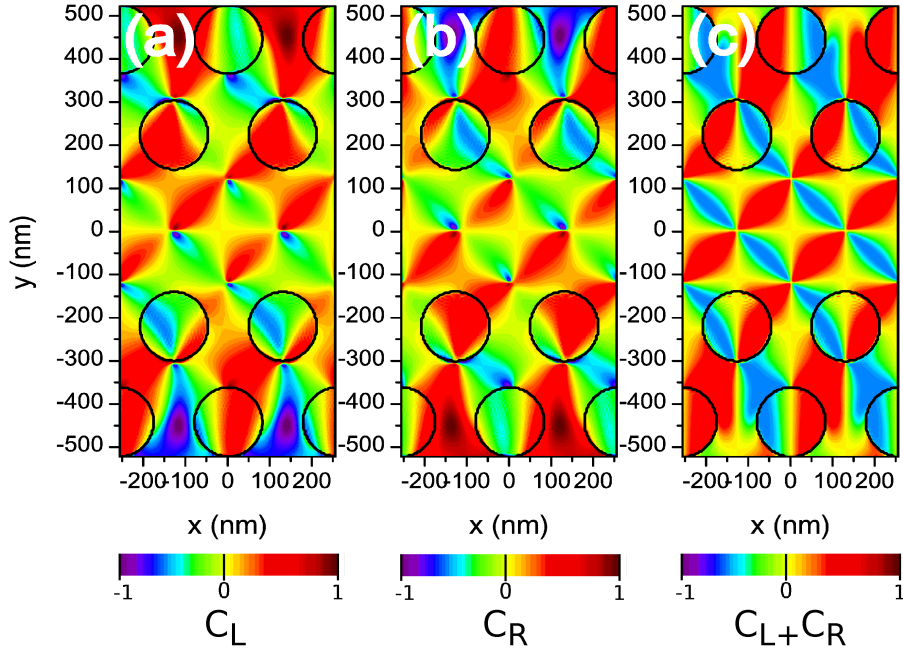


Figure 5.18: Contrast in emission intensity between elliptically polarised dipole sources ($\delta = 0.1\pi$) visible from (a) left and (b) right ends of a W1 photonic crystal waveguide (c) Sum of contrast in emission intensity from opposite ends of the waveguide.

Plotting the contrasts from opposite directions for each point in Figure 5.18, one again obtains a statistical distribution which shows the expected contrast observed for an emitter placed at each location within the W1 waveguide. These results are plotted in Figure 5.19(a)-(f) for $0 \leq \delta \leq 0.5\pi$. Unlike the same plots obtained for the ridge waveguide, the plots exhibit an elliptical distribution. This behaviour may be attributed to the modal fields reaching complete diagonal polarisation at certain locations within the waveguide: the same distribution is not observed for the outcoupler-terminated ridge waveguide which does not possess fully diagonally polarised fields.

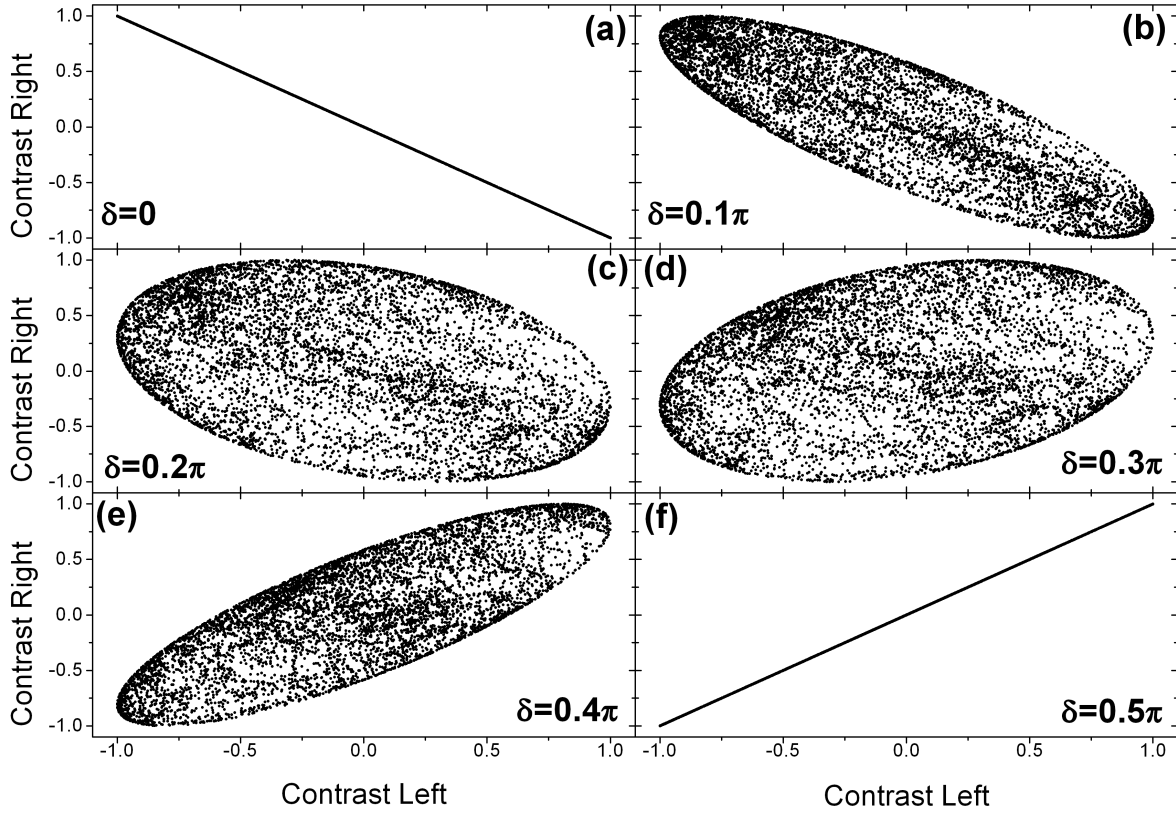


Figure 5.19: Plot of directional emission contrast for dipole sources in a W1 photonic crystal waveguide for $0 \leq \delta \leq 0.5\pi$.

This statistical distribution is supported by experimental observations of many single QDs in different waveguides using PL spectroscopy. In each case, the QD is situated in a random location within the waveguide and the contrast is measured using the intensity form of Equation 5.10. All experimental data were taken by Dr. Maxim Makhonin, James Dixon and David Price. The results of their analysis are shown in Figure 5.20. As can be seen from the data, there is a large deviation from the diagonal with some points exhibiting a high contrast from one end of the waveguide and almost zero from the other, suggesting again that the QDs are elliptically polarised with significant phase perturbation δ . There are no points which show contrast exceeding 0.8 from both outcouplers which demonstrates the strict spatial constraints of the C-points: since the QD growth is non-deterministic the QD locations are random and the probability of finding a selectively coupled QD is low. In addition, since

the C-points of the W1 waveguide occur near to minima in the modal field intensity, QDs that are selectively coupled have a reduced coupling efficiency and will therefore be expected to exhibit reduced intensity in experimental measurements.

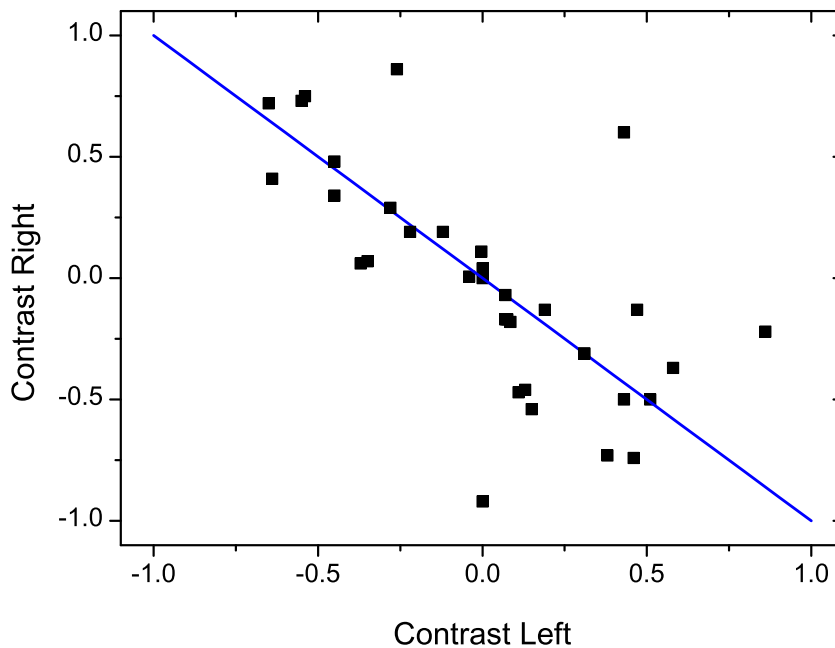


Figure 5.20: Plot of contrast between oppositely polarised QD emission from the outcouplers of a photonic crystal waveguide from experimental results. Data was obtained experimentally by Dr. Maxim Makhonin, James Dixon and David Price through statistical analysis of many QDs in waveguides. Ideal trend of $C_L = -C_R$ is plotted in blue.

5.5 Comparison Between Nanobeam Waveguide and Photonic Crystal Waveguide

5.5.1 Theoretical Comparison

To enable quantitative comparison of spin readout between the two waveguide architectures, statistical analysis was employed over the range of the calculated fields profiles presented in previous sections. The results of these analyses are presented in Figure 5.21.

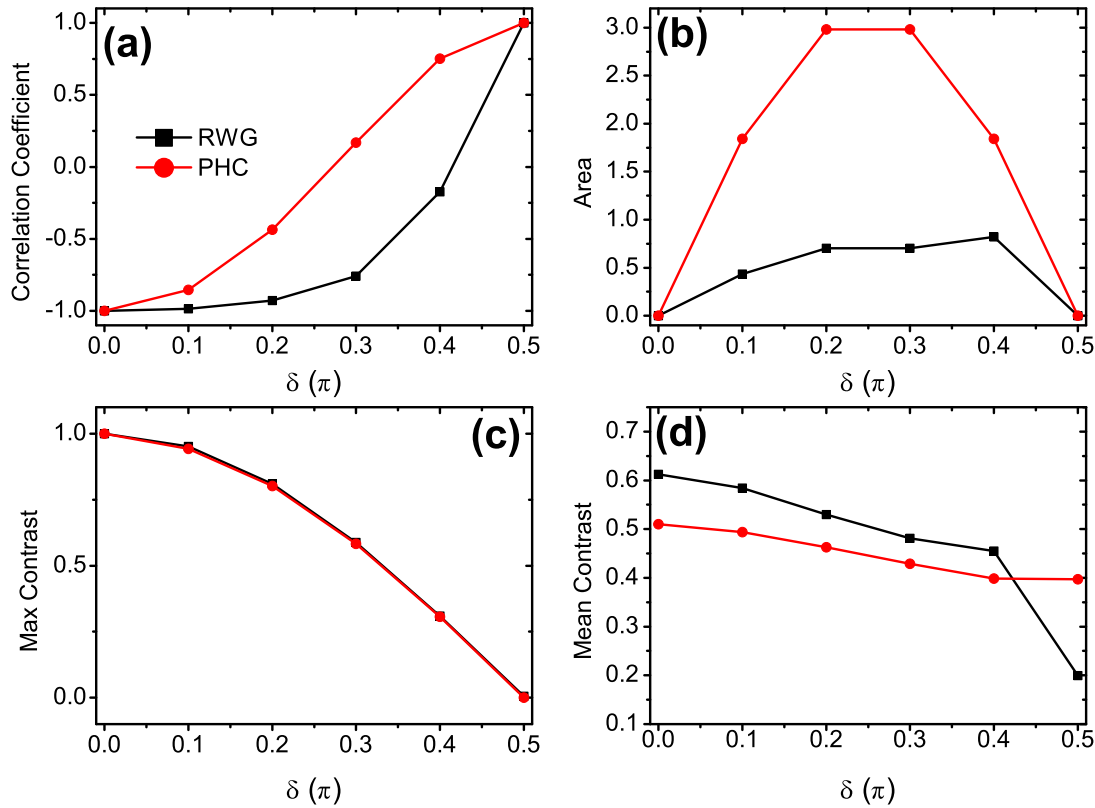


Figure 5.21: Comparison of theoretical spin readout statistics between ridge and photonic crystal waveguides. (a) Pearson correlation coefficient. (b) Area enclosed by statistical distribution of contrast in spin readout. (c) Maximum contrast available when $C_L = -C_R$. (d) Mean contrast.

Since the ideal trend of contrast between the outcouplers is $C_L = -C_R$, the Pearson correlation coefficient was calculated for the data plots of Figures 5.13 and 5.19 which represents

the degree of linear dependence between the contrast from the outcouplers. The Pearson correlation coefficient is defined as

$$\rho = \frac{\text{cov}(C_L, C_R)}{\sigma_{C_L} \sigma_{C_R}} \quad (5.12)$$

where $\text{cov}(C_L, C_R)$ is the covariance between C_L and C_R , and σ_{C_L} and σ_{C_R} are the standard deviations in C_L and C_R respectively. These results are plotted in Figure 5.21(a) where it is observed that over the range of QD phase perturbations considered the ridge waveguide consistently exhibits a greater degree of linear dependence. The degree of spread in the data was estimated by calculating the area enclosed by the statistical distributions of Figures 5.13 and 5.19, and is presented in Figure 5.21(b). The maximum area enclosed for the ridge waveguide is 0.82 whilst for the photonic crystal the area tends towards π at maximum (since the statistical distribution tends towards a filled circle) and is always greater than that for the ridge waveguide. The maximum contrast available is plotted in Figure 5.21(c) which is calculated as the highest contrast attainable whilst $C_L = -C_R$. Both waveguides exhibit a similar dependence for this quantity. Finally, the average contrast expected was calculated by taking the weighted mean of the contrast distributions of Figures 5.13 and 5.19 which is plotted in Figure 5.21(d). In general, the mean contrast is $\sim 10\%$ higher for the ridge waveguide except for large phase perturbations approaching $\delta = 0.5$.

5.5.2 Experimental Comparison

Assessment of the reliability of QD spin readout in experiment was performed by similar statistical analysis for the theoretical data. Histograms of the data from Figures 5.11 and 5.20 are presented in Figure 5.22 (a) and (b) for the ridge and photonic crystal waveguides respectively. From observation of these data, it is clear that the maximum contrast in spin readout is higher for the ridge waveguide than for the photonic crystal waveguide. A weighted mean of the two datasets reveals that the average spin readout contrast is also $\sim 20\%$ higher for the ridge waveguide. Comparison with theoretical data from the previous section in Figures 5.22(c) and (d) reveal a similar statistical trend with a $\sim 7\%$ higher average contrast for

the ridge waveguide. The data for the ridge waveguide also suggest that twice as many QDs exhibit contrast of $> 80\%$ than those for the photonic crystal waveguide.

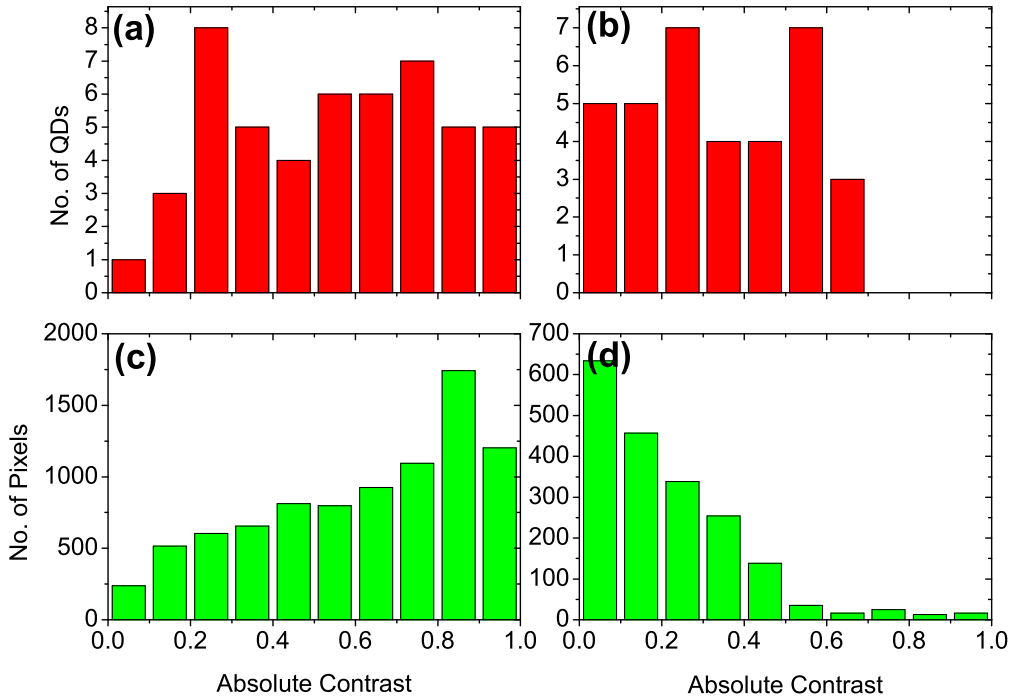


Figure 5.22: Comparison of statistical distribution of QD spin readout contrasts from experimental data (red) for (a) nanobeam and (b) photonic crystal waveguides and theoretical data (green) for (c) nanobeam and (d) photonic crystal waveguides. Labels on x-axis show upper limit of histogram bins.

These data confirm the predictions laid out by theory in that statistically a high degree of QD spin readout is more readily observed for the ridge waveguide than for the photonic crystal waveguide. Indeed, the maximum spin readout contrast observed for the photonic crystal is $\sim 80\%$ whereas several QDs are observed with spin readout fidelities approaching unity for the nanobeam.

5.6 Further Work

5.6.1 Increased Coupling Efficiency

For the application of this chiral QD spin coupling to integrated quantum optics applications, there are several improvements which must be made. The first is to improve the total coupling efficiency of the QD to the propagating modes. For the ridge waveguide system, the total coupled power for circular polarisation at a C-point is $\sim 68.5\%$ which is a substantial reduction from the coupled power of a linearly polarised QD at the waveguide centre (L-point) at $\sim 95\%$. This is due to the coupling of the E_y fields to leaky modes at the C-point.

A similar challenge presents itself for the W1 waveguide, where the C-points occur in close proximity to minima in the electric field intensity. Schemes to remedy this have been proposed which adjust the electric field profiles through displacement of the holes adjacent to the waveguide [78] and through the use of glide plane waveguides [171]. In these cases the coupling efficiency for the QD approaches unity and in the latter scheme (glide plane waveguides) the spatial constraint on directional coupling is substantially reduced.

5.6.2 Lifetime Limited Coherence

A second parameter which must be optimised is the distinguishability of the photons emitted by the QD. For the photonic crystal waveguide, the spontaneous emission (SE) enhancement provided by the slow light mode (Section 7.2) facilitates QD emission in the lifetime limited coherence regime. However, for the ridge waveguide the Purcell factor ~ 1 so the QD remains in the dephasing limited coherence regime. This lack of SE enhancement compared to the photonic crystal waveguide arises from the higher group velocity of the ridge waveguide mode which is $\sim c/n$.

One way to increase the LDOS is to confine a resonant mode to the waveguide. It has been shown that a linear photonic crystal cavity cannot provide direct mapping of QD spin states to the cavity modes [67]. However the degenerate, counter-propagating resonant modes of a whispering gallery mode (WGM) resonator (Figure 5.23(b)) closely resemble the propagating modes of the ridge waveguide system and may therefore be used to provide SE enhancement.

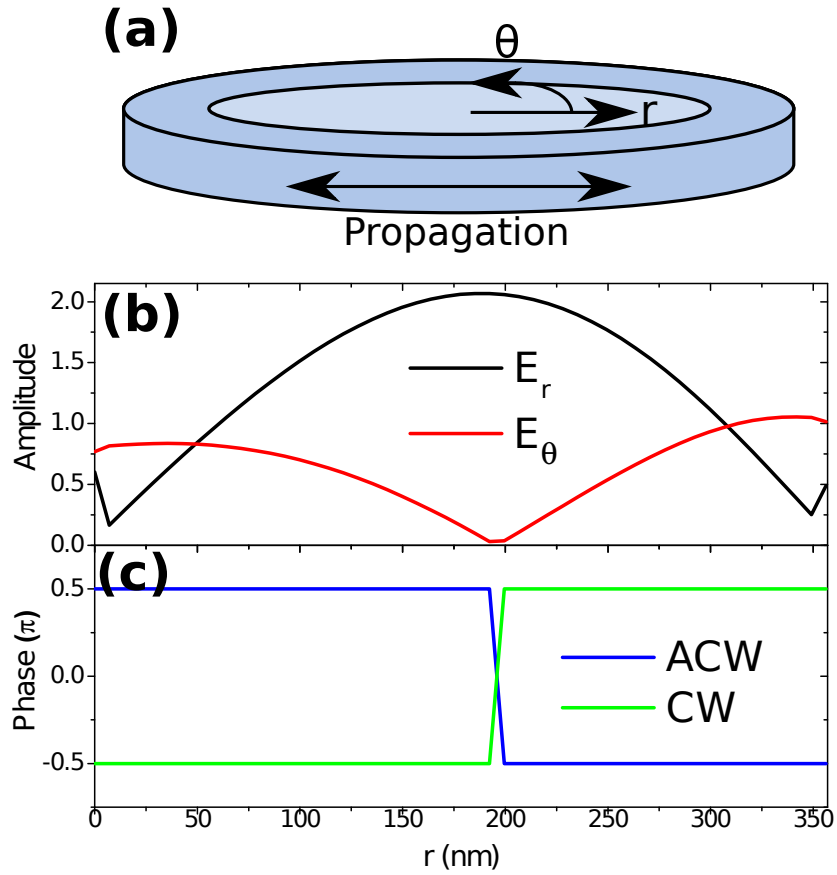


Figure 5.23: (a) Schematic of whispering gallery mode resonator. (b) Electric field profiles and (c) phase of a micro-ring resonator of radius $2\mu\text{m}$ and width 350nm. Phase is shown for clockwise (CW) and anticlockwise (ACW) propagation.

Similar demonstrations are made in [169] and [170] for cold atom systems. The electric field profiles of a micro-ring resonator with radius $2\mu\text{m}$ and width 350nm at $\theta = 0, z = 0$ are plotted in Figure 5.23(a) where the orthogonal electric field components are presented as the equivalent of E_x and E_y fields in cylindrical coordinates, E_θ and E_r respectively.

The electric field profiles closely resemble those of the ridge waveguide system and the relative phase in Figure 5.23(c) shown for clockwise (CW) and anticlockwise (ACW) propagation confirms that they also share a similar phase dependence. The mode profiles are asymmetric along r due to the orbital nature of the whispering gallery mode as presented in Chapter 6.

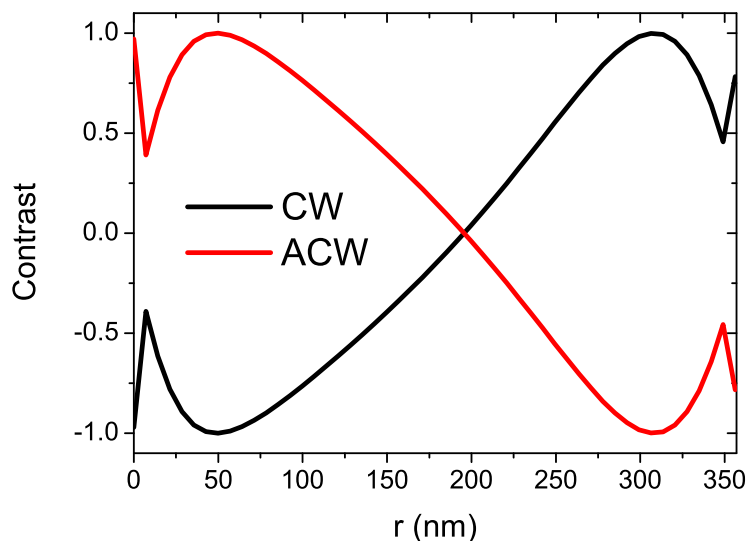


Figure 5.24: Contrast in emission intensity between oppositely polarised dipoles coupled to counter-propagating whispering gallery modes

Calculation of the directional emission contrast from Equation 5.10 reveals that directional emission is indeed possible from this device as shown in Figure 5.24 where the contrast reaches unity approximately 50nm from the inner and outer edges of the ring.

If the micro-ring resonator is evanescently coupled to a single-mode ridge waveguide then a contrast in emission intensity for a single QD in the micro-ring resonator may be observed between the two outputs of the waveguide. If the Q-factor of the cavity mode is sufficiently high so that the Purcell factor for the QD exceeds ~ 5 then subsequent photons will be indistinguishable from one another. The additional benefit of this approach is that the increased coupling efficiency of the QD is inherent to the design.

5.7 Summary

In summary, a scheme to produce deterministic spin readout of a circularly polarised QD has been presented and demonstrated for a ridge and photonic crystal waveguide. For an infinite ridge waveguide, the circularly polarised QD states can couple selectively with unity contrast

at a lateral displacement of $|y| = 93nm$ with no dependence on the longitudinal position. When terminated with outcoupler gratings, the modal field profiles develop a longitudinal phase dependence due to back reflections and the degree of selective coupling becomes a function of longitudinal and lateral position. Despite this, contrasts of spin readout exceeding 95% are obtained. In addition, the presence of diagonally polarised modal field components creates non-symmetrical contrast between spin states observed from the outcouplers for elliptically polarised QDs. The same phenomenon is observed in a W1 photonic crystal waveguide with stricter constraints upon the QD position. The presence of diagonally polarised modal field components again produces asymmetrical contrast for elliptical QD spins. Ongoing improvements to the outcoupler design to reduce reflectivity are expected to eliminate the presence of diagonally polarised fields in the ridge waveguide, however the Bloch periodicity of the photonic crystal dominates over the contributions from the outcouplers and so these field components are inherent to this architecture. Finally, plans for future work on improving the coupling efficiency of the QD have been presented through embedding of the QD within a WGM resonator.

Chapter 6

On-Chip Spectral Filtering using Whispering Gallery Mode Resonators

6.1 Introduction

Quantum dots (QDs) in whispering gallery mode resonators (WGMs) of the type shown in Figure 6.1 possess many beneficial features for quantum photonic applications [41, 44, 47, 49]. Previous demonstrations have shown that the spontaneous emission enhancement provided by high Q-factors of up to $\sim 10^6$ [180] cavities enables bright, deterministic single photon sources [44, 45, 49], lasing [48, 181] and strong coupling [46, 47] of embedded QDs. The ability to easily integrate with other monolithic circuit elements [41, 50] affords functionality such as optical switching using single photons [182–184] in addition to provision of on-chip spectral filtering for the incorporation of on-chip optical detection [19, 83, 84, 185] with up to 100% transmission at resonance [186]. The degenerate counter-propagating modes of the whispering gallery mode resonator [181] increase the functional density of such a filter over other nanocavity-based filters as two signal lines can be filtered by the same structure since the counter-propagating modes are orthogonal [187–189].

This chapter investigates the application of WGMs for on-chip spectral filtering applications. The mode structure and transmission spectra of microdisks coupled to a single mode waveguide are studied using FDTD simulations and optimised designs are produced for filtering at QD wavelengths. Experimental results are presented where the single photon emission from a single self-assembled InAs QD within the microdisk is split between two waveguide outputs and spectrally filtered by the degenerate propagating modes of the microdisk. Finally, future plans for the use of add-drop filters are discussed using microdisks and micro-ring type resonators for improved free spectral range of the filter.

6.2 Simulation and Design of Whispering Gallery Mode Resonators

6.2.1 Formation of Whispering Gallery Mode Resonances

A planar optical WGM resonator is comprised of a dielectric material with cylindrical symmetry, where the mode is confined in-plane by total internal reflection (TIR) at the outer radial dielectric interface: this one-sided confinement mechanism is a defining characteristic of WGMs. The modal fields of the microdisk resonator can be obtained by solving the 2D Helmholtz equation in cylindrical coordinates for the radial H_z fields [38, 190]

$$\left(\frac{\partial^2}{\partial r^2} + \frac{1}{r} \frac{\partial}{\partial r} + \frac{1}{r^2} \frac{\partial^2}{\partial \theta^2} + k^2 \right) H_z(r, \theta) = 0 \quad (6.1)$$

with solutions for the fields internal and external to the disk

$$H_z(r, \theta) \sim \begin{cases} J_m(k_1 r) e^{i(\pm m\theta - \omega t)} & r \leq R \\ H_m^{(1)}(k_2 r) e^{i(\pm m\theta - \omega t)} & r > R \end{cases} \quad (6.2)$$

where J_m and $H_m^{(1)}$ are the m -th order Bessel and Hankel functions of the first kind respectively, k_1 and k_2 are the propagation constants for the internal and external fields respectively, m is the azimuthal mode index (an integer representing the number of optical periods the

fields complete around the circumference of the resonator) and R is the outer radius of the microdisk resonator. The radial electric field profiles for the (40,1) mode in a GaAs microdisk with $r = 2\mu\text{m}$ are shown in Figure 6.1. The modes propagate with wavenumber k_1 which, from the orbital nature of the modes, can be resolved into an azimuthal (k_θ) and radial (k_r) component.

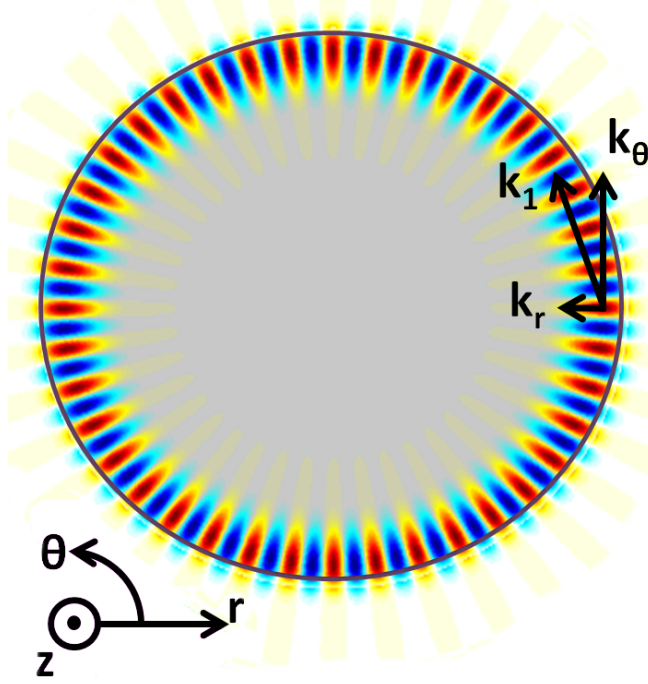


Figure 6.1: Simulated E_r field profile of (m,p)=(40,1) whispering gallery mode in the $z = 0$ plane for a $2\mu\text{m}$ radius GaAs microdisk cavity.

Due to the cylindrical symmetry of the system, the modes are doubly degenerate for $\pm m$. These modes propagate azimuthally around the microdisk in opposite directions, creating standing waves which place a resonance condition on the azimuthal k-vector. Resonances are formed when

$$\lambda_{m,p} = \frac{2\pi n_{eff} R}{BesselZero(m,p)} \quad (6.3)$$

where $\lambda_{(m,p)}$ is the free-space wavelength of the (m,p) -th WGM, $n_{eff} = \lambda_{(m,n)} k_1 / 2\pi$ is the effective index of the WGM and $BesselZero(m,p)$ is the p -th root of the m -th order Bessel

function of the first kind, J_m [50]. For a WGM resonator with only a single family of radial modes, Equation 6.3 reduces to $\lambda_m = 2\pi n_{eff}R/m$.

Using FDTD Simulations with cylindrical symmetry applied to the simulation domain [110] the mode structure of an ideal microdisk resonator can be calculated. A schematic of the simulated cavity is shown in Figure 6.2(a) including the supporting AlGaAs pedestal beneath the disk. As explained in Section 2.2.1, the use of cylindrical symmetry reduces the problem to an efficient 2D calculation in the r, z plane where the azimuthal fields are calculated assuming $E_r(r, \theta, z) = E_r(r, z)e^{im\theta}$ which is solved for a range of m . The amplitude and complex frequency of each mode are calculated using a harmonic inversion monitor [146] the results of which are plotted in Figure 6.2(b). The spectral separation between subsequent radial modes (same p) is around 25nm but the presence of radial modes up to $p = 4$ reduces the overall FSR to ~ 4 nm.

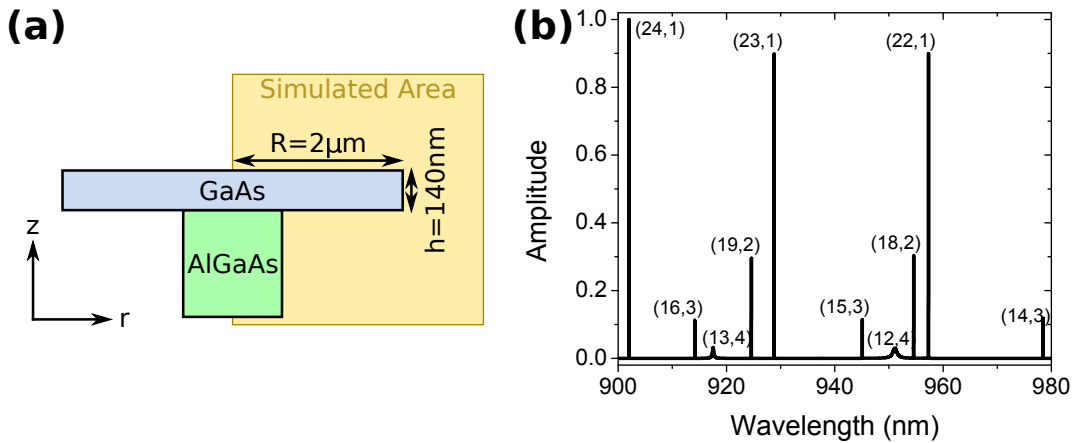


Figure 6.2: (a) Schematic of GaAs microdisk cavity used in simulations including AlGaAs pedestal. (b) Simulated mode spectrum of isolated GaAs microdisk resonator with $r = 1.5\mu\text{m}$.

Since the simulation is assumed to have perfect cylindrical symmetry, the outer sidewall of the microdisk is perfectly smooth. In addition, the resonator radius is sufficiently large so that radiative losses due to bending of the mode are negligible [38]. The absence of significant scattering losses due to sidewall roughness and radiative losses from these conditions suggests that the intrinsic loss rate of the resonator is negligible and therefore calculation of

the Q-factors are not computationally feasible as this requires running the simulation for very long times to accurately resolve the envelope of the decay transient. The linewidths of the resonances shown in Figure 6.2(b) are resolution-limited so calculation of the Q-factors is also impractical via linewidth extraction. Modes with radial order $p > 4$ are not observed due to leakage into the AlGaAs pedestal since the maximum amplitude of higher order radial modes occur closer towards the disk center with increasing p .

6.2.2 Design of an On-Chip Filtering Beam Splitter using a GaAs Microdisk Resonator

The WGMs possess evanescent field components in the air region surrounding the disk which facilitate in-plane coupling to an adjacent single-mode waveguide. Such a coupled device is shown schematically in Figure 6.3(a). As the propagating mode of the waveguide passes the disk, it couples to the WGMs and power is transferred from the waveguide to the disk, with a rate dependent on the field overlap between the waveguide and cavity modes. Depending on the direction of propagation of the waveguide mode, only one of the two degenerate propagating WGMs is excited. The WGM completes a ‘lap’ of the disk and returns to the coupling region where it again couples to the waveguide and optical power is transferred back to the waveguide. On resonance, the fields return to the waveguide with a π phase shift [38]. In the steady-state, this phase shift destructively interferes with the incoming waveguide mode producing notches in the transmission spectrum for the waveguide. When the amplitudes of the fields returning from the disk are equal to those propagating through the waveguide, complete destructive interference occurs and the transmission drops to zero: the device is critically coupled. Such a device is known as an all-pass filter as it does not modulate the amplitude of transmitted fields but imposes a wavelength-dependent phase shift. If the WGMs are excited by an optical pulse, the transmission is unity for all wavelengths (neglecting any optical losses). However for a CW source, interference occurs between the driving field and the cavity modes, producing notches in the transmission spectrum at resonance with the cavity modes.

Intuitively, the coupling rate between the waveguide and disk is dependent on the separation between them. The effect of adjusting the separation was calculated using 2.5D FDTD [111] and the minimum transmission through the waveguide at resonance with a WGM is shown in Figure 6.3(b). At large separation, the interaction is weak and the waveguide fields dominate in determining the transmission: the device is undercoupled. In this scenario, complete destructive interference does not occur since the amplitude of the waveguide mode greatly exceeds that of the returning cavity mode. At small separation, the interaction is strong and the cavity fields dominate over the waveguide fields in transmission: the device is overcoupled. In this scenario, complete destructive interference does not occur since the amplitude of the returning cavity mode greatly exceeds that of the waveguide mode. Critical coupling is achieved at a separation of 100nm where the transmission drops to $T = 0.028$. Critical coupling occurs when the amplitudes of the cavity and waveguide modes are equal, producing complete destructive interference at the coupling region.

A second factor in determining the coupling rate between the cavity and waveguide fields is the width of the waveguide. Specifically, the two modes must be phase-matched so that the relative phase between the cavity and waveguide mode is π at resonance: the round-trip phase of the WGM is a multiple of 2π , so the waveguide mode must complete an integer number of cycles along the coupling region to be phase matched. This is achieved when the azimuthal propagation constant of the WGM, $k_\theta = 2\pi n_{eff}^{WGM}/\lambda$ is equal to the propagation constant of the waveguide mode, $\beta = 2\pi n_{eff}^{WG}/\lambda$. At resonance, this means that the effective indices of the modes must be equal. Since the effective index of the waveguide mode is dependent on the cross sectional area of the waveguide, matching is achieved by adjustment of the waveguide width. The results of 2.5D FDTD simulations where this parameter is adjusted are presented in Figure 6.3(c), where minimum transmission is achieved for a waveguide width $W = 290\text{nm}$. The simulated transmission spectrum for the critically coupled device is shown in Figure 6.3(d). The contribution of higher order radial modes is suppressed due to poor index matching with the waveguide mode. Conversely, similar transmission is observed for neighbouring $p = 1$ WGM resonances. The Q-factor for the WGM with minimum transmission

is $\sim 68,000$. The intrinsic loss rate of the disk in a real experimental simulation is expected to be higher than for simulations of the uncoupled disk (since the sidewalls are not perfectly smooth) which, combined with the waveguide coupling rate, is expected to dramatically reduce the Q factor from the value for the uncoupled resonator.

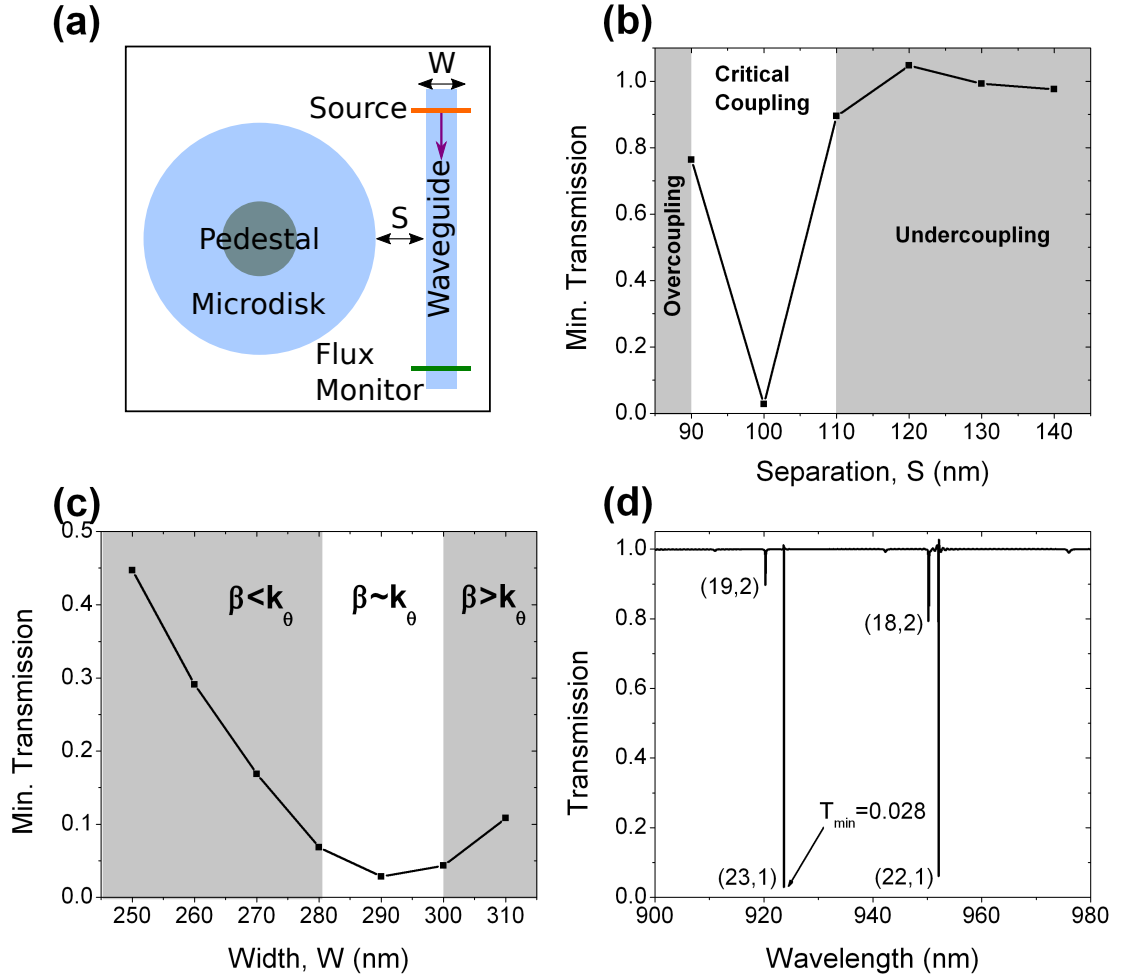


Figure 6.3: FDTD simulation results for all-pass filter using a microdisk resonator with $r = 1.5\mu\text{m}$. (a) Schematic of simulated structure. (b) Minimum transmission through the waveguide, at resonance, as a function of cavity-waveguide separation for (23,1) mode using $W = 290$ nm. (c) Minimum transmission through the waveguide, at resonance, as a function of waveguide width for (23,1) mode using $S = 100$ nm. (d) Simulated waveguide transmission spectrum for $S = 100$ nm and $W = 290$ nm.

If a two-level emitter, such as a QD, is incorporated within the disk and coupled to a pair of counter-propagating WGMs then the emission is divided between clockwise and anticlockwise propagation. This directionality is carried over to the waveguide through the coupling region and the photons are divided between the waveguide outputs. In this arrangement, the device acts as a filtering beam splitter where the QD emission is enhanced at resonance by the Purcell effect [89]. If the cavity contains many emitters, then only those spectrally and spatially coincident with the cavity modes will be observed from the waveguides due to this SE enhancement and efficient coupling of the cavity modes to the waveguides. Such a system can be used to realise an on-chip Hanbury-Brown and Twiss experiment without the need for off-chip filtering.

6.3 Sample Details

The waveguide-coupled cavities were fabricated by Dr. Ben Royall using the procedures presented in Section 2.3.2 on a 140nm GaAs membrane containing a low density of self-assembled InAs QDs with a $1\mu\text{m}$ sacrificial AlGaAs layer between the membrane and substrate. The duration of the HF acid underetch to remove the AlGaAs layer was carefully monitored to ensure complete removal beneath the waveguide and outcouplers but leaving a supporting pedestal beneath the microdisk of $< 1\mu\text{m}$ diameter. An SEM image of a typical all-pass filter device is shown in Figure 6.4. Grating outcouplers with $\lambda/2n$ periods were added to the ends of the waveguide to scatter PL emission out of the device plane and into the detection apparatus.

6.4 Characterisation of Waveguide-Coupled Microdisk Cavities

PL measurements were performed using an 808nm diode laser for above bandgap excitation of the QD ensemble, focussed to a $\sim 1\mu\text{m}$ spot by a microscope objective lens with NA=0.5. The sample was held in an Oxford Instruments liquid helium cold finger cryostat at 4K. Spatial separation of the excitation and collection spots on the sample allows for transmission

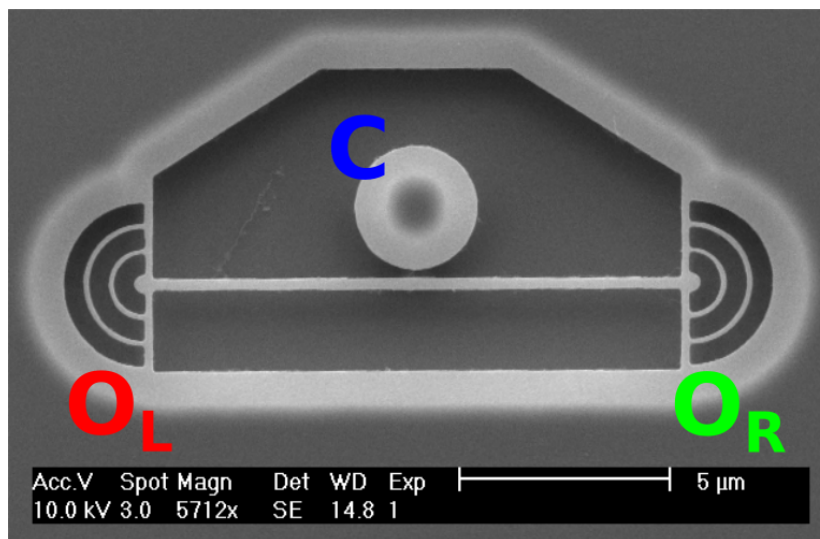


Figure 6.4: SEM image of an all-pass filter using microdisk cavity with $r = 1.5\mu\text{m}$. Cavity and outcoupler nomenclature is defined.

measurements of QD PL through the structure.

Similar to Chapter 3, a shorthand notation is defined when referring to the cavity and outcouplers respectively. C denotes the cavity, O_L and O_R denote the left and right outcouplers respectively. For example, when the laser excitation is aligned with the cavity and the collection spot is aligned with the left outcoupler this arrangement is denoted CO_L . These points are illustrated in Figure 6.4 for an all-pass filter comprising a microdisk resonator with $1.5\mu\text{m}$ radius.

Characterisation of the microdisk spectrum was achieved using $30\mu\text{W}$ laser excitation power, exciting the entire ensemble QD PL for use as an internal white light source. A typical PL spectrum obtained using the CO_R configuration is presented in Figure 6.5. The radial mode families can be identified by comparison with Figure 6.2(b) since the centre wavelengths and spacing agree well with simulated data. The first three radial mode families have comparable Q-factors, but the fourth radial modes exhibit Q-factors an order magnitude below these. This is due to leakage of the fourth order mode into the AlGaAs pedestal beneath the microdisk.

The dependence of the cavity Q-factor on waveguide separation was studied for the (17,3)

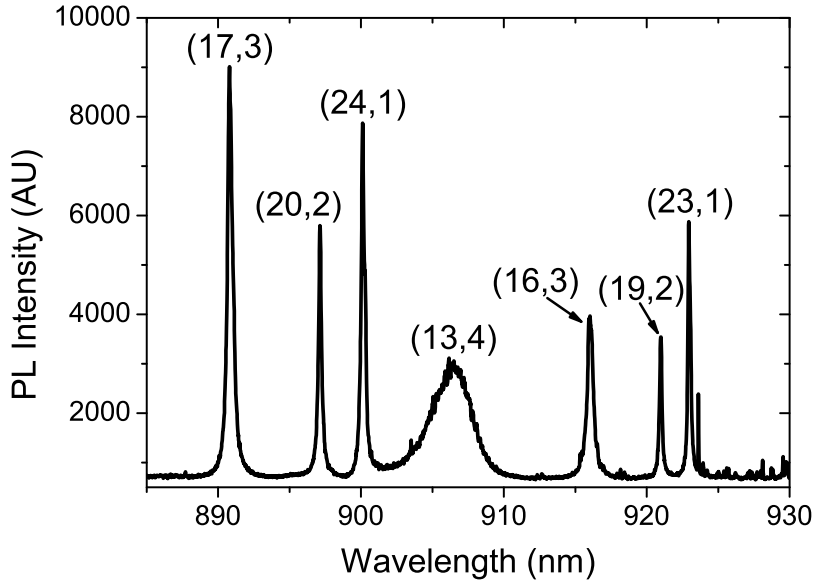


Figure 6.5: PL spectrum of all-pass filter using microdisk cavity with $r = 1.5\mu\text{m}$ taking using the CO_R configuration.

mode by taking PL spectra for devices over a range of waveguide separations with nominally constant width. These spectra are presented in Figure 6.6(a). Figure 6.6(b) plots the Q factors of these modes as a function of cavity-waveguide separation. As expected, the cavity Q-factor decreases with reducing waveguide separation and tends towards the intrinsic (uncoupled) Q-factor at large separation. Since the Q-factor decreases as the waveguide separation is reduced, a compromise is made between coupling efficiency and bandwidth. A larger separation establishes a lower coupling rate but a smaller bandwidth, due to an increased Q-factor, which is better for filtering applications. The linewidths demonstrated should be sufficient for isolation of a single QD emission line provided that the average free spectral range between QD lines is $>1\text{nm}$.

The coupling rate between the cavity and waveguide is proportional to the field overlap integral between the evanescent components of the two modes [191]. Therefore, to estimate the intrinsic Q-factor, a fit of $Q = Q_u(1 - e^{-2(S-S_0)/\tau})$ is applied to the experimental data, where S_0 is the separation at which $Q = 0$, τ is a decay constant and $Q_u = 6515 \pm 15$ is

the intrinsic (uncoupled) Q-factor. This intrinsic Q-factor is an order of magnitude below the predicted Q-factor from simulations which may be due to scattering by the sidewall roughness of the microdisk and/or scattering by the embedded QD ensemble [47]. However, the intrinsic loss rate is sufficiently low that the effects of waveguide proximity can be observed and QD PL emission within the disk is visible from the outcouplers.

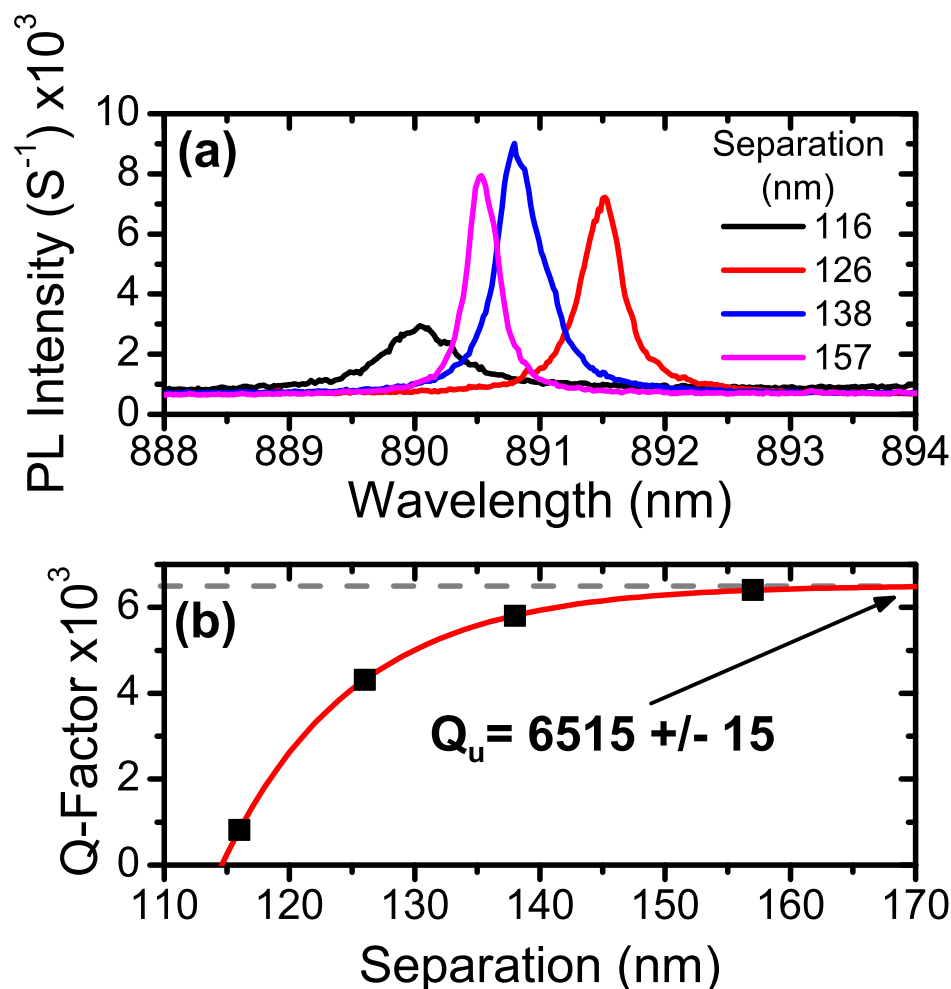


Figure 6.6: (a) PL spectra of a single WGM for a range of waveguide separations. (b) Dependence of the microdisk WGM Q-factor on the waveguide separation obtained from PL measurements (Black). (Red) Fit of $Q = Q_u(1 - e^{-2(S-S_0)/\tau})$ to the experimental data, yielding $Q_u = 6515 \pm 15$.

6.5 On-Chip Splitting and Spectral Filtering of Single QD Emission

Characterisation of single QDs was performed as in the previous section, but with reduced laser power at 500nW. This power is below the typical QD saturation power so that individual QD emission lines can be observed in the PL spectra. QDs in the microdisk were excited directly by positioning the excitation spot over the cavity whilst collecting emission from the outcouplers with the aim of observing a single QD line coupled to a cavity mode. Figure 6.7 shows a temperature tuning PL measurement taken for a single QD coupled to a WGM resonance. At 4K the QD and cavity mode are in resonance. The emission wavelength of the QD is more sensitive to temperature changes than the cavity mode [45, 184] so that as the temperature is increased the QD is shifted off-resonance with the cavity mode to lower energy. The QD emission intensity increases by a factor of 35 when brought onto resonance with the cavity, indicating that the QD is well coupled to the cavity mode.

To assess the filtering capabilities of the microdisk, low power spectra were taken at 4K when exciting and collecting PL from the disk (CC) and comparing with the spectra when collecting PL from the outcouplers (CO_L and CO_R). The spectrum of the QD ensemble in the microdisk is shown in Figure 6.8(a) where the coupled QD can be seen at 890.5nm, the QD ensemble 900-960nm and the wetting layer emission at 865nm. The PL spectra taken from the outcouplers when exciting PL in the microdisk is shown in Figure 6.8(b) where the dominant spectral feature is the coupled QD at 890.5nm. The inset to Figure 6.8(b) shows a zoom of the spectrum around the QD emission, showing the splitting of the PL for this QD between the outcouplers. Applying a Lorentzian fit to the QD emission line in Figure 6.8(b) yields an intensity splitting ratio for the QD of 63:37 between the two outcouplers. The observation of an uneven splitting ratio from the outcouplers may be due to unequal transmission of the outcouplers from to unintentional variation in fabricated parameters.

Instead of a single cavity mode peak in Figure 6.7, a pair of peaks are observed with a splitting of 0.3nm. Defects within, or on the surface of, the microdisk cavity may act to split the WGM modes into symmetric and anti-symmetric superpositions with respect to the

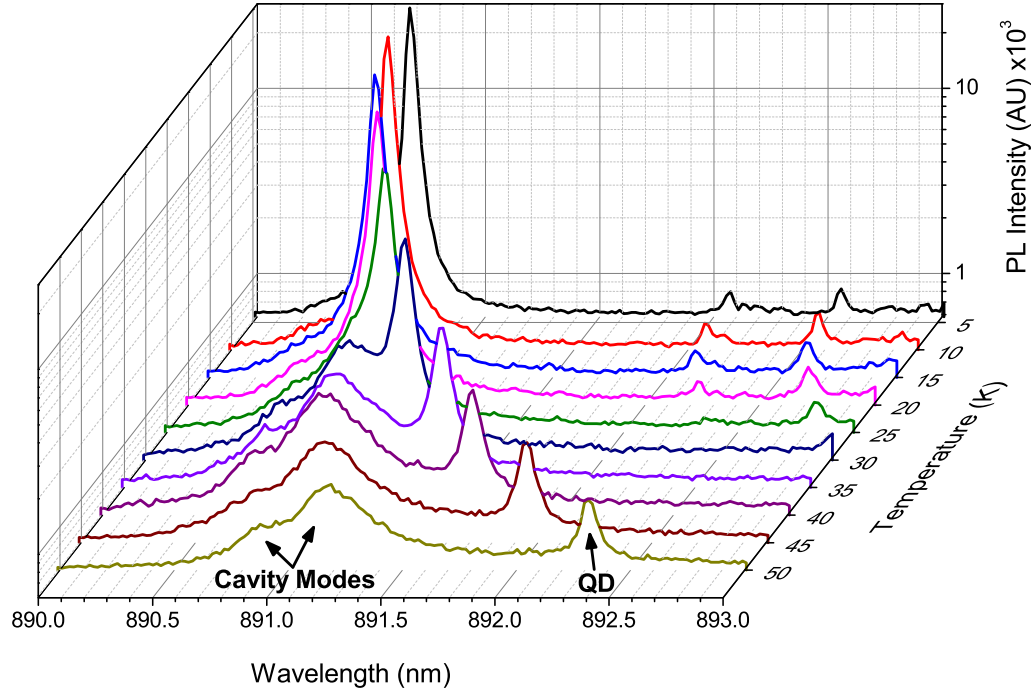


Figure 6.7: Temperature tuning of single QD coupled to WGM in microdisk cavity. The cavity modes appear split by 0.3nm with Q factors of $\sim 8,900$ (3,200) for the shorter (longer) wavelength peak.

defect. Such defects may take the form of embedded defects [192], notch or peak defects on the outer surface of the resonator [181] or defects on the vertical surfaces of the resonator [193]. In [193] this effect is deliberately induced by design. These defects act as a scattering centre for the WGMs so in general the symmetric supermode is expected to have a lower Q-factor since it shares the largest field overlap with the defect [192]. The splitting observed in Figure 6.7 is consistent with these effects since the Q-factor of the shorter (longer) wavelength peak is $\sim 8,900$ (3,200). If the defect is of higher refractive index than the microdisk itself, the symmetric supermode will be at lower energy than the anti-symmetric supermode. The mode energies in 6.7 are consistent with this observation. If the defect were of an air notch type, the energies of the modes would be reversed. What is surprising is the observation of WGM

splitting at these relatively low Q-factors. In [181] it is found that WGMs exhibiting splitting have a Q-factor of around half of than of devices with degenerate supermodes. It may be then, that the 'cold' Q-factor (i.e. in a cavity without embedded emitters) is in fact higher than that calculated in Figure 6.6 but is reduced due to interactions with defects. The cavity radius in [181] was $2.5\mu\text{m}$ and has almost double the thickness so it has a much larger modal volume when compared to the WGMs presented here. For comparable Q-factors, therefore, the devices presented here possess a greater or comparable Q/V and a similar interaction strength can be expected.

It is unclear from these measurements exactly what comprises the defect, but what follows here is a qualitative discussion of what may cause the splitting. The effect of a defect internal to or on the surface of the WGM is to 'lock' the phase of the supermodes to the scattering centre. If the defect is not due to the QD it is a striking coincidence that the QD spatially coincides with the symmetric supermode created by a non-QD defect within the cavity. When the QD is off-resonance with the WGMs, both peaks can be observed in Figure 6.7 however when the QD is brought into resonance with the symmetric mode, the intensity of the anti-symmetric mode peak does not increase. It may therefore be that the QD itself is acting as the defect in which case the supermodes will 'lock' to the position of the QD which ensures maximal field overlap for the symmetric mode and minimal overlap for the antisymmetric mode. It was unfortunately not possible to tune the QD emission peak into resonance with the antisymmetric peak using temperature control to fully verify this.

Despite this non-ideal behaviour the splitting ratio is sufficient for use as a beam splitter within a HBT measurement, as demonstrated in Section 4.6, where the coincidence rate detected will follow the lower intensity signal.

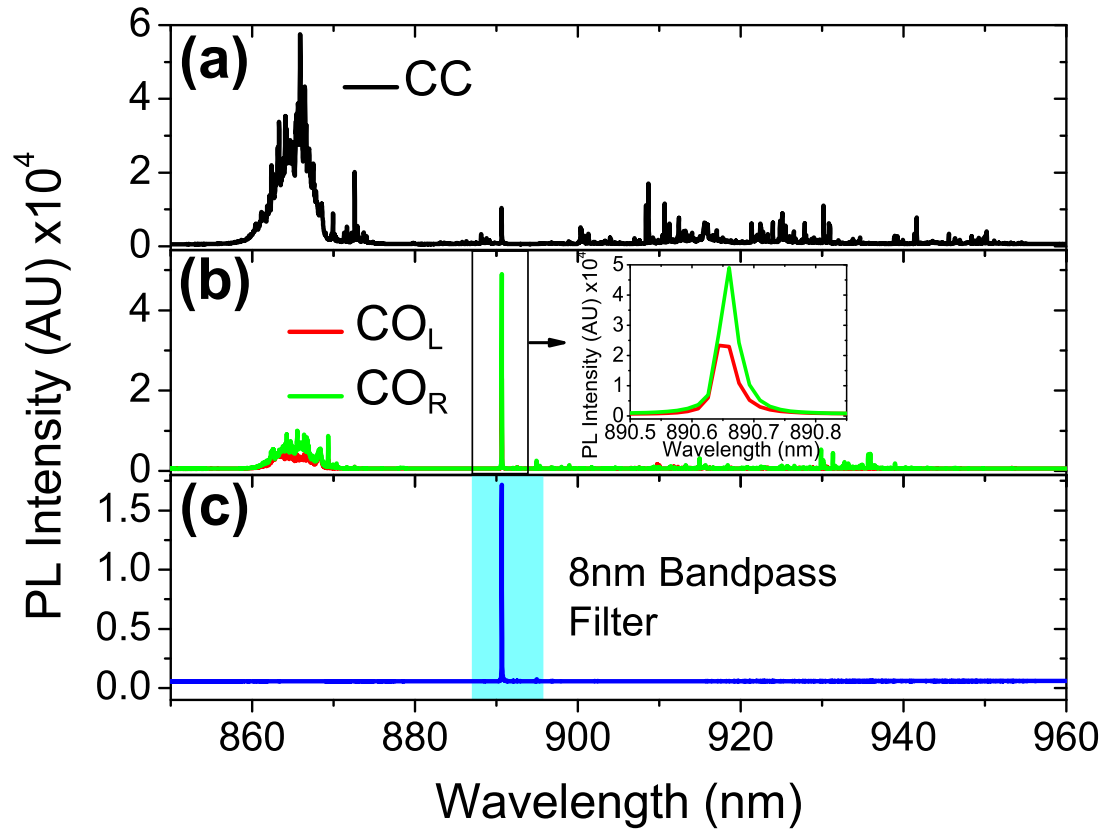


Figure 6.8: (a) Low power PL spectrum taken using CC configuration. (b) Low power PL spectrum taken using CO_L and CO_R configuration. (inset) Single QD emission line filtered and split between waveguide outputs by WGM. (c) Low power PL spectrum as in (d), but with 8nm bandpass applied around QD emission line.

In addition to the QD at 890.6nm, other spectral features are seen in Figure 6.8(a). The wetting layer emission is attenuated by a factor ~ 3 compared to cavity collection, which can be attributed to filtering by the microdisk or absorption in the membrane. Due to the regular spacing of modes and the presence of higher order radial mode families the QD ensemble emission at 900-960nm is suppressed only where the QDs are not resonant with any WGMs. The intensity ratio between the coupled QD and ensemble is ~ 3 . Figure 6.8(c) shows the spectrum from one outcoupler when an 8nm bandpass filter is inserted which is centred on the coupled QD emission. The addition of a bandpass filter is necessary for any cross-correlation measurements taken from the outcouplers due to the presence of spectral features in the outcoupler spectra but within this bandwidth the microdisk is filtering the PL emission adjacent to the QD.

6.6 Future Work

6.6.1 Add-Drop Filters

The previous section has demonstrated a design for spectral filtering and splitting of single photon emission when the QD is embedded within the cavity. However, for other quantum optical circuits the QD emission occurs elsewhere in the circuit and the guided photons must be filtered prior to on-chip detection. For this scheme, a passive filter must be used which only transmits specific wavelengths from QD emission elsewhere in the circuit. WGM resonators offer a solution for this problem if a second waveguide is introduced.

In an all-pass filter, destructive interference occurs at the coupling region between the input/output waveguide producing notches in the transmission spectrum at resonance with the WGMs. If a second waveguide is added to the device on the opposite side of the cavity to the input waveguide (Figure 6.9(a)) the cavity modes can couple to both waveguides. In the absence of any driving fields in the output waveguide no interference occurs and the transmission of the second waveguide is high at resonance. The optical power is essentially taken from the input waveguide and ‘dropped’ to the second waveguide; hence this device is

referred to as an ‘add-drop’ filter [182, 186, 189, 194–196]. Figure 6.9(b) plots the simulated transmission through the input waveguide (through) and the drop waveguide as a function of cavity-waveguide separation. For $S = 110\text{nm}$, the minimum transmission through the input waveguide, $T_{min} = 0.002$ whilst the maximum transmission to the second waveguide, $D_{max} = 0.928$: $T_{min} + D_{max} \neq 1$ due to scattering losses from the microdisk. The index matching between the cavity and waveguide modes is investigated in Figure 6.9(c) by varying the waveguide width. Minimum transmission through the input waveguide and maximum transmission to the output waveguide is achieved for $W = 220\text{nm}$. The simulated transmission spectrum for an add-drop filter with $S = 110\text{nm}$ and $W = 220\text{nm}$ is presented in Figure 6.9(d). The amplitude of the higher order radial modes is greater than those observed for the all-pass filter, which act to reduce the FSR of the add-drop filter. A scheme to improve the filter rejection is discussed in the next section.

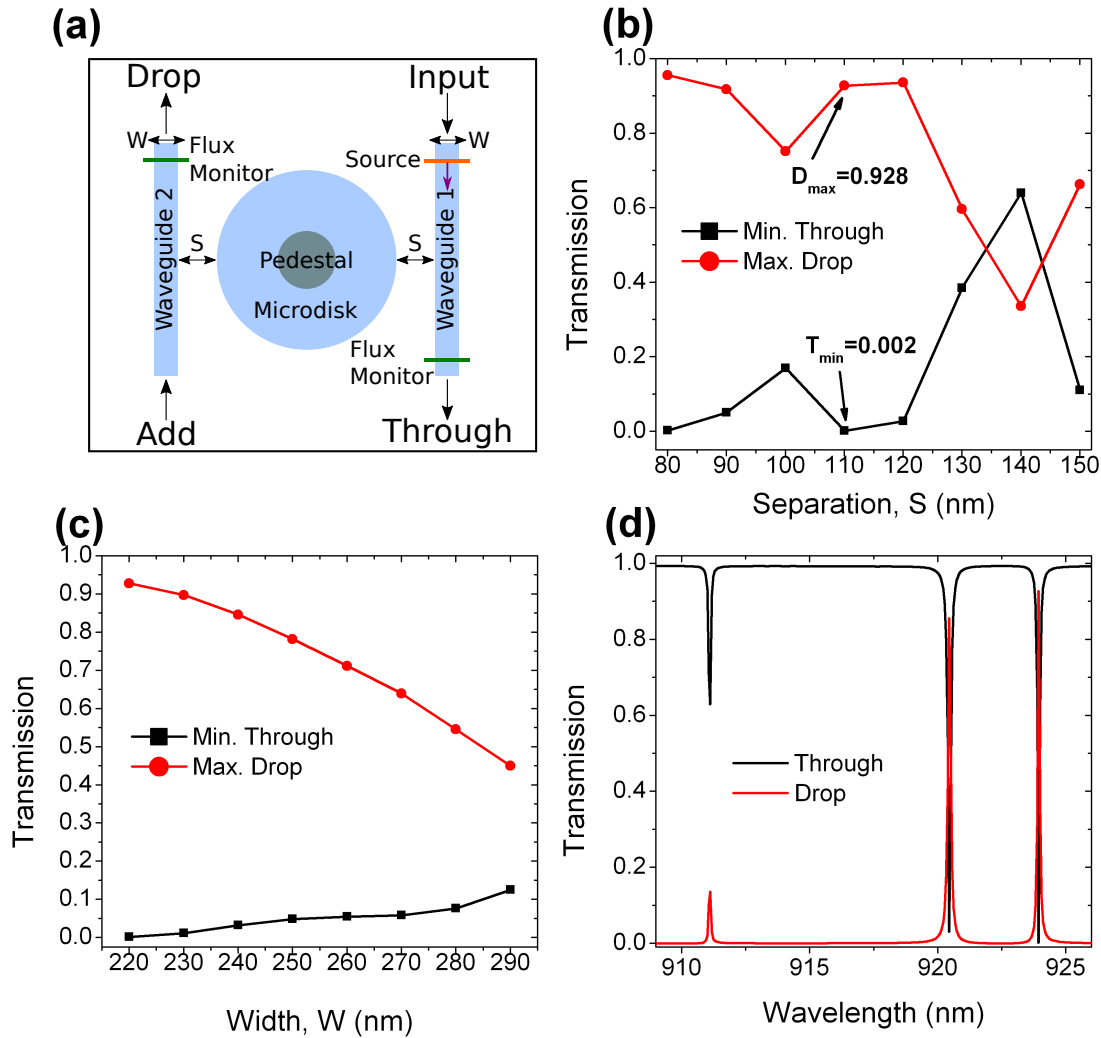


Figure 6.9: FDTD simulation results for add-drop filter using a microdisk resonator with $r = 1.5\mu\text{m}$. (a) Schematic of simulated structure. (b) Minimum transmission through the input waveguide and maximum transmission through the drop waveguide as a function of cavity-waveguide separation for $(23,1)$ mode. (c) Minimum transmission through the input waveguide and maximum transmission through the drop waveguide as a function of waveguide width for $(23,1)$ mode. (d) Simulated waveguide transmission spectrum for $S = 110$ nm and $W = 220$ nm.

6.6.2 Add-Drop Filters using Ring Resonators

The use of an add-drop filter design provides functionality for spectral filtering by separation of light at particular wavelengths between separate waveguides. The use of microdisks as the filter has limited benefit for filtering due to the presence of higher order radial modes reducing the FSR of the filter. In this section, the proposal for an add-drop filter using a single-radial mode family resonator is presented.

As presented in Section 6.2.1, optical WGMs are confined radially by total internal reflection at the outer dielectric interface. However, the modes are also confined from the inner edge by a caustic boundary, beyond which the ‘optical inertia’ is too great to sustain the mode [38]. The caustic radius is illustrated in Figure 6.10 as the curved potential section for $r < 2.5\mu\text{m}$. The modes are therefore confined within a potential well between the inner caustic and outer dielectric radii as illustrated in Figure 6.10. The caustic radius decreases with radial mode index p and therefore higher p modes penetrate further into the disk. Therefore if an inner dielectric boundary is introduced only those modes whose caustic radius exceeds this inner dielectric radius will be confined to the resonator.

Such a device is known as a ring resonator and resembles a nanobeam waveguide bent into a loop. The dashed lines in Figure 6.10 shows the dielectric radii required to produce a ring resonator which confines only a single radial mode family. Since the resonator is air-clad it still requires a supporting pedestal of AlGaAs which is incompatible with a true ring resonator. To circumvent this, the microdisk center is only partially etched to form a ‘flywheel’ resonator as shown in Figure 6.11(a). The partially etched disk in the center of the resonator is optically thin at QD emission wavelengths so that no modes are sustained in this region: only the unetched ring around the edge of the disk confines light at these wavelengths. A transmission spectrum of an add-drop filter utilising a flywheel resonator with $2\mu\text{m}$ radius and ring width of 350nm is presented in Figure 6.11(b). The spectrum is composed of first order radial modes with reduced amplitude of the second order mode: higher order radial modes are not observed at all. As can be seen from the data, the FSR of $\sim 20\text{nm}$ is only governed by the first order radial modes and can be increased further by reducing the radius of the resonator: a factor

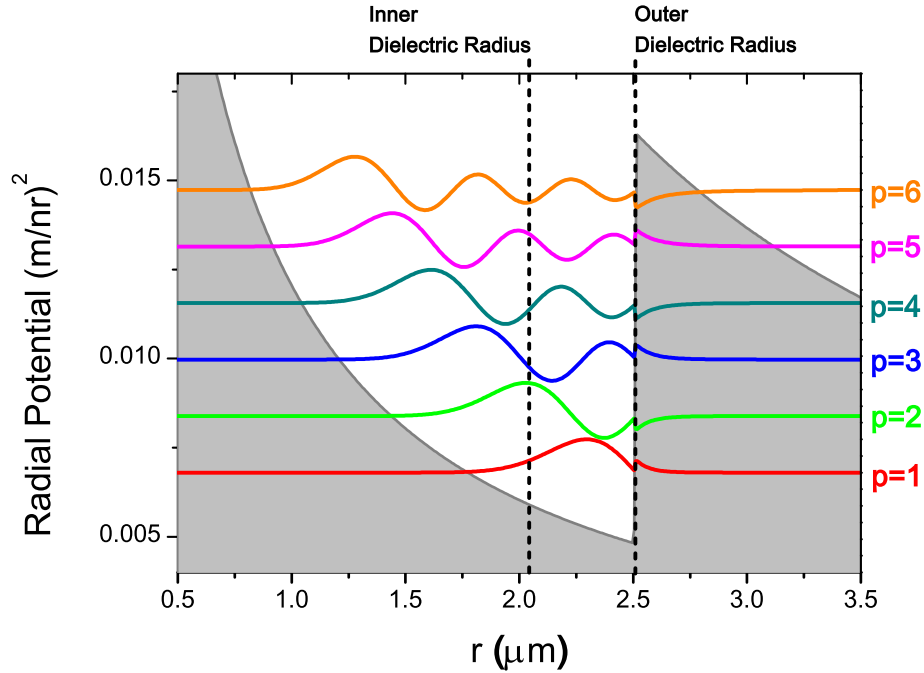


Figure 6.10: Confinement potential of microdisk resonator and confined modes labelled according to the radial mode index, p . Inner and outer dielectric radii of ring resonator are shown in dotted lines.

of 5 improvement over the FSR of the microdisk. Such a device is better suited towards on-chip filtering techniques using QDs due to this increased free spectral range. At the time of writing, these devices are in the process of fabrication by Dr. Ben Royall.

6.7 Summary

In conclusion, the splitting and spectral filtering of photon emission from a single QD has been demonstrated using a monolithic waveguide coupled microdisk device. From FDTD simulations, the device parameters were optimised to produce critical coupling in the QD PL band. Using photoluminescence spectroscopy measurements, the splitting and filtering of the QD emission between two waveguide outputs was shown.

Proposals for future work were also presented for improved filter rejection through the use of add-drop filters and ring-resonator designs.

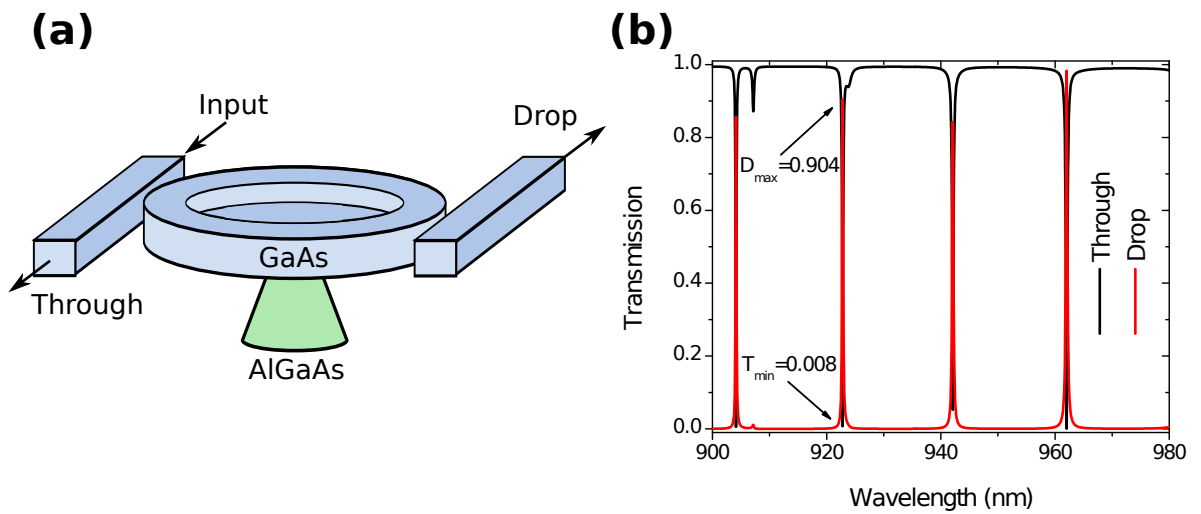


Figure 6.11: (a) Schematic of add-drop filter using 'flywheel' resonator with $r = 2\mu\text{m}$. (b) Simulated waveguide transmission spectrum for the device in (a) with $S = 80\text{nm}$ and $W = 220\text{nm}$.

Chapter 7

Towards Broadband Spontaneous Emission Enhancement of Single Quantum Dots in Photonic Crystal Waveguides

7.1 Introduction

This chapter investigates the spontaneous emission enhancement of a single quantum dot (QD) coupled to a photonic crystal waveguide for the purpose of producing a broadband indistinguishable single photon source. Spontaneous emission enhancement of the QD via slow light phenomena over a broadband range is studied using eigenmode simulations. Two designs of waveguides with a modified dispersion profile engineered to produce ‘flatband’ slow light are presented for this purpose. Finally, preliminary experimental measurements of the radiative lifetimes of emitters within the waveguide are presented.

7.2 Overview

For quantum information processing with photons, the photons must be indistinguishable [15]. Furthermore, one of the key challenges associated with all-optical quantum computing is the realization of a high-efficiency single photon source. The two level system of a QD presents an ideal candidate for a deterministic single photon source due to atomic-like emission single-photon lines [49, 87] which can be excited by electrical [197] or optical pumping [42] and can be readily integrated into semiconductor optical circuits. However, for this system to be usable as an indistinguishable single photon source, the QD coherence needs to approach the lifetime limited regime. The QD coherence time is given by

$$\frac{1}{T_2} = \frac{1}{2T_1} + \frac{1}{T_2^*} \quad (7.1)$$

where T_1 and T_2^* are the radiative lifetime and pure dephasing time (i.e. not due to population decay) of the QD, respectively [70]. For indistinguishable single photon emission, the radiative lifetime must dominate over the dephasing time in determining the coherence time, when $T_2 \sim 2T_1$. For the neutral exciton of a typical InAs QD in bulk GaAs $T_1 \sim 1ns$ and $T_2 \sim 400ps$: the emitted photons are distinguishable due to dephasing [148]. Whilst it is extremely difficult to completely eliminate dephasing processes and increase T_2^* it is possible to reduce the radiative lifetime so that the photon is emitted before the exciton experiences significant dephasing. By incorporating the QD into a photonic structure with an increased photon local density of states (LDOS), the radiative lifetime is shortened due to the Purcell effect. To achieve indistinguishability, $T_1 \sim T_2/2 = 200ps$ corresponding to a Purcell factor of ~ 5 [148].

The Purcell effect is greatest when the QD is placed at the antinode of a photonic cavity with small mode volume, such as a photonic crystal cavity. However, this imposes restrictions on the spatial and spectral coincidence of the QD with the cavity mode. It is therefore desirable to have a photonic structure in which the QD experiences a Purcell enhancement over a broadband spectral range with large tolerance to the position of the QD [76, 77, 79, 198]. The slow light region of a photonic crystal waveguide mode provides such an environment since

the slow light region of the photonic crystal waveguide occurs over a much broader range than a cavity resonance. Furthermore, since the waveguide is a linear defect with discrete translational symmetry, efficient QD coupling can be achieved at many locations along the waveguide axis rather than at a single specific location as with a cavity defect. In addition, due to the low group velocity of the waveguide mode in the slow light regime, high coupling efficiencies (β -factors) can be achieved over a large area within each unit cell of the photonic crystal waveguide.

7.3 Theoretical Background

As presented in Section 1.2.2, the W1 photonic crystal waveguide supports a series of propagating modes confined to the high index material of the slab. Due to an anticrossing with the ‘index-guided’ mode at the top of the dielectric band, the ‘gap-guided’ mode at the bottom of the photonic bandgap exhibits a reduction in group velocity ($d\omega/dk$) as it nears the edge of the Brillouin zone as shown in Figure 7.1. Termed the ‘slow light’ region of the dispersion curve, group velocities as low as $\sim 10^{-3}c$ can be attained, leading to a longer interaction time between the waveguide mode and the material comprising the waveguide [73].

Using a Dyadic Greens Function approach [75] the Purcell enhancement experienced by a dipole emitter embedded within the waveguide has been shown by Manga Rao et al. to be given by

$$F_P(r) = \frac{3\pi c^3 a |\mathbf{e}_k(r) \cdot \hat{\mathbf{n}}|^2}{\omega^2 \sqrt{\epsilon} v_g} \quad (7.2)$$

where a is the lattice constant of the photonic crystal, v_g and $\mathbf{e}_k(r)$ are the group velocity and electric field of the propagating mode respectively, ϵ is the dielectric constant of the waveguide and ω is the angular frequency of the QD.

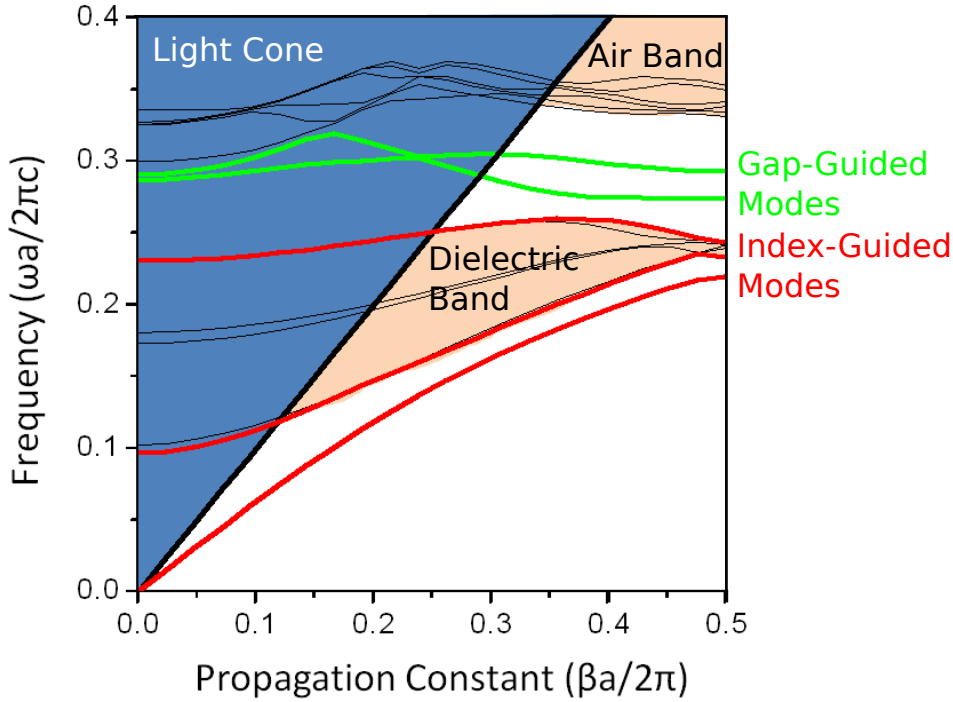


Figure 7.1: Dispersion curve for a W1 photonic crystal waveguide. An anticrossing is observed within the photonic bandgap between the first gap-guided mode and the last index-guided mode of the dielectric band.

For a co-polarised QD positioned at an antinode of the modal fields, Equation 7.2 reduces to

$$F_P = \frac{3\pi c^3 a}{V_{eff} \omega^2 \epsilon^{3/2} v_g} \quad (7.3)$$

where the effective mode volume V_{eff} is calculated using

$$V_{eff} = \frac{\int \epsilon(r) |\mathbf{e}_{\mathbf{k}}(r)|^2 \mathbf{d}\mathbf{r}^3}{\max(\epsilon(r) |\mathbf{e}_{\mathbf{k}}(r)|^2)} \quad (7.4)$$

The group index ($n_g = c/v_g = c \frac{dk}{d\omega}$) exhibits a monotonic increase as it approaches the band edge (black line, Figure 7.3(b)) with a corresponding dependence of the Purcell factor (black line, Figure 7.9(c)). Near the band edge, where the Purcell enhancement is greatest, the group velocity dispersion (GVD) is very large so that a small change in wavelength produces a large change in Purcell enhancement of an emitter in the waveguide. This highly dispersive

characteristic is undesirable, so to address this schemes have been proposed whereby the waveguide dispersion is modified by displacing the holes in the first two rows of holes adjacent to the waveguides [199, 200]. These modifications produce a region of low GVD by adjusting the anticrossing between the 'index-guided' and 'gap-guided' waveguide modes.

7.4 Dispersion Modification using Lateral Hole Displacement

The first technique reported by Li et al. displaces the first two rows of holes in the photonic crystal adjacent to the waveguide in a direction transverse to the waveguide axis [199], as illustrated in Figure 7.2. Since the 'index-guided' and 'gap-guided' modes are confined to the high index material in the waveguide, both are sensitive to changes in the positions of the holes adjacent to the waveguide. Displacing the first two rows of holes adjusts the relative dispersion between these modes and using appropriate displacements can produce a region of 'flatband' slow light in which both the group velocity and GVD are small.

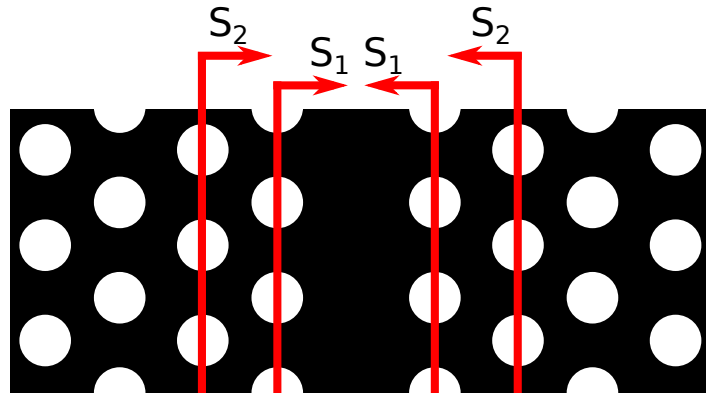


Figure 7.2: Schematic defining the lateral displacements applied to the first and second row of holes adjacent to the waveguide.

Using the displacement values from [199] the dispersion curves were calculated using MIT Photonic Bands (MPB) [54] and the results of these simulations are shown in Figure 7.3. The calculated dispersion curves in Figure 7.3(a) compare the dispersion of the unmodified W1 waveguide to four designs of modified waveguides. The unmodified W1 dispersion exhibits a

continuous change in gradient, whereas for the modified waveguides a region of constant slope of varying bandwidth can be observed. Figure 7.3(b) shows the calculated group index for the same waveguide parameters as Figure 7.3(a). Flatband regions where the group index varies by less than 10% can clearly be seen, which vary in magnitude and bandwidth for different waveguide displacement parameters.

The Purcell factor for these waveguides is plotted in Figure 7.3(c). In the ‘flatband’ region, the Purcell factors exceed 5 for most of the modified waveguide designs. The bandwidth of these regions are several nanometers wide, demonstrating the advantage of this method over resonant cavity systems where typical cavity linewidths are sub-nanometer.

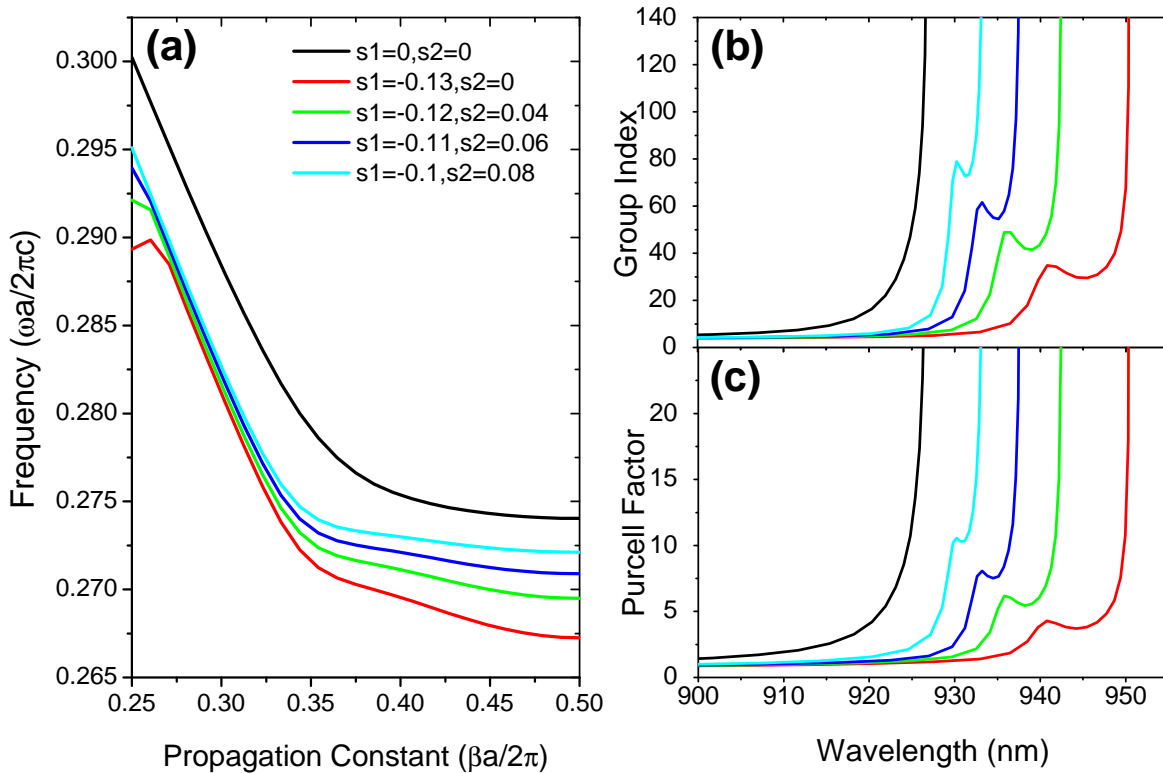


Figure 7.3: (a) Dispersion curves and (b) group index of the fundamental gap-guided mode of photonic crystal waveguides with laterally displaced holes. (c) Calculated Purcell factor for a dipole placed at an antinode of the modal fields.

To investigate the experimental performance of the waveguides, devices were fabricated using the method outlined in Section 2.3.2. The waveguides were fabricated on a 140nm air-clad GaAs membrane using the parameters given above with a lattice constant of $a=243\text{nm}$ with grating outcouplers added to the ends of the waveguide. For characterisation of the waveguides, the QD ensemble was excited non-resonantly using a 850nm CW Ti:Sapphire laser above the QD saturation power and PL collected from one of the outcoupler gratings. An SEM image of a typical waveguide with outcoupler gratings is shown in Figure 7.4.

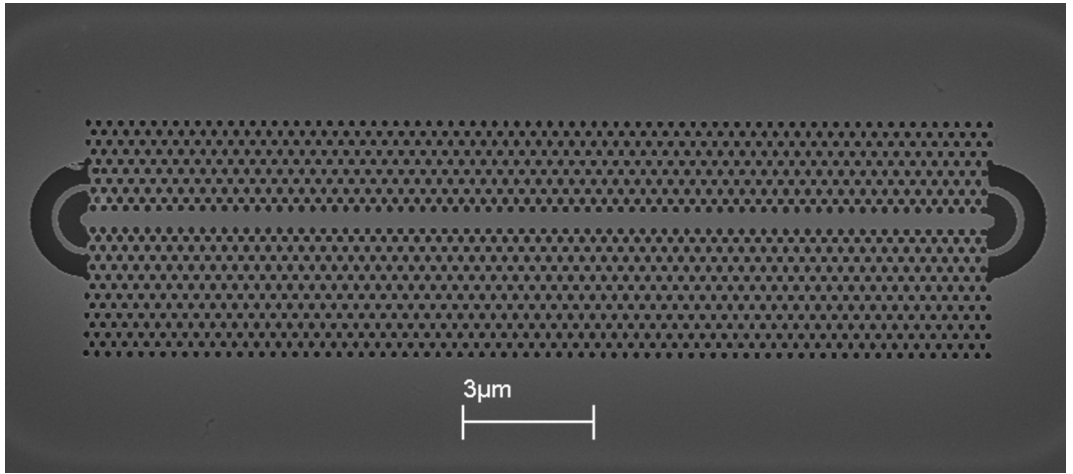


Figure 7.4: SEM image of a photonic crystal waveguide with transverse displacement applied to the two rows of holes adjacent to the waveguide. Outcoupler gratings are added to the waveguide ends to scatter light out of the device plane.

The PL spectrum of an unmodified W1 waveguide is shown in Figure 7.5(a). As observed in [148], the finite reflectivity of the outcoupler gratings cause the formation of Fabry-Perot modes within the waveguide. Extraction of the group index is possible from these Fabry-Perot resonances using $n_g = \lambda_0^2 / 2\Delta\lambda L$ where λ_0 is the centre wavelength of a Fabry Perot resonance, $\Delta\lambda$ is the free spectral range (FSR) and L is the cavity length. The group index dispersion (GID) obtained from the spectrum in Figure 7.5(a) is plotted alongside the calculated GID from simulation in Figure 7.5(b). There is good agreement between the two, confirming the accuracy of this method of obtaining the GID from experiment.

The experiment was repeated for a range of waveguides with modified dispersion. The

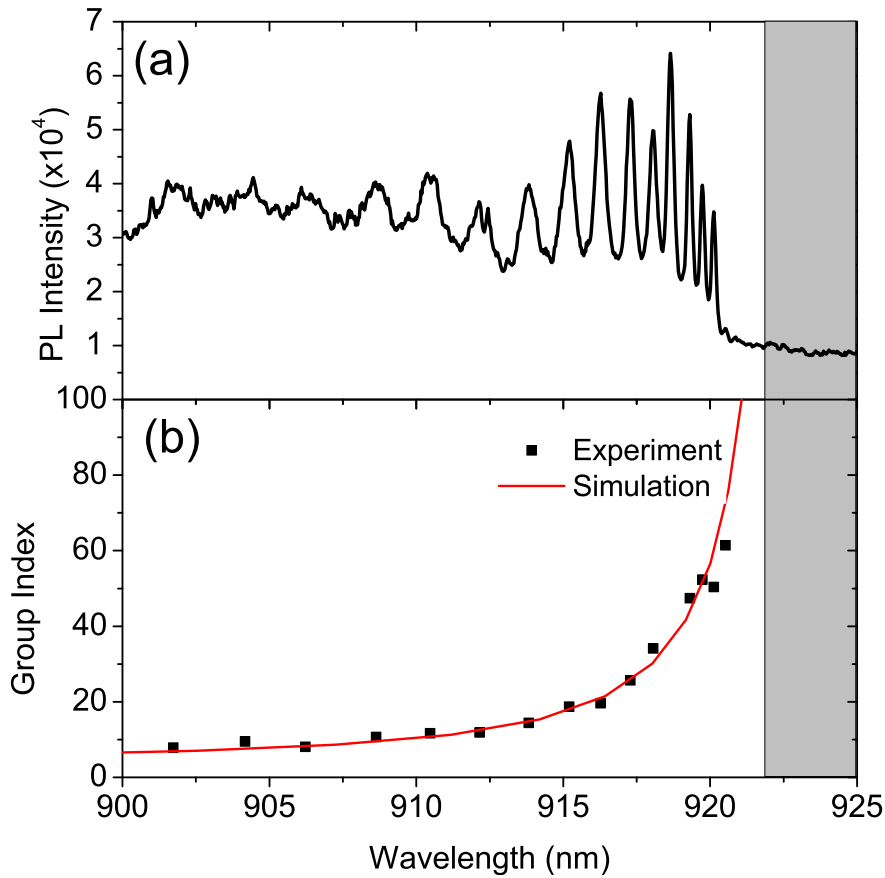


Figure 7.5: (a) Photoluminescence spectrum of an unmodified W1 photonic crystal waveguide. (b) Extracted group index of the waveguide (black points) mode with simulated group index (red). The waveguide cut-off region is highlighted in grey.

PL spectrum obtained for the device with $s_1 = -0.13a$, $s_2 = 0$ is shown in Figure 7.6(a) and the extracted GID is compared to simulation in Figure 7.6(b). The simulated curve presented is for a device with increased hole radius ($r = 0.31a$) to reflect the slight overetching of the waveguides used in experiment, producing the peak in group index around 933nm. The bandwidth and group index of the ‘flatband’ region agrees well with simulation. However there is a notable departure from the theoretical curve around 920nm. Analysis of the dispersion curve for this waveguide reveals the cause of the peak in group index for the modified waveguide. As shown in Figure 7.7, the band edge of the second ‘gap-guided’ mode is spectrally coincident with the first ‘gap-guided’ mode in a region of low group index. The second mode also exhibits

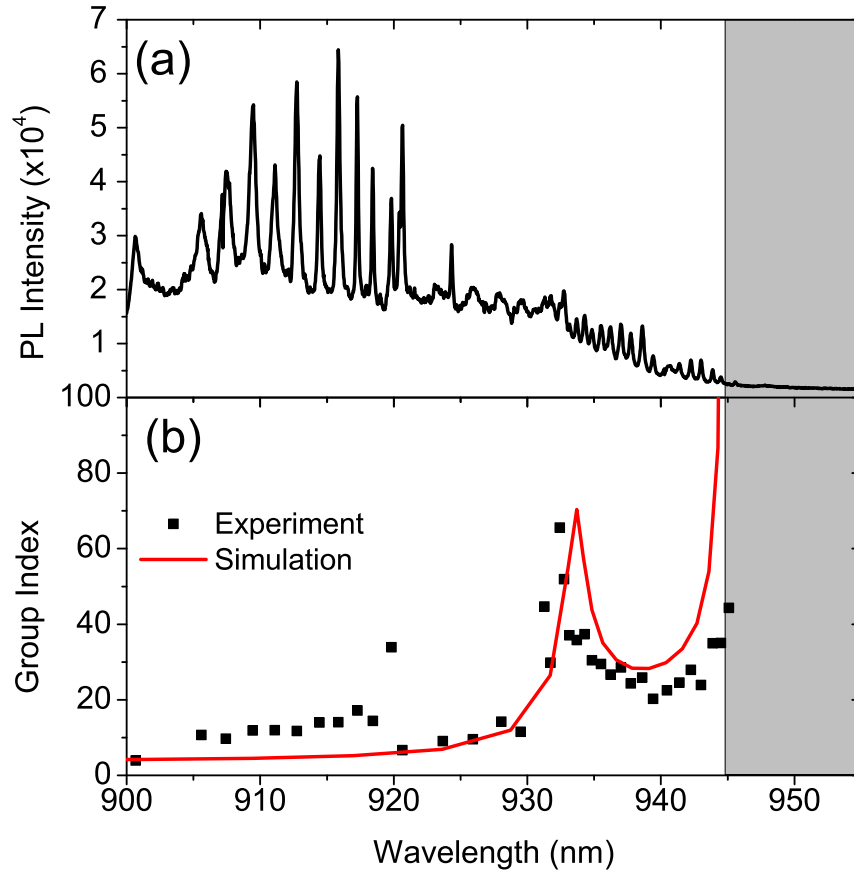


Figure 7.6: (a) Photoluminescence spectrum of a W1 photonic crystal waveguide with the $s_1=-0.13a$, $s_2=0$. (b) Extracted group index of the waveguide (black points) mode with simulated group index (red). The waveguide cut-off region is highlighted in grey.

a slow light region towards the edge of the Brillouin zone, which manifests as a peak in the extracted GID where both modes are excited by ensemble QD PL. This effect is also visible in the PL spectrum of Figure 7.6(a) as bunching of the Fabry Perot modes up to 920nm. The manifestation of this effect is due to the displacement of the adjacent holes of the photonic crystal waveguide laterally outwards which acts to redshift the guided modes. The second mode experiences a greater degree of spectral shift than the first mode and as the holes are displaced the spectral separation is reduced until the band edge of the second gap-guided mode overlaps with the first mode as shown in Figure 7.7. In an unmodified W1 waveguide, the modes do not spectrally overlap beneath the light line.

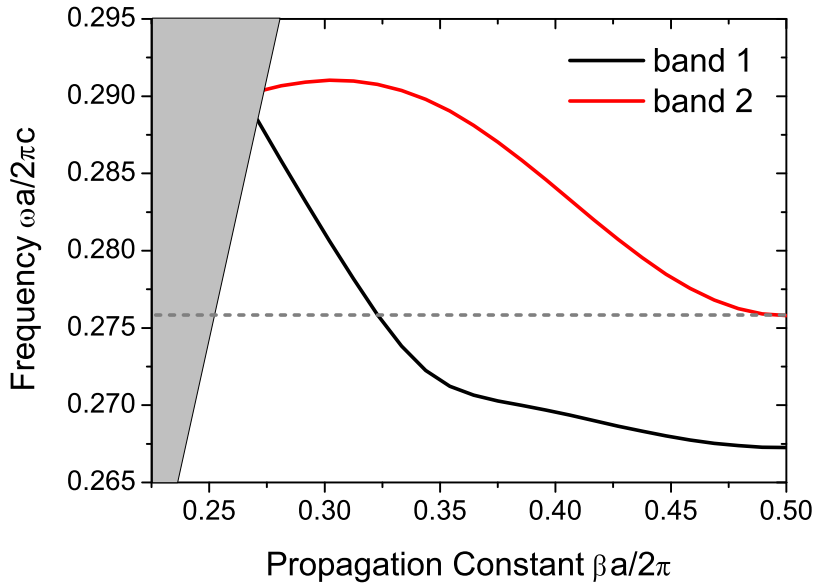


Figure 7.7: Dispersion curves for the first and second guided modes of a photonic crystal waveguide with $s_1=-0.13a$, $s_2=0$, calculated using MIT Photonic Bands (MPB) [54]. Grey dashed horizontal line shows the frequency of the band edge of the second mode.

7.5 Dispersion Modification using Longitudinal Hole Displacement

The second method employed for achieving broadband Purcell enhancement in photonic crystal waveguides was to displace the first row of holes adjacent to the waveguide longitudinally and the second hole row laterally, following the designs presented by Liang et al. in [200] as defined in Figure 7.8. This method maintains the effect of producing a broadband region of low GVD but since the waveguide width is not modified substantially the spectral separation of the two ‘gap-guided’ modes is expected to be maintained.

The calculated dispersion curves for waveguides modified using this method are shown in Figure 7.9(a), from which the ‘flatband’ region can be observed. The group index for these devices is shown in Figure 7.9(b) which again demonstrates that the ‘flatband’ region spans several nanometers of spectral width. Figure 7.9(c) plots the calculated Purcell factor for

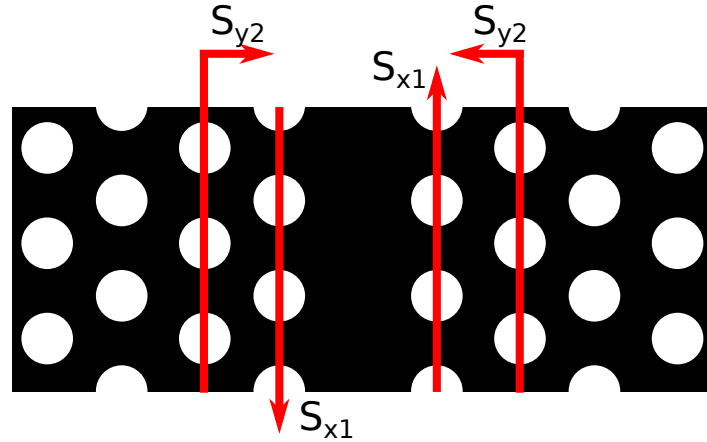


Figure 7.8: Schematic defining the longitudinal and lateral displacements applied to the first and second row of holes adjacent to the waveguide respectively.

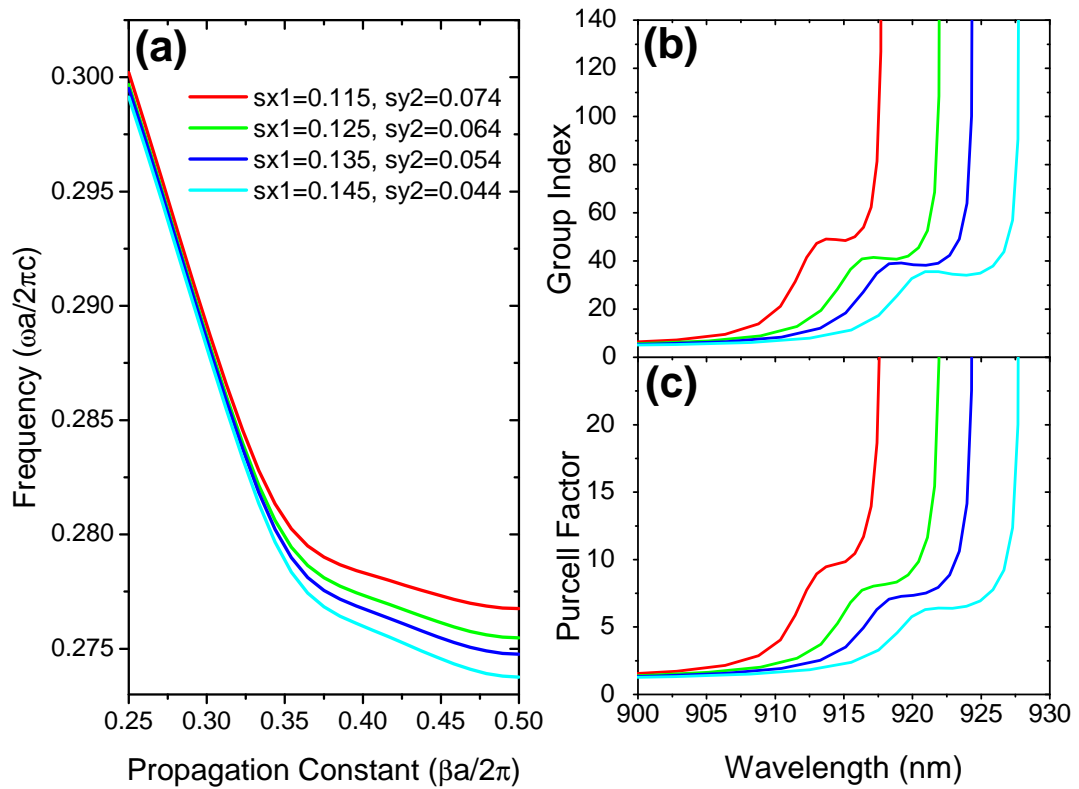


Figure 7.9: (a) Dispersion curves and (b) group index of the fundamental gap-guided mode of photonic crystal waveguides with lateral and longitudinal hole displacement. (c) Calculated Purcell factor for a dipole placed at an antinode of the modal fields.

these waveguides where $F_P > 5$ within the ‘flatband’ region for all devices.

It is apparent from comparison of Figures 7.9(b) and (c) with Figures 7.3(b) and (c) that the Purcell factor achieved for a given group index for waveguides with longitudinal hole displacement exceeds that for a waveguide with lateral hole shifts by $\Delta F_P \sim 3$: this comparison is shown in Figure 7.10(b). Comparison of the calculated mode volumes for the two waveguides illustrated in Figure 7.10(a) reveals that the effective mode volume for the case of longitudinal shifts is always lower than for lateral shifts. The cause of this effect is clear: since the holes are displaced longitudinally, the overall waveguide width is not modified significantly which preserves an effective mode volume, V_{eff} , comparable to the unmodified W1 waveguide. Referring to Equation 7.3 where the mode volume appears in the denominator and all other quantities are equal, a smaller mode volume produces a greater Purcell factor for a given group index in the waveguides with longitudinal hole shifts.

The PL spectrum is shown for a waveguide with $s_{x1} = 0.145a$, $s_{y2} = 0.044a$ in Figure 7.11(a) where the Fabry-Perot modes are again observed to have a reducing FSR and linewidth as the band edge of the waveguide is approached. Figure 7.11(b) plots the group index $n_g = \lambda_0^2/2\Delta\lambda L$ obtained from the data of Figure 7.11(a) for this waveguide against the group index spectrum obtained from simulation. The flatband is observed with $n_g \approx 40$ over $\sim 3\text{nm}$ up to 930nm. Unlike the waveguides with lateral hole displacement, the group index peak due to the second guided mode is not observed since the waveguide width is not altered significantly in these designs.

To investigate the degree of spontaneous emission enhancement the laser excitation power is lowered to 500nW, below the QD saturation power, so that individual emission lines can be observed. Lifetime measurements were performed using a 100 fs pulse duration Ti:Sapphire laser to obtain the radiative lifetime of the QDs as a function of wavelength. Figure 7.12(a) shows the lifetime histogram spectrum obtained from time-resolved measurements of the QD PL. The data were obtained by passing the PL through a 0.55m monochromator onto a fibre-coupled avalanche photodiode (APD) and scanning the diffraction grating to record a lifetime histogram over a range of wavelengths: the method is detailed further in Section

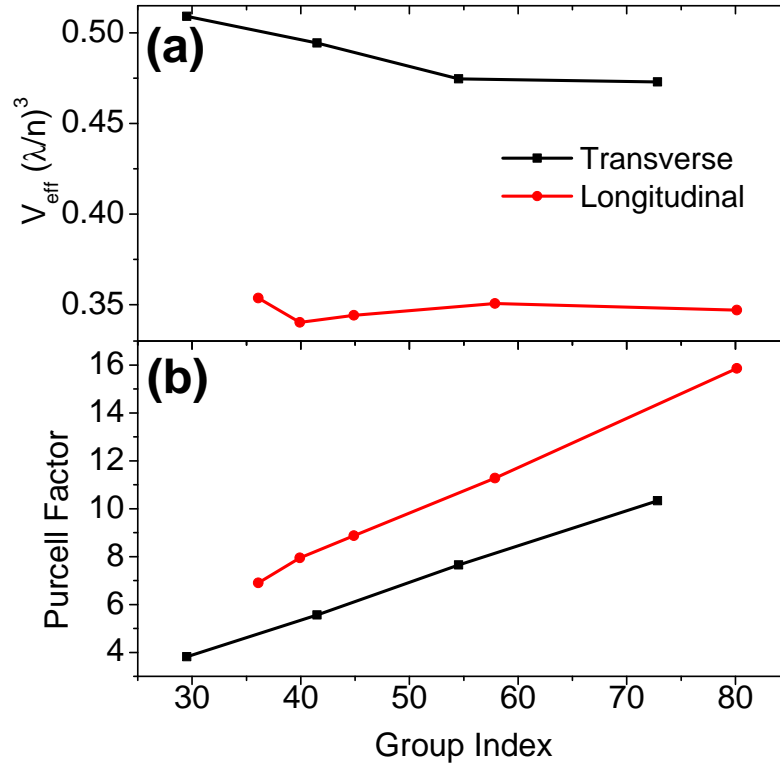


Figure 7.10: Comparison of the (a) effective mode volume V_{eff} and (b) Purcell factor for photonic crystal waveguides with transverse and longitudinal hole shifts taken at the centre of the 'flat band' region of the waveguide dispersion.

2.3.5. The QD ensemble PL spectrum is shown in Figure 7.12(b), taken from the APD. Fitting the decay curve of the histogram at each wavelength allows extraction of the radiative lifetimes, which are plotted in Figure 7.12(c). As can be seen from the data, there is a clear trend of reducing radiative lifetimes for increasing emission wavelength. Assuming a radiative emission lifetime for the QD of 1ns, the measured decay times for QDs in the waveguide are on average longer than those predicted by simulations by ~ 200 ps which may be attributed to random spatial distribution of the QDs: misalignment from the antinode of the modal fields reduces the maximum Purcell enhancement attainable as shown in Figure 7.12(c). These simulations were performed by calculating the Purcell factor over a unit cell of the photonic crystal waveguide [75] and averaging to estimate the enhancement of a randomly positioned QD within the waveguide. Three cases of QD position range were considered: QDs randomly

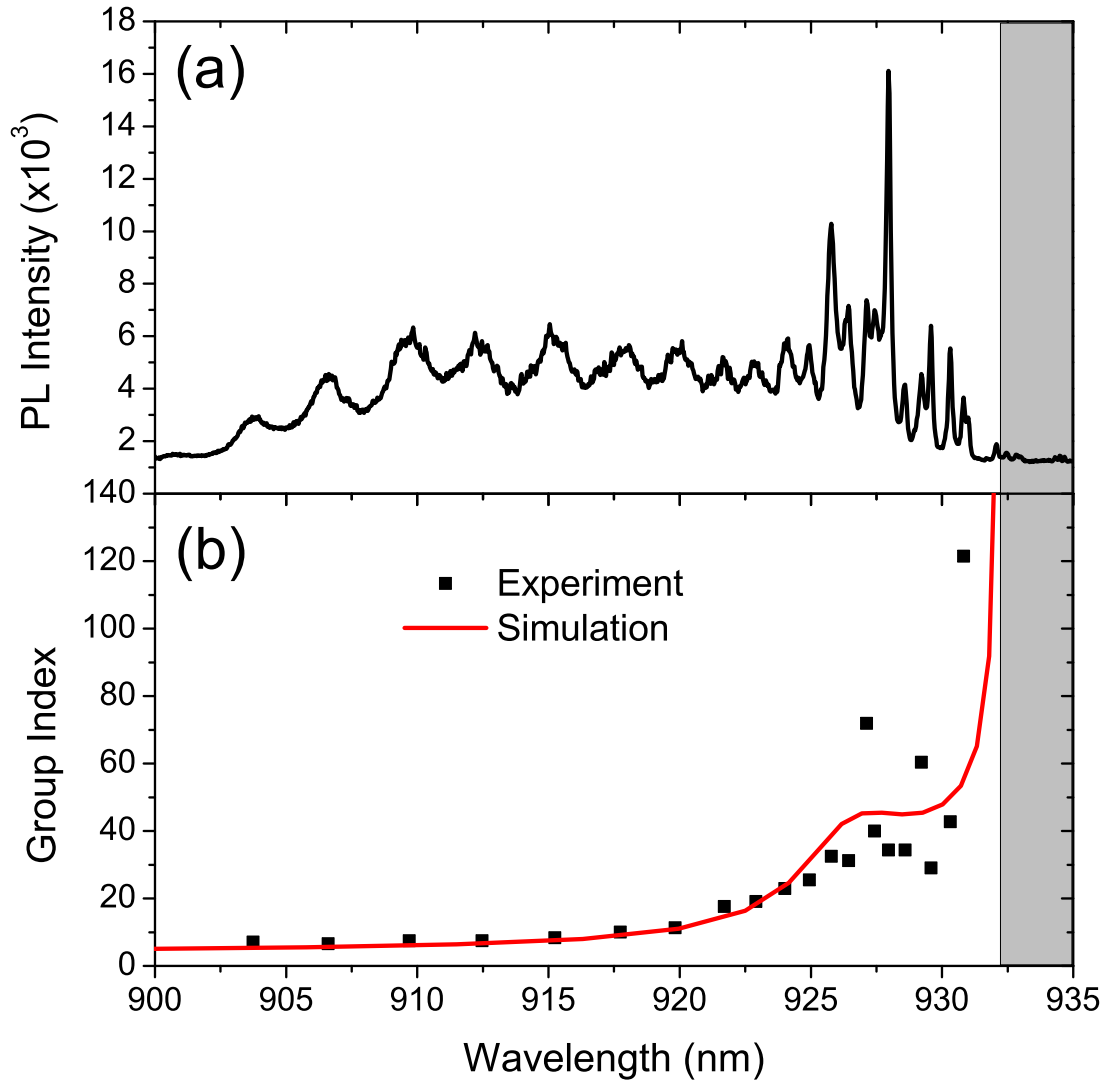


Figure 7.11: (a) Photoluminescence spectrum of a W1 photonic crystal waveguide with $s_{x1} = 0.145a$, $s_{y2} = 0.044a$. (b) Extracted group index of the waveguide (black points) mode with simulated group index (red). The waveguide cut-off region is highlighted in grey.

arranged within the waveguide core, QDs randomly arranged up to the first two rows of holes (including the core) and QDs located at the modal field antinodes. The waveguide mode is confined within these areas and therefore QD emission is not expected to be observed from the outcouplers for QDs outside of these regions. However this does not take into account the effects of the Fabry-Perot resonances.

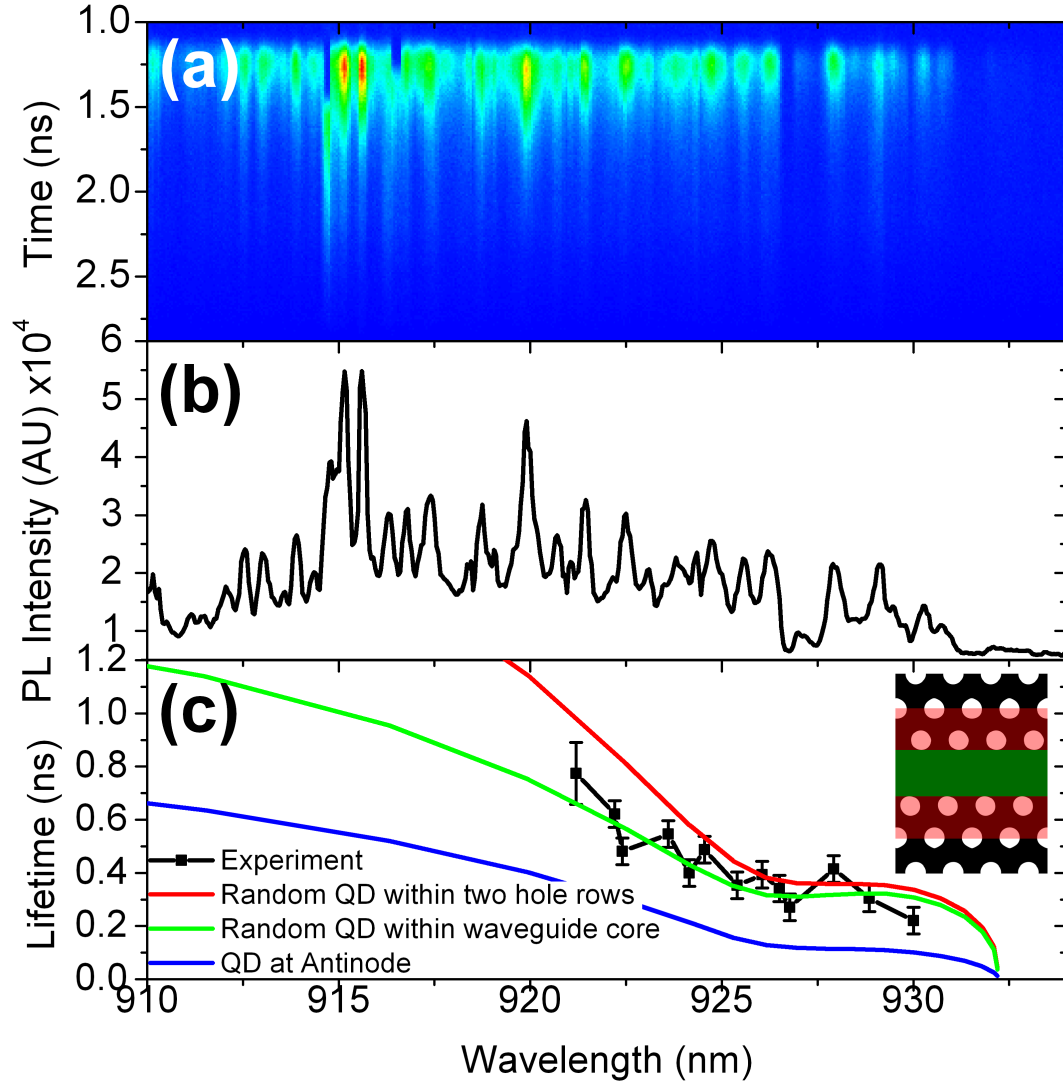


Figure 7.12: (a) Time-resolved PL emission, (b) PL spectrum from the APD and (c) radiative lifetimes of quantum dots in a photonic crystal waveguide with $s_{x1} = 0.145a$, $s_{y2} = 0.044a$ from experiment (black) from simulations where the QD is always at the field antinode (blue) and an average for randomly positioned QDs within the first two rows of holes (red) and within the waveguide core (green). (Inset) schematic showing regions of waveguide where QD lifetimes were estimated from simulation. A bulk lifetime of 1ns was assumed.

Due to a low signal:noise ratio in the measured PL signal, it is unclear whether the lifetime dependence of Figure 7.12(c) is solely due to the emission of single QDs, but also possibly from contribution from unresolved background emission.

7.6 Discussion and Future Work

As stated in the last section, due to limits on spectral and temporal resolution of the detection system used for experiment, it cannot be concluded unambiguously that the Purcell enhancement of single QDs was observed, although the trend is consistent with simulation and experiments from other researchers [76, 77, 79].

These results do indicate that the principle of the device is sound. However improvements must be made to the experimental apparatus and sample for future attempts at clear demonstration. Firstly a sample with a lower QD density will increase the spectral separation between emission lines of different QDs, which should increase the signal to noise ratio. Secondly, upgrades and enhancements made to the experimental apparatus since this work have improved the overall light collection efficiency to further improve the reliability of time-resolved measurements in these devices.

Chapter 8

Conclusions and Future Directions

8.1 Summary

This thesis has focussed on a number of devices and principles that are relevant to the development of integrated quantum optical circuits using III-V semiconductors and SAQDs.

Chapter 1 introduced the general principles of quantum information processing and the associated physics for implementation using SAQDs in III-V semiconductor photonic systems.

Following this introductory chapter, Chapter 2 contained the details of the computational, experimental and fabrication methods used to perform the measurements presented in the experimental chapters of the thesis.

Chapter 3: Waveguide Coupled Photonic Crystal Cavity for Quantum Dot Spin Readout

Chapter 3 presented a proposal for an on-chip spin-photon interface using which-path encoding by embedding a SAQD in the center of an unpolarised optical cavity which was selectively coupled to separate waveguides. The selectivity of the device was demonstrated using FDTD simulations and ensemble QD photoluminescence (PL) experiments. Demonstration of single photon routing using electrical control of the SAQD was also made.

Chapter 4: Monolithic Integration of a Quantum Emitter with an On-Chip Beam-Splitter

This chapter demonstrated a directional coupler using III-V materials, a key component of any quantum optical circuit, with embedded quantum emitters. The device was demonstrated to operate at the single photon level for correlation measurements between the two output ports of the coupler using an embedded SAQD at the input.

Chapter 5: Directional Readout of Single Quantum Dot Spins in Non-Chiral Photonic Waveguides

The principle of direct readout of single QD spin states in a non-chiral waveguide system was presented. The origin of directional emission of the QD was explained using FDTD and eigenmode solver simulations, and confirmed using SAQD PL experiments for two types of nanophotonic waveguides.

Chapter 6: On-Chip Spectral Filtering using Whispering Gallery Mode Resonators

This chapter explored the application of whispering gallery mode resonators (WGMs) to optical filtering applications in preparation for the incorporation of on-chip single photon detection. The on-chip filtering and splitting of emission from a single QD was demonstrated.

Chapter 7: Towards Broadband Spontaneous Emission Enhancement of Single Quantum Dots in Photonic Crystal Waveguides

This chapter presented the development towards broadband spontaneous emission enhancement of SAQDs in photonic crystal waveguides for realisation of on-chip indistinguishable single photon generation. Due to limits on spectral and temporal resolution of the detection system used for experiment, it could not be concluded unambiguously that the Purcell enhancement of single QDs was observed, although the observed behaviour was consistent with simulation and experiments from other research.

8.2 Outlook

A number of possible directions for future work leading on from the investigations in this thesis have been suggested at the end of each chapter. Where appropriate, details of simulations or preliminary experimental results were provided which have or may lead on to more long-term development. These proposals are aggregated and summarised in this section.

8.2.1 Chapter 3: Waveguide Coupled Photonic Crystal Cavity for Quantum Dot Spin Readout

Single Photon Routing using Electro-Optical Tuning

Further to the demonstration of selective coupling for a non-degenerate cavity, with application of an electric field across the device, tuning of the QD emission energy via the quantum confined Stark effect is possible. This additional control allows for the QD to be tuned from resonance with one cavity mode to the other mode. For a selectively coupled cavity, this facilitates the switching of QD emission from one waveguide to the other. Such a device may be used to form an electrically controlled single photon router, whereby single photons emitted by the QD can be switched between two output channels.

The principle of single photon routing is as follows. When the QD is off-resonance, the in-plane emission is suppressed as the QD emission lies within the photonic bandgap of the photonic crystal. When tuned into resonance with the first cavity mode, the QD emission rate is enhanced by the increased photon LDOS at resonance and the QD emits into this cavity mode with increased intensity. The QD is non-resonant with the second cavity mode and does not couple to it. Since the cavity is selectively coupled, the QD emission is channelled into the corresponding waveguide and is detected from one of the two waveguides. When the QD is tuned into resonance with the second cavity mode, the situation is reversed and the QD emission is transmitted into the other waveguide.

PL measurements presented in this chapter, submitted to Applied Physics Letters in March 2015 and to be presented in full in the thesis of C. Bentham, demonstrate the principle of single photon routing using a photonic crystal cavity selectively coupled to two waveguides,

whereby routing is controlled by electrical tuning of a QD between the cavity resonances.

8.2.2 Chapter 5: Monolithic Integration of a Quantum Emitter with an On-Chip Beam-Splitter

On-Chip Two-Photon Quantum Interference

This chapter demonstrated the on-chip splitting of single photons between two output ports of a directional coupler, which originate from a single QD. However, by incorporating two QDs into the directional coupler, such that one resides in each input waveguide it is possible to perform two-photon interference experiments on-chip. The principal challenges involved in realisation of such a device are ensuring that each QD is optimally positioned in each waveguide, achieving indistinguishability of the photons emitted by the QD and fine control of the splitting ratio of the directional coupler. Each of these challenges is currently being addressed by other researchers in the LDS group at the University of Sheffield. The ability to guarantee that the QDs are optimally located in the input waveguides is under investigation by J.E. Dixon and M.N. Makhonin via post-growth QD registration techniques. Fine control of the directional coupler can be realised using integrated electromechanical actuators, where around 100nm displacement is required to completely switch the transmission which is achievable using lateral electric fields [160]. This is currently under investigation by L. Wilson and Z. Bishop. Realisation of this device, currently being undertaken by J. O'Hara, C. Bentham and N. Prtljaga, is expected to demonstrate the functionality required for an on-chip Hong-Ou-Mandel experiment. It is expected that when the QDs are detuned from one another using the QCSE, no interference is observed and when tuned to resonance the Hong-Ou-Mandel dip is observed.

8.2.3 Chapter 5: Directional Readout of Single Quantum Dot Spins in Non-Chiral Photonic Waveguides

Increased Coupling Efficiency and Lifetime Limited Coherence

For the application of the chiral QD spin coupling to integrated quantum optics applications, there are several improvements which must be made to the system demonstrated in this chapter. The first is to improve the coupling efficiency of the QD to the propagating modes. For the ridge waveguide system, the total coupled power for a circularly polarised QD is $\sim 68.5\%$. Whilst the directionality of the emission is close to unity at the C-point (where the modal fields are locally circular) the QD coupling efficiency may be improved further. A scheme to overcome this is to use a resonant mode to increase the LDOS. This improves the coupling efficiency of the QD using the Purcell effect, which intrinsically reduces the radiative lifetime of the QD, potentially into the lifetime limited coherence regime. The degenerate, counter-propagating resonant modes of a whispering gallery mode (WGM) resonator closely resemble the propagating modes of the ridge waveguide system and may therefore be used to provide SE enhancement whilst maintaining directionality. The use of photonic crystal waveguides may also provide spontaneous emission enhancement for spin-readout applications when operating in the slow light regime.

Future applications for this technique include single photon logic elements and spin communication. Since the QD spin is coupled to photon states this arrangement can be used to transmit spin information on-chip. In addition, an optical switch may be realised if the QD spin states can be flipped using an ultrafast optical pulse [95], which modifies the transmission of the waveguide depending on the QD spin state. A similar demonstration is presented in [171] using microwave pulses to flip the QD spin states for realisation of an optical CNOT gate.

8.2.4 Chapter 6: On-Chip Spectral Filtering using Whispering Gallery Mode Resonators

Add-Drop Filters using Ring Resonators

The use of an add-drop filter design provides functionality for spectral filtering by separation of light at particular wavelengths between separate waveguides. The use of microdisks as the filter has limited benefit for filtering due to the presence of higher order radial modes reducing the FSR of the filter. The proposal for an add-drop filter using a ‘flywheel’ ring-like resonator was presented.

The partially etched disk in the center of the resonator is optically thin at QD emission wavelengths so that no modes are sustained in this region: only the unetched ring around the edge of the disk confines light at these wavelengths. The spectrum is composed of first order radial modes with reduced amplitude of the second order mode: higher order radial modes are not observed at all. The FSR is only governed by the first order radial modes, a factor of 5 improvement over the FSR of the microdisk. Such a device is better suited towards on-chip filtering techniques using QDs due to this increased free spectral range. At the time of writing, these devices are in the process of fabrication by Dr. Ben Royall. In addition, other approaches such as the use of nanobeam cavity based filters [201] are being investigated.

Bibliography

- [1] R. P. Feynman, *International Journal of Theoretical Physics* **21**, 467 (1982).
- [2] P. Shor, *Proceedings 35th Annual Symposium on Foundations of Computer Science* , 124 (1994).
- [3] S. R. White, *Physical Review B* **48**, 10345 (1993).
- [4] M. A. Nielsen and I. L. Chuang, *Cambridge University Press* (Cambridge University Press, 2011) p. 702.
- [5] D. P. DiVincenzo, *Fortschritte der Physik* **48**, 771 (2000).
- [6] A. J. Ramsay, *Semiconductor Science and Technology* **25**, 103001 (2010).
- [7] D. Loss and D. P. DiVincenzo, *Physical Review A* **57**, 120 (1998).
- [8] R. Warburton, *Nature Materials* **12**, 483 (2013).
- [9] G. Burkard, H.-A. Engel, and D. Loss, *Fortschritte der Physik* **48**, 15 (2000).
- [10] M. A. Nielsen, *Physical Review Letters* **93**, 40503 (2004).
- [11] V. Giovannetti, S. Lloyd, and L. MacCone, *Physical Review Letters* **96**, 13 (2006).
- [12] P. G. Kwiat, K. Mattle, H. Weinfurter, A. Zeilinger, A. Sergienko, and Y. Shih, *Physical Review Letters* **75**, 4337 (1995).
- [13] J. Cirac and P. Zoller, *Physical Review Letters* **74**, 4091 (1995).

- [14] Y. Nakamura, Y. A. Pashkin, and J. S. Tsai, *Nature* **398**, 4 (1999).
- [15] J. L. O'Brien, *Science (New York, N.Y.)* **318**, 1567 (2007).
- [16] N. A. Gershenfeld, *Science* **275**, 350 (1997).
- [17] A. Imamoglu and D. D. Awschalom, *Physical Review Letters* **83**, 4204 (1999).
- [18] M. G. Thompson, A. Politi, J. C. F. Matthews, and J. L. O'Brien, *IET Circuits, Devices & Systems* **5**, 94 (2011).
- [19] G. Reithmaier, S. Lichtmanecker, T. Reichert, P. Hasch, K. Müller, M. Bichler, R. Gross, and J. J. Finley, *Scientific Reports* **3**, 1901 (2013).
- [20] C. K. Hong, Z. Y. Ou, and L. Mandel, *Physical Review Letters* **59**, 2044 (1987).
- [21] J. O'Brien, J. A. Furusawa, and J. Vuckovic, *Nature Photonics* **3**, 687 (2009).
- [22] D. Englund, A. Faraon, B. Zhang, Y. Yamamoto, and J. Vuckovic, *Optics Express* **15**, 9 (2006).
- [23] G. J. Milburn, *Physical Review Letters* **62**, 2124 (1989).
- [24] B. Korzh, C. C. W. Lim, R. Houlmann, N. Gisin, M. J. Li, D. Nolan, B. Sanguinetti, R. Thew, and H. Zbinden, *Nature Photonics* **9**, 7 (2015).
- [25] A. Shields and Y. Zhiliang, *Physics World* **20**, 24 (2007).
- [26] A. R. Dixon, Z. L. Yuan, J. F. Dynes, A. W. Sharpe, and A. J. Shields, *Optics express* **16**, 18790 (2008).
- [27] A. R. Dixon, Z. L. Yuan, J. F. Dynes, A. W. Sharpe, and A. J. Shields, *Applied Physics Letters* **96** (2010), 10.1063/1.3385293.
- [28] K. Patel, J. Dynes, A. Sharpe, Z. Yuan, R. Penty, and A. Shields, *Electronics Letters* **48**, 111 (2012).
- [29] E. Knill, R. Laflamme, and G. J. Milburn, *Nature* **409**, 46 (2001).

-
- [30] C. Hong and L. Mandel, *Physical Review Letters* **56**, 58 (1986).
- [31] H. J. Kimble, M. Dagenais, and L. Mandel, *Physical Review Letters* **39**, 691 (1977).
- [32] P. Michler, A. Imamoglu, M. Mason, P. Carson, G. Strouse, and S. Buratto, *Nature* **406**, 968 (2000).
- [33] P. Lodahl, S. Mahmoodian, and S. Stobbe, *Reviews of Modern Physics* **87**, 14352 (2015).
- [34] Y. A. Vlasov, M. O'Boyle, H. F. Hamann, and S. J. McNab, *Nature* **438**, 65 (2005).
- [35] P. J. Shadbolt, M. R. Verde, A. Peruzzo, A. Politi, A. Laing, M. Lobino, J. C. F. Matthews, M. G. Thompson, and J. L. O'Brien, *Nature Photonics* **6**, 45 (2011).
- [36] P. Stepanov, A. Delga, X. Zang, J. Bleuse, E. Dupuy, E. Peinke, P. Lalanne, J.-M. Gérard, and J. Claudon, *Applied Physics Letters* **106**, 041112 (2015).
- [37] A. W. Snyder and J. Love, *Optical Waveguide Theory*, Science paperbacks (Springer, 1983).
- [38] J. Heebner, R. Grover, T. Ibrahim, and T. A. Ibrahim, *Optical Microresonators: Theory, Fabrication, and Applications* (Springer, 2007).
- [39] S. Fattah poor, T. B. Hoang, L. Midolo, C. P. Dietrich, L. H. Li, E. H. Linfield, J. F. P. Schouwenberg, T. Xia, F. M. Pagliano, F. W. M. van Otten, and A. Fiore, *Applied Physics Letters* **102**, 131105 (2013).
- [40] N. Prtljaga, R. J. Coles, J. O'Hara, B. Royall, E. Clarke, A. M. Fox, and M. S. Skolnick, *Applied Physics Letters* **104**, 231107 (2014).
- [41] S. Koseki, B. Zhang, K. De Greve, and Y. Yamamoto, *Applied Physics Letters* **94**, 2007 (2009).
- [42] M. N. Makhonin, J. Dixon, R. J. Coles, B. Royall, I. Luxmoore, E. Clarke, M. Hugues, M. Skolnick, and A. Fox, *Nano Letters* **14**, 6997 (2014).

- [43] I. Friedler, C. Sauvan, J. P. Hugonin, P. Lalanne, J. Claudon, and J. M. Gérard, *Optics express* **17**, 2095 (2009).
- [44] B. Gayral, J.-M. Gérard, A. Lemaître, C. Dupuis, L. Manin, and J. L. Pelouard, *Applied Physics Letters* **75**, 1908 (1999).
- [45] A. Kiraz, P. Michler, C. Becher, B. Gayral, A. Imamolu, L. Zhang, E. Hu, W. V. Schoenfeld, and P. M. Petroff, *Applied Physics Letters* **78**, 3932 (2001).
- [46] E. Peter, P. Senellart, D. Martrou, A. Lemaître, J. Hours, J. M. Gérard, and J. Bloch, *Physical Review Letters* **95**, 1 (2005).
- [47] K. Srinivasan and O. Painter, *Nature* **450**, 862 (2007).
- [48] P. Michler, A. Kiraz, L. Zhang, C. Becher, E. Hu, and A. Imamoglu, *Applied Physics Letters* **77**, 184 (2000).
- [49] P. Michler, A. Kiraz, C. Becher, W. V. Schoenfeld, P. M. Petroff, L. Zhang, E. Hu, and A. Imamoglu, *Science (New York, N.Y.)* **290**, 2282 (2000).
- [50] S. Koseki, *Monolithic Waveguide Coupled Gallium Arsenide Microdisk Microcavity Containing Indium Gallium Arsenide Quantum Dots* (Stanford University, 2008).
- [51] E. Yablonovitch, *Physical review letters* **58**, 2059 (1987).
- [52] J. D. Joannopoulos, S. G. Johnson, J. N. Winn, and R. D. Meade, *Photonic Crystals: Molding the Flow of Light (Second Edition)* (Princeton University Press, 2008).
- [53] A. Faraon, A. Majumdar, D. Englund, E. Kim, M. Bajcsy, and J. Vučković, *New Journal of Physics* **13**, 055025 (2011).
- [54] S. S. G. S. Johnson and J. D. J. Joannopoulos, *Optics Express* **8**, 363 (2001).
- [55] E. Yablonovitch, T. Gmitter, R. Meade, A. Rappe, K. Brommer, and J. Joannopoulos, “Donor and acceptor modes in photonic band structure,” (1991).
- [56] Y. Akahane, T. Asano, B.-S. Song, and S. Noda, *Nature* **425**, 944 (2003).

-
- [57] T. Yoshie, A. Scherer, J. Hendrickson, G. Khitrova, H. M. Gibbs, G. Rupper, C. Ell, O. B. Shchekin, and D. G. Deppe, *Nature* **432**, 200 (2004).
- [58] A. Faraon, I. Fushman, D. Englund, N. Stoltz, P. Petroff, and J. Vuckovic, *Optics Express* **16**, 12154 (2008).
- [59] W.-H. Chang, W.-Y. Chen, H.-S. Chang, T.-P. Hsieh, J.-I. Chyi, and T.-M. Hsu, *Physical Review Letters* **96** (2006).
- [60] M. Shirane, S. Kono, J. Ushida, S. Ohkouchi, N. Ikeda, Y. Sugimoto, and A. Tomita, *Journal of Applied Physics* **101**, 073107 (2007).
- [61] O. Painter, J. Vučković, and A. Scherer, *JOSA B* **16**, 275 (1999).
- [62] O. Painter, K. Srinivasan, J. D. O'Brien, A. Scherer, and P. D. Dapkus, *Journal of Optics A: Pure and Applied Optics* **3**, S161 (2001).
- [63] O. Painter and K. Srinivasan, *Optics letters* **27**, 339 (2002).
- [64] H.-Y. Ryu, M. Notomi, and Y.-H. Lee, *Applied Physics Letters* **83**, 4294 (2003).
- [65] I. J. Luxmoore, E. D. Ahmadi, A. M. Fox, M. Hugues, and M. S. Skolnick, *Applied Physics Letters* **98**, 041101 (2011).
- [66] I. J. Luxmoore, E. D. Ahmadi, B. J. Luxmoore, N. A. Wasley, A. I. Tartakovskii, M. Hugues, M. S. Skolnick, and A. M. Fox, *Applied Physics Letters* **100**, 121116 (2012).
- [67] A. C. T. Thijssen, M. J. Cryan, J. G. Rarity, and R. Oulton, *Optics Express* **20**, 22412 (2012).
- [68] M. Tinkham, *Group Theory and Quantum Mechanics*, Dover Books on Chemistry and Earth Sciences (Dover Publications, 2003).
- [69] Y. Ota, M. Shirane, M. Nomura, N. Kumagai, S. Ishida, S. Iwamoto, S. Yorozu, and Y. Arakawa, *Applied Physics Letters* **94**, 033102 (2009).

- [70] S. Laurent, S. Varoutsis, L. Le Gratiet, A. Lematre, I. Sagnes, F. Raineri, A. Levenson, I. Robert-Philip, and I. Abram, *Applied Physics Letters* **87**, 163107 (2005).
- [71] M. Notomi, K. Yamada, A. Shinya, J. Takahashi, C. Takahashi, and I. Yokohama, *Physical Review Letters* **87**, 1 (2001).
- [72] H. Gersen, T. Karle, R. Engelen, W. Bogaerts, J. Korterik, N. van Hulst, T. Krauss, and L. Kuipers, *Physical Review Letters* **94**, 3 (2005).
- [73] T. F. Krauss, *Journal of Physics D: Applied Physics* **40**, 2666 (2007).
- [74] S. J. Dewhurst, D. Granados, D. J. P. Ellis, A. J. Bennett, R. B. Patel, I. Farrer, D. Anderson, G. A. C. Jones, D. A. Ritchie, and A. J. Shields, *Applied Physics Letters* **96**, 031109 (2010).
- [75] V. Manga Rao and S. Hughes, *Physical Review B* **75**, 1 (2007).
- [76] T. Lund-Hansen, S. Stobbe, B. Julsgaard, H. Thyrrerstrup, T. Sünner, M. Kamp, A. Forchel, and P. Lodahl, *Physical Review Letters* **101**, 1 (2008).
- [77] A. Laucht, S. Pütz, T. Günthner, N. Hauke, R. Saive, S. Frédérick, M. Bichler, M.-C. Amann, A. Holleitner, M. Kaniber, and J. Finley, *Physical Review X* **2**, 1 (2012).
- [78] A. B. Young, A. Thijssen, D. M. Beggs, L. Kuipers, J. G. Rarity, and R. Oulton, *ArXiv* , 1406.0714 (2014).
- [79] H. Thyrrerstrup, L. Sapienza, and P. Lodahl, *Applied Physics Letters* **96**, 231106 (2010).
- [80] T. Ba Hoang, J. Beetz, L. Midolo, M. Skacel, M. Lerner, M. Kamp, S. Hoffing, L. Balet, N. Chauvin, and A. Fiore, *Applied Physics Letters* **100**, 061122 (2012).
- [81] T. B. Hoang, J. Beetz, M. Lerner, L. Midolo, M. Kamp, S. Höfling, and A. Fiore, *Optics express* **20**, 21758 (2012).
- [82] M. Arcari, I. Söllner, A. Javadi, S. L. Hansen, S. Mahmoodian, J. Liu, H. Thyrrerstrup, E. H. Lee, J. D. Song, S. Stobbe, and P. Lodahl, *ArXiv* , 1402.2081 (2014).

- [83] J. P. Sprengers, A. Gaggero, D. Sahin, S. Jahanmirinejad, G. Frucci, F. Mattioli, R. Leoni, J. Beetz, M. Lermer, M. Kamp, S. Hfling, R. Sanjines, and A. Fiore, *Applied Physics Letters* **99**, 2013 (2011).
- [84] C. C. M. Natarajan, M. M. G. Tanner, and R. H. Hadfield, *Superconductor Science and Technology* **25**, 63001 (2012).
- [85] Lumerical Solutions Inc., “Lumerical FDTD Solutions,” (2014).
- [86] J. Y. Marzin, J. M. Gérard, A. Izraël, D. Barrier, G. Bastard, and A. Izrael, *Physical Review Letters* **73**, 716 (1994).
- [87] A. Zrenner, *The Journal of Chemical Physics* **112**, 7790 (2000).
- [88] M. Bayer, G. Ortner, O. Stern, A. Kuther, A. Gorbunov, A. Forchel, P. Hawrylak, S. Fafard, K. Hinzer, T. Reinecke, S. Walck, J. Reithmaier, F. Klopff, and F. Schäfer, *Physical Review B* **65**, 1 (2002).
- [89] B. Gayral and J. M. Gérard, *Physica E: Low-Dimensional Systems and Nanostructures* **7**, 641 (2000).
- [90] C. Matthiesen, M. Geller, C. H. H. Schulte, C. Le Gall, J. Hansom, Z. Li, M. Hugues, E. Clarke, and M. Atatüre, *Nature Communications* **4**, 1600 (2013).
- [91] W. B. Gao, P. Fallahi, E. Togan, J. Miguel-Sanchez, and A. Imamoglu, *Nature* **491**, 426 (2012).
- [92] Y. Benny, S. Khatsevich, Y. Kodriano, E. Poem, R. Presman, D. Galushko, P. M. Petroff, and D. Gershoni, *Physical Review Letters* **106**, 1 (2011).
- [93] D. Press, T. D. Ladd, B. Zhang, and Y. Yamamoto, *Nature* **456**, 218 (2008).
- [94] E. Poem, O. Kenneth, Y. Kodriano, Y. Benny, S. Khatsevich, J. E. Avron, and D. Gershoni, *Physical Review Letters* **107**, 1 (2011).

- [95] T. M. Godden, J. H. Quilter, A. J. Ramsay, Y. Wu, P. Brereton, S. J. Boyle, I. J. Luxmoore, J. Puebla-Nunez, A. M. Fox, and M. S. Skolnick, *Physical Review Letters* **108**, 1 (2012).
- [96] P. Borri, W. Langbein, S. Schneider, U. Woggon, R. Sellin, D. Ouyang, and D. Bimberg, *Physical Review Letters* **87**, 157401 (2001).
- [97] P. Borri, W. Langbein, U. Woggon, V. Stavarache, D. Reuter, and A. D. Wieck, *Physical Review B - Condensed Matter and Materials Physics* **71**, 1 (2005).
- [98] A. J. Ramsay, R. S. Kolodka, F. Bello, P. W. Fry, W. K. Ng, A. Tahraoui, H. Y. Liu, M. Hopkinson, D. M. Whittaker, A. M. Fox, and M. S. Skolnick, *Physical Review B - Condensed Matter and Materials Physics* **75**, 1 (2007).
- [99] M. Munsch, J. Claudon, J. Bleuse, N. S. Malik, E. Dupuy, J. M. Gérard, Y. Chen, N. Gregersen, and J. Mørk, *Physical Review Letters* **108**, 1 (2012).
- [100] C. Matthiesen, A. N. Vamivakas, and M. Atatüre, *Physical Review Letters* **108**, 1 (2012).
- [101] M. Kroutvar, Y. Ducommun, D. Heiss, M. Bichler, D. Schuh, G. Abstreiter, and J. J. Finley, *Nature* **432**, 81 (2004).
- [102] E. A. Chekhovich, A. B. Krysa, M. S. Skolnick, and A. I. Tartakovskii, *Physical Review Letters* **106**, 1 (2011).
- [103] C. Santori, D. Fattal, J. Vucković, G. S. Solomon, and Y. Yamamoto, *Nature* **419**, 594 (2002).
- [104] M. Fox, *Quantum Optics: An Introduction*, Oxford Master Series in Physics (OUP Oxford, 2006).
- [105] J. Gérard, B. Sermage, B. Gayral, B. Legrand, E. Costard, and V. Thierry-Mieg, *Physical Review Letters* **81**, 1110 (1998).

- [106] E. T. Jaynes and F. W. Cummings, Proceedings of the IEEE **51**, 89 (1963).
- [107] J. P. Reithmaier, G. Sek, A. Löffler, C. Hofmann, S. Kuhn, S. Reitzenstein, L. V. Keldysh, V. D. Kulakovskii, T. L. Reinecke, and A. Forchel, Nature **432**, 197 (2004).
- [108] K. Hennessy, A. Badolato, M. Winger, D. Gerace, M. Atatüre, S. Gulde, S. Fält, E. L. Hu, and A. Imamolu, Nature **445**, 896 (2007).
- [109] A. Taflove, IEEE Transactions on Electromagnetic Compatibility The Artech House antenna and propagation library, **EMC-22**, 191 (1980).
- [110] A. F. Oskooi, D. Roundy, M. Ibanescu, P. Bermel, J. D. Joannopoulos, and S. G. Johnson, Computer Physics Communications **181**, 687 (2010).
- [111] Lumerical Solutions Inc., “Lumerical MODE Solutions,” (2014).
- [112] K. Yee, IEEE Transactions on Antennas and Propagation **14**, 302 (1966).
- [113] A. Taflove and S. Hagness, (2000).
- [114] R. Courant, K. Friedrichs, and H. Lewy, IBM journal of Research and ... (1967).
- [115] J.-P. Berenger, Journal of Computational Physics **114**, 185 (1994).
- [116] A. F. Oskooi, L. Zhang, Y. Avniel, and S. G. Johnson, Optics express **16**, 11376 (2008).
- [117] P.-R. Loh, A. Oskooi, M. Ibanescu, M. Skorobogatiy, and S. Johnson, Physical Review E **79**, 065601 (2009).
- [118] M. Koshiba, Y. Tsuji, and S. Sasaki, Microwave and Wireless ... **11**, 152 (2001).
- [119] M. Hammer and O. V. Ivanova, Optical and Quantum Electronics **41**, 267 (2009).
- [120] P. Y. Yu and M. Cardona, *Fundamentals of Semiconductors: Physics And Materials Properties*, 3rd ed., Advanced texts in physics No. 3 (Springer, 2005).
- [121] I. Stranski and L. Krastanow, Akademie der Wissenschaften Wien **146**, 797 (1938).

- [122] E. Bauer, *Zeitschrift fur Kristallographie* **110**, 372 (1958).
- [123] L. Goldstein, F. Glas, J. Y. Marzin, M. N. Charasse, and G. Le Roux, *Applied Physics Letters* **47**, 1099 (1985).
- [124] A. Cohen, *Scanning Electron Microscopy* **II**, 303 (1979).
- [125] R. Heitz, M. Veit, N. Ledentsov, A. Hoffmann, D. Bimberg, V. Ustinov, P. Kopev, and Z. Alferov, *Physical Review B* **56**, 10435 (1997).
- [126] N. H. Bonadeo, *Science* **282**, 1473 (1998).
- [127] S. Sauvage, P. Boucaud, R. P. S. M. Lobo, F. Bras, G. Fishman, R. Prazeres, F. Glotin, J. M. Ortega, and J.-M. Gérard, *Physical review letters* **88**, 177402 (2002).
- [128] E. Zibik, L. Wilson, R. Green, J. Wells, P. Phillips, D. Carder, J. Cockburn, M. Skolnick, M. Steer, H. Liu, and M. Hopkinson, *Semiconductor Science and Technology* **316**, 8 (2004).
- [129] K. Kuroda, T. Kuroda, K. Watanabe, T. Mano, K. Sakoda, G. Kido, and N. Koguchi, *Applied Physics Letters* **90**, 051909 (2007).
- [130] A. Muller, E. B. Flagg, P. Bianucci, X. Y. Wang, D. G. Deppe, W. Ma, J. Zhang, G. J. Salamo, M. Xiao, and C. K. Shih, *Physical Review Letters* **99**, 187402 (2007).
- [131] J. Johansen, B. Julsgaard, S. Stobbe, J. r. M. Hvam, and P. Lodahl, *Physical Review B - Condensed Matter and Materials Physics* **81**, 1 (2010).
- [132] J. Puebla, E. A. Chekhovich, M. Hopkinson, P. Senellart, A. Lemaitre, M. S. Skolnick, and A. I. Tartakovskii, *Physical Review B - Condensed Matter and Materials Physics* **88**, 1 (2013).
- [133] F. Grazioso, B. R. Patton, and J. M. Smith, *The Review of scientific instruments* **81**, 093705 (2010).

- [134] I. J. Luxmoore, N. A. Wasley, A. J. Ramsay, A. C. T. Thijssen, R. Oulton, M. Hugues, S. Kasture, V. G. Achanta, A. M. Fox, and M. S. Skolnick, *Physical Review Letters* **110**, 037402 (2013).
- [135] I. J. Luxmoore, N. A. Wasley, A. J. Ramsay, A. C. T. Thijssen, R. Oulton, M. Hugues, A. M. Fox, and M. S. Skolnick, *Applied Physics Letters* **103**, 241102 (2013).
- [136] M. Paillard, X. Marie, P. Renucci, T. Amand, A. Jbeli, and J. M. Gérard, *Physical Review Letters* **86**, 1634 (2001).
- [137] K. De Greve, L. Yu, P. L. McMahon, J. S. Pelc, C. M. Natarajan, N. Y. Kim, E. Abe, S. Maier, C. Schneider, M. Kamp, S. Höfling, R. H. Hadfield, A. Forchel, M. M. Fejer, and Y. Yamamoto, *Nature* **491**, 421 (2012).
- [138] H. Takagi, Y. Ota, N. Kumagai, S. Ishida, S. Iwamoto, and Y. Arakawa, *Optics express* **20**, 28292 (2012).
- [139] M. Larqué, T. Karle, I. Robert-Philip, and A. Beveratos, *New Journal of Physics* **11**, 033022 (2009).
- [140] G.-H. Kim, Y.-H. Lee, A. Shinya, and M. Notomi, *Optics Express* **12**, 6624 (2004).
- [141] Y. Yu, M. Heuck, S. Ek, N. Kuznetsova, K. Yvind, and J. Mork, *Applied Physics Letters* **101**, 251113 (2012).
- [142] A. Faraon, E. Waks, D. Englund, I. Fushman, and J. Vuckovic, *Applied Physics Letters* **90**, 073102 (2007).
- [143] A. R. Alija, L. J. Martinez, P. A. Postigo, C. Seassal, and P. Viktorovitch, *Applied Physics Letters* **89**, 101102 (2006).
- [144] L. J. Martinez, A. Garcia-Martin, and P. A. Postigo, in *Microtechnologies for the New Millennium 2005*, edited by G. Badenes, D. Abbott, and A. Serpenguzel (International Society for Optics and Photonics, 2005) pp. 879–884.

- [145] A. Schwagmann, S. Kalliakos, D. J. P. Ellis, I. Farrer, J. P. Griffiths, G. A. C. Jones, D. A. Ritchie, and A. J. Shields, *Optics express* **20**, 28614 (2012).
- [146] V. A. Mandelshtam and H. S. Taylor, *The Journal of Chemical Physics* **107**, 6756 (1997).
- [147] Y. Sato, Y. Tanaka, J. Upham, Y. Takahashi, T. Asano, and S. Noda, *Nature Photonics* **6**, 56 (2011).
- [148] N. A. Wasley, I. J. Luxmoore, R. J. Coles, E. Clarke, A. M. Fox, and M. S. Skolnick, *Applied Physics Letters* **101**, 051116 (2012).
- [149] E. Waks and J. Vuckovic, *Optics express* **13**, 5064 (2005).
- [150] E. Moreau, I. Robert, J. M. Gérard, I. Abram, L. Manin, and V. Thierry-Mieg, *Applied Physics Letters* **79**, 2865 (2001).
- [151] M. Winger, T. Volz, G. Tarel, S. Portolan, A. Badolato, K. Hennessy, E. Hu, A. Beveratos, J. Finley, V. Savona, and A. Imamolu, *Physical Review Letters* **103**, 207403 (2009).
- [152] C. Bentham, I. E. Itskevich, R. J. Coles, B. Royall, E. Clarke, J. . O' Hara, N. Prtljaga, A. M. Fox, M. S. Skolnick, and L. R. Wilson, *Applied Physics Letters* **106**, 221101 (2015).
- [153] S. Tanzilli, A. Martin, F. Kaiser, M. P. De Micheli, O. Alibart, and D. B. Ostrowsky, *Laser & Photonics Reviews* **6**, 115 (2012).
- [154] H. J. Kimble, *Nature* **453**, 1023 (2008).
- [155] A. Yariv and P. Yeh, *Photonics: Optical Electronics in Modern Communications*, The Oxford series in Electrical and Computer Engineering (Oxford University Press, 2007).
- [156] B. E. A. Saleh and M. C. Teich, *Fundamentals of Photonics*, Wiley Series in Pure and Applied Optics (Wiley, 2007).

-
- [157] J. Bleuse, J. Claudon, M. Creasey, N. S. Malik, J. M. Gérard, I. Maksymov, J. P. Hugonin, and P. Lalanne, *Physical Review Letters* **106**, 2 (2011).
- [158] D. Marcuse, *Quantum Electronics, IEEE Journal of* **29**, 2957 (1993).
- [159] D. Marcuse, A. Telephone, and T. Company, *Theory of Dielectric Optical Waveguides, Quantum Electronics—Principles & Applications* (Academic Press, 1991).
- [160] R. Ohta, Y. Ota, H. Takagi, N. Kumagai, K. Tanabe, S. Ishida, S. Iwamoto, and Y. Arakawa, **1**, 60 (2012).
- [161] J. P. Bradley, I. E. Itskevich, B. Royall, C. Bentham, N. Prtljaga, E. Clarke, A. M. Fox, M. S. Skolnick, and L. R. Wilson, in *UK Semiconductors 2015* (Sheffield, 2015).
- [162] A. Laucht, F. Hofbauer, N. Hauke, J. Angele, S. Stobbe, M. Kaniber, G. Böhm, P. Lodahl, M.-C. Amann, and J. J. Finley, *New Journal of Physics* **11**, 023034 (2009).
- [163] R. Brouri, A. Beveratos, J. P. Poizat, and P. Grangier, *Optics letters* **25**, 1294 (2000).
- [164] R. B. Patel, A. J. Bennett, I. Farrer, and C. A. Nicoll, *Nature Photonics* **4**, 632 (2010).
- [165] F. Hofbauer, S. Grimminger, J. Angele, G. Bohm, R. Meyer, M. C. Amann, and J. J. Finley, *Applied Physics Letters* **91**, 201111 (2007).
- [166] R. Mitsch, C. Sayrin, B. Albrecht, P. Schneeweiss, and a. Rauschenbeutel, *Nature Communications* **5**, 1 (2014).
- [167] J. Petersen, J. Volz, and A. Rauschenbeutel, *Science (New York, N.Y.)* **346**, 67 (2014).
- [168] M. Neugebauer, T. Bauer, P. Banzer, and G. Leuchs, *Nano Letters* **14**, 2546 (2014).
- [169] C. Junge, D. O’Shea, J. Volz, and A. Rauschenbeutel, *Physical Review Letters* **110**, 1 (2013).
- [170] F. J. Rodríguez-Fortuño, I. Barber-Sanz, D. Puerto, A. Griol, and A. Martinez, *ACS Photonics* , 140826134849006 (2014).

- [171] I. Söllner, S. Mahmoodian, S. L. Hansen, L. Midolo, A. Javadi, G. Kiršansk, T. Pregnolato, H. El-Ella, E. H. Lee, J. D. Song, S. Stobbe, and P. Lodahl, ArXiv , 1406.4295 (2015).
- [172] S. Hughes, L. Ramunno, J. Young, and J. Sipe, Physical Review Letters **94**, 1 (2005).
- [173] L. O’Faolain, T. P. White, D. O’Brien, X. Yuan, M. D. Settle, and T. F. Krauss, Optics express **15**, 13129 (2007).
- [174] S. M. Saad, IEEE Transactions on Microwave Theory and Techniques **33**, 894 (1985).
- [175] D. Gammon, E. Snow, B. Shanabrook, D. Katzer, and D. Park, Physical Review Letters **76**, 3005 (1996).
- [176] R. Seguin, A. Schliwa, S. Rodt, K. Potschke, U. W. Pohl, and D. Bimberg, Physical Review Letters **95**, 10 (2005).
- [177] A. Kuther, M. Bayer, A. Forchel, A. Gorbunov, V. Timofeev, F. Schäfer, and J. Reithmaier, Physical Review B **58**, R7508 (1998).
- [178] M. Bayer, A. Kuther, A. Forchel, A. Gorbunov, V. B. Timofeev, F. Schäfer, and J. P. Reithmaier, Physical Review Letters **82**, 22 (1999).
- [179] J. Finley, D. Mowbray, M. Skolnick, A. Ashmore, C. Baker, A. Monte, and M. Hopkinson, Physical Review B **66**, 4 (2002).
- [180] M. Soltani, S. Yegnanarayanan, and A. Adibi, Optics Express **15**, 4694 (2007).
- [181] B. D. Jones, M. Oxborrow, V. N. Astratov, M. Hopkinson, A. Tahraoui, M. S. Skolnick, and A. M. Fox, Optics express **18**, 22578 (2010).
- [182] E. Waks and J. Vuckovic, Physical Review Letters **96**, 1 (2006).
- [183] A. Auffèves-Garnier, C. Simon, J.-M. Gérard, and J.-P. Poizat, Physical Review A **75**, 053823 (2007).

- [184] D. Englund, A. Faraon, I. Fushman, N. Stoltz, P. Petroff, and J. Vucković, *Nature* **450**, 857 (2007).
- [185] M. G. Tanner, C. M. Natarajan, V. K. Pottapenjara, J. A. O'Connor, R. J. Warburton, R. H. Hadfield, B. Baek, S. Nam, S. N. Dorenbos, E. B. Urea, T. Zijlstra, T. M. Klapwijk, and V. Zwiller, *Applied Physics Letters* **96**, 2 (2010).
- [186] A. Yariv, *Electronics Letters* **36**, 321 (2000).
- [187] I. Teraoka, S. Arnold, and F. Vollmer, *Journal of the Optical Society of America B* **20**, 1937 (2003).
- [188] A. B. Matsko and V. S. Ilchenko, *Selected Topics in Quantum Electronics*, *IEEE Journal of* **12**, 3 (2006).
- [189] V. S. Ilchenko and A. B. Matsko, *IEEE Journal on Selected Topics in Quantum Electronics* **12**, 15 (2006).
- [190] N. C. Frateschi and A. F. J. Levi, *Applied Physics Letters* **2934**, 2932 (1995).
- [191] Y. Panitchob, G. S. Murugan, M. N. Zervas, P. Horak, S. Berneschi, S. Pelli, G. Nunzi Conti, and J. S. Wilkinson, *Optics express* **16**, 11066 (2008).
- [192] K. R. Hiremath and V. N. Astratov, *Optics express* **16**, 5421 (2008).
- [193] L. Feng, Z. J. Wong, R.-M. Ma, Y. Wang, and X. Zhang, *Science* **346**, 972 (2014).
- [194] C. Manolatou, M. J. Khan, S. Fan, P. R. Villeneuve, H. A. Haus, and J. D. Joannopoulos, *IEEE Journal of Quantum Electronics* **35**, 1322 (1999).
- [195] D. Rafizadeh, J. P. Zhang, S. C. Hagness, A. Taflove, K. A. Stair, S. T. Ho, and R. C. Tiberio, *Optics letters* **22**, 1244 (1997).
- [196] E. A. J. Marcatili, *Bell System Technical Journal* **48**, 2103 (1969).
- [197] M. J. Conterio, N. Skold, D. Ellis, I. Farrer, D. A. Ritchie, A. J. Shields, and N. Sköld, *Applied Physics ...* **103**, 162108 (2013).

- [198] A. Laucht, T. Gunthner, S. Putz, R. Saive, S. Frederick, N. Hauke, M. Bichler, M.-C. Amann, A. W. Holleitner, M. Kaniber, and J. J. Finley, *Journal of Applied Physics* **112**, 093520 (2012).
- [199] J. Li, T. P. White, L. O’Faolain, A. Gomez-Iglesias, and T. F. Krauss, *Optics express* **16**, 6227 (2008).
- [200] J. Liang, L.-Y. Ren, M.-J. Yun, X. Han, and X.-J. Wang, *Journal of Applied Physics* **110**, 063103 (2011).
- [201] J. S. Foresi, P. R. Villeneuve, and J. Ferrera, *Nature* , 143 (1997).